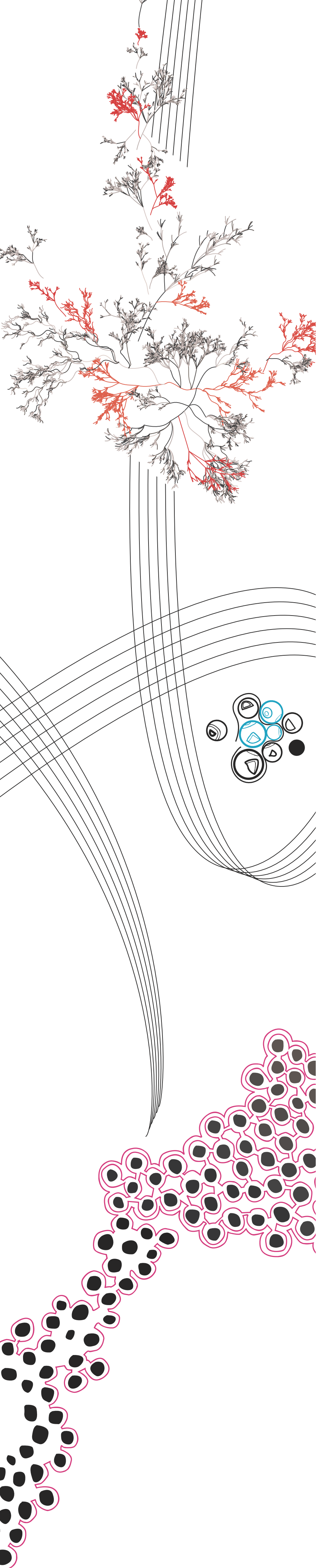

MASTER INTERNSHIP ASSIGNMENT

INLINE MIXING OF HIGHLY VISCOUS SLUDGE

Author
S.A.M. Lensink-Ebing, s1565567

Company
Witteveen+Bos
Energy, Water & Environment
Wastewater - Mechanical Engineering

Address
Van Twickelostraat 2, Deventer, the Netherlands

Internship Period
21 February 2017 - 7 July 2017

Supervisors Witteveen+Bos
M. van der Werf
C. Roose

Supervisor University of Twente
C.H. Venner

Faculty of Engineering Technology (ET)
Mechanical Engineering

Thermal & Fluid Engineering

UNIVERSITY OF TWENTE.

Preface

This report is meant to give an overview of what I have done and learned during my internship at Witteveen+Bos and to serve as a reference for the water board and future trainees or graduates who would like to continue this research.

At the start of my internship I did not know anything about waste water treatment plants, sludge, non-Newtonian fluids and how to work with a commercial CFD software package. Or about the value of a coffee machine and a daily lunch walk.

Several weeks I struggled to find out how I should approach the problem. A lot of time I spent on looking for a suitable validation instrument, learning what the many options of the CFD software were and which I should use and based on this deciding which software package to employ. The learning curve of the CFD software was very high and till the end I kept on learning. Hence, this research is not flawless and can still be improved.

Truth and honesty I consider to be of supreme importance, and those two were my guidances when writing the report. In the final three weeks I discovered that the mesh quality was not as good as I hoped, which was disappointing. Moreover, I found out that the results of one of the models were mesh dependent and I did not had time to resolve this problem. This was very distressing and I rather would not have mentioned it at all, but I considered truth and honesty more valuable.

Furthermore I would like to thank all my colleagues who warmly welcomed me, helped me out and gave me a good time. I want to thank Evan for reading part of my report and giving feedback especially on my use of English and Arie for his support concerning the CFD modelling. I also want to thank my supervisors Chris and Mark for giving feedback and thinking along with me during the process. Lots of appreciation also to my husband Daan for supporting me in the tough start, encouraging me, thinking along with me, and giving feedback on this enormous report. Without his support, also in the practical matters such as shopping, preparing dinner and taking care of the household, I would not have made it this far. And above all I want to thank God, who gave me new life, strengthened me and kept me up, beyond all expectations.

> “*Great are the works of the LORD;*
> *They are studied by all who delight in them.*”
>
> Psalm 111:2, *New American Standard Bible*

Abstract

After implementing a new process, Thermal Hydrolysis Process (THP), at the wastewater treatment plant (WWTP) in Hengelo, the mixing in the digester was not homogeneous anymore. The goal of this research was to improve the inline mixing of three types of sludge in the pipeline entering the digester.

Sludge behaves as a non-Newtonian fluid. Rheological measurements were performed on the different sludge types to determine the relation between the viscosity and shear rate, and to fit a non-Newtonian model. This was used as input in a CFD model made in ANSYS FLUENT of the relevant pipes to test the mixing of five different geometries. The $k-\varepsilon$ turbulence model was used together with the species transport and discrete model. The CFD model was validated using pressure measurements.

The power law was chosen as non-Newtonian model and fitted on viscosity measurements performed by the TU Delft. The main conclusion of the CFD modelling was that a venturi with a diameter of 40 mm gave the best mixing results. However, when determining the discretization error, the numerical solution appeared to be mesh dependent. This was likely caused by the sensitivity of the $k-\varepsilon$ model to disturbances which arose due to the turbulence generated by the venturi. Hence, validation on pressure did not fully succeed.

A next step would be to choose a more suitable turbulence model and perform the simulations on a mesh with a higher resolution.

Keywords: CFD modelling, inline mixing, $k-\varepsilon$ model, non-Newtonian, power law model, sludge, venturi.

Contents

Nomenclature

Acronyms

CFD	Computational Fluid Dynamics	
RMSE	Root mean square error	-
$\mathrm{VBI}_{\mathrm{mix}}$	Viscosity Blending Index of the mixture	-
VBI_i	Viscosity Blending Index of component i	-
WVS	Water board Vechtstromen	
WWTP	Wastewater Treatment Plant	
R^2	Coefficient of determination	-
Re	Dimensionless Reynolds number	-
Re_p	Dimensionless relative Reynolds number of the particle	-
Sc_t	Dimensionless turbulent Schmidt number	-

Greek Symbols

α_i	Torque	%
$\bar{\mu}$	Viscosity of the mixture	$\mathrm{Pa \cdot s}$
$\bar{\rho}$	Density of the mixture	$\mathrm{kg/m^3}$
δ_{ij}	The Dirac delta function	-
ϵ	Dimensionless constant in equation (2.2.20)	-
γ	Shear rate	$\mathrm{s^{-1}}$
λ	Relaxation time; natural time	s
μ	(Apparent dynamic) viscosity	$\mathrm{Pa \cdot s}$
μ_0	Zero shear viscosity; plateau viscosity	$\mathrm{Pa \cdot s}$
μ_∞	Infinite shear viscosity	$\mathrm{Pa \cdot s}$
μ_{eff}	Effective viscosity	$\mathrm{Pa \cdot s}$
μ_B	Plastic viscosity	$\mathrm{Pa \cdot s}$
μ_t	Turbulent viscosity; eddy viscosity	$\mathrm{Pa \cdot s}$
ν	Kinematic viscosity	cS
ω	Angular velocity	rad/s
ϕ	Dry solid contents	$10^{-3}\mathrm{kg/L}$
ϕ_j	Solution of the key variable on grid j	?
ρ	Density	$\mathrm{kg/m^3}$
ρ_p	Density of the particle	$\mathrm{kg/m^3}$
τ	Shear stress	Pa
τ_0	Yield shear stress	Pa
τ_{ij}	Deviatoric stress tensor component	Pa

Roman Symbols

$\bar{T}$	Average temperature	K
ΔP	Pressure drop	Pa

$\vec{A}_i$	Area factor of face i	-
$\vec{c}_i$	Vector of the centroid of the cell to the centroid of the adjacent cell sharing face i	-
$\vec{f}_i$	Vector of the centroid of the cell to the centroid of face i	-
$\vec{J}_i$	Diffusion flux of species i	m
$\vec{u}$	Velocity	m/s
$\vec{u}_p$	Velocity of the particle	m/s
a	Constant of the Refutas equation (2.2.27)	14.534
b	Constant of the Refutas equation (2.2.27)	0.8
c	Constant of the Refutas equation (2.2.27)	10.975
C_D	Drag coefficient	-
C_{vm}	Virtual mass factor	-
d	Constant of the Chevron equation (2.2.30)	$3\ln 10$
D_i	Mass diffusion coefficient of species i	$\mathrm{m^2/s}$
d_p	Diameter of the particle	m
D_t	Turbulent diffusivity	$\mathrm{m^2/s}$
$D_{i,T}$	Thermal diffusion coefficient of species i	$\mathrm{kg \cdot s/m}$
ds	Dry solid contents	%
E_a	Activation energy	kJ/mol
F_i	All forces working on the object in direction i	N
g_i	Gravitation acceleration in direction i	$\mathrm{m/s^2}$
G_k	Generation of turbulent kinetic energy	Pa/s
h	Height of the measured fluid on the inner cylinder	m
h	Representative mesh size	m
K	Emperical constant of equation (2.2.17)	$\mathrm{Pa \cdot s}$
k	Dimensionless constant in equation (2.2.20)	-
k	Fluid consistency coefficient	$\mathrm{Pa \cdot s^n}$
k	Kinetic turbulent energy	J/kg
$k_{\alpha\tau}$	Spindle constant	-
$k_{N\gamma}$	Spindle and flow index constant	-
L	Characteristic length scale	m
M	Measured torque	$\mathrm{N \cdot m}$
m_{tot}	Total mass of the mixture	kg
m_i	Mass of species i	kg
N	Rotational speed	rpm
n	Flow behaviour index; power index	-
P	Pressure	Pa
p	(Apparent) order of convergence	-
R	The universal gas constant	$8.314 \cdot 10^{-3}$ $\mathrm{kJ \cdot mol/K}$
R_i	Net rate of production of species i by chemical reaction	$\mathrm{kg \cdot s/m^3}$
R_i	Radius of the inner cylinder	m
R_o	Radius of the outer cylinder	m
S	Modulus of the mean rate-of-strain tensor	$\mathrm{s^{-1}}$
S_i	Rate of creation of species i by other sources	$\mathrm{kg \cdot s/m^3}$
T	Temperature	K
t	Time	s
T_0	Standard temperature	293.15 K
U_i	Ensemble-averaged or time-averaged velocity in the i-th direction	m/s
U_i	Fluctuating velocity component in the i-th direction	m/s

u_i	Velocity in the i-th direction	m/s
V_{tot}	Total volume of the mixture	m^3
V_i	Volume species i occupies	m^3
v_i	Volume fraction of component i	-
x_i	Distance component in the i-th direction	m
y_i	Mass fraction of component i	-

Chapter 1

Introduction

At a wastewater treatment plant (WWTP) wastewater is purified. During this purification process sludge is formed. This sludge is often digested at the wastewater treatment plant in order to stabilize the sludge, to reduce the amount of sludge and to produce biogas.

1.1 Problem Definition

In order to digest more sludge at the location and to increase the biogas production, pre-treatment processes can be applied to the sludge before entering the digester. At the wastewater treatment plant in Hengelo a thermal treatment step, Thermal Hydrolysis Process (THP, or TDH in Dutch), is implemented. This results in a higher dry solids feed to the digester.

It was expected that the increase in dry solids content would be levelled out by the lower viscosity of the THP sludge. However, after realization of the THP process, the mixing system in the digester was not able to maintain a homogeneous mixture of the sludge. To improve the mixing in the digester, alternative mixing systems are considered by the water board but the expectation is that these will not be able to maintain a sufficient homogeneous mixture.

Problem
The mixing of the sludge in the digester is not homogeneous.

1.2 Goal

The digester is fed with three different types of sludge, namely THP, primary and digested sludge recirculated from the digester. Those three kinds differ in dry solids content, temperature and viscosity. To improve the mixing in the digester it would be beneficial for the sludge entering the tank to be homogeneous.

To achieve this, THP and primary sludge are injected in a recirculation pipe of the digester in order to create inline mixing of the sludge entering the digester. Turbulent flow was provoked by partially closing the pipe, but this caused clogging. At the moment a venturi is installed to provoke turbulent flow and hence achieve a good mixing. It is not clear yet how effective this pre-mixing in the pipe is.

Goal
Improve the mixing of sludge in the pipeline entering the digester.

1.3 Method

By building a Computational Fluid Dynamics (CFD) model of the relevant piping system the flow, is visualised and the geometry of the pipes can be optimized to attain a good mixture. Because sludge tends to behave as a non-Newtonian fluid, viscosity measurements are needed to correctly model the sludge.

Since this is a computer model, it needs validation to determine how good it models the flow. Therefore measurements of the flow in the pipes are required.

1.3.1 CFD Model

A CFD model of the relevant piping system was build up and five different geometries were tested, one being the baseline, without adjustments to improve the flow, the other four containing optimizations to improve mixing.

Although there were three types of sludge, first a single phase flow of one type of sludge was assumed to reduce the computational effort and to get an impression of the behaviour of the flow. Digested sludge of the digester was chosen as this one had the highest flow rate. Next a multiphase flow was assumed using the species transport model in which the densities and viscosities of the three types of sludge mixed.

1.3.2 Viscosity Measurements

Most types of sludge behave as a non-Newtonian fluid. This implies that the viscosity is not constant but depends upon, among other things, time, shear rate and geometry. The composition of sludge greatly differs per plant and per season. It is therefore difficult to establish a general model for the viscosity of sludge, especially for sludge with a high dry solids content. That is why viscosity measurements of the three types of sludge were needed to model the mixing.

1.3.3 Validation Measurements

To validate the CFD model the pressure drop over a venturi with a narrowing of 40 mm was measured. Besides, five samples were taken behind the venturi, over the diameter, and the dry solids content was determined. This gave an indication of the mixing.

1.4 Structure of the Report

First a literature study is done in Chapter 2 in order to make clear what a WWTP is and how the different sludge types are formed, to explain the behaviour of sludge as a non-Newtonian fluid and how this can be measured, and to investigate the possibilities of the CFD software package FLUENT.

In Chapter 3 the research method is described concerning the measurements of viscosity, how the CFD simulations were produced and validated. The results of the viscosity measurements and the CFD simulations and validation is described in Chapter 4.

Final conclusions are drawn and described together with some remarks in Chapter 5. At last recommendations are given for further research and enhancement of the mixing in Chapter 6.

The following appendices are attached. In Appendix A I wrote an essay about Witteveen+Bos as employer and my working experience. Appendix B describes the mathematical procedure to convert relative viscosity values to absolute viscosity values and a non-Newtonian model is fitted on the measurements of WVS. To investigate which geometry would give best mixing nine smaller models were simulated. These models and their results are found in Appendix C. Additional CFD results are given in Appendix D, consisting of plots of the mass fractions of digested sludge for all models. Also a description and the results of Model 6 - Venturi D50 are given. This model was intended to be validated, but this did not take place. Finally, a short overview of the quest for a suitable validation instrument is given in Appendix E.

Chapter 2

Literature

A literature study is done to make clear what a wastewater treatment plant is and how the different types of sludge are formed, to explain the behaviour of sludge as a non-Newtonian fluid and how this can be measured, and to investigate the possibilities of the CFD software package FLUENT.

2.1 Wastewater Treatment Plant

The goal of a wastewater treatment plant (WWTP) is to purify wastewater and to do this as environmentally friendly as possible. Municipal, and in some areas industrial, wastewater is collected at a WWTP and is processed in several steps before it is discharged into the surface water. In figure 2.1.1 a picture of the WWTP in Hengelo is depicted.

Figure 2.1.1: Wastewater treatment plant in Hengelo (Vechtstromen, 2013).

WWTPs differ in which processes they use to purify the wastewater. This depends upon, among other thing, the composition of the wastewater (mainly municipal or heavy industries), the area in which the treatment plant is located (outside or in a residential area) and new insights (for example the Nereda technology). Still the principal processes remain the same.

First the water is elevated by a pump, in Hengelo this is done by a screw pump, as the water flows through the rest of the plant only by gravity. The next step, sometimes executed before the elevation, is to mechanically filter the wastewater in order to remove large waste, such as wood, plastic, toilet wipes, and tampons, which could damage pumps and cause clogging. This is usually done by a bar screen or rack. Sometimes there is a special filter after this stage, such as a sand trap to remove smaller particles like sand or clay.

The wastewater is then pretreated in large pre-settling basins. Particles which can settle and are not dissolved in the water are separated from the water in this tank by sedimentation. These particles form primary sludge. During this process particles can have a tendency to form flakes. This flocculation occurs especially at higher concentrations of undissolved particles and can be influenced by adding chemicals. Primary sludge is characterized by a highly inhomogeneous structure. After pre-settling primary sludge settles further in a settling basin.

Then secondary treatment of the wastewater follows. This step consists of biological filtering of the wastewater by bacteria. They convert harmful substances into less harmful substances and feed on the biological content present in the wastewater. This is usually done by aerobic bacteria which require oxygen to live.

After this stage the wastewater with the bacteria flows to secondary sedimentation tanks to give particles enough time to settle. Sludge formed in these basins is called secondary sludge. Secondary sludge then flows to a settling tank to enable the particles to settle even further. Usually after this sedimentation the water is clean enough to meet the discharge requirements, but sometimes additional nitrogen or phosphate removal is necessary (Delft, 2008).

2.1.1 Sludge

The sludge formed during the purification of the wastewater is usually treated at the WWTP to reduce the total amount of sludge and to de-water it as much as possible before it is carried away by truck to Moerdijk. There the sludge undergoes some additional treatments depending on the WWTP it is originating from because of emission to the environment when it is burned in the last stage.

One way to reduce the amount of sludge is by digestion. In Hengelo three digesters are available. During this process biogas arises which is burned to generate electricity and heat. In the context of the WWTP as an energy factory a new process treatment is implemented in Hengelo, namely Thermal Hydrolysis Process (THP), in Dutch Thermische Druk Hydrolyse (TDH). In this process steam is formed under a pressure of 11 bara at a temperature of 180 °C and this is injected in a reactor containing sludge, heating it to 160 °C under a pressure of 7 bara. In this way structures which are difficult to process by bacteria are broken down to components which they can process. The resulting sludge, called THP sludge, has a lower viscosity and is therefore easier to process by for example pumps. Hence the digester loading can be increased as the sludge is easier to digest for the bacteria and the biogas production can therefore be increased. Besides, the sludge is more stable (Delft, 2008).

After the sludge is digested in the digester, it is de-watered to reduce the amount of sludge further and driven away to Moerdijk.

Three different types of sludge are present at the WWTP in Hengelo, namely primary sludge, secondary sludge (both also originating from smaller WWTPs in the local area) and THP sludge. The composition of these sludge types differ on for example the dry solids content (the amount of solids when the water is evaporated from the sludge), the temperature and the viscosity. Per type the composition also changes with the seasons, due to for example rainfall and seasonal eating habits. Although sludge still contains a lot of water, its flow behaviour differs quite a lot from water. Sludge behaves as a non-Newtonian fluid whereas water can be considered as a Newtonian fluid (Eshtiaghi, Markis, Yap, Baudez, & Slatter, 2013).

2.2 Non-Newtonian Fluids

The main difference between Newtonian fluids and non-Newtonian fluids are their viscous behaviour. Viscosity can be described as the resistance of the material to flow. If a fluid has a high viscosity, such as honey, there is a lot of internal friction against the shearing of layers in the fluid. Water is an example of a fluid with a relatively low viscosity.

In the case of a Newtonian fluid in laminar flow, the shear stress has a linear relationship with the shear rate, namely by

$$\tau = \mu\gamma = \mu\frac{du}{dy}, \tag{2.2.1}$$

with

τ shear stress[Pa]
μ dynamic viscosity [Pa · s]
u velocity in x-direction [m/s]
γ shear rate [s^{-1}]

For a schematic representation see Figure 2.2.2.

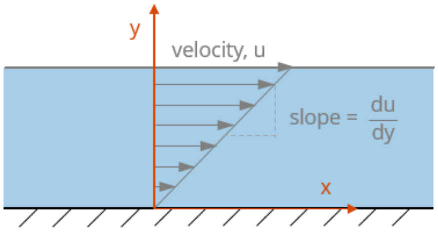

Figure 2.2.2: Unidirectional shearing laminar flow.

The ratio of of the shear stress to the shear rate is called the Newtonian dynamic viscosity μ. For Newtonian fluids it is constant, independent of the shear stress and shear rate exercised and it depends only on the material, its temperature and pressure (Chhabra & Richardson, 2008). A plot of the shear stress against the shear rate, also called a flow curve or rheogram, is therefore a straight line, passing through the origin with slope μ, see figure 2.2.3.

2.2.1 Definition

A non-Newtonian fluid can be defined as a fluid whose flow curve is non-linear or does not pass through the origin. The viscosity in this case is called the apparent dynamic viscosity and frequently depicted by η. In the rest of this report it will be referred to with μ and the prefix ‘apparent dynamic’ is dropped for ease. The viscosity of a non-Newtonian fluid does not have to be constant at a given temperature and pressure, but may also depend on the shear stress, shear rate, geometry, time and so on.

Non-Newtonian fluids are frequently encountered in real life and industry. Biological fluids, such as blood and salvia, are non-Newtonian, as well as paints, drilling muds, sewage sludge and ice-cream. The non-Newtonian behaviour can be characterized by time-independent, time-dependent and viscoelastic fluid behaviour. Often fluids display a combination of these characteristics (Chhabra & Richardson, 2008).

2.2.2 Time-independent

The behaviour of non-Newtonian fluids can be independent of time. In this case, the shear stress is only a function of shear rate (note that it still may depend on temperature, pressure and so on). Three types of time-independent behaviour can be distinguished, namely shear-thinning, viscoplastic and shear-thickening. The flow curves are displayed in figure 2.2.3.

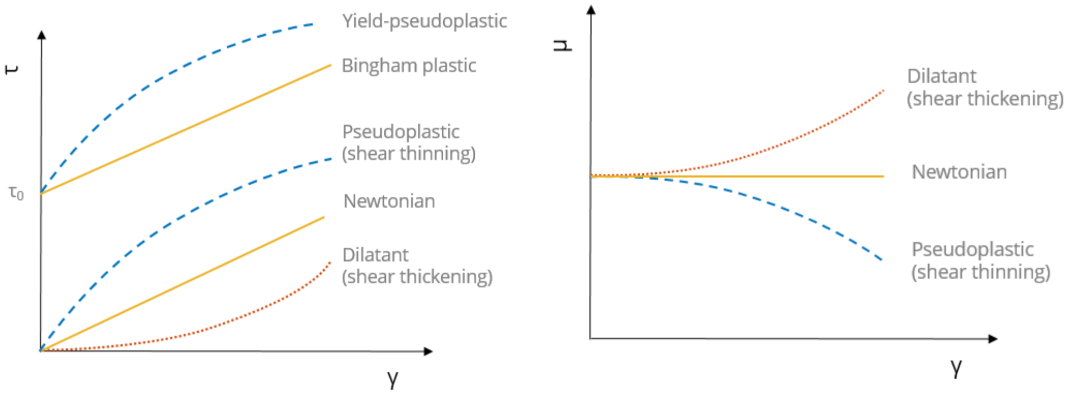

(a) Shear stress τ against shear rate γ.   (b) Viscosity μ against shear rate γ.

Figure 2.2.3: Types of time-independent flow behaviour.

Shear-thinning

For shear-thinning fluids, also called pseudo plastics, the viscosity decreases with increasing shear rate. In the case of very low shear rates, $\gamma < 10^{-2}$ s^{-1}, and very high shear rates, $\gamma > 10^5$ s^{-1}, shear-thinning fluids often exhibit Newtonian behaviour. These limits are called the zero shear viscosity μ_0 and infinite shear viscosity μ_∞. Examples of shear-thinning fluids are paint, nail polish, ink and blood (Chhabra & Richardson, 2008; Sahin & Sumnu, 2006).

Several mathematical models are developed to link the shear rate to the shear stress and viscosity for shear-thinning fluids. Four of them are discussed.

Power law model
The power law, also called the Ostwald-de Waele law named after its inventors, relates the shear stress to the shear rate by

$$\tau = \mu\gamma = k\gamma^n, \tag{2.2.4}$$

and the viscosity to the shear rate by

$$\mu = k\gamma^{n-1}. \tag{2.2.5}$$

with

k fluid consistency coefficient [Pa·s^n]
n flow behaviour index [-]

The values for k and n are empirically determined. In a loglog plot of the viscosity against the shear rate, see figure 2.2.6, the following relationship exists $\log \mu = \log k + (n-1)\log \gamma$. Hence, $n-1$ is the slope of the straight line and k determines the height. As the name of n implies it indicates the flow behaviour:

$n < 1$ shear-thinning behaviour
$n = 1$ Newtonian behaviour
$n > 1$ shear-thickening behaviour

The power law model is one of the most simple among all non-Newtonian models and is most widely applied, despite several drawbacks such as that it applies to a limited range of shear rates and the value of k typically depends on n (Chhabra & Richardson, 2008).

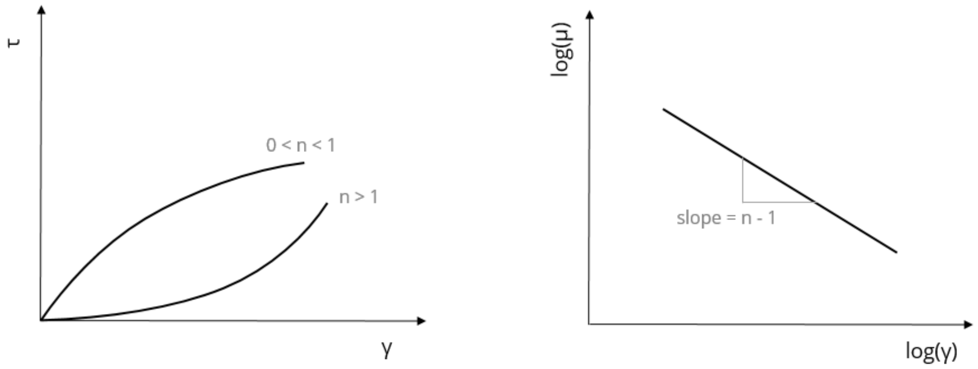

(a) Plot of the shear stress τ against the shear rate γ.

(b) Loglog plot of the viscosity μ against shear rate γ, for a shear-thinning fluid with $n < 1$.

Figure 2.2.6: Plots of the power-law model.

Carreau model

The Carreau model takes the zero shear and infinite shear viscosities into account by

$$\frac{\mu - \mu_\infty}{\mu_0 - \mu_\infty} = \left[1 + (\lambda\gamma)^2\right]^{(n-1)/2}, \tag{2.2.7}$$

with

λ relaxation time [s]
$n(< 1)$ power index [-]

The values for λ and n are determined by fitting the model to the flow curve (Chhabra & Richardson, 2008). At very low shear rates and high shear rates the fluid behaves Newtonian and at medium shear rates the fluid conforms to the power law. See figure 2.2.8 for a loglog plot of the viscosity against the shear rate of the Carreau model.

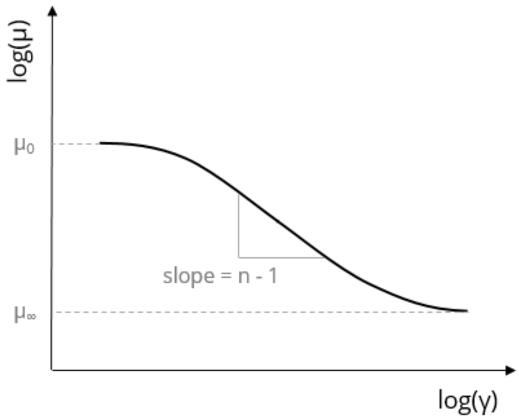

Figure 2.2.8: Plot of the Carreau and Cross model.

Cross model
Just as the Carreau model, the Cross model takes the zero shear and infinite shear viscosities into account by

$$\frac{\mu - \mu_\infty}{\mu_0 - \mu_\infty} = \frac{1}{1 + (\lambda\gamma)^n}, \tag{2.2.9}$$

with

λ	natural time [s]
$n(< 1)$	power index [-]

The values for λ and n are determined by fitting the model to the flow curve. For $\lambda \to 0$ the flow reduces to Newtonian behaviour (Chhabra & Richardson, 2008). In figure 2.2.8 a loglog plot of the viscosity against the shear rate of the Cross model is displayed.

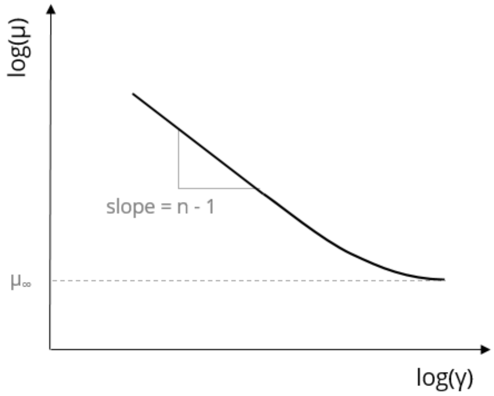

Figure 2.2.10: Plot of the Sisko model.

Sisko model
The Sisko model takes only the infinite shear viscosity into account

$$\mu = \mu_\infty + k\gamma^{n-1}. \tag{2.2.11}$$

Hence, for high shear rates the Sisko model conforms to the power law. This model was originally designed for lubricating oils at high shear rates (Barnes, Hutton, & Walters, 1989). See Figure 2.2.10 for a loglog plot of the viscosity against the shear rate.

Viscoplastic

Viscoplastic fluids exhibit a yield stress which must be exceeded before the fluid starts to flow. When the applied stress is smaller than the yield stress, the material will deform elastically. This can be explained by the assumption that three-dimensional structures exist in the material with sufficient rigidity to withstand a certain amount of stress. When the applied stress is large enough, the structures break down and the material starts to flow. This flow can be linear or non-linear (Chhabra & Richardson, 2008).

If the flow is linear, so the viscosity is constant, the fluid is called a Bingham plastic. Examples of Bingham plastic fluids are toothpaste, tomato paste, mayonnaise and ketchup (Sahin & Sumnu, 2006). Shear-thinning behaviour, non-linear flow, is also possible and a fluid is then called a yield-pseudoplastic. Examples of these are minced fish paste and molten chocolate (Sahin & Sumnu, 2006).

Practically it is difficult to determine whether a material has a yield stress and what its value is as measurements at very low shear rates are affected by wall-slip or end effects. There is currently still a debate as to whether yield stress really exists (Eshtiaghi et al., 2013). However, since the concept of yield stress proves to be convenient in practice it is used in several non-Newtonian models. Two mathematical models are discussed, one for Bingham plastic fluids and one for yield-pseudoplastic fluids (Chhabra & Richardson, 2008).

Bingham plastic model

In the Bingham model the shear stress is related to the shear rate as follows

$$\begin{cases} \tau = \tau_y + \mu_B \gamma & \text{for } |\tau| > |\tau_y| \\ \gamma = 0 & \text{for } |\tau| < |\tau_y| \end{cases} \tag{2.2.12}$$

with

τ_y	the yield stress for the specific Bingham fluid [Pa]
μ_B	the plastic viscosity [Pa s]

The values for τ_y and μ_B are determined by fitting the model to the flow curve (Chhabra & Richardson, 2008). If the yield stress is exceeded a Bingham fluid behaves Newtonian: the viscosity is constant for increasing shear rate. In figure 2.2.13 a plot of the shear stress against the shear rate is depicted for a Bingham plastic fluid.

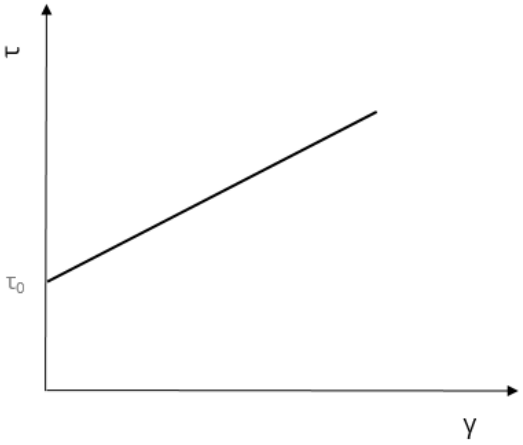

Figure 2.2.13: Plot of the Bingham plastic model.

Herschel-Bulkley model
Combining both the power law model and the Bingham Plastic model, the Herschel-Bulkley model arises

$$\begin{cases} \tau = \tau_y + k\gamma^n & \text{for } |\tau| > |\tau_y| \\ \gamma = 0 & \text{for } |\tau| < |\tau_y| \end{cases} \tag{2.2.14}$$

The value for the yield stress τ_y is determined by fitting the model to the flow curve and k and n are empirically determined (Chhabra & Richardson, 2008). The parameter n is the same as in the power law model and indicates the flow behaviour, whether it is shear thinning or shear thickening. A plot of the shear stress against the shear rate for the Herschel-Bulkley model is found in figure 2.2.15.

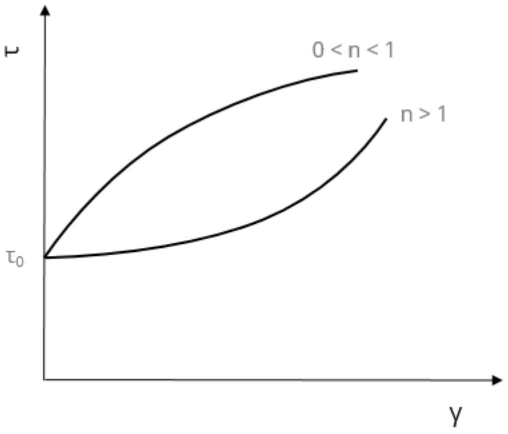

Figure 2.2.15: Plot of the Herschel-Bulkley model.

Shear-thickening

If the apparent viscosity increases with increasing shear rate, the fluid is called shear-thickening or dilatant. This behaviour was thought to be rare so not much attention was paid to research on shear-thickening fluids. However, recently it has appeared to be more widespread. Examples of shear-thickening fluids are suspensions of corn starch (maizena) or sand in water (Sahin & Sumnu, 2006).

There are still few models available for this type of flow. A model which can be used is the power-law model with $n > 1$, see equations (2.2.4) and (2.2.5), or the Herschel-Bulkley model, see equation (2.2.14) (Chhabra & Richardson, 2008).

2.2.3 Time-dependent

The viscosity depends on time for some fluids. When those fluids are subjected to a constant shear rate for a longer period of time, the viscosity and shear stress tend to decrease or increase over time, see figure 2.2.16 (c).

By measuring the shear stress when first increasing and then decreasing the shear rate, a hysteresis loop can be drawn plotting the shear stress against the shear rate, see figure 2.2.16 (a) and (b). The size of the enclosed area is an indication of the degree of time-dependent behaviour. For time-independent fluids there is no hysteresis loop.

If for some time a constant shear is applied to a time-dependent fluid and then removed, and if the fluid is allowed to rest, it may fully, partially or not regain its initial value of viscosity. So the time-dependent process may or may not be reversible.

Two types of time-dependent behaviour can be distinguished, namely thixotrophic and rheopectic. Fluids can behave both thixotropic and rheopectic depending on the shear rate and dry solids content. The models discussed in the time-independent section can be adjusted by making the viscosity, shear stress, shear rate and parameters time-dependent. However, these properties and in particular the parameters are difficult to determine when they are made time-dependent (Chhabra & Richardson, 2008).

A lot of research is still needed in order to shed light on the area of time-dependent fluid behaviour. In current literature there are many inconsistencies, for example Eshtiaghi et al. (2013) suggests that whether a hysteris loop can be drawn depends on the rheological procedure and the accuracy of the rheometer, while Chhabra and Richardson (2008) say that the enclosed area by the hysteresis loop is a measure of its time-dependent behaviour. Up to now there is not a consistent laboratory protocol developed to measure this behaviour, nor are there reliable measuring instruments available or parameters to characterize time-dependent fluid behaviour (Eshtiaghi et al., 2013).

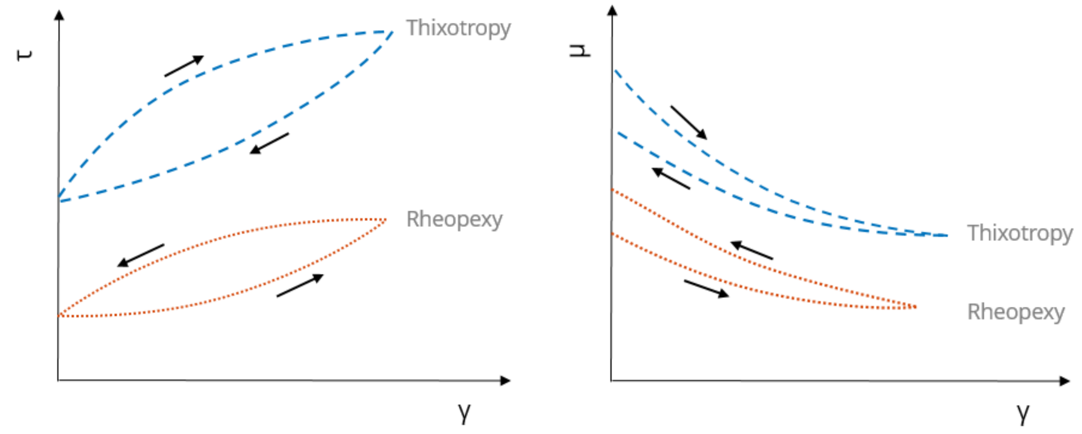

(a) Plot of the shear stress τ against the shear rate γ.

(b) Plot of the viscosity μ against the shear rate γ.

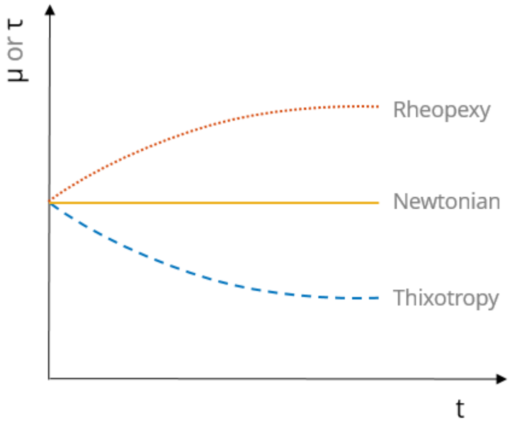

(c) Plot of the viscosity μ against the time t when a constant shear rate is applied.

Figure 2.2.16: Plots of thixotropic and rheopectic, time-dependent, flow behaviour.

Thixotropy

If the viscosity decreases over time when the fluid is sheared at a constant rate, the fluid is characterized as thixotropic. This decrease can be explained by the tearing down of the internal structure. As the structure breaks down, new linkages are also made. Eventually a dynamic equilibrium is reached and the viscosity stays constant over time. An example of a thixotropic fluid is cement paste (Chhabra & Richardson, 2008).

Rheopexy

Fluids are said to behave rheopectic if the viscosity increases with time when subjected to constant shearing. In this case the internal structure is built up when shear is applied and broken down when it is at rest (Chhabra & Richardson, 2008).

2.2.4 Viscoelastic Fluid Behaviour

Some fluids may respond under certain circumstances like an elastic solid and under other circumstances as a viscous liquid. When no time-dependent behaviour is present these kind of fluids are called viscoelastic. Examples are dough and synovial fluids. When a viscoelastic fluid is stirred and the stirring stops, the motion will die out because of viscous forces and a small upwind will be seen due to elastic forces (Chhabra & Richardson, 2008).

2.2.5 Dependency on Temperature

There is general agreement in literature that the viscosity decreases exponentially for increasing temperature (Garakani et al., 2011). Several correlations are proposed to describe the relation between the viscosity, temperature and possible other variables.

A correlation described by Eshtiaghi et al. (2013) for the limiting viscosity, also called infinite viscosity, and also described for the viscosity by Singh and Heldman (2014), is based on the Arrhenius equation which relates reaction rates and temperature, and is given by

$$\mu_\infty = K \exp\left(\frac{E_a}{RT}\right) \tag{2.2.17}$$

with

K	an empirical constant [Pa·s]
E_a	the activation energy [kJ/mol]
R	the universal gas constant [kJ/K·mol]
T	the temperature [K]

The impact of temperature on the limiting viscosity is more apparent for sludge with a high dry solids content than for sludge with a low dry solids content (Cao, Jiang, Cui, Wang, & Yang, 2016).

Another correlation described by Eshtiaghi et al. (2013) for the viscosity is based on the Vogel-Tamman-Fulcher (VTF) model, and it reads

$$\mu = a \exp\left(\frac{b}{T - T_0}\right) + c, \tag{2.2.18}$$

with a, b and c dimensionless coefficients and

T_0	the standard temperature [293.15 K]

2.2.6 Rheological Characterization of Sludge

In literature mostly three types of sludge are discussed, namely primary sludge, secondary sludge and digested sludge. Primary sludge originates from large pre-settling basins and contains merely flakes of settled particles. Secondary sludge contains solids, bacteria and micro-organisms which are formed during aerobic treatment processes. This type of sludge is sometimes referred to as activated sludge. Digested sludge is usually a combination of primary and secondary sludge after anaerobic digestion in for example a digester. Most of the literature focuses on secondary and digested sludge (Baroutian, Eshtiaghi, & Gapes, 2013).

According to a literature review done by Eshtiaghi et al. (2013) sludge is always non-Newtonian, it behaves like a shear-thinning fluid with thixotropic properties and sometimes it has a yield stress. Furthermore, the rheological behaviour of sludge with a high dry solids content is complex and depends to a great extent on the treatment process.

Non-Newtonian Model for Sludge

According to Eshtiaghi et al. (2013) a combined Herschel-Bulkley model for activated sludge generally gave the best results. The power law models the viscosity for a moderate shear rate regime well, but for very high shear rates, the viscosity drops below the viscosity of water. This should not be the case. By coupling the Herschel-Bulkley model with the Bingham model this can be rectified (Eshtiaghi et al., 2013)

$$\tau = \tau_0 + \left(k\gamma^{n-1} + \mu_0\right)\gamma, \tag{2.2.19}$$

with

μ_0 a plateau viscosity [Pa·s]

Data over a large shear rate range is needed if the Carreau or Cross model is used. The results of Garakani et al. (2011) indicated that the Carreau model predicted the viscosity best over a range of dry solids content.

Dependency on Dry Solids Content

The viscosity of sludge increases exponentially for increasing dry solids content. A change in dry solids content or shear rate has a more profound effect on the viscosity than a change in temperature (Garakani et al., 2011).

Much research is done on the influence of the dry solids content on the limit viscosity. Consistent results show that the limit viscosity increases with increasing dry solids content. This could be explained by stronger inter-particle interactions due to larger flakes of particles in proximity of each other. Especially the particle size appears to be important. If the particles are smaller the limit viscosity increases, probably due to the larger area applicable for inter-particle interaction (Eshtiaghi et al., 2013).

A correlation which encompasses the influence of the shear rate, temperature and dry solids content is

$$\mu = k\phi_p^{\epsilon} \exp\left(\frac{E_a}{RT}\right), \tag{2.2.20}$$

with k and ϵ dimensionless constants (Garakani et al., 2011) and

ϕ the dry solids content [g/L]

2.2.7 Calculating the Viscosity of a Mixture

For the CFD model it is necessary to know how the viscosity changes when two or more fluids of different viscosity meet and mix. Several methods are developed to estimate the viscosity of a blend. Pure mixing rules use the viscosity of the components and volume or mass fractions of these components present in the mixture. Examples of pure mixing rules are linear, Arrhenius and Bingham (Ancheyta, 2013). Some mixing rules use a viscosity blending index. In this case it is assumed that the viscosity does not blend linearly, but the viscosity blending index does. Examples of these rules are Refutas and Chevron (Ancheyta, 2013).

Linear

According to Ancheyta (2013) the linear mixing rule can be defined as

$$\mu = \sum_i v_i \mu_i \tag{2.2.21}$$

with

v_i the volume fraction of fluid i [-]

μ_i the viscosity of fluid i [Pa·s]

In addition the linear mixing rule is also defined using mass fractions as this one is included in the CFD software FLUENT

$$\mu = \sum_i y_i \mu_i \tag{2.2.22}$$

with

y_i mass fraction of fluid i [-]

Arrhenius

The mixing rule of Arrhenius is as follows (Ancheyta, 2013)

$$\mu = \prod_i \mu_i^{v_i}. \tag{2.2.23}$$

Replacing the volume fractions by the mass fractions the Arrhenius rule is adjusted to

$$\mu = \prod_i \mu_i^{y_i}. \tag{2.2.24}$$

Bingham

The Bingham mixing rule reads Ancheyta (2013)

$$\frac{1}{\mu} = \sum_i \frac{v_i}{\mu_i}. \tag{2.2.25}$$

Substituting mass fractions instead of volume fractions it turns into

$$\frac{1}{\mu} = \sum_i \frac{y_i}{\mu_i}. \tag{2.2.26}$$

Refutas equation

The Refutas equation is based on weight blending. The viscosity blending index VBI_i for fluid i is defined as follows (Ancheyta, 2013)

$$\mathrm{VBI}_i = a \ln\left(\ln(\nu_i + b)\right) + c, \tag{2.2.27}$$

with

ν_i kinematic viscosity of fluid i [cS = centistokes] and the parameters a, b and c are in general estimated to be $a = 14.534, b = 0.8$ and $c = 10.975$. The viscosity blending index for the mixture is then defined as

$$\mathrm{VBI}_{mix} = \sum_i y_i \mathrm{VBI}_i. \tag{2.2.28}$$

The kinematic viscosity of the mixture is estimated to be

$$\nu_{mix} = \exp\left(\exp((\mathrm{VBI}_{mix} - c)/a)\right) - b. \tag{2.2.29}$$

Chevron equation

The Chevron equation resembles the Refutas equation but is based on volumetric blending. The viscosity blending index for fluid i is defined as follows (Ancheyta, 2013)

$$\mathrm{VBI}_i = \frac{\ln(\nu_i)}{d + \ln(\nu_i)}, \tag{2.2.30}$$

with the parameter d in general estimated to be $d = 3 \ln 10$. The viscosity blending index for the mixture is then defined as

$$\mathrm{VBI}_{mix} = \sum_i v_i \mathrm{VBI}_i. \tag{2.2.31}$$

The kinematic viscosity of the mixture is estimated to be

$$\nu_{mix} = \exp\left(\frac{d \cdot \mathrm{VBI}_{mix}}{1 - \mathrm{VBI}_{mix}}\right). \tag{2.2.32}$$

2.3 Rheometry

According to the Webster dictionary rheology is “a science dealing with the deformation and flow of matter”. A rheometer can be used to measure properties such as the shear stress, yield stress and viscosity of a flowing material. A viscometer can be used to measure the viscosity as a function of shear stress or temperature. It is in general less expensive than a high-end rheometer, but also less advanced.

Different types of rheometers and viscometers exist, such as capillary and rotational viscometers. Examples of rotational viscometers are the concentric cylinder, the disc-spindle and the cone-and-plate meters. The meter used at the water board Vechtstromen (WVS) is a disc-spindle viscometer of Brookfield, DV2T. The one used at the TU Delft is a concentric cylinder high-end rheometer of Anton Paar, the specific type is unknown.

2.3.1 Rotational Viscometer

A rotational viscometer measures the torque on a rotating motor at a certain rotational speed. This torque is caused by the friction of the fluid on the measuring device, and the viscosity can be determined from it. If the flow in the measuring geometry is known, absolute values of viscosity can be measured. Relative viscometers do not have a known geometry and the viscosity values depend on the apparatus, spindle type, rotational speed etc.

Spindle Viscometer

A spindle viscometer measures relative viscosity values by rotating a spindle in the form of a cylinder or disc, see figure 2.3.1. The viscosity values are calculated based on the torque using conversion factors provided by the manufacturer, which depend on the specific spindle used.

To convert the relative viscosity values to absolute values a mathematical procedure is developed for the Brookfield DV-series, see Mitschka (1982) and Appendix B.

Figure 2.3.1: Spindles of DV2T Brookfield viscometer.

Concentric cylinder

In the case of a concentric cylinder the sample is contained in the gap between the inner and outer cylinder. Two types of meters are possible: the Searle type in which the inner cylinder rotates and the Couette type in which the outer one rotates. The last one is more common Chhabra and Richardson (2008).

A schematic representation of a Searle type concentric cylinder viscometer is depicted in figure 2.3.2.

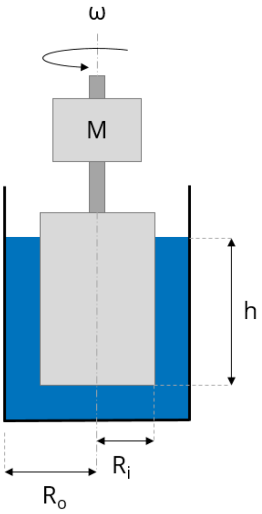

Figure 2.3.2: Schematic representation of a Searle type concentric viscometer.

The viscosity can be calculated using the following formula (Pharmacopoeia, 2008)

$$\mu = \frac{M}{4\pi\omega h}\left(\frac{1}{R_i^2} - \frac{1}{R_o^2}\right) \tag{2.3.3}$$

with

M	the measured torque [Nm]
ω	the angular velocity [rad/s]
h	the height of the measured fluid on the inner cylinder [m]
R_i	the radius of the inner cylinder [m]
R_o	the radius of the outer cylinder [m]

The shear stress and the shear rate are in this case given by

$$\tau = \frac{M}{4\pi h}\left(\frac{1}{R_o^2} + \frac{1}{R_i^2}\right), \qquad \gamma = \omega\frac{R_o^2 + R_i^2}{R_o^2 - R_i^2}. \tag{2.3.4}$$

2.3.2 Considerations Regarding Rheological Measurements on Sludge

Measuring the viscosity of sludge is complicated as sludge is very sensitive to changes, as has already been discussed for non-Newtonian fluids. The way in which the sample is obtained, handled and how it is stored influences the rheological properties measured. As a consequence it is important to perform measurements on sludge as soon as possible after taking a sample in order to prevent for example settling and further digestion of the sludge.

Thermal history influences the data as well. After heating and cooling the viscosity was found to be higher than before the thermal treatment. This might be caused by a partially irreversible process in which solids are being converted to dissolved compounds (Eshtiaghi et al., 2013).

It is important to perform measurements on sludge with the particular application of interest in mind. For example if the viscosity needs to be determined of sludge undergoing slow laminar pipe flow it should be handled with care, subjecting it to as little shear as possible, for instance when pouring it into a measurement container. Whereas if the viscosity of sludge going through a pump needs to be measured, it should be thoroughly mixed and possibly manually pre-sheared before measuring (Chhabra & Richardson, 2008).

Another important aspect is to measure the viscosity in a shear rate range of interest. Pipeline flow of sewage has a shear rate in the range of $5 - 200\ \mathrm{s}^{-1}$ according to Sanin, Clarkson, and Vesilind (2011). However, this is for laminar pipe flow. In case of turbulent flow the peaks in the turbulent boundary layer can be $5000\ \mathrm{s}^{-1}$, see Rudman, Graham, Blackburn, and Pullum (2002).

2.4 CFD Software: Background information

Computational Fluid Dynamics (CFD) provides a prediction of fluid motion by numerically solving a mathematical model describing the flow using CFD software. Benefits of a CFD simulation over experimental methods are its costs, its speed and the fact that many physical quantities can be solved in the same time. Experimental methods provide a description of the flow instead of a prediction, but they are more expensive and slower to perform, and only a limited amount of physical quantities can be viewed during one experiment. The sources of error are different as well. Measurement errors are present in the experimental methods, whereas modelling and discretization errors occur in CFD models. Overall CFD is a fast and cheap method to provide detailed predictive information about the flow, and is especially suited to use in optimizing design at low costs. However, validation is needed to determine how well the model fits reality.

First the domain of interest is modelled and thereafter meshed into a computational grid consisting of cells. One or more mathematical models are chosen depending on the problem to be solved and the corresponding equations are discretized. A numerical solution to these equations is determined and stored for every cell in the domain. Finally the numerical results are analysed and the model is verified, and validated when possible (Kuzmin, 2010; Marshall & Bakker, 2002).

ANSYS FLUENT CFD software was used. Hence, the options and methods mentioned in the coming sections are not all-encompassing, but restricted to the options and methods available in FLUENT and used for this assignment.

2.4.1 Geometry

First the geometry of the domain of interest is modelled. In ANSYS Workbench this can be done using the DesignModeler. Where possible, small details are left out as they have negligible effect on the whole stream but require high computational effort. The model can be built up in 2D, using for example axial symmetry, or in 3D, in which symmetry can also be used to reduce the computational effort.

2.4.2 Meshing

The geometry modelled is still continuous. In order to compute a numerical solution for the domain it needs to be discretized into cells, generating a grid. In general automatic mesh generation of the current CFD software is able to produce good meshes. Still it is sometimes necessary to manually adjust the mesh. Two aspects are important in this case, namely the shape of the cells and the amount of cells.

Structured or Unstructured Mesh

The geometry is discretized using a mesh. This mesh consists of 2D or 3D elements. In figure 2.4.1 elements available in FLUENT for mesh generation are displayed.

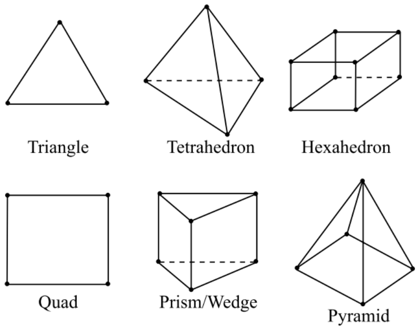

Figure 2.4.1: Elements types available in FLUENT (Marshall & Bakker, 2002).

The mesh can be structured so that every element has a unique address in the i, j, k-coordinate frame of the indices. This coordinate frame doesn't have to be aligned with the x, y, z-coordinates. When the flow is aligned with the grid as in laminar pipe flow this mesh type is a good choice. The mesh can also be unstructured. In this case elements do not have a unique address. Meshes that use different types of elements are called hybrid (Marshall & Bakker, 2002). In figure 2.4.2 (a) and (b) two examples are depicted.

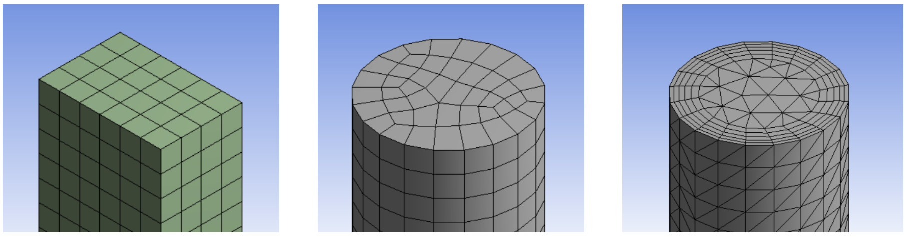

(a) Structured mesh. (b) Unstructured mesh. (c) Hybrid mesh.

Figure 2.4.2: Examples of a structured, unstructured and hybrid mesh, the latter one also contains inflation.

Mesh Size

The mesh should be fine enough to capture essential flow details, but not so fine that the number of cells is unnecessarily large and the computational effort does not weigh up against the additional accuracy. For both laminar and turbulent flow it is important that the mesh is fine enough near the boundaries. Inflation can be used to create a boundary layer grid which is able to capture the boundary layer flow by layering cells near the boundary. At least five layers are recommended (Marshall & Bakker, 2002). In figure 2.4.2 (c) an example of a hybrid mesh with inflation is shown.

Mesh Quality

The quality of the mesh is important for the reliability and accuracy of the CFD results. Low mesh quality can result, among other things, in convergence difficulties and non-scalable meshes which show inconsistencies in CFD results when the mesh is refined. Several criteria have been developed to judge the quality of the mesh. Three of these are the skewness, orthogonal quality and aspect ratio.

The difference in shape of a cell and an equilateral cell of equivalent volume is defined as the skewness. The values for skewness range from 0 to 1. Large values indicate that the element is highly skewed and this can decrease accuracy and destabilize the solution. The maximum skewness should be smaller than 0.95 and the average skewness should be much lower. In figure 2.4.4 recommendations by ANSYS with respect to skewness are displayed in a spectrum.

The orthogonal quality is defined as follows

$$\text{Orthogonal Quality } = \min \left\{ \frac{\vec{A}_i \cdot \vec{f}_i}{|\vec{A}_i||\vec{f}_i|}, \frac{\vec{A}_i \cdot \vec{c}_i}{|\vec{A}_i||\vec{c}_i|} \right\} \tag{2.4.3}$$

with

$\vec{A}_i$	the area vector of face i
$\vec{f}_i$	the vector of the centroid of the cell to the centroid of face i
$\vec{c}_i$	the vector of the centroid of the cell to the centroid of the adjacent cell sharing face i

Values of the orthogonal quality range from 0, worst, to 1, best. Generally, it is recommended by FLUENT to keep the minimum orthogonal quality of all cells above 0.1. In figure 2.4.4 recommendations by ANSYS with respect to the orthogonal quality are displayed in a spectrum.

Skewness

Excellent	Very good	Good	Acceptable	Bad	Unacceptable
0-0.25	0.25-0.50	0.50-0.80	0.80-0.94	0.95-0.97	0.98-1

Orthogonal Quality

Unaccpetable	Bad	Acceptable	Good	Very good	Excellent
0-0.001	0.001-0.14	0.15-0.20	0.20-0.69	0.70-0.95	0.95-1

Figure 2.4.4: Recommended values and spectra for the skewness and orthogonal quality by ANSYS (ANSYS, 2014).

How much a cell is stretched is described by the aspect ratio. It is defined as the ratio of the maximum normal distance of the cell centroid to the face centroids or end nodes over the minimum normal distance. The aspect ratio should be kept below 100 and in areas in which the flow field exhibits large changes the aspect ratios of these cells should be smaller and roughly of the same size (ANSYS, 2013b, 2014).

2.4.3 Physical Models

Many physical models are available in FLUENT to solve different kind of problems, such as laminar flow, turbulence, chemical reactions, and mixing. Relevant models for this assignment are turbulence models, non-Newtonian viscosity, the discrete model and species transport. Each of these models can be described mathematically by a set of equations.

Conservation equations

The conservation equations consist of the continuity equation and two (2D) or three (3D) equations of momentum conservation. These contain three or four unknowns, namely the pressure and two or three velocity components. From this the pressure distribution and the flow field can be resolved. Hence, these equations are solved in every model.

The continuity equation is derived from the conservation of mass and in Cartesian coordinates is given by

$$\frac{\partial \rho}{\partial t} + \frac{\partial}{\partial x_i}\left(\rho u_i\right) = 0, \tag{2.4.5}$$

using the Einstein summation convention and with

t	time [s]
ρ	the density [kg/m^3]
u_i	the velocity component in the i-th direction [m/s]
x_i	the distance component in the i-th direction [m]

The momentum equations are derived from the conservation of momentum in the direction of each of the coordinate axes. They are also called the Navier-Stokes equations. In Cartesian coordinates they are given by

$$\frac{\partial\left(\rho u_i\right)}{\partial t} + \frac{\partial}{\partial x_j}\left(\rho u_i u_j\right) = -\frac{\partial P}{\partial x_i} + \frac{\partial \tau_{ij}}{\partial x_j} + \rho g_i + F_i, \tag{2.4.6}$$

with

P	the pressure [Pa]
δ_{ij}	the Dirac delta function, $\delta_{ij} = 0$ for $i \neq j$ and $\delta_{ij} = 1$ for $i = j$, [-]
τ_{ij}	the deviatoric stress tensor component [Pa]
g_i	the gravitational acceleration in direction i [m/s^2]
F_i	all forces which work on the object in the i-th direction [N]

The left-hand terms represent respectively a change over time and convection, the terms on the righ- hand respectively the pressure gradient, the diffusion of momentum, gravitational forces and other forces.

Laminar and Turbulence Models

In laminar flow the viscous forces dominate over the gravitational forces. The fluid moves in parallel layers with no unsteady macroscopic mixing or overthrowing of layers. If the velocity increases beyond a critical value the flow becomes unsteady, and chaotic macroscopic mixing takes place. This flow regime is called turbulent. Generally the dimensionless Reynolds number gives a good indication whether there is laminar or turbulent flow (Kundu, Cohen, & Dowling, 2012). It is defined as the ratio of inertial over viscous forces and for Newtonian fluids it yields

$$Re = \frac{\rho u L}{\mu}, \tag{2.4.7}$$

with

L	the characteristic length scale [m]

In case of pipe flow the characteristic length scale is the diameter D. Flow in a pipe is laminar for $Re < 2100$ and turbulent for $Re > 4000$. In between there is a transition regime. For non-Newtonian fluids several expressions are proposed for the Reynolds number, also depending on the non-Newtonian model assumed. These will not be treated here.

To solve for laminar flow the conservation equations presented in the previous section are sufficient. In order to solve for turbulent flows, a model has to be chosen with corresponding equations.

Three types of modelling are used nowadays, namely classical statistical models based on the Reynolds-Averaged Navier-Stokes (RANS) equation for momentum, Scale Resolving Simulations (SRS) and Direct Numerical Simulations (DNS).

DNS is computationally very expensive as it resolves very small flow scale such as the turbulent boundary layer. It is only used for research and not available in commercial CFD software such as FLUENT. SRS resolves large eddies, the swirling of fluid in turbulent flow. The effect of smaller scale eddies, smaller than a typical cell size, is modelled by using a sub-grid-scale model. It is only recently available in commercial CFD software. Models based on RANS do not model the details of the turbulent fluctuations but instead time-average them. These models are widely used and computationally inexpensive. However, when inherently unsteady processes take place they will likely give incorrect results.

The turbulent boundary layer consists of a narrow viscous sublayer and a log-law layer. For turbulent RANS models a function in the near-wall regions is advised. These functions help to capture these layers correctly. Another option would be to make a suitable mesh using inflation containing many thin layers near the boundary in order to capture the boundary layer. As this is very difficult to do properly wall functions are generally preferred

In table 2.4.19 a short description and a summary of the pros and cons of several turbulence models available in FLUENT are presented. Because the Realizable $k-\varepsilon$ model is so commonly used it will be treated here shortly as an example of a turbulence model.

Realizable $k-\varepsilon$ model
First the velocity field is decomposed by Reynolds decomposition into a mean velocity component and a fluctuating component

$$u_i = U_i + u_i' \tag{2.4.8}$$

with
U_i the ensemble-averaged or time-averaged velocity [m/s]
u_i' the fluctuating velocity component [m/s]

This can also be done for other equations such as the energy or species equations. Substituting this decomposed velocity field in the continuity and Navier-Stokes equations, and taking a time or ensemble average this yields the Reynolds-averaged Navier-Stokes equations (RANS)

$$\frac{\partial \rho}{\partial t} + \frac{\partial}{\partial x_i}(\rho U_i) = 0 \tag{2.4.9}$$

$$\frac{\partial(\rho U_i)}{\partial t} + \frac{\partial}{\partial x_j}(\rho U_i U_j) = -\frac{\partial P}{\partial x_i} + \frac{\partial}{\partial x_j}\left[\mu\left(\frac{\partial U_i}{\partial x_j} + \frac{\partial U_j}{\partial x_i} - \frac{2}{3}\delta_{ij}\frac{\partial U_k}{\partial x_k}\right)\right] + \frac{\partial}{\partial x_j}\left(-\rho\overline{u_i' u_j'}\right) + \rho g_i + F_i \tag{2.4.10}$$

with the solution variables representing ensemble- or time-averaged values and with $-\rho\overline{u_i' u_j'}$ the Reynolds stresses.

A common method to solve the Reynolds stresses is to employ the Boussinesq Hypothesis

$$-\rho\overline{u_i' u_j'} = \mu_t\left(\frac{\partial U_i}{\partial x_j} + \frac{\partial U_j}{\partial x_i}\right) - \frac{2}{3}\left(\rho k + \mu_t\frac{\partial u_k}{\partial x_k}\right)\delta_{ij} \tag{2.4.11}$$

with
k the kinetic turbulent energy [J/kg]
μ_t the turbulent or eddy viscosity [Pa·s]

The advantage of the Boussinesq hypothesis is that it is computationally inexpensive in calculating the turbulent viscosity μ_t. In case of the $k-\varepsilon$ model the turbulent viscosity is calculated as a function of k and ε, the turbulence dissipation rate, which are solved from two transport equations for k and ε. In this hypothesis the turbulent viscosity is assumed to be an isotropic quantity which is not strictly true, but for most flows approximately the case.

The effective viscosity is introduced and defined as

$$\mu_{\text{eff}} = \mu + \mu_t \tag{2.4.12}$$

and the kinetic energy of turbulence is described by

$$k = \frac{1}{2}\left(\overline{u'^2} + \overline{v'^2} + \overline{w'^2}\right), \tag{2.4.13}$$

with $\bar{\cdot}$ indicating a time or ensemble average. The two additional transport equations for the Realizable $k-\varepsilon$ model, which differ slightly for the other $k-\varepsilon$ models, are

$$\frac{\partial(\rho k)}{\partial t}+\frac{\partial}{\partial x_i}(\rho U_i k)=\frac{\partial}{\partial x_i}\left[\left(\mu+\frac{\mu_t}{\sigma_k}\right)\frac{\partial k}{\partial x_i}\right]+G_k-\rho\varepsilon \tag{2.4.14}$$

$$\frac{\partial(\rho \varepsilon)}{\partial t}+\frac{\partial}{\partial x_i}(\rho U_i \varepsilon)=\frac{\partial}{\partial x_i}\left[\left(\mu+\frac{\mu_t}{\sigma_\varepsilon}\right)\frac{\partial \varepsilon}{\partial x_i}\right]+\rho C_1 S\varepsilon-\rho C_2\frac{\varepsilon^2}{k+\sqrt{\nu\varepsilon}} \tag{2.4.15}$$

with

$$C_1=\max\left\{0.43,\frac{\eta}{\eta+5}\right\},\qquad \eta=S\frac{k}{\varepsilon},$$
$$S=\sqrt{2S_{ij}S_{ij}},\qquad S_{ij}=\frac{1}{2}\left(\frac{\partial U_i}{\partial x_j}+\frac{\partial U_j}{\partial x_i}\right).$$

The meaning of the following parameters is

G_k	the generation of turbulent kinetic energy [Pa/s]
S	the modulus of the mean rate-of-strain tensor [s^{-1}]

The parameters C_2, σ_k and σ_ε are empirically determined constants such that the model performs well for canonical flows. The default values are $C_2 = 1.9, \sigma_k = 1.0$ and $\sigma_\varepsilon = 1.2$. The turbulent viscosity is calculated with

$$\mu_t=\rho C_\mu\frac{k^2}{\varepsilon}. \tag{2.4.16}$$

The variable C_μ is constant in the other $k-\varepsilon$ models, but depends in the Realizable $k-\varepsilon$ model on the local strain rate S and the rotation of the fluid Ω. The production of turbulent kinetic energy is computed with

$$G_k=\mu_t\left[\left(\frac{\partial U_i}{\partial x_j}+\frac{\partial U_j}{\partial x_i}\right)\frac{\partial U_j}{\partial x_i}\right]. \tag{2.4.17}$$

The overall solution procedure is to first solve the transport equation for k and ε. From this the turbulent viscosity μ_t can be calculated. Using μ_t and k the Reynolds stresses can be computed and substituting these in the momentum equations the velocity components can be computed. Finally, the generation of turbulent kinetic energy G_k is updated and the solution procedure repeats (ANSYS, 2013a, 2013b; Marshall & Bakker, 2002).

Newtonian and non-Newtonian Flows

FLUENT has several non-Newtonian models built-in. However, these are not available by default using turbulence. One option is to make a user-defined function. Another option is a bypass to make these built-in functions still accessible in turbulent flow by typing in the command line

```
define/models/viscous/turbulence-expert/turb-non-newtonian
```

In FLUENT the following non-Newtonian models are built-in: the Cross model, the Carreau model, the Herschel-Bulkley and the power law model (under the name ‘non-newtonian-power-law’). All models are shear rate dependent and the parameters can be made temperature dependent (ANSYS, 2013a, 2013b).

Type	Model	Short Description.	Strength	Weakness
RANS	Spalart-Allmaras	Consists of one equation for the turbulent viscosity. Originally developed for aeronautics and aerospace and gaining popularity in turbomachinery.	Simple and economical model which converges quickly.	Not recommended as general purpose model by FLUENT because it is not well calibrated for free shear flows. It shows poor performance on separated flow as well. Furthermore it is not widely tested.
	$k-\varepsilon$	Consists of two equations: one for the kinetic energy of turbulence k, and another for the rate of dissipation of turbulence ε. Besides the standard model two improved models are developed, RNG and Realizable. The latter one is recommended by FLUENT with Enhanced Wall Treatment.	Robust, economical, and achieves reasonable accuracy. Most widely used model in engineering.	Not recommended for flows which separate from smooth surfaces, such as airfoils.
	$k-\omega$	Is developed as an improvement of the $k-\varepsilon$ model. Consists of two equations: one for the kinetic energy of turbulence k, and another for the rate of dissipation of turbulence per time ω. Besides the standard model two improved models are developed, SST and low-Re. The SST is recommended.	Economical and the SST model is widely used for aerodynamic flows.	Compared to the $k-\varepsilon$ model it converges with more difficulty and it is relatively sensitive to initial conditions.
	Reynolds Stress Model (RSM)	This is the most complete model which solves seven (3D, or 5 in 2D) equations: one for the rate of dissipation of turbulence ε, and six others for the Reynold stresses.	Provides good predictions for all types of flows, especially recommended for flows with strong swirl or rotation.	Not generally recommended by FLUENT because of the high computational effort caused by both the extra equations and reduced convergence in comparision to the increased accuracy.
LES	Large Eddie Simulation	The Navier-Stokes equations are solved for large scale turbulent fluctuations and only the small scale eddies are modelled.	Provides excellent results for all types of flows.	Excessively high requirements are set for the near wall boundary layers. These can only be met for flows with low Re. Therefore it is only recommended for laminar flows or for flows where the wall boundary layers are not relevant.

Table 2.4.19: Description and comparison of different turbulence models available in FLUENT based on Marshall and Bakker (2002), ANSYS (2013b) and Bakker (2006).

Species Transport

When species are involved an additional 'conservation of species' equation needs to be solved. The mass fraction of species i is defined as

$$y_i = \frac{m_i}{m_{tot}} \tag{2.4.18}$$

with

m_i	the mass of species i [kg]
m_{tot}	the total mass of the mixture [kg]

The mass fraction y_i of species i is calculated by solving the following convection-diffusion equation

$$\frac{\partial}{\partial t}(\rho_i y_i) + \frac{\partial}{\partial x_j}(\rho_i u_j y_i) = -\nabla \cdot \vec{J}_i + R_i + S_i \tag{2.4.20}$$

with

ρ_i	the density of species i [kg/m^3]
$\vec{J}_i$	the diffusion flux of species i [kg/m^2·s]
R_i	the net rate of production of species i by chemical reaction [kg/m^3·s]
S_i	the rate of creation of species i by other sources [kg/m^3·s]

The mass diffusion is calculated in FLUENT using the dilute approximation, or Fick's law, for the laminar case

$$\vec{J}_i = -\rho_i D_i \nabla y_i - D_{i,T}\frac{\nabla T}{\bar{T}}, \tag{2.4.21}$$

and for the turbulent case

$$\vec{J}_i = -\left(\rho_i D_i + \frac{\mu_t}{Sc_t}\right)\nabla y_i - D_{i,T}\frac{\nabla T}{\bar{T}}, \tag{2.4.22}$$

with the turbulent Schmidt number defined as

$$Sc_t = \frac{\mu_t}{\rho_i D_t}, \tag{2.4.23}$$

which has a default value of 0.7 and with

D_i	the mass diffusion coefficient of species i [m^2/s]
$D_{i,T}$	the thermal diffusion coefficient of species i [kg/m·s]
D_t	the turbulent diffusivity [m^2/s]
$\bar{T}$	the average temperature of the mixture [K]

Assuming no chemical reactions take place, no other source terms are present and no heat transfer takes place, the species transport equation yields in the turbulent case

$$\frac{\partial}{\partial t}(\rho_i y_i) + \frac{\partial}{\partial x_j}(\rho_i u_j y_i) = \frac{\partial}{\partial x_j}\left[\left(\rho_i D_i + \frac{\mu_t}{Sc_t}\right)\frac{\partial y_i}{\partial x_j}\right]. \tag{2.4.24}$$

One can define characteristics such as how the density and viscosity of the different species should mix. User-defined functions are possible or built-in mixing laws can be used. In case of an incompressible fluid the built-in option for the mixing of the density is the volume-weighted-mixing-law. In this case the density of the mixture $\bar{\rho}$ is calculated as follows

$$\bar{\rho} = \sum_i v_i \rho_i = \sum_i \frac{V_i}{V_{tot}} \rho_i = \sum_i \frac{m_i}{V_{tot}} = \frac{m_{tot}}{V_{tot}}, \tag{2.4.25}$$

with

V_i	the volume species i occupies [m^3]
V_{tot}	the total volume of the mixture [m^3]

In case of an incompressible fluid the mass-weighted-mixing-law is the built-in option for the mixing of viscosity (ANSYS, 2013a, 2013b; Marshall & Bakker, 2002). The viscosity of the mixture $\bar{\mu}$ is calculated as

$$\bar{\mu} = \sum_i y_i \mu_i \tag{2.4.26}$$

with

μ_i	the viscosity of species i [Pa·s]

Discrete Model

When the option for the discrete model is enabled a discrete second phase is simulated consisting of spherical particles dispersed in the continuous phase flow. These particles can interact with the flow when desired and the exchange of mass, momentum and energy can be taken into account. The trajectories of these particles can be analysed to see for example what the quality of mixing is. When the particle-particle interactions are neglected the calculations are considerably easier.

The trajectory of a discrete particle is predicted by integrating the following force balance

$$\frac{\mathrm{d}\vec{u_p}}{\mathrm{d}t} = F_D(\vec{u} - \vec{u_p}) + \vec{g}\frac{\rho_p - \rho}{\rho_p} + \vec{F} \tag{2.4.27}$$

with the drag force F_D given by

$$F_D = \frac{18\mu}{\rho_p d_p^2} \frac{C_D Re_p}{24}, \qquad Re_p = \frac{\rho d_p(\vec{u_p} - \vec{u})}{\mu} \tag{2.4.28}$$

and with

$\vec{u_p}$	the velocity of the particle [m/s]
$\vec{g}$	the gravitational acceleration [m/s^2]
ρ_p	the density of the particle [kg/m^3]
$\vec{F}$	optional additional forces [N]
C_D	the drag coefficient [-]
Re_p	the relative Reynolds number [-]
d_p	the diameter of the particle [m]

The drag coefficient C_D depends on the Reynolds number and, in case of non-spherical particles, on the shape of the particle. The spherical drag law in FLUENT is given by

$$C_D = a_1 + \frac{a_2}{Re_p} + \frac{a_3}{Re_p^2}, \tag{2.4.29}$$

with the parameters a_1, a_2 and a_3 depending on the flow regime.

Two of the optional additional forces in the force balance are the virtual mass force and the pressure gradient force. The first force represents the force required to accelerate the fluid around the particle and is given by

$$\vec{F} = C_{vm} \frac{\rho}{\rho_p} \left(\vec{u_p} \nabla \vec{u} - \frac{\mathrm{d}\vec{u_p}}{\mathrm{d}t} \right) \tag{2.4.30}$$

with

C_{vm} the virtual mass factor

which has a default value of 0.5.

The second force arises because of the pressure gradient of the fluid and is described by

$$\vec{F} = \frac{\rho}{\rho_p} \vec{u_p} \nabla \vec{u}. \tag{2.4.31}$$

These forces have negligible influence on the particles when the density of the particles is much higher than the density of the fluid, $\frac{\rho}{\rho_p} \ll 1$. When the ratio of the densities is sufficiently large, $\frac{\rho}{\rho_p} > 0.1$, it is recommended to include these forces in the discrete model.

One of the other options available in the discrete model is to include the turbulence dispersion on the particles. This can be predicted with stochastic tracking or, for steady particle tracking, the cloud model (ANSYS, 2013a, 2013b).

2.4.4 Numerical Methods

In order to solve the continuous differential equations of the models treated in the previous section they need to be discretized. First a solution method is chosen, then an initial solution is determined and finally the numerical solution can be computed.

Discretization schemes

In order to solve the Navier-Stokes equations FLUENT uses the finite volume method. In this case the solution variables are all stored in the cell center. The diffusive terms in the differential equations are calculated using second order central discretization. But in order to determine the convective terms in the differential equations, the face values are needed. These values have to be interpolated from the cell center values. This can be accomplished by several spatial discretization schemes. Well-known schemes available in FLUENT are central differencing, first order upwind and second order upwind.

The central difference scheme is suitable when diffusion dominates convection as this scheme assumes that there is no convection. It interpolates the face values linearly from adjacent cell centers. This scheme is generally not recommended because it can lead to errors and loss of accuracy when convection is present.

The first and second order upwind schemes compute the face value from the upstream, or upwind, neighbor and, in case of the second order scheme, its neighbors. The first order upwind scheme is more stable and better to use to start the calculation before switching to a higher order scheme. The second order scheme requires additional computational effort and is less stable, but more accurate. It is suitable for flows in the whole range from no convection to flow dominated by convection.

When a transient solution is sought, the spatial discretized equations need to be solved for every time step. Both explicit and implicit methods are available. The explicit method uses only previous time steps to calculate the current time step whereas the implicit method also uses in this calculation the current time step. Hence iteration is needed to solve the implicit equation. This requires more computational effort, but it is unconditionally stable with respect to the time step size (ANSYS, 2013a, 2013b; Marshall & Bakker, 2002).

Solution methods

Two types of solvers are available in FLUENT, namely the pressure-based and density-based solver. Originally the pressure-based solver was developed for incompressible and mildly compressible flows and the density-based for high-speed compressible flows. Nowadays they are both applicable for all types of flows but the density-based solver remains superior on high-speed compressible flows. Important to note is that not all physical models are available for both solvers in FLUENT.

Both solvers solve the velocity field from the Navier-Stokes momentum equations, but they differ in how the pressure is calculated. The pressure-based solver uses an additional pressure or pressure correction equation obtained from the continuity and momentum equations to solve the pressure field, while the density-based solver solves the density from the continuity equation and the pressure from the equation of state (ANSYS, 2013a, 2013b; Marshall & Bakker, 2002).

Pressure-based solver

FLUENT has two types of pressure-based solver algorithms, namely a segregated and a coupled algorithm. In the segregated approach one variable at a time is solved throughout the entire domain, while in the coupled algorithm all variables are solved in one cell at a time. The coupled algorithm requires more memory, but improves the convergence speed.

FLUENT has three types of segregated algorithms available, namely SIMPLE, SIMPLEC and PISO. The first two are recommended for steady-state calculations while the latter is recommended for transient solutions. One coupled algorithm is available, namely 'Coupled' (ANSYS, 2013a, 2013b).

Density-based solver

There are also two density-based solver algorithms available in FLUENT, namely an explicit and an implicit algorithm. Both algorithms solve the continuity, momentum, energy and species equations simultaneously for a cell and other variables in a segregated way. The explicit algorithm solves a variable in a cell using known values of that and other variables in adjacent cells, while the implicit algorithms also uses unknown values. The implicit algorithm requires more memory, but has better stability characteristics (ANSYS, 2013a, 2013b).

Under-relaxation

Under-relaxation factors are used to control the update of computed variables at each iteration of all equations of the pressure-based solver and the non-coupled equations of the density-based solver. Generally the default values give sufficient results for most cases. However, if the residuals increase after several iterations the under-relaxation factors can be decreased in order to obtain convergence (ANSYS, 2013a, 2013b).

Initialization

FLUENT needs an initial guess to start the computation. It is important that this initial solution will allow the solver to reach the final solution. Two options are available by default. The first one is standard initialization by which the whole domain is initialized with constant values for the problem variables. The second one is hybrid initialization which consists of a collection of methods to find a suitable initial guess (ANSYS, 2013a, 2013b).

2.4.5 Sources of Error

Several sources of error in a CFD model can be distinguished. First the physical model is a simplification. It might be too simplified leaving out crucial variables or the chosen model might not be suited for the type of flow. For example the $k-\varepsilon$ model is not suited for modelling turbulence in the case of airfoils.

Another, and probably the most important source of error is the discretization error. This error is made when discretizing the continuum equations of the physical models. If the grid spacing of the mesh decreases to zero, this error should also decrease to zero. The discretization error depends on the quality of the grid.

Usage errors, which should be of negligible importance in the ideal case, are another source of error. These may show up as modelling errors, in choosing an improper model, or discretization errors due to improper parameters or grid generation. But these errors can also show up in incorrect conclusions drawn from the numerical results (Slater, 2008).

Estimating the Discretization Error

The Journal of Fluids Engineering has an editorial policy statement on the control of numerical accuracy in which the GCI method is described for estimating the discretization error (Celik, Ghia, Roache, & Freitas, 2008). The estimation is as follows.

Step 1
A representative mesh size h needs to be defined. An example for 3D calculations would be

$$h = \left[\frac{1}{N}\sum_{i=1}^{N} \Delta V_i\right]^{\frac{1}{3}}, \tag{2.4.32}$$

with
N the total number of cells [-]
ΔV_i the volume of cell i [m^3]

Step 2
Three grids with different mesh sizes are generated and simulated. On basis of these simulations key problem variables are selected critical to the conclusions drawn. The grid refinement factors are defined as

$$r_{21} = \frac{h_2}{h_1}, \qquad r_{32} = \frac{h_3}{h_2} \tag{2.4.33}$$

with $h_1 < h_2 < h_3$. Based on experience the grid refinement factor should be larger than 1.3.

Step 3
The apparent order of convergence p is calculated with

$$p = \frac{1}{\ln(r_{21})} \left| \ln \left| \frac{\varepsilon_{32}}{\varepsilon_{21}} \right| + q(p) \right|, \tag{2.4.34}$$

$$q(p) = \ln \left(\frac{r_{21}^p - s}{r_{32}^p - s} \right), \tag{2.4.35}$$

$$s = \text{sign} \left(\frac{\varepsilon_{32}}{\varepsilon_{21}} \right), \tag{2.4.36}$$

with $\varepsilon_{32} = \phi_3 - \phi_2$ and $\varepsilon_{21} = \phi_2 - \phi_1$, and ϕ_j the solution of the key variable on grid j. If $\frac{\varepsilon_{32}}{\varepsilon_{21}} < 0$, this is an indication of oscillatory convergence.

Step 4
The extrapolated values of the key variables can be calculated using

$$\phi_{ext}^{21} = \frac{r_{21}^p \phi_1 - \phi_2}{r_{21}^p - 1}, \tag{2.4.37}$$

$$\phi_{ext}^{32} = \frac{r_{32}^p \phi_2 - \phi_3}{r_{32}^p - 1}. \tag{2.4.38}$$

Step 5
The following error estimates: the approximate relative error, the extrapolated relative error and the fine-grid convergence index, can be calculated using the following equations

$$e_a^{21} = \left| \frac{\phi_1 - \phi_2}{\phi_1} \right|, \qquad e_{ext}^{21} = \left| \frac{\phi_{ext}^{12} - \phi_1}{\phi_{ext}^{12}} \right|, \qquad \text{GCI}_{fine}^{21} = \frac{1.25 e_a^{21}}{r_{21}^p - 1}. \tag{2.4.39}$$

In order to report the numerical accuracy these estimates along with the estimated order of p of equation (2.4.34) have to be reported in the Journal of Fluids Engineering.

Chapter 3

Research Method

In this chapter it is described how the viscosity measurements were performed and how the CFD simulations were produced and validated.

3.1 Measuring Viscosity

As described in sections 2.2.5 and 2.2.6 the viscosity of the sludge is influenced a lot by temperature and dry solids content. However, this was not taken into account, as many measurements would be needed to fit a model on these parameters and due to limited resources this was not realizable. Besides, for adjusting the dry solids content there was another obstacle, namely that the structure of sludge is easily distorted when adding or detracting water.

Two sets of viscosity measurements were considered: one collected by Delft and the other at WVS.

3.1.1 Viscosity Measurements TU Delft

The first data set consists of viscosity measurements performed by the TU Delft on the 6th of December 2016 with a high-end rheometer from Anton Paar. This rheometer measured absolute viscosity over a shear rate range of 0.01 - 1000 s^{-1}.

Four samples, namely primary sludge, THP sludge, digestate, which is discharged sludge at the top of the digester, and AD sludge, which originates from the middle of the digester, were collected at the WWTP in Hengelo and transported the same day by car to the TU Delft. It is not clear whether all the measurements were performed on the same day.

Three shear rate ramps at 40 °C were performed on every type of sludge, each increasing the shear rate logarithmically from 0.01 s^{-1} up to 1000 s^{-1}. For every type of sludge the mean of these speed ramps was determined. The yield stress and dry solids content were measured as well.

Primary sludge appeared difficult to measure as it was quite inhomogeneous compared to the others. Therefore the viscosity was also measured after sieving the sludge. However, as it is not clear what the connection is between these measurements and practice, this data set was disregarded.

On the 20th of June 2017 another set of viscosity measurements were performed by the TU Delft on six samples of sludge. This time shear rate ramps, yield stress, density and dry solids content measurements were carried out. The shear rate ramps were performed at 40 °C from 0.1 to 500 s^{-1}. The density was measured using a 500 ml measuring cup and a scale. The six samples were

1. primary sludge thickened,
2. primary sludge thickened mechanically,
3. digested sludge,
4. THP sludge,
5. a manual mixture of primary sludge thickened mechanically, digested and THP sludge in proportion to the flow,
6. a sample taken after a venturi with a 45 mm diameter of the narrowing.

The goal of these measurements was to determine the viscosity of the mixture after the venturi needed for another application and to validate the use of the mass-weighted-mixing-law for the viscosity used in the species transport model, see equation (2.4.26).

3.1.2 Viscosity Measurements WVS

The second data set was collected with the Brookfield DV2T viscometer of WVS on the 23th of March 2017. This meter measured relative viscosity over a rotational speed range of 0 - 200 rpm.

The sludge samples were one day old and were instantaneous samples and not an average over the day. The samples of digested and THP sludge were stored in the fridge and the samples of primary sludge were stored inside, near a door exposing it to cold outdoor air. Of every type of sludge two samples were available.

Due to lack of a thermal bath, the jars containing the sludge were warmed up in the sink with hot water from the tap. The sludge was gently shaken before pouring it in a beaker by rotating the jar about three times up and down. The measurements were performed without guard leg as the beaker was wide enough to leave room for deviation of the placement of the spindle in the middle of the beaker.

(a) Overview.

(b) Brookfield viscometer DV2T.

(c) Warming up of the jars in the sink.

(d) Viscosity measurement.

Figure 3.1.1: Measuring arrangement at WVS.

Two types of measurements were performed. Firstly, the viscosity at constant speed was measured for all types of sludge for a duration of five minutes using the same spindle, RV-2. For primary sludge this was done at two temperatures and for the other sludge types at one. Secondly, rotational speed ramps were performed increasing the speed from 0 rpm to 200 rpm and back. Again this was done at two temperatures for primary sludge with spindle RV-4 and at one for THP and digested sludge using spindle RV-2. The density and dry solids content were measured as well. The density was determined using a 100 ml measuring cylinder and a scale. This was done a second time on the 12th of May 2017.

3.1.3 Converting Relative Viscosity Values

In order to feed the CFD model and to compare the data sets the relative viscosity values should be converted to absolute values. In technical paper AR-82 of Mitschka (1982) supplied by Brookfield, a mathematical procedure is outlined for this conversion consisting of four steps. Note that the subscript i denotes a data point.

1. The torque α_i and viscosity μ_i need to be measured at different values of the rotational speed N_i (rpm).
2. The torque α_i, which is measured ranging from 0 - 100 percent, is converted to shear stress τ_i in Pa, by multiplying it with a constant $k_{\alpha\tau}$ specific for the spindle used: $\tau_i = k_{\alpha\tau}\alpha_i$.

3. A loglog plot is made of τ against N.
   (a) If there is a sufficient linear correlation between τ and N, the flow index of the fluid n is said to be equal to the slope. The shear rate γ_i in s^{-1} can be determined by multiplying the rotational speed N_i with a constant $k_{N\gamma}(n)$ which is specific for the spindle and the flow index: $\gamma_i = k_{N\gamma}N_i$.
   (b) If the correlation is not linear, a smooth curve is fitted through the points. The slope at every point is the apparent flow index n'_i for that particular rotational speed N_i: $n'_i = \mathrm{d}\log\tau/\,\mathrm{d}\log N_i\big|_{N=N_i}$. The shear rate γ_i in s^{-1} is determined by multiplying the rotational speed N_i with a constant $k_{N\gamma}(n'_i)$ depending on the spindle type and the apparent flow index n'_i: $\gamma_i = k_{N\gamma}(n'_i)N_i$.

Values for $k_{\alpha\tau}$ and $k_{N\gamma}$ can be found in Table 1 of Mitschka (1982) and, for the spindles used, in table B.1.4.

3.2 CFD Model

Based on the situation on site several CFD models were build using ANSYS 14.0. First a CFD model was build to determine which parts of the recirculation pipe were relevant. Taking these parts into account a model was build, the baseline model, which did not include adjustments already made at the WWTP to induce mixing.

Based on good experiences in mixing at another WWTP a venturi was installed in order to induce turbulence which tends to accelerate mixing. Hence, a second model was set up including a venturi. The dimensions of the installed venturi were provided verbally and were approximations.

Those two models, the baseline and venturi model, were run first with one type of sludge in all pipelines. This was done with digested sludge as this type of sludge has the highest flow rate. The second time a mixture was run.

To improve the mixing, adjustments of the geometry were considered. To determine which adjustments would improve the mixing most, nine smaller models were set up. These can be found in Appendix C. Based on the results of these simulations, two models were chosen which were superior in effectiveness and realizability. These two smaller models were implemented in the piping system and simulated with a mixture.

Finally, two validation models were build based on two different geometries of a venturi. These were run with a mixture in order to validate on pressure over the venturi. In the end, only one was validated. The results of the other model can be found in Appendix D.2.

3.2.1 Situation on Site

A simplified process flow diagram (PFD) of the relevant processes is depicted in figure 3.2.1. Relevant parts included the junction of primary sludge and THP sludge, and the junction of those two and digested sludge.

The situation on site was changed significantly with respect to the piping and its arrangement two times during this assignment. Photos of the situation at the start of the assignment, referred to as situation I, are shown in figure 3.2.2.

On the 20th of April 2017 the situation was different with respect to the junction of primary and THP sludge. Before it was a T-junction located near digester 3 and now it was a 45 degree junction located near digester 1, see the photos of situation II in figure 3.2.3.

A little while later some other changes were made. The piping between the venturi and the junction of primary and THP sludge drastically changed: another existing pipeline was used, namely the middle one instead of the lower one, a different type of pipe was used, namely stainless steel 168 mm instead of cast iron 150 mm, and the arrangement of the pipes was changed including some other type of bends and another junction between digested sludge and the combination of primary and THP sludge. This third situation, situation III, is captured in several photos in figure 3.2.4.

The modelling included situation I and II. However, the last changes of situation III were not included.

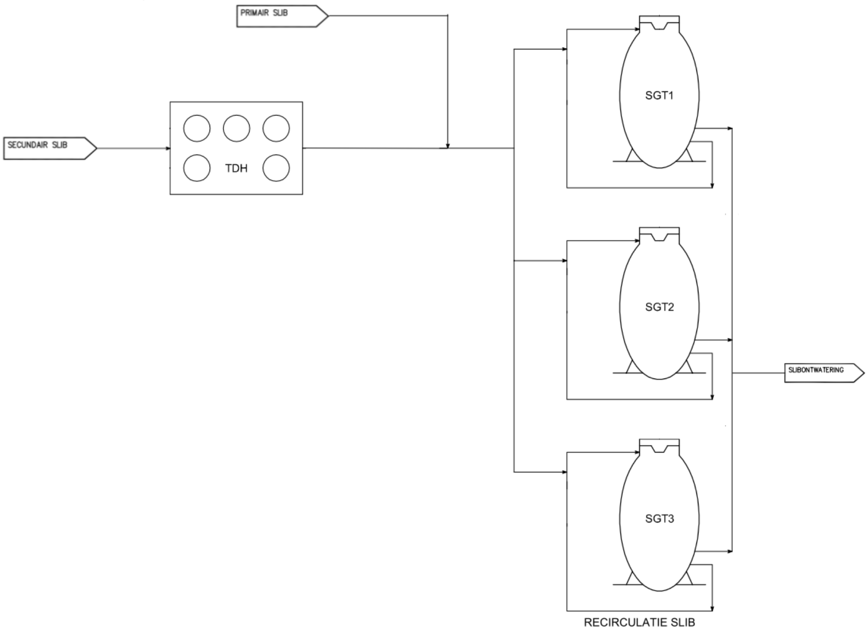

Figure 3.2.1: Simplified process flow diagram (PFD) in Dutch of the relevant sludge streams with primary sludge (primair slib), secondary sludge (secundair slib), recirculation or digested sludge (recirculatie slib), sludge dewatering (slibontwatering) and digesters (slib gistingstank - SGT).

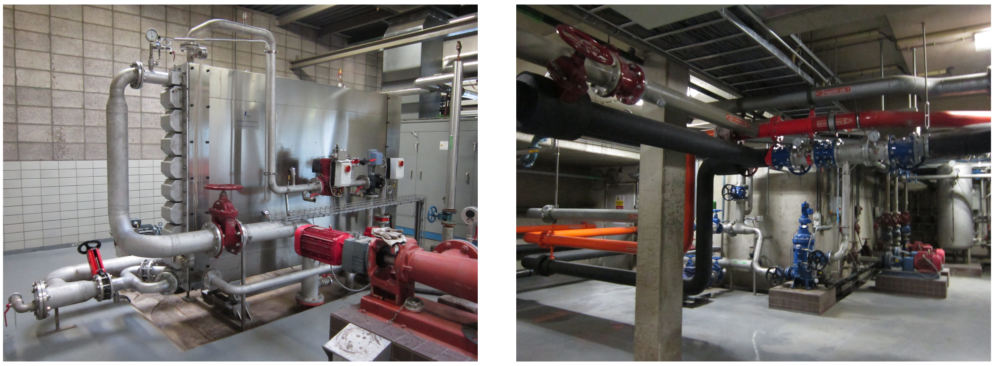

(a) Heat exchanger on the first floor.

(b) Venturi on the ground floor (lower black pipe).

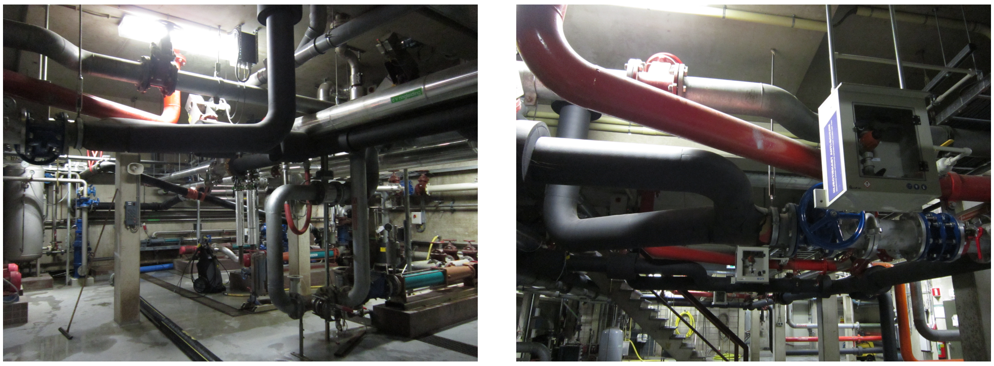

(c) Recirculation pipe (black, middle top) from heat exchanger at first floor.

(d) Junction (middle) of primary and THP sludge (left), and digested sludge (top left) from first floor.

(e) Venturi and pipeline feeding the digester (lower black pipe).

(f) T-junction of primary sludge (left) and THP sludge (right).

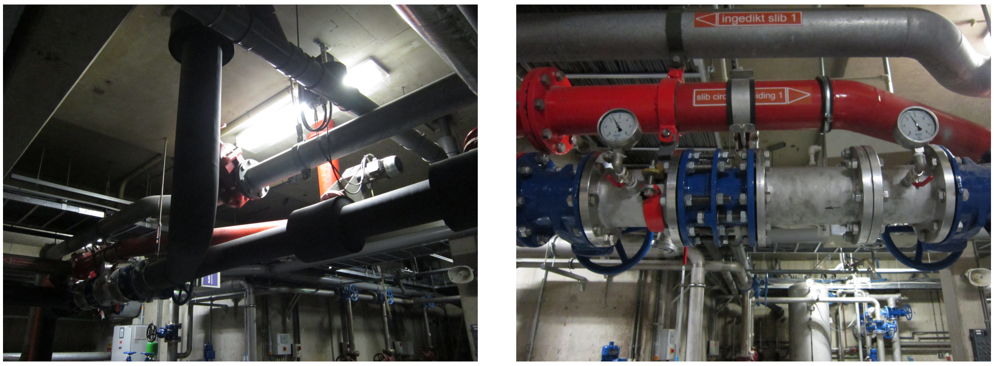

(g) Rear view of the junction of recirculation pipe from first floor (top middle) and THP and primary sludge (right).

(h) Venturi.

Figure 3.2.2: Situation I on site on the 8th of March 2017.

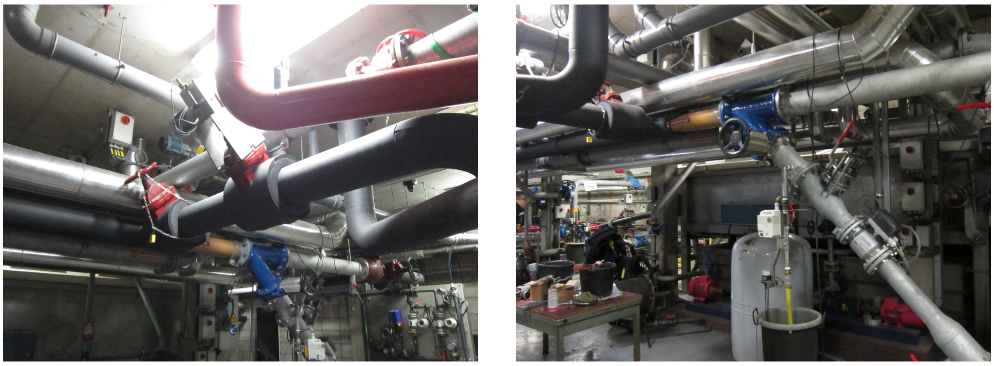

(a) 45 degree junction (at the back) of primary and THP sludge.

(b) 45 degree junction of primary (lower pipe) and THP sludge (upper pipe).

(c) 45 degree junction of primary (lower pipe) and THP sludge (upper pipe).

Figure 3.2.3: Situation II on site on the 20th of April 2017. The junction between primary and THP sludge had changed with respect to situation I.

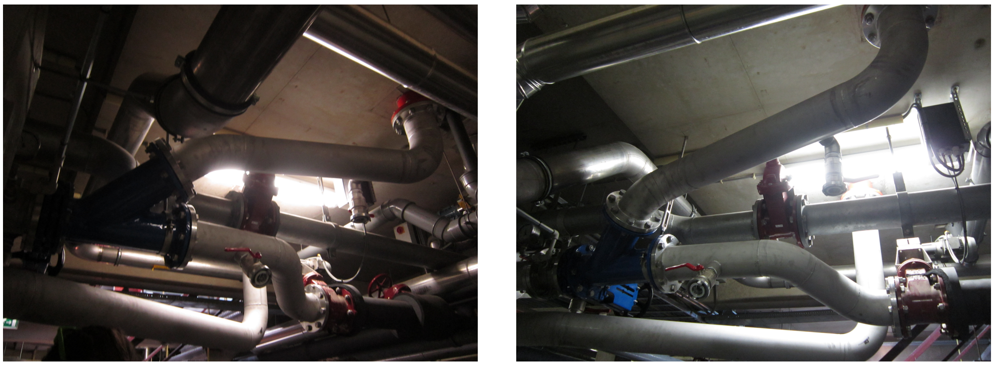

(a) Front side view of the 45 degree junction (left) of primary and THP sludge and digested sludge (top right).

(b) Side rear view of the 45 degree junction (left) of primary and THP sludge (bottom right) and digested sludge (top right).

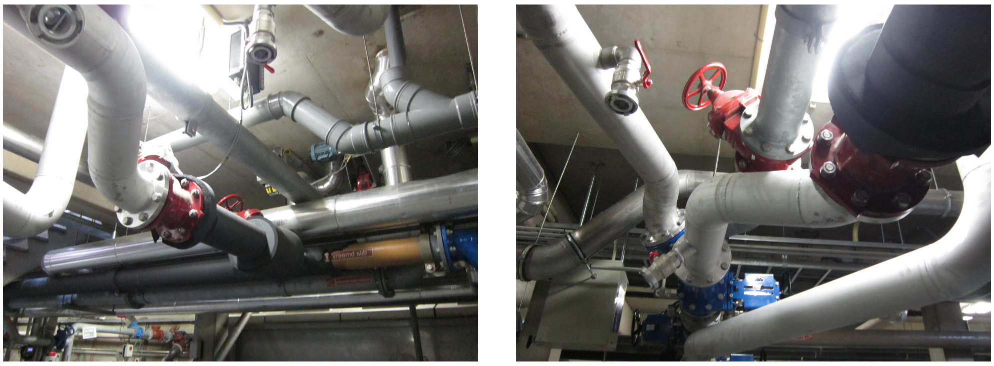

(c) T-junction of primary and THP sludge with the 45 degree junction between these (right).

(d) Bottom rear view of the 45 degree junction (middle bottom) of digested sludge (top left) and primary and THP sludge (top right).

Figure 3.2.4: Situation III on site on the 30th of May 2017. The junction between digested and primary and THP sludge had changed with respect to situation I and II and the pipe arrangement and diameter was changed.

3.2.2 Geometry of the Models

Three models were made of the recirculation pipe coming from the heat exchanger to determine how much of this pipeline had to be modelled in the whole model. Then a model of all the relevant piping was build up starting from the 45 degree junction between the pipes of primary and THP sludge, including the relevant parts of the digester pipe coming from the heat exchanger, and modelling the pipes behind the venturi including the straight pipe before the bend downwards. In total five models of the whole piping system are run with variations in the geometry to induce mixing.

Recirculation Pipe

The recirculation pipe coming from the heat exchanger was divided into three models. The first model included the two elbows, referred to as Recirculation 1, the second model, Recirculation 2, included one elbow and the third model, Recirculation 3, consisted of a single straight pipe, see figure 3.2.5 for pictures of the model and drawings including the dimensions.

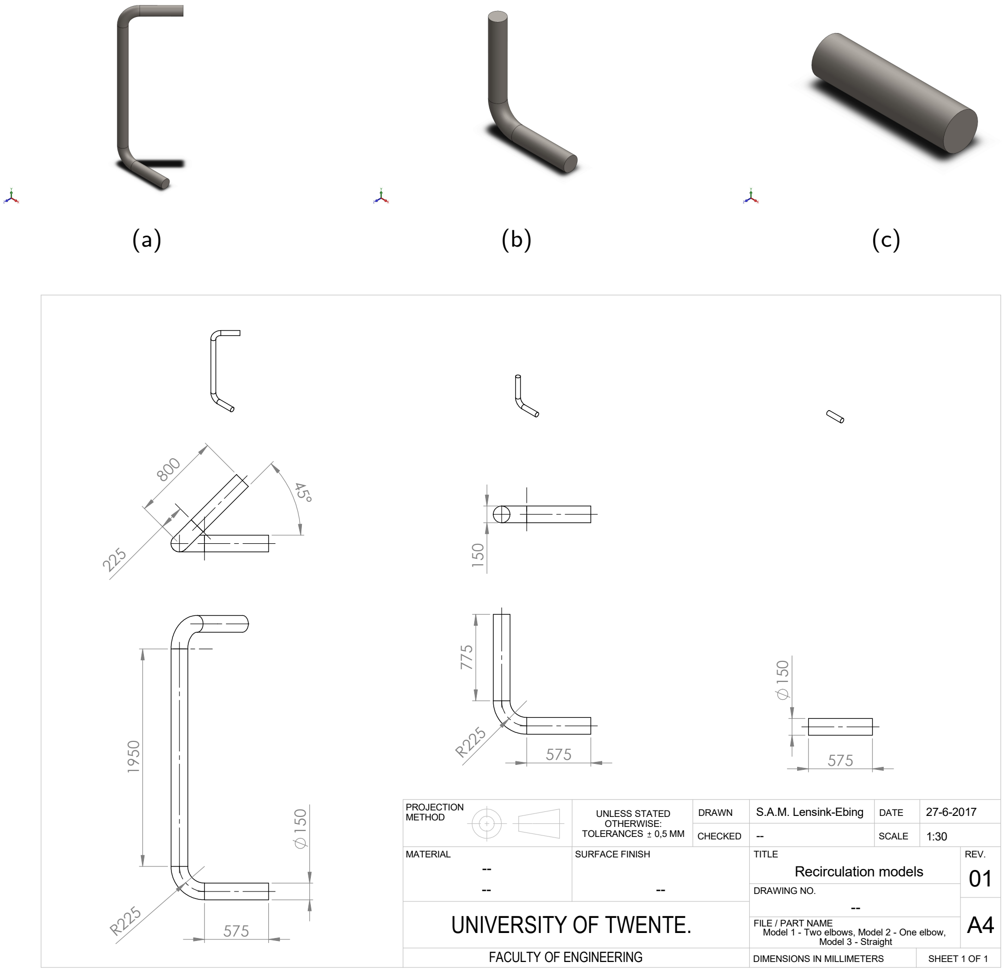

(a) (b) (c)

(d)

Figure 3.2.5: Solidworks models and drawings of the models of the recirculation pipe.

Model 1 - Baseline

The baseline model did not include adjustments already made at the WWTP to induce mixing. The Solidworks model and drawing is depicted in figure 3.2.6.

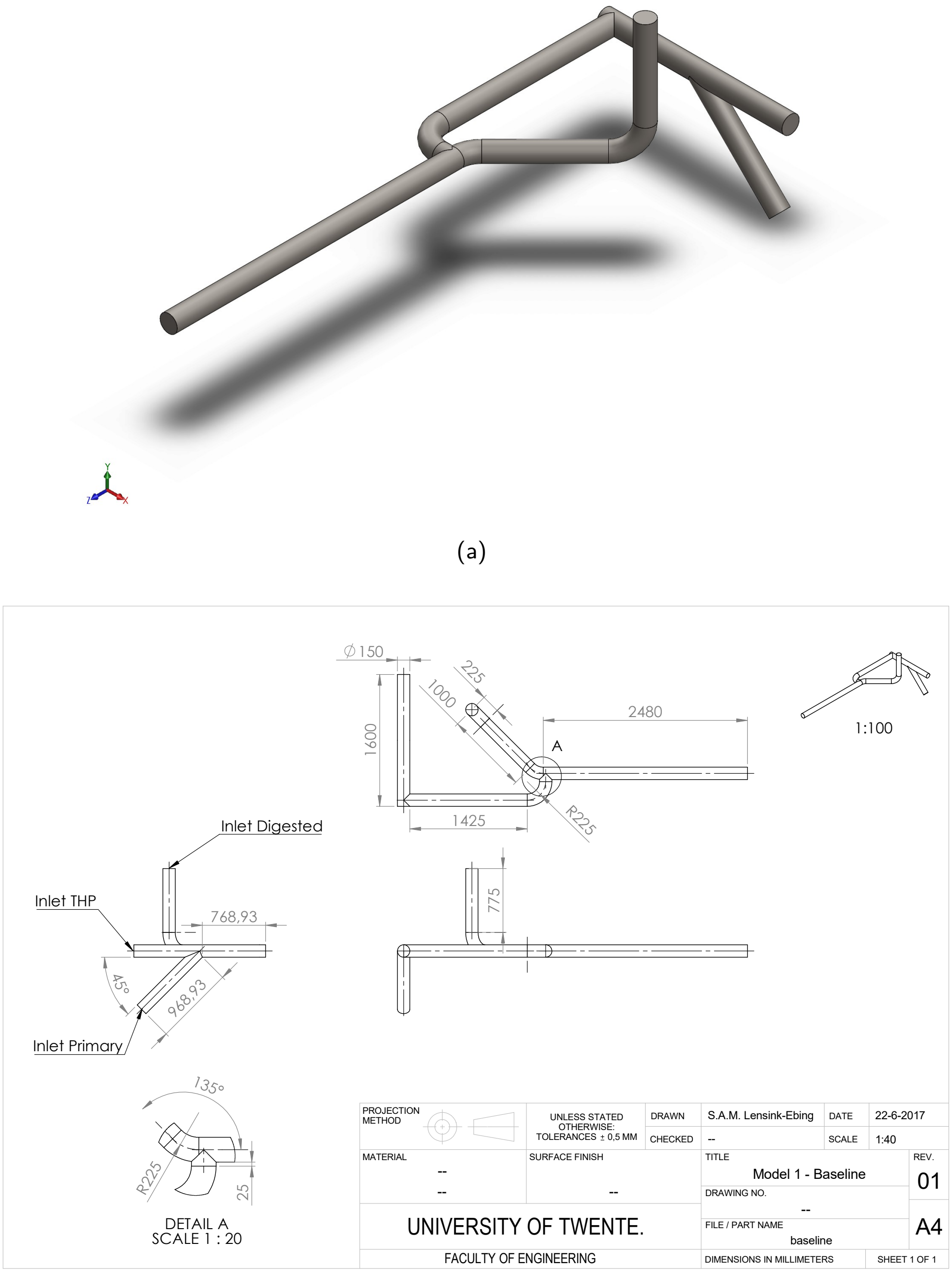

(a)

(b)

Figure 3.2.6: Solidworks model and drawing of Model 1 - Baseline.

Model 2 - Venturi

The second model included the venturi which was already installed at the WWTP to induce turbulence and hence improve mixing. As already stated, the dimensions of the venturi were provided verbally and were approximations, see figure 3.2.7 for the Solidworks model and drawing.

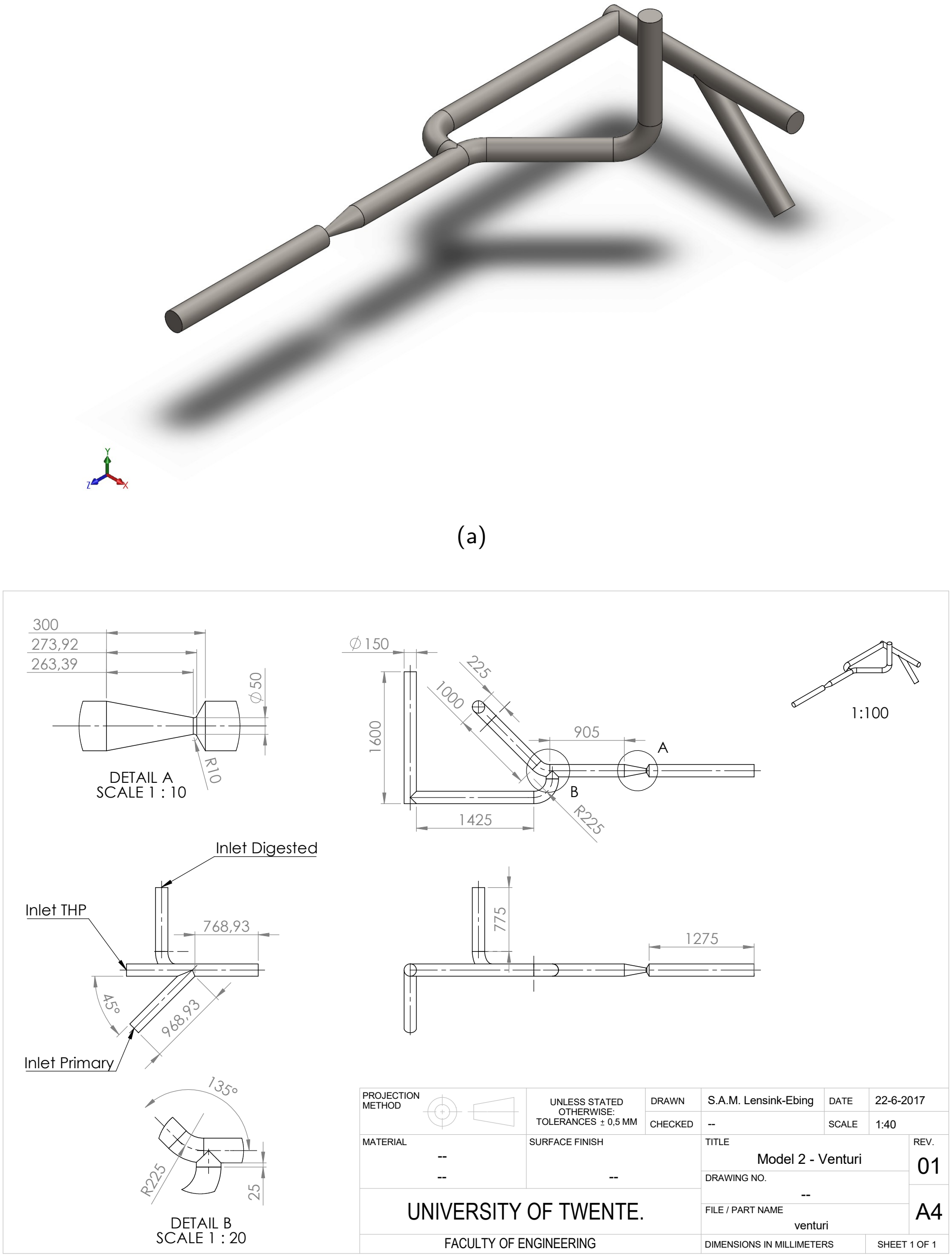

(a)

(b)

Figure 3.2.7: Solidworks model and drawing of Model 2 - Venturi.

Model 3 - Static Mixer

The third model included one of the two chosen geometries to improve mixing. It included one helical element of a static mixer produced by Primix, see figure 3.2.8 (a) for a picture. The element can be inserted into the pipe and removed for cleaning. Normally, a static mixer includes two or more elements, but only one element was modelled. If one element would yield sufficient mixing this would be preferred because of the high risk of clogging due to the high dry solids content and the inhomogeneity of primary sludge. Furthermore, the cleaning maintenance was assumed to be less with one element.

In figure 3.2.8 (b) and (c) the helical element is depicted inside the pipe. The diameter of the element was equal to the pipe, the length was 1.6 times the diameter and the thickness was 6 mm. In figure 3.2.9 the Solidworks model and drawing are displayed.

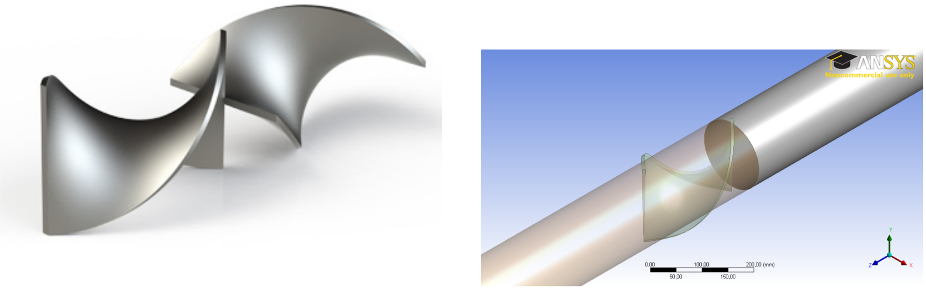

(a) Primix helical element, (Primix, 2017).

(b)

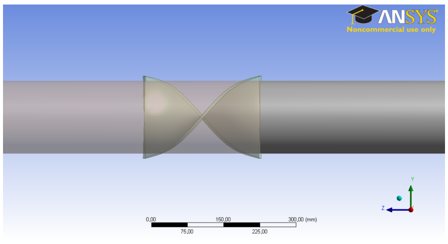

(c)

Figure 3.2.8: Details of the helical element of Model 3 - Static Mixer.

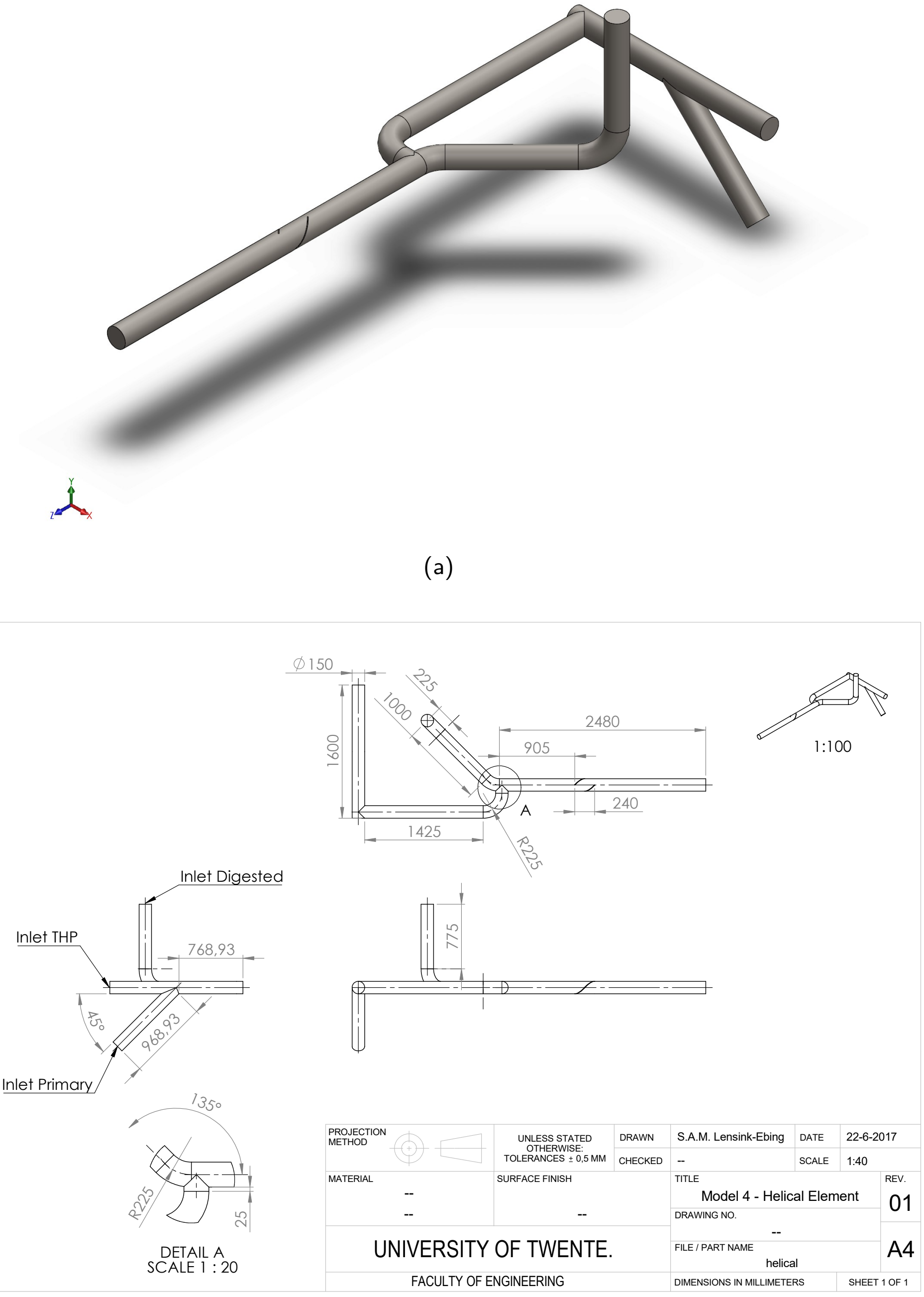

(a)

(b)

Figure 3.2.9: Solidworks model and drawing of Model 3 - Static Mixer.

Model 4 - Corkscrew

The fourth model was the second of the two chosen geometries to improve mixing. It consisted of a pipe in the form of a corkscrew. The internal diameter of the corkscrew followed the path of a helix. This helix could be described mathematically by $x = r\cos a, y = r\cos a$ and $z = ct$ with the radius $r = 100$ mm, and as one turn is made $0 \leq a \leq 2\pi$, and $c = \frac{800}{2\pi}$ mm. The diameter of the corkscrew was adjusted to 100 mm as this would be cheaper in production. In figure 3.2.10 the Solidworks model and drawing of the corkscrew are displayed.

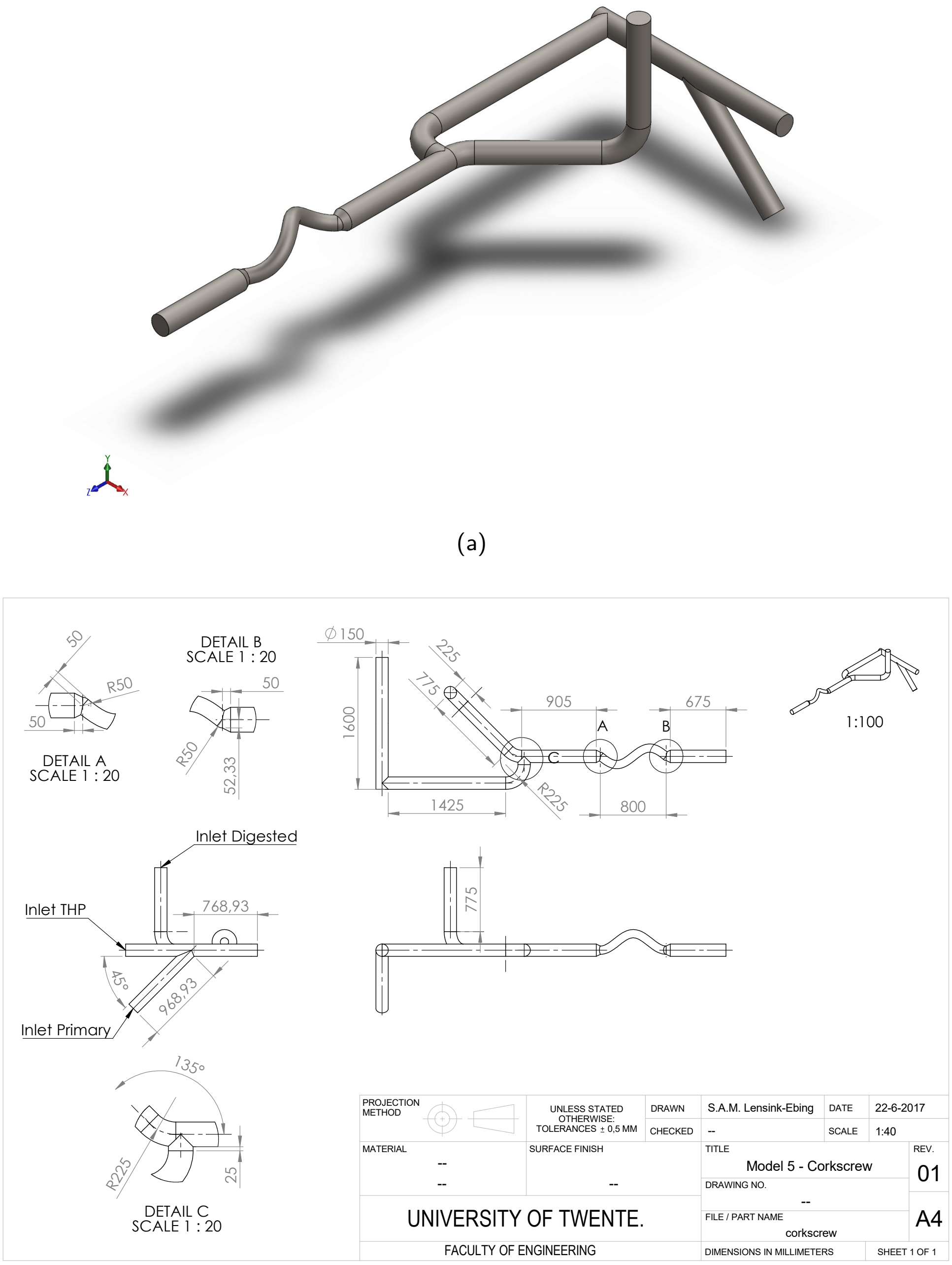
(a)

(b)

Figure 3.2.10: Solidworks model and drawing of Model 4 - Corkscrew.

Model 5 - Venturi D40

The fifth model included a venturi with a narrowing of 40 mm. The dimensions were measured at the workshop of the WWTP in Hengelo. This model was build in order to validate the CFD model on pressure. The Solidworks model and drawing are shown in figure 3.2.11.

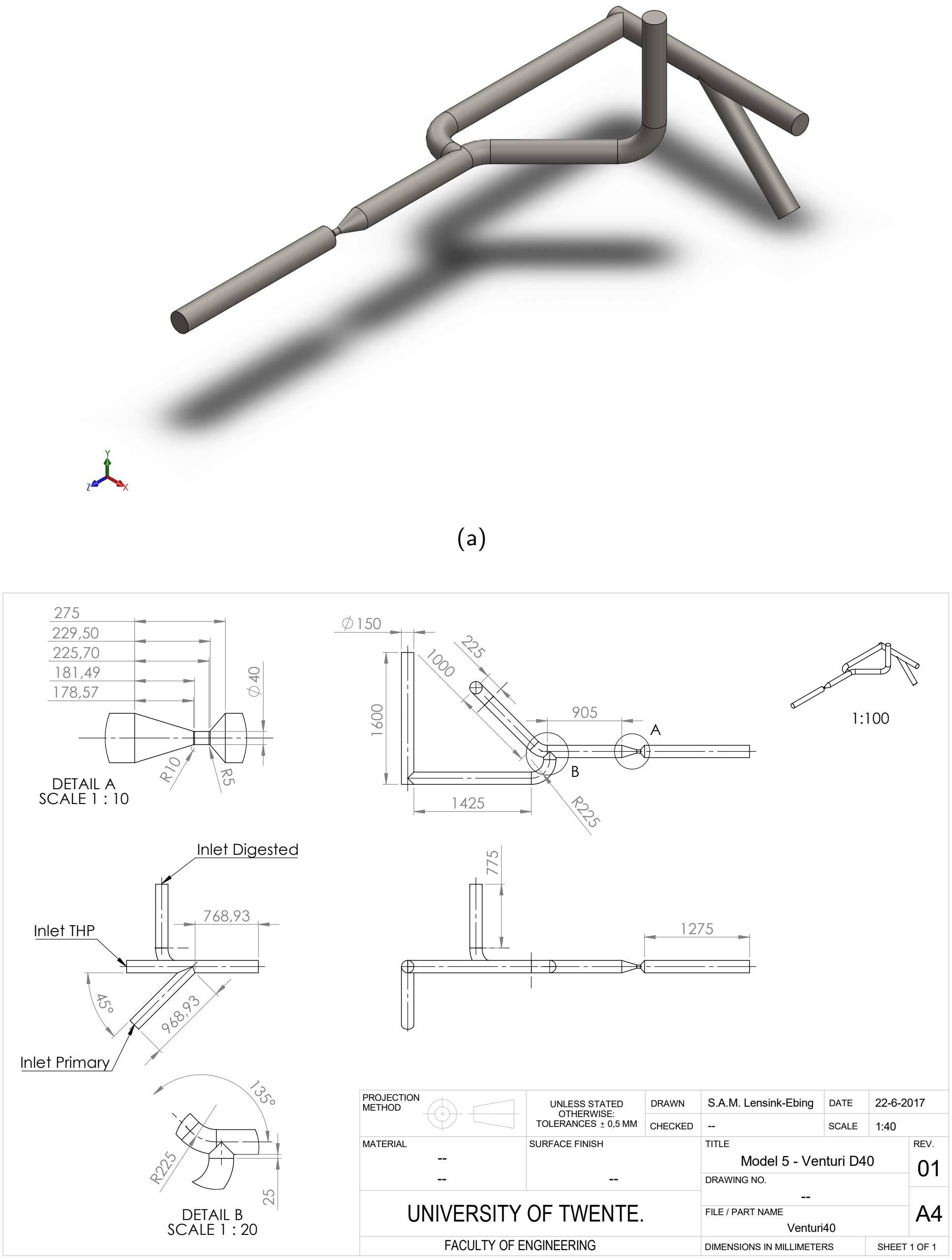

(a)

(b)

Figure 3.2.11: Solidworks model and drawing of Model 5 - Venturi D40.

3.2.3 Mesh

In table 3.2.12 information about the used meshes is displayed. These values were retrieved from FLUENT with one exception being the skewness, as these values were retrieved from ANSYS Meshing. The maximum values of skewness, and the minimum values of the orthogonal quality can be compared with the recommended values by ANSYS described in 2.4.2. Comparing these it is concluded that the meshes of the recirculation models were of good quality and the meshes of the other models were generally of acceptable quality.

The lower quality was possibly in part due to the complex geometry of some models. By refining the mesh the quality could be increased. However, this was not possible due to the limitation on the academic license of ANSYS, which restricted the number of cells to be solved to 512,000, the computational effort would be too big and the available memory of the computer used too small.

Model	# elements	V (m^3)	Orth. Q.	Asp. R.	Skew.
Recirculation 1	54981	0.06642	0.3102	14.168	0.7533
Recirculation 2	24366	0.02973	0.3527	13.047	0.7595
Recirculation 3	29315	0.01011	0.3681	12.724	0.6843
Model 1 - Baseline	195305	0.1559	0.1725	15.298	0.9160
Model 2 - Venturi	192156	0.1531	0.1478	23.009	0.8974
Model 3 - Helical Element	194705	0.1542	0.1389	33.598	0.9670
Model 4 - Corkscrew	192793	0.1488	0.1758	21.547	0.9288
Model 5 - Venturi D40	238198	0.1526	0.1715	54.766	0.9356

Table 3.2.12: Relevant information about the meshes used. From left to right the number of elements, the volume of the mesh, the minimum value of the orthogonal quality, the maximum value of the aspect ratio and the maximum value of the skewness.

3.2.4 Physical Models

In table 3.2.13 values of the three sludge streams are summarized for the situation in April 2017 and the future situation in Phase 2 of the Energy factory. The mean velocity was calculated using a diameter of 150 mm.

	Current Situation (April 2017), 1 digester in use			Future Situation (Phase 2) 3 digesters in use		
	Digested	Primary	THP	Digested	Primary	THP
Divided over # tanks	1	1	1	1	3	3
Flow (m^3/d)	1200	100	100-120	1200	240	215
Mean Flow (m^3/h)	50	4.2	4.2-5.0	50	10.0	8.9
Mean Velocity (m/s)	0.79	0.066	0.066-0.079	0.79	0.15	0.14
Temperature (°C)	35-40	8-22	60-80	35-40	8-22	60-80
Dry Solids Content (%)	5-7	6-7	10-14.3	12	6-7	10-14.3

Table 3.2.13: Values of the three sludge streams of the current and future situation at the WWTP in Hengelo.

Based on the values in table 3.2.13, verbally provided information, and results of the measurements of densities, see tables 4.1.5 and 4.1.6, values for the sludge streams of the models were chosen. These can be found in table 3.2.14.

Most types of sludge are at least to some extent compressible according to Patil (2009). However, just as in the article of Bechtel (2003) it was assumed that sludge could be treated as an incompressible fluid. Uniform flow was assumed at the inlet of digested, primary and THP sludge. At the outlet the relative pressure was assumed to be zero.

The three types of sludge were modelled as non-Newtonian fluids in time (transient). The influence of temperature and dry solids content on the viscosity was left out when fitting a non-Newtonian model as this would require in-depth research to determine the influence of these factors on viscosity. Besides, the model would become increasingly complex and probably not solvable on the machine used.

Furthermore, gravity was included in the model with a constant gravitational acceleration of -9.81 m/s^2 in y-direction and the operating pressure was assumed to be 2.5 atm.

	Digested	Primary	THP
Density (kg/m^3)	910	1100	1000
Molecular weight (g/mole)	18.0152	18.0152	18.0152
k	1.2987	7.8853	3.5219
n	0.3155	0.1280	0.3379
Flow (m^3/h)	50	3.8	5.1
Velocity (m/s)	0.79	0.06	0.08

Table 3.2.14: Values used for the three types of sludge. From top to bottom, the density, the molecular weight, the parameters k and n of the non-Newtonian power law model, the flow and the corresponding velocity assuming a diameter of 150 mm.

Because turbulence was expected when modelling a venturi, the Realizable $k - \epsilon$ model was chosen with Enhanced Wall Treatment and default values of the parameters. Based on the turbulence models described in 2.4.3 it was expected that this model would give accurate enough results with a reasonable computational effort.

The species transport model was used to simulate the mixing of the three types of sludge. The volume-weighted-mixing-law was chosen as a mixing rule for the density and the mass-weighted-mixing-law as a law for the viscosity. For the diffusion of mass the constant dilute approximation was used. The mass fractions of the species were set to 1 at the inlet corresponding to the species. Only two mass fractions had to be provided as the third could be derived from these. For example, at the inlet of THP the mass fraction of THP was 1 and of primary was 0. The mass fraction of digested could be derived from these to be 0.

Finally, the discrete model was simulated. A particle density of 1200 kg/m^3 was assumed for all solid sludge particles, averaging the densities mentioned by Dammel and Schroeder (1991) and Turovskiy and Mathai (2006). No interaction with the continuous phase was assumed. In this license or version of ANSYS the virtual mass force and the pressure gradient force were not available. This was unfortunate, as they might have had significant influence because the densities of the sludge and the particles were of the same order. The particles were injected at the inlets at the same moment. For the simulations of digested sludge this was done at $t = 0.21$ s and for the simulations of the mixture this was done at $t = 4.01$ s. The Rosin-Rammler distribution was assumed for the diameter with a minimum diameter of 0.1 mm, a maximum diameter of 1 mm and a mean of 0.5 mm, see for an explanation ANSYS (2013b).

3.2.5 Numerical Methods

A pressure-based solver was chosen as it was originally developed for incompressible flows. As a transient solution was sought the PISO algorithm was used, which is recommended by ANSYS in this case. Except for the recirculation models all models were initialized using the hybrid initialization option of FLUENT. The recirculation models were initialized using the values of the inlet throughout the entire domain.

In order to obtain a converging solution an initial solution was determined using lower order discretization schemes, as these schemes are more stable. The final solution was calculated using higher order schemes. All models, except the recirculation models, used under-relaxation factors for the body forces and momentum to obtain converging solutions.

In table 3.2.15 the settings deviating from the default settings for the simulations of the recirculation models are displayed. The discrete model was not included in these calculations.

Recirculation models		Initial Solution	Final Solution
Spatial Discretization	*Pressure*	Standard	2nd Order
	Turbulent Kinetic Energy	1st Order Upwind	2nd Order Upwind
	Turbulent Dissipation	1st Order Upwind	2nd Order Upwind
Transient Formulation		1st Order Implicit	2nd Order Implicit
Time Step Size (s)		0.01	0.01
Max Iterations/Time Step		10	20
Number of Time Steps		20	410

Table 3.2.15: Settings for the calculation of the transient solution of the first, second and third recirculation model. For the first recirculation model the settings of the final solution are used for the total calculation with the number of time steps being 710.

In table 3.2.16 the settings deviating from the default settings for the simulations of Model 1 - Baseline and Model 2 - Venturi with digested sludge in all pipelines are displayed. Under-relaxation factors were necessary to obtain a converging solution.

Digested		Initial Solution	Final Solution
Spatial Discretization	*Pressure*	Standard	2nd Order
	Turbulent Kinetic Energy	1st Order Upwind	2nd Order Upwind
	Turbulent Dissipation Rate	1st Order Upwind	2nd Order Upwind
Transient Formulation		1st Order Implicit	2nd Order Implicit
Under-relaxation Factors	*Body Forces*	0.7	0.7
	Momentum	0.3	0.3
Time Step Size (s)		0.01	0.01
Number of Time Steps		20	3980

Table 3.2.16: Settings for the calculation of the transient solution of Model 1 - Baseline and Model 2 - Venturi with digested sludge in all pipelines.

In table 3.2.17 the settings deviating from the default settings for the simulations of the models 1 - 5 with a mixture of sludge are shown. A first solution was calculated because the hybrid initialization initialized all pipes with digested sludge and hence the mass fractions were not correct. Because of the low velocities of primary and THP sludge, the digested sludge remained in the pipes of primary and THP. Therefore a first solution was determined with high velocities for all three types of sludge. Then the final solution was computed.

Mixture		Initial Solution	First Solution	Final Solution
Spatial Discr.	*Pressure*	Standard	2nd Order	2nd Order
	Turb. Kin. Energy	1st Order Upwind	2nd Or. Up.	2nd Or. Up.
	Turb. Dis. Rate	1st Order Upwind	2nd Or. Up.	2nd Or. Up.
Transient Form.		1st Order Implicit	2nd Or. Impl.	2nd Or. Impl.
Under-relax. Factors	*Body Forces*	0.7	0.7	0.7
	Momentum	0.3	0.3	0.3
Time Step Size (s)		0.01	0.01	0.01
Num. of Time Steps		20	130	3850
Inlet Velocity (m/s)	*Digested*	4	4	0.79
	Primary	2	2	0.06
	THP	2	2	0.08

Table 3.2.17: Settings for the calculation of the transient solutions of models 1 - 5 with a mixture.

3.2.6 Estimation of the Discretization Error

The discretization error was determined for two models, namely Model 1 - Baseline and Model 5 - Venturi D40, both with a mixture of sludge. As already stated the used version of ANSYS FLUENT was an academic license and had a limitation on the number of cells to be solved of 512,000 cells. Hence, the grid was refined once and coarsened once in order to generate three grids with the right refinement factors. So the 'medium' grid was the grid for which the solution was originally solved. In tables 3.2.18 and 3.2.19 relevant values of the meshes of respectively Model 1 and Model 5 are displayed. Comparing these to the recommended values by FLUENT of figure 2.4.4 the quality was judged to be acceptable to good.

Mesh of Model 1 - Baseline	# elements	V (m^3)	Orth. Q.	Asp. R.	Skew.
Coarse	55210	0.1533	0.2147	15.645	0.8585
Medium	195305	0.1559	0.1725	15.298	0.9160
Fine	483289	0.1565	0.2291	15.545	0.9160

Table 3.2.18: Relevant information about the coarse, medium and fine mesh of Model 1 - Baseline. From left to right the number of elements, the volume of the mesh, the minimum value of the orthogonal quality, the maximum value of the aspect ratio and the maximum value of the skewness.

Mesh Model 5 - Venturi D40	# elements	V (m^3)	Orth. Q.	Asp. R.	Skew.
Coarse	71631	0.1463	0.1762	38.972	0.9380
Medium	238198	0.1526	0.1715	54.766	0.9351
Fine	501740	0.1531	0.2152	27.973	0.9160

Table 3.2.19: Relevant information about the coarse, medium and fine mesh of Model 5 - Venturi D40. From left to right the number of elements, the volume of the mesh, the minimum value of the orthogonal quality, the maximum value of the aspect ratio and the maximum value of the skewness.

Values of the representative mesh sizes calculated with equation (2.4.32) and the grid refinement factors are found in table 3.2.20. Three of the grid refinement factors were above the preferred value of 1.3. Only the value of r_{21} of Model 5 did not exceed 1.3. This was because the medium mesh of Model 5 was too large to generate a mesh with the preferred refinement factor and fewer cells than 512,000.

The local order of convergence was calculated for 25 points along the y-axis, 50 mm in front of the outlet.

	Model 1	Model 5
h_1	$6.962 \cdot 10^{-3}$	$6.732 \cdot 10^{-3}$
h_2	$9.267 \cdot 10^{-3}$	$8.620 \cdot 10^{-3}$
h_3	$1.405 \cdot 10^{-2}$	$1.269 \cdot 10^{-2}$
r_{21}	1.332	1.280
r_{32}	2.019	1.885

Table 3.2.20: Values of the representative mesh sizes and grid refinement factors for the coarse, medium and fine grids of Model 1 - Baseline and Model 5 - Venturi D40.

3.3 Validation of the CFD Model

In Appendix E the quest for a suitable validation measurement instrument is recorded. The CFD model was validated by comparing the pressure drop over the venturi with the prediction of the model. This would be done for two different geometries of the venturi, but eventually this was only done for a venturi with a narrowing of 40 mm. This one is modelled in Model 5 - Venturi D40, see figure 3.2.11 for its Solidworks model and drawing. The other model and its results can be found in Appendix D.2. It was assumed that if this validation was successful, the other models which used the same settings could considered to be reliable as well.

Furthermore, the dry solids content of five samples over the diameter behind the venturi were determined on the 21th of June 2017, see figure 3.3.1. These were not used as a validation of the particle tracking or the species transport model as the pipe geometry on site was changed and did not match the model anymore. Nevertheless, they served as an indication of the mixing.

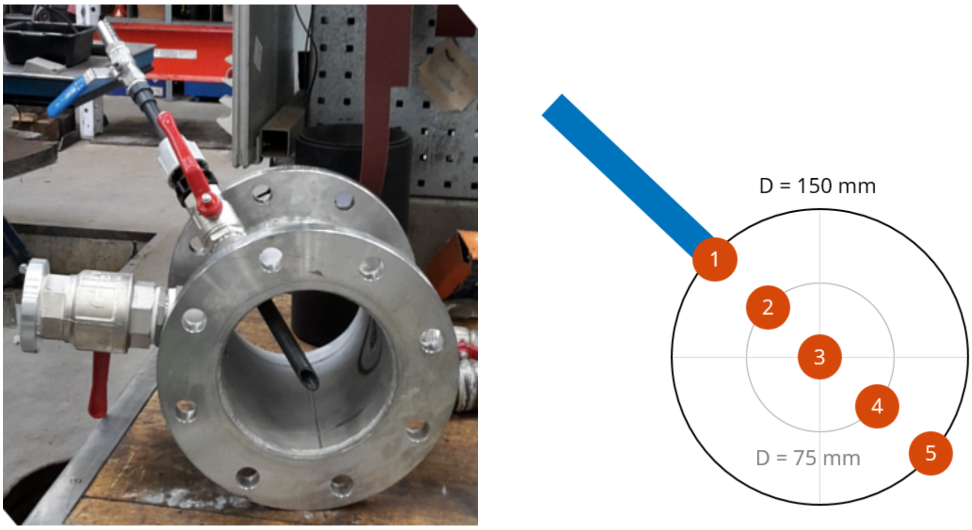

(a) Sampling point build in behind the venturi. (b) Schematic representation of the samples taken.

Figure 3.3.1: Picture of the sampling point and a schematic representation of the samples taken.

Chapter 4

Results

In this chapter the results of the viscosity measurements on the three types of sludge, the results of the CFD models and the validation are analysed.

4.1 Viscosity Measurements

The viscosity of the three types of sludge were measured at the TU Delft, using a high-end Anton Paar rheometer, and at WVS, using a Brookfield viscometer. As described in section 2.3.2 measuring viscosity is a sensitive and complicated procedure. With this in mind both data sets were assessed on reliability and usability in order to choose one for which a non-Newtonian model for the viscosity of each type of sludge could be determined.

4.1.1 Results TU Delft

The TU Delft measured the viscosity and the shear stress for a range of shear rates, and the dry solids content and yield stress of four samples, namely primary sludge, THP sludge, digestate and AD sludge. See also 3.1.1 for more information about the measuring procedure. The primary sludge was also sieved and measured after this, but as already mentioned in 3.1.1 this data was disregarded. It was assumed that the AD sludge sample, taken from the middle of the digester, resembled digested sludge in the recirculation pipe, which was extracted at three quarters of the digester, best. Hence in the following, digested sludge refers to AD sludge.

In table 4.1.1 the average dry solids content and the average measured yield stress are shown for the three types of sludge. The yielding process was not always abrupt.

One type of measurement was performed, namely a speed ramp, increasing the shear rate logarithmically from 10^{-2} to 10^{3} s^{-1}.

TU Delft	Digested	Primary	THP
Average dry solids content (%)	5.3	4.2	11.0
Average yield stress (Pa)	0.28	4.1	1.3

Table 4.1.1: Dry solids content and yield stress measured at TU Delft, December 2016.

Speed Ramp

In figure 4.1.2 loglog plots of the shear stress τ against the shear rate γ are plotted for each type of sludge separately, depicting the three separate measurements of each type and the average of those, and the average measurements of all types plotted together.

For shear rates larger than 1 s^{-1} the shear stress measurements on primary sludge showed a large deviation and fluctuation. This was due to many irregular components with large sizes in primary sludge that influenced the rheological measurement. Hence, the repeatability was not good. Digested, and THP sludge in particular, showed similar results in the three measurements.

Comparing all types of sludge it was observed that primary sludge had a higher shear stress for lower shear rates than digested and THP sludge. THP had a higher shear stress than digested sludge which could be accounted for by the higher dry solids content of THP.

The slopes of the measurements were all smaller than 1 and hence it could be concluded that all types of sludge behaved as shear-thinning non-Newtonian fluids which corresponds to literature, see sections 2.2.2 and 2.2.6.

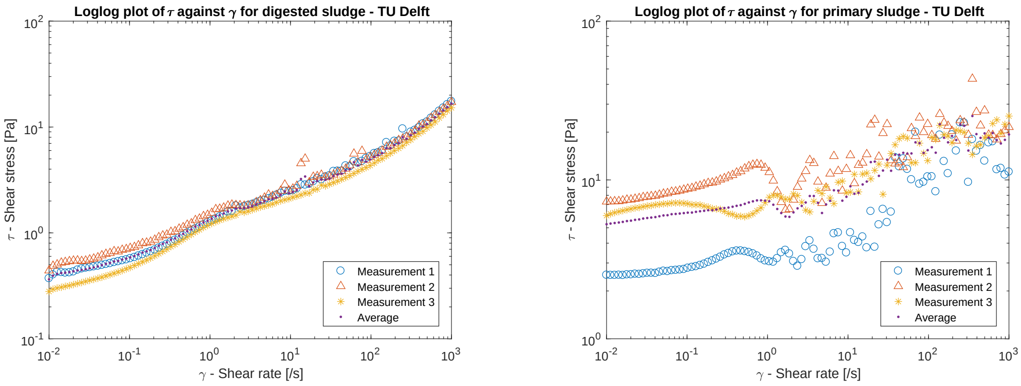

(a) Digested, 5.3 % ds, 40 °C.

(b) Primary, 4.2 % ds, 40 °C.

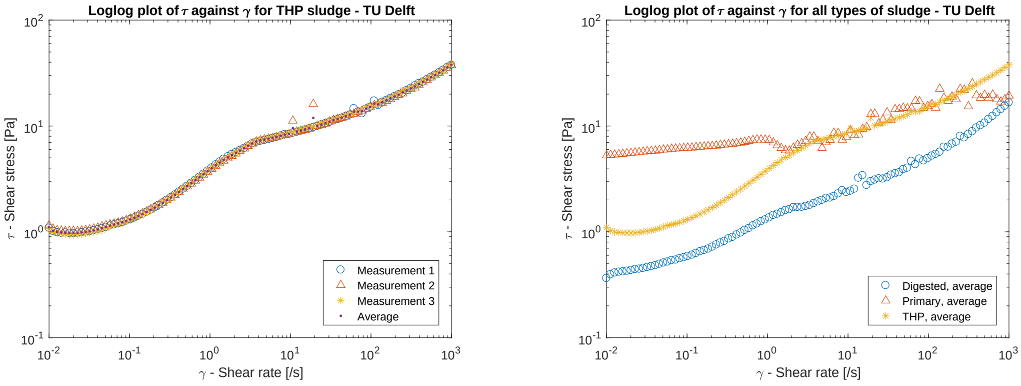

(c) THP, 11.0 % ds, 40 °C.

(d) All types.

Figure 4.1.2: Plots of the shear stress τ against the shear rate γ measured at the TU Delft.

In figure 4.1.3 loglog plots of the viscosity μ against the shear rate γ are plotted for each type of sludge separately, depicting the three separate measurements of each type and the average of those, and the average measurements of all types plotted together.

For shear rates larger than 1 s^{-1} the viscosity measurements on primary sludge showed also a deviation and fluctuation, but to a lesser extent than for the shear stress measurements in figure 4.1.2 (b). Digested and THP sludge in particular showed similar results in the three measurements.

Comparing all types of sludge similar observations could be made as for the shear stress measurements, namely that primary sludge had a higher viscosity for lower shear rates than digested and THP sludge, and THP had a higher viscosity than digested sludge which could be accounted for by the higher dry solids content of THP.

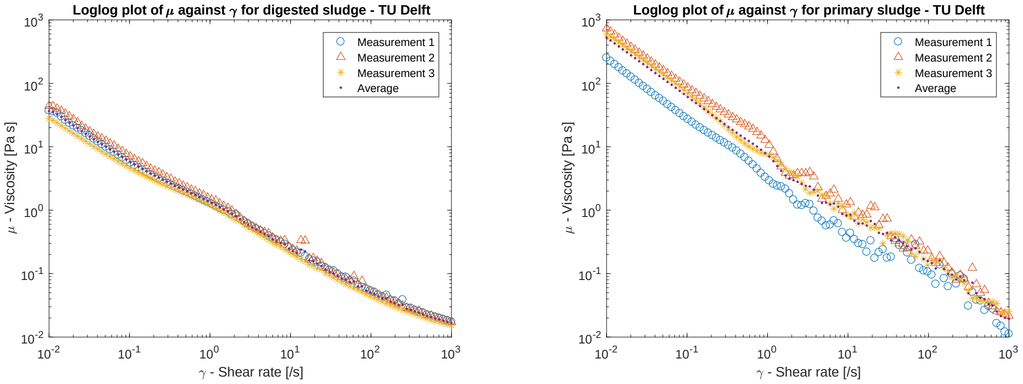

(a) Digested, 5.3 % ds, 40 °C. (b) Primary, 4.2 % ds, 40 °C.

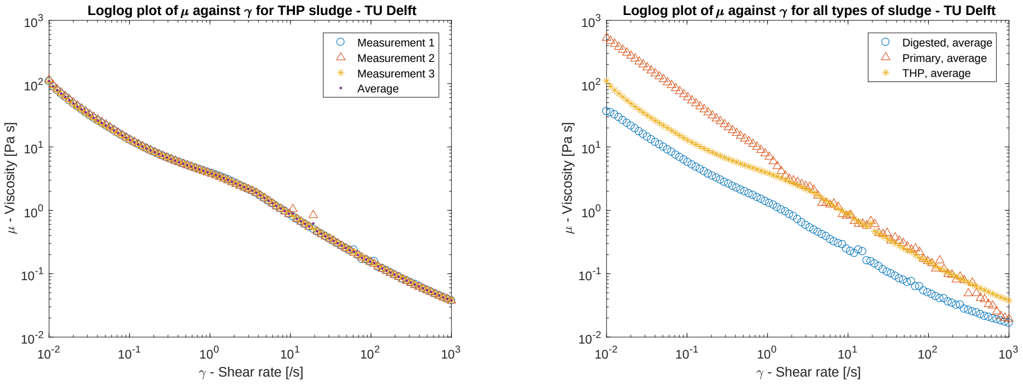

(c) THP, 11.0 % ds, 40 °C. (d) All types.

Figure 4.1.3: Plots of the viscosity μ against the shear rate γ measured at the TU Delft.

4.1.2 Results WVS

At WVS the viscosity and the shear stress of primary, digested and THP sludge were measured for a range of rotation speeds. Furthermore the dry solids content and density were determined. See also section 3.1.2 for more information about the measuring procedure.

In Ttable 4.1.5 the average dry solids content and the density are shown for the three types of sludge on which the measurements were performed. The second measurement of the density is presented in table 4.1.6. The measurement error was not known, but was assumed to be of significant influence as a 100 ml measuring cylinder is not very accurate.

As already discussed in sections 2.1.1 and 2.2.6 the three types of sludge differed in composition and this translated into a specific odour and colour for each type of sludge, see figure 4.1.4 (a). Primary sludge was typically very inhomogeneous which negatively influenced the repeatability and reliability of these measurements. A photo of such an irregular component is depicted in figure 4.1.4.

(a) Jars containing (from left to right) THP, digested and primary sludge.

(b) An irregular component in primary sludge.

Figure 4.1.4: Photos of the differences in colour between the types of sludge, and an example of the inhomogeneity of primary sludge.

Two types of measurements were performed, namely a measurement of the viscosity at constant rational speed in time to determine the time-dependent behaviour of sludge and a speed ramp, increasing the rotational speed from 0 to 200 rpm and back. It should be noted that the depicted values are relative values which cannot be compared one-to-one with the values of TU Delft.

WVS	Digested	Primary	THP
Average dry solids content (%)	5.7	6.3	9.5
Density (kg/m^3)	9.2e2	1.0e3	1.0e3

Table 4.1.5: Dry solids content and density measured at WVS, March 2017.

WVS	Digested	Primary	THP
Density (kg/m^3)	9.0e2	1.2e3	1.0e3

Table 4.1.6: Density measured at WVS, May 2017.

Constant Speed

For the duration of five minutes the viscosity was measured of the three types of sludge using spindle RV-2 at 1 rpm. The samples were approximately 30 °C during the measurement and for primary sludge a second measurement was performed at about 13 °C. This was done with two different jars of primary sludge to prevent history influencing the measurements. In table 4.1.7 the temperature range is presented

Constant speed	Digested	Primary	THP
Temperature range (°C)	31.7 - 30.5	12.7 - 13.6 29.6 - 28.4	31.4 - 30.4

Table 4.1.7: Temperature range of constant speed measurements performed at WVS.

A plot of the (relative) viscosity over time is supplied in figure 4.1.8. The viscosities of the different types of sludge can be compared because they are measured using the same spindle. The viscosity of primary sludge was higher for both measurements than the viscosities of digested and THP sludge. It showed fluctuations over time, which are likely caused by the inhomogeniety, and the viscosity decreased over time. This corresponded to thixotropic time-dependent behaviour, see section 2.2.3 and also corresponded to findings in literature. However, the viscosity of digested sludge remained roughly constant, and the viscosity of THP seemed to increase over time (rheopectic time-independent behaviour) which was odd behaviour for sludge as it was not recorded in current literature.

The viscosity of the colder sample of primary sludge was higher than the viscosity of the warmer sample. This corresponded to findings in literature that the viscosity decreases with increasing temperature, see section 2.2.5.

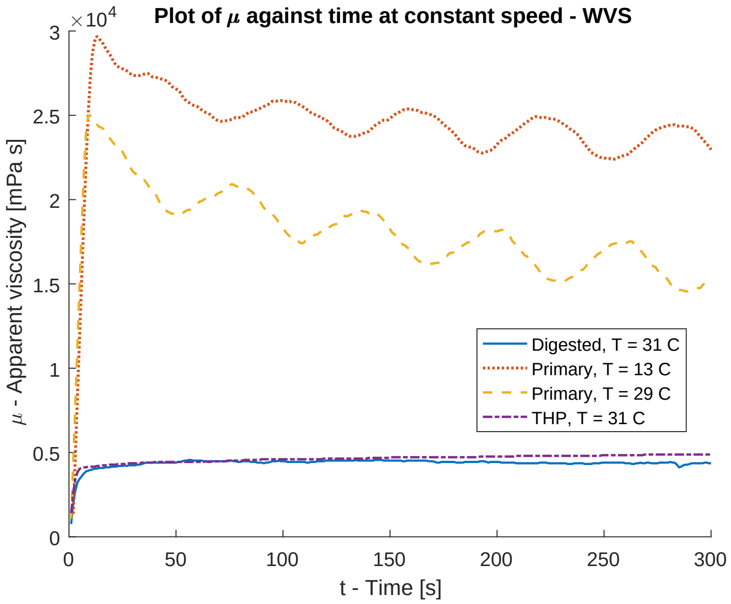

Figure 4.1.8: Plot of the apparent viscosity μ as a function of time measured with spindle RV-2 at WVS at constant rotational speed of 1 rpm.

Speed Ramp

Four speed ramps were carried out, measuring the shear stress and viscosity at different rotational speeds. One ramp was performed on digested, one on THP sludge and again two on primary sludge for two different temperature ranges. In table 4.1.9 the used spindles and temperature ranges are summarized. The first three measuring points and the last were discarded because of high unrealistic values due to start-up conditions. It should be noted that the measuring values are still relative values, thus only values measured by the same spindle can be compared.

Speed ramp	Digested	Primary	THP
Spindle	RV-2	RV-4	RV-2
Temperature range (°C)	34.3 - 33.1	14.3 - 14.4 32.1 - 31.4	34.1 - 32.6

Table 4.1.9: Parameters of the speed ramp measurements of WVS, measured over a range of rotational speeds from 0 - 200 rpm.

In figures 4.1.10 and 4.1.11 loglog plots of respectively the shear stress and the viscosity against the rotational speed are displayed with which the time-dependent behaviour can be determined as well. Comparing the paths of the ramp ‘forwards’, from low to high speed, and ‘backwards’, from high to low speed, to the plots in figure 2.2.16 (a) and (b), the time-dependent behaviour could be classified. These confirmed the conclusions of the constant speed ramp as well, namely digested and primary sludge behaved thixotropic in time, whereas THP behaved rheopectic in time.

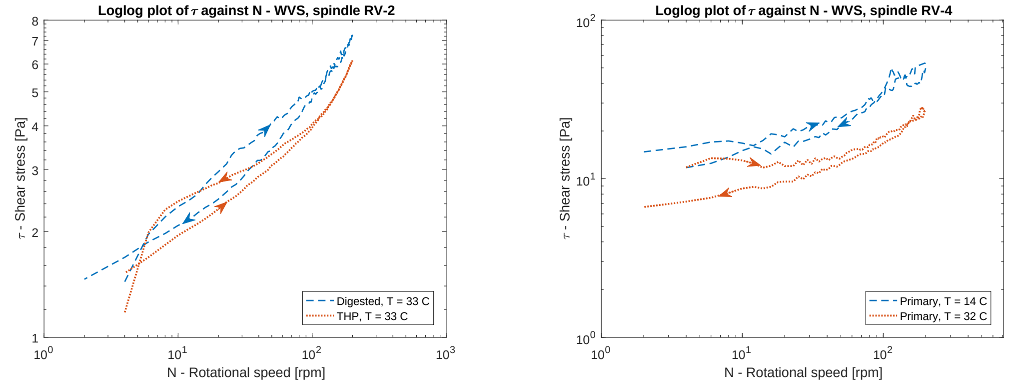

(a) RV-2: Digested (5.7 % ds, 33 °C), THP (9.5 % ds, 33 °C).

(b) RV-4: Primary (6.3 % ds, 14 °C), Primary (6.3 % ds, 32 °C).

Figure 4.1.10: Loglog plots of the shear stress τ against the rotational speed N measured at WVS.

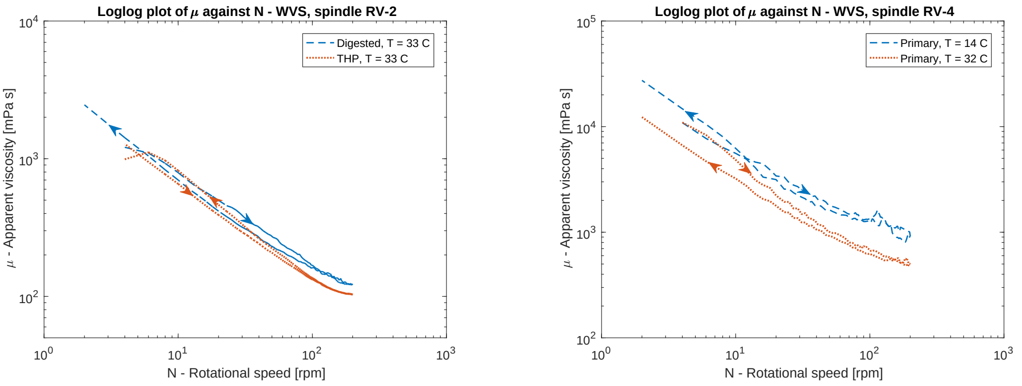

(a) RV-2: Digested (5.7 % ds, 33 °C), THP (9.5 % ds, 33 °C).

(b) RV-4: Primary (6.3 % ds, 14 °C), Primary (6.3 % ds, 32 °C).

Figure 4.1.11: Loglog plots of the apparent viscosity μ against the rotational speed N measured at WVS.

4.1.3 Comparing the Measurements of TU Delft and WVS

In order to be able to compare the speed ramp measurements performed using the viscometer of WVS with the shear rate ramp measurements of the TU Delft, the relative values of the measurements of WVS should be converted to absolute values. The mathematical procedure to do this for the Brookfield DV2T viscometer is outlined and applied in Appendix B.

In order to convert the relative values to absolute values only the first part of the speed ramp was considered, the measurements when turning up the speed. Moreover, in order to find a relation between the scaled shear stress and rotational speed a first order polynomial, a linear relation, and a third order polynomial were used to fit the data points.

Digested Sludge

In figure 4.1.12 the shear stress measurements on digested sludge of the TU Delft are compared with those obtained at WVS. They were in good agreement. For higher shear rates the shear stresses of WVS deviated more from the shear stresses of TU Delft. The polynomials showed similar results.

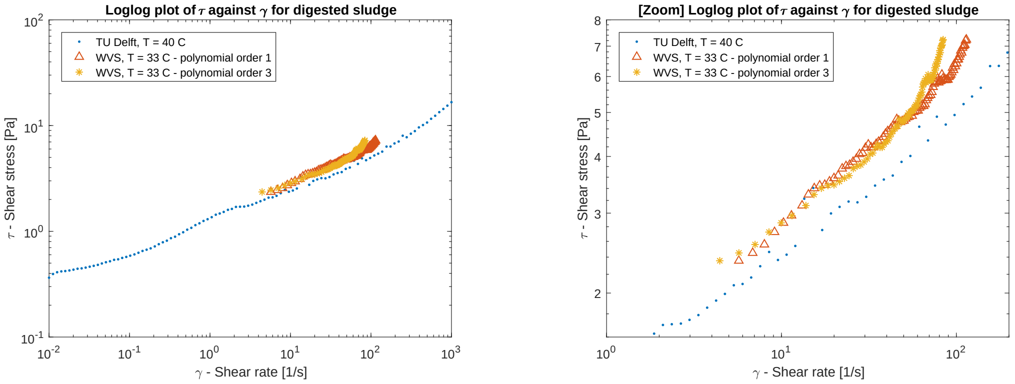

(a) Digested TU Delft: T = 40 °C, 5.3% ds. Digested WVS: T = 33.5 °C, 5.7% ds.

(b) {Zoom} Digested TU Delft: T = 40 °C, 5.3% ds. Digested WVS: T = 33.5 °C, 5.7% ds.

Figure 4.1.12: Loglog plots comparing the shear stress τ against the shear rate γ between the measurements of TU Delft and WVS for digested sludge.

In figure 4.1.13 the viscosity measurements on digested sludge of the TU Delft are compared with those obtained at WVS. These showed good agreement as well, but to a lesser extent than for the shear stresses. The viscosity measured at WVS was higher, which could both be due to a lower temperature and a slightly higher dry solids content. Both the measurements of TU Delft and WVS showed approximately the same slope.

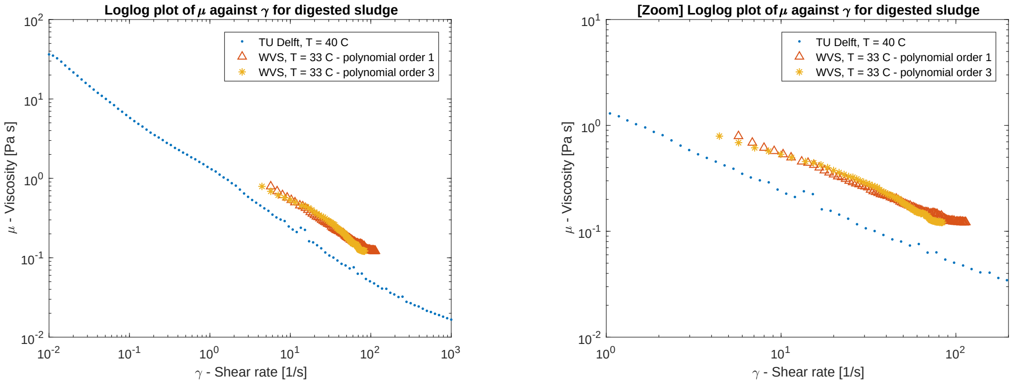

(a) Digested TU Delft: T = 40 °C, 5.3% ds. Digested WVS: T = 33.5 °C, 5.7% ds.

(b) {Zoom} Digested TU Delft: T = 40 °C, 5.3% ds. Digested WVS: T = 33.5 °C, 5.7% ds.

Figure 4.1.13: Loglog plots comparing the viscosity μ against the shear rate γ between the measurements of TU Delft and WVS for digested sludge.

Primary Sludge

In figure 4.1.12 the shear stresses of primary sludge obtained at the TU Delft and at WVS are compared. Due to the inhomogeneity of primary sludge the measurements showed large fluctuations and deviated from each other. The third order polynomial gave physically unrealistic values, as at one shear rate two shear stresses were possible, and was not deemed reliable, although it gave a better fit on the scaled shear stresses and rotational speed, see figure B.1.3 (b).

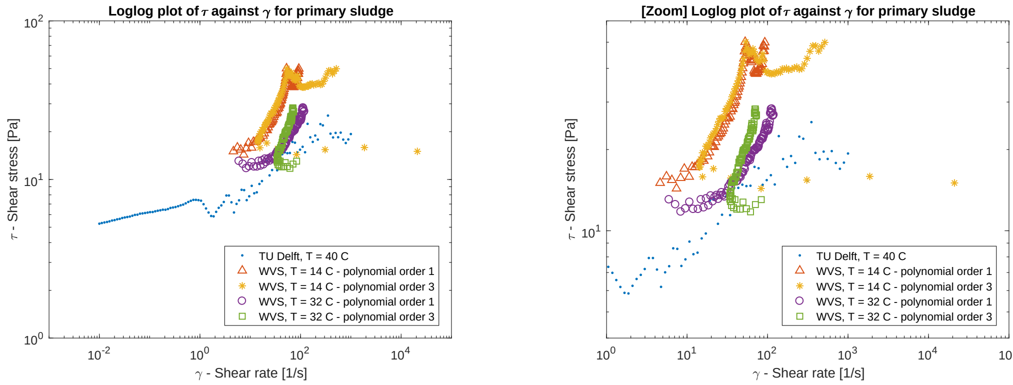

(a) Primary TU Delft: T = 40 °C, 4.2% ds. Primary WVS: T = 14.4 °C, 6.3% ds, and T = 32.0 °C, 6.3% ds.

(b) {Zoom} Primary TU Delft: T = 40 °C, 4.2% ds. Primary WVS: T = 14.4 °C, 6.3% ds, and T = 32.0 °C, 6.3% ds.

Figure 4.1.14: Loglog plots comparing the shear stress τ against the shear rate γ between the measurements of the TU Delft and WVS for primary sludge.

In figure 4.1.15 the viscosity measurements on primary sludge of the TU Delft are compared with those obtained at WVS. Again the third order polynomials exhibited strange, unrealistic behaviour. The first order polynomials showed more realistic behaviour, although the colder sample of T = 14.4 °C had a strange peak around 50 s^{-1}. The slope of the first order polynomial of T = 32.0 °C was roughly the same as the one of TU Delft. The viscosity of the primary sludge measured at WVS was higher than the viscosity measured at TU Delft, which could both be due to the lower temperature and higher dry solids content at WVS.

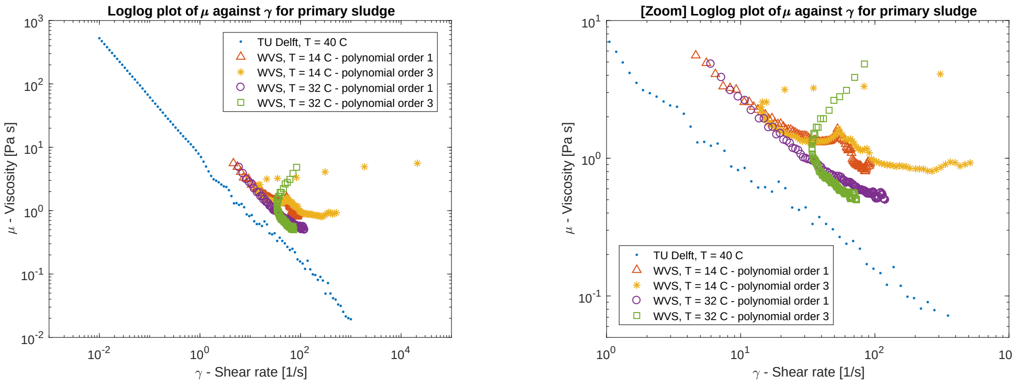

(a) Primary TU Delft: T = 40 °C, 4.2% ds. Primary WVS: T = 14.4 °C, 6.3% ds, and T = 32.0 °C, 6.3% ds.

(b) {Zoom} Primary TU Delft: T = 40 °C, 4.2% ds. Primary WVS: T = 14.4 °C, 6.3% ds, and T = 32.0 °C, 6.3% ds.

Figure 4.1.15: Loglog plots comparing the viscosity μ against the shear rate γ between the measurements of the TU Delft and WVS for primary sludge.

THP Sludge

In figure 4.1.16 the shear stresses of THP sludge obtained at the TU Delft and at WVS are compared. The first order polynomial of WVS had the same shape as TU Delft in the range of shear rates of WVS. The first and third order polynomial deviated from each other for higher shear rates. The shear stress measured at WVS was lower than measured at the TU Delft.

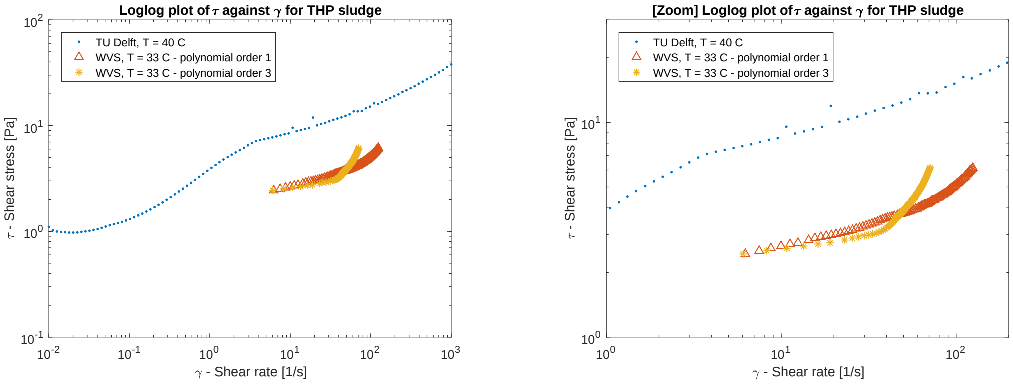

(a) THP TU Delft: T = 40 °C, 11.0% ds. THP WVS: T = 33.4 °C, 9.5% ds.

(b) {Zoom} THP TU Delft: T = 40 °C, 11.0% ds. THP WVS: T = 33.4 °C, 9.5% ds.

Figure 4.1.16: Loglog plots comparing the shear stress τ against the shear rate γ between the measurements of the TU Delft and WVS for THP sludge.

In figure 4.1.17 the viscosity measurements of THP sludge of the TU Delft are compared with those obtained at WVS. These showed better agreement than the shear stresses. The viscosity measured at WVS is slightly lower, which could be due to a balancing of a lower temperature which would result in a higher viscosity, and a lower dry solid contents, which would result in a lower viscosity. The slope of both the TU Delft and the first order polynomial of WVS was roughly the same.

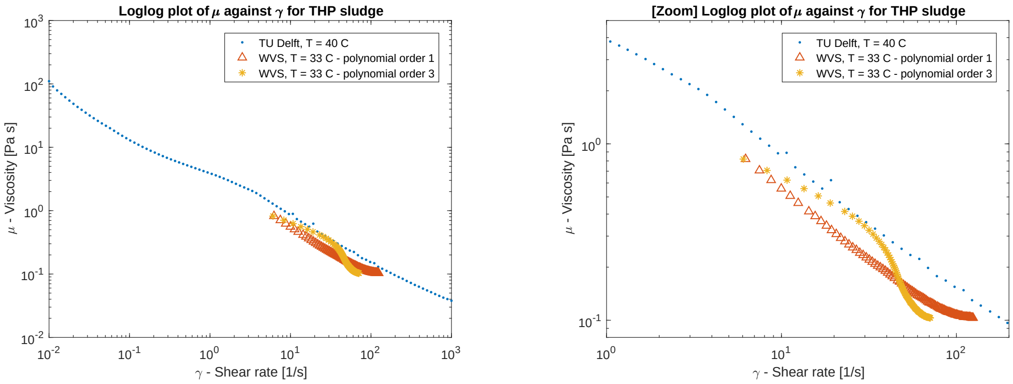

(a) THP TU Delft: T = 40 °C, 11.0% ds.
THP WVS: T = 33.4 °C, 9.5% ds.

(b) {Zoom} THP TU Delft: T = 40 °C, 11.0% ds.
THP WVS: T = 33.4 °C, 9.5% ds.

Figure 4.1.17: Loglog plots comparing the viscosity μ against the shear rate γ between the measurements of the TU Delft and WVS for THP sludge.

4.1.4 Considerations for Choosing a Viscosity Dataset

The viscosity data set of the TU Delft was considered most suitable for this assignment and it was assumed to offer a more reliable fitting of a non-Newtonian model. A first reason was that the shear rate range of interest for this assignment was for shear rates in both the laminar and turbulent flow regime. Hence, measurements should be performed in a large range as possible, as mentioned in section 2.3.2. The TU Delft was able to measure the shear rate from 10^{-2} to 10^{3} s^{-1}, whereas the viscometer of WVS was restricted to a smaller range of about two orders of magnitude of which the actual values depended on the mathematical conversion of the relative values.

A second reason to choose for the measurements of TU Delft was that an extra source of error is introduced by the conversion of the relative values measured at WVS to absolute values. The size of this error is unknown.

A third reason was that the third order polynomial in the mathematical conversion of the values of WVS described the relation between the scaled shear stress and rotational speed better than the first order polynomial. However, it gave, especially in the case of primary and THP sludge, worse and sometimes even physically unrealistic results.

4.1.5 Fitting a non-Newtonian Model

Considering the loglog plots of the measurements of the TU Delft in both figures 4.1.2 and 4.1.3 a straight line can be distinguished. This indicated that a power law model or a Herschel-Bulkley model would fit the data well. Because hardly any upper or lower limit of the viscosity was visible in the loglog plots in figure 4.1.3 the Cross and Carreau model were discarded. The Herschel-Bulkley and the power law model have the same equation for viscosity, but the Herschel-Bulkley includes the yield stress in describing the shear stress. As the CFD model required the viscosity as input of the model, the yield stress of the Herschel-Bulkley model was not taken into account and a power law model was assumed.

The fitting was done using Matlab cftool, which used the method of least-squares to fit the data. Because of the very small and large values adopted by both the viscosity and shear rate the fitting was done using a first order polynomial on log-values of the viscosity and shear rate to ensure a more equal weighting of all data points. The values of R^2 and RMSE were used to judge the goodness of fit. Values of R^2 range from 0 to 1, with values closer to 1 indicating a better fit. Values of RMSE should be positive, with values closer to 0 indicating a fit with greater predictive value (MathWorks, 2017).

In table 4.1.18 the fitted values for the parameters k and n of the power law model, and R^2 and RMSE values are displayed for the viscosity measurements of the TU Delft. In figure 4.1.19 the power law fits are plotted together with the viscosity measurements. The slopes of digested and THP sludge, which are given by $n - 1$, were quite similar, with a greater height, k, of THP. Primary sludge had the greatest height of all, but also the smallest value for n, and hence the steepest slope $n - 1$. Hence, primary sludge behaved more viscous for lower shear rates than both digested and THP sludge, but for very high shear rates it behaved less viscous than THP sludge.

Sludge	k	n	R^2	RMSE
Digested	1.2987	0.3155	0.9975	0.1161
Primary	7.8853	0.1280	0.9964	0.1780
THP	3.5219	0.3379	0.9959	0.1449

Table 4.1.18: Fitted values for k and n of the non-Newtonian power law model for measurements of the TU Delft, with R^2 and RMSE values to judge the goodness of fit.

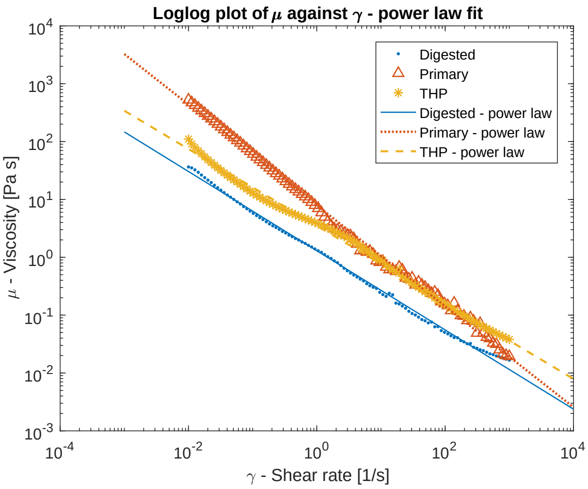

Figure 4.1.19: Loglog plots of the non-Newtonian power law fit on the viscosity measurements of the TU Delft.

4.1.6 Viscosity of a Mixture

Simulating a mixture of sludge a mixing law for the viscosity had to be assumed, see sections 2.2.7 and 3.2.4. The mass-weighted-mixing-law was assumed for the viscosity. To validate this the TU Delft performed another set of viscosity measurements, measuring the viscosity, density and dry solids content of six samples.

In table 4.1.20 the average density and dry solids content of the six samples measured at the TU Delft in June 2017 are presented together with the flow at the moment of sampling. The density of all samples were of the same order and a bit higher than the density of water. The difference in density of digested sludge measured at the TU Delft and WVS, see table 4.1.6, were partly due to deviations in the process such as the forming of foam in the digester during the measurements of WVS which could explain the smaller value.

As density mixing law the volume-weighted-mixing law was assumed. Calculating the density of the mixture this gave $\rho_{mix} = 1013$ kg/m^3. This deviated about 0.5% from the measured average density of the manual mixture, and agreed well with the density of the mixture after the venturi. This difference could be due to a measurement error or a slight deviation in the actual ratio with which the sludge was mixed.

Calculating the average dry solids content of the mixture based on volume fractions the result was 6.58 % ds. The manual mixture agreed well with this average. However the dry solids content of the mixture after the venturi deviated quite a lot. This indicated that the sludge was not well mixed at the sampling point.

TU Delft	Density (kg/m^3)	ds (%)	Flow (m^3/h)
Digested	1014	5.69	50
Primary thickened	1005	3.46	
Primary thickened mechanically	1005	5.33	6.5
THP	1015	13.6	7.5
Manual mixture	1008	6.52	-
Mixture after venturi	1012	5.39	-

Table 4.1.20: Density and dry solids content measured at TU Delft, June 2017, and the flows at the moment of sampling.

In figure 4.1.21 a loglog plot of the viscosity against the shear rate for five samples, discarding the primary thickened sample, is depicted including the theoretically estimated viscosity of the mixture. As one can see, this estimate agreed well with the measured viscosity of the manual mixture. Unlike expected, the viscosity of the mixture after the venturi was lower than the viscosities of all separate components. This could be due to the sensitivity of the sludge for changes in its structure because of heavy shearing by the venturi or to the handling of this specific sample during sampling, transport and measuring.

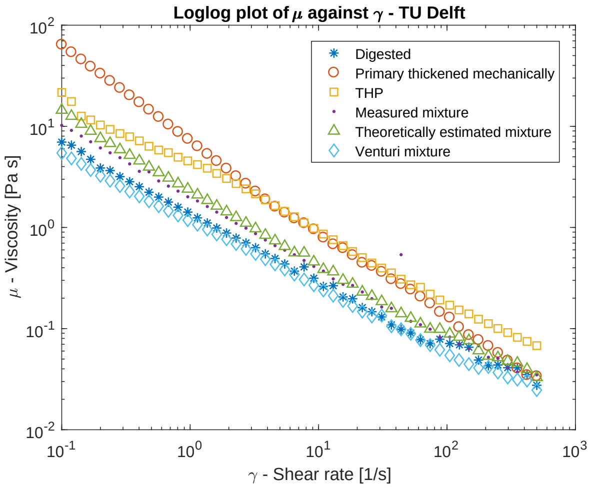

Figure 4.1.21: Loglog plot of the viscosity measurements of the TU Delft of June 2017 including the theoretically estimated viscosity of the mixture.

4.1.7 Validation of the Chosen non-Newtonian Models

In order to determine how well the fitted power law of the previous section was able to describe the last viscosity measurements of the TU Delft, a power law fit of this data was made. The results of the fitted k and n parameters are displayed in table 4.1.22 and a loglog plot in figure 4.1.24. Comparing these values of k and n to the ones from the measurements done in December 2016 and used in the model there is a good agreement, see table 4.1.23. As can be seen in figure 4.1.25 the fitted values of December 2016 do well in describing the viscosity measurements done in June 2017. Hence, this strengthens the confidence in the power law models used.

Sludge	k	n	R^2	RMSE
Digested	1.3774	0.3527	0.9952	0.1149
Primary thickened mechanically	7.3449	0.1135	0.9987	0.0820
THP	4.1289	0.3308	0.9974	0.0868
Manual mixture	1.9969	0.3224	0.9874	0.1963
Mixture after venturi	1.1471	0.3622	0.9984	0.0654

Table 4.1.22: Fitted values for k and n of non-Newtonian power law model for measurements of the TU Delft in Juni 2017, with R^2 and RMSE values to judge the goodness of fit.

Sludge	k (used)	k	n (used)	n	R^2	RMSE
Digested	1.2987	1.3774	0.3155	0.3527	0.9952	0.1149
Primary thickened mechanically	7.8853	7.3449	0.1280	0.1135	0.9987	0.0820
THP	3.5219	4.1289	0.3379	0.3308	0.9974	0.0868
Manual mixture		1.9969		0.3224	0.9874	0.1963
Mixture after venturi		1.1471		0.3622	0.9984	0.0654

Table 4.1.23: Comparing the fitted k and n parameters of the viscosity measurements performed at the DU Delft in December 2016 and June 2017.

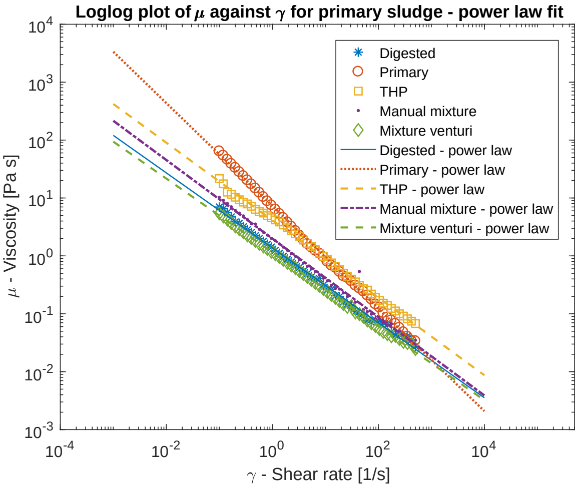

Figure 4.1.24: Loglog plot of the viscosity measurements of the TU Delft of June 2017 including the fitted power law models.

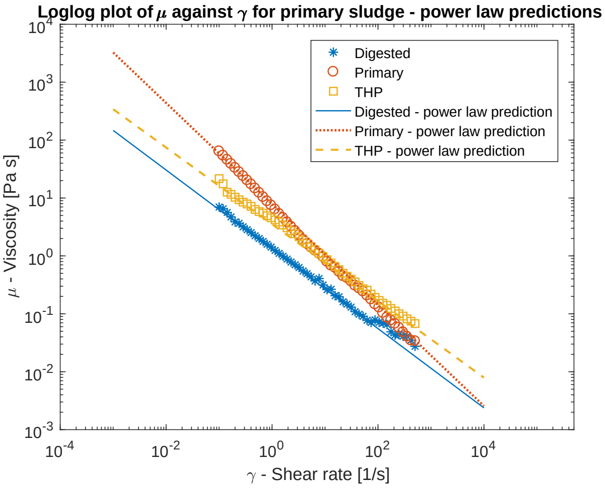

Figure 4.1.25: Loglog plot of the viscosity measurements of the TU Delft of June 2017 of digested, primary and THP sludge including the power law models of the TU Delft measurements of December 2016.

4.2 CFD Model

The results of the different CFD models are discussed in this section. Relevant problem variables were considered to be density, mass fractions of the species, pressure, velocity and viscosity. Contour plots of these variables were made by slicing the pipes through the centrelines. Furthermore, the particle tracks gave relevant information about the mixing and were plotted using different colours according to their origins.

4.2.1 Recirculation Pipe

To start with, the recirculation pipe was considered to see whether the model could be simplified. The recirculation pipe passed a heat exchanger on the first floor before being fed with primary and THP sludge on the ground floor. The question was which parts of the pipeline behind the heat exchanger had significant influence on the flow field.

In figure 4.2.1 contours of the velocity of the final solution for all three models are depicted. And in figure 4.2.2 the velocity profile of the vertical cross-section of the outlet of the pipe is compared for all three models.

The velocity profile of the first, which is the full model, and second model, including one elbow, hardly showed any difference. Both showed asymmetric behaviour of the flow due to the elbow in vertical direction. However the velocity profile of the third model, a straight pipe, was axisymmetric. This difference might be important for the junction with primary and THP sludge. Hence it was decided to include the elbow, the second model, but not the full recirculation pipeline, the first model.

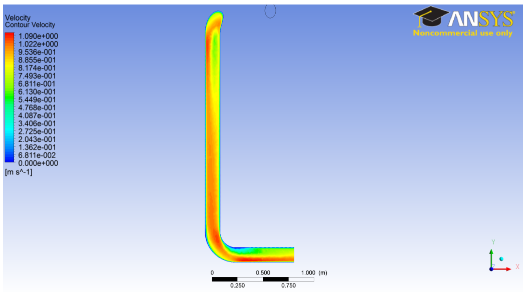

(a) First model

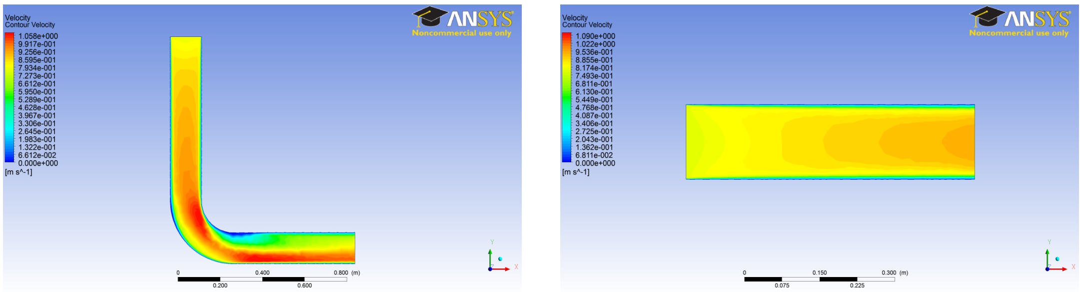

(b) Second model (c) Third model

Figure 4.2.1: Velocity contours of the final solution.

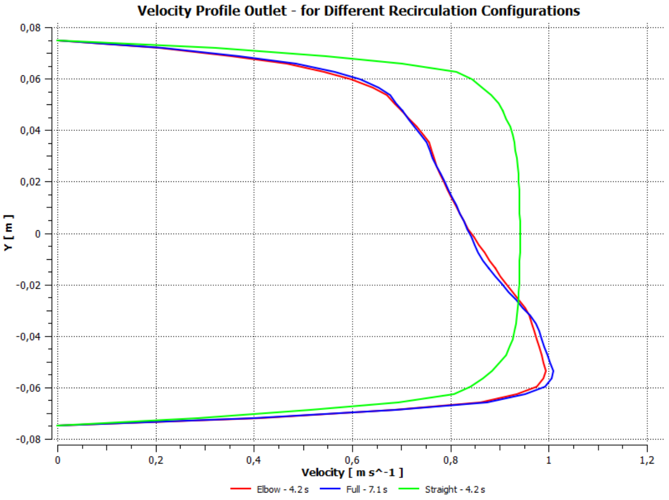

Figure 4.2.2: Velocity profile outlet of the first (blue), the second (red), and third (green) model.

4.2.2 Model 1 - Baseline

The baseline model was first run with one type of sludge, namely digested sludge. Unfortunately, FLUENT had some issues saving the variables but not the particles tracks, hence a second run was needed. Because of limited resources, this run was only computed for 6 seconds instead of 34 seconds. It was assumed that the solution was converged to a steady solution at this time.The second simulation was done using a sludge mixture.

Digested sludge

Three views of the pressure field are depicted in figure 4.2.3. The pressure drop from the inlet of digested sludge to the outlet was $\Delta P = 1.10$ kPa.

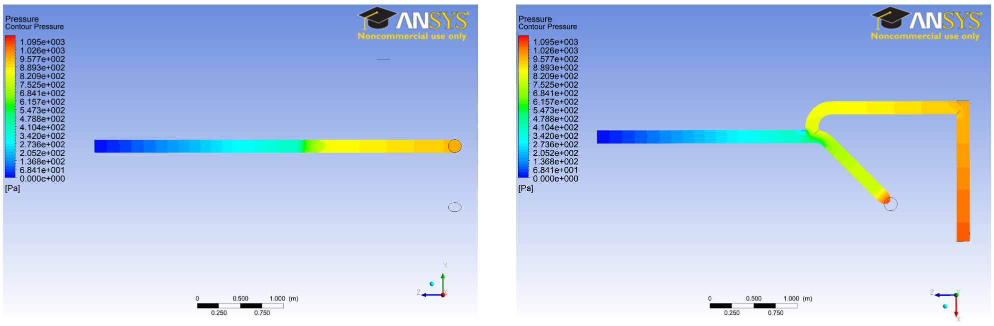

(a) Side view, YZ-plane.

(b) Top view, ZX-plane.

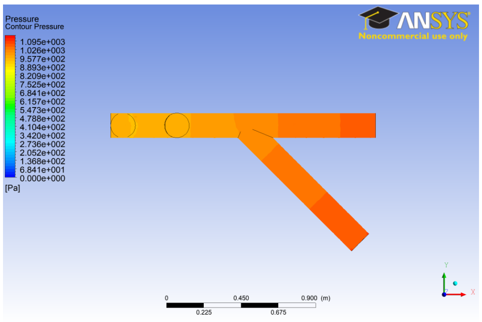

(c) Front view, XY-plane.

Figure 4.2.3: Pressure of the baseline model with digested sludge at $t = 6$ s, with ΔP = 1.10 kPa.

In figure 4.2.4 plots of the velocity profile are depicted. The velocity profile at the outlet was roughly axisymmetric.

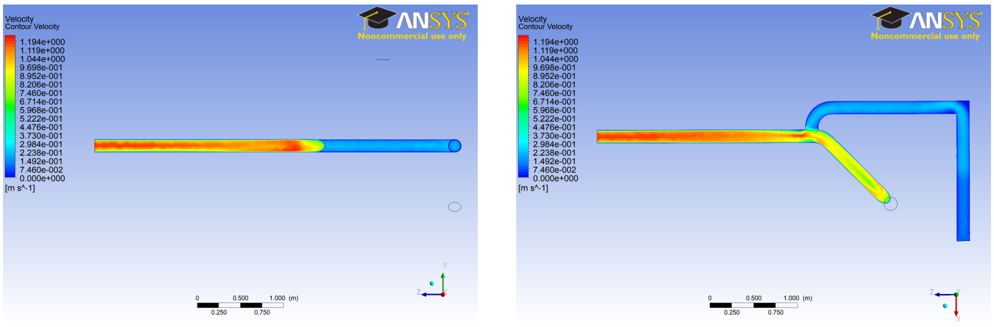

(a) Side view, YZ-plane. (b) Top view, ZX-plane.

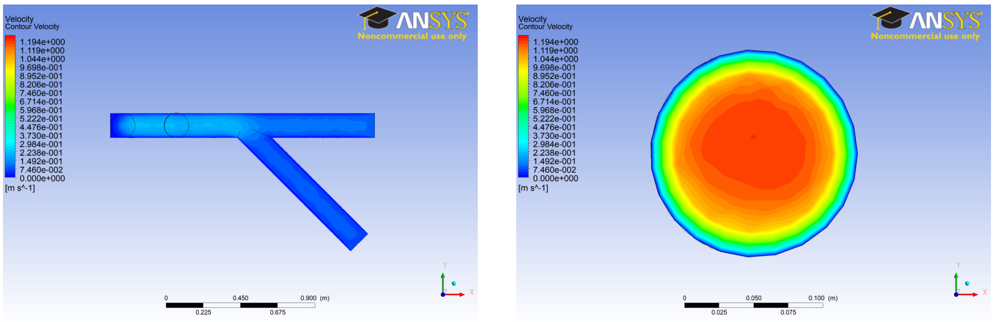

(c) Front view, XY-plane. (d) Front view, XY-plane, outlet.

Figure 4.2.4: Velocity of the baseline model with digested sludge at $t = 6$ *s, with* $\max(\vec{u}) = 1.19$ *m/s.*

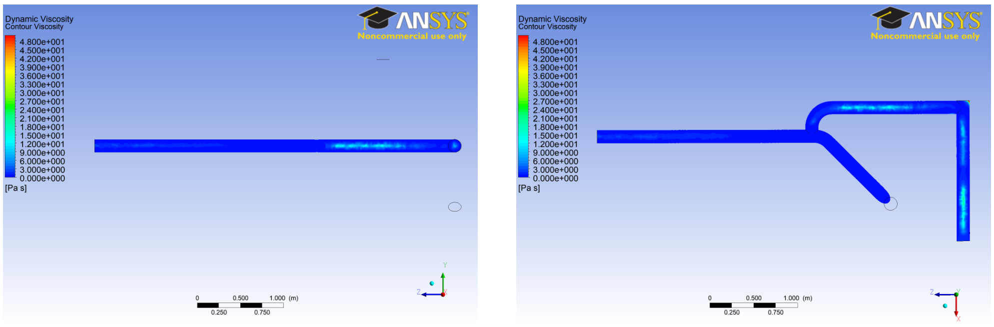

(a) Side view, YZ-plane.

(b) Top view, ZX-plane.

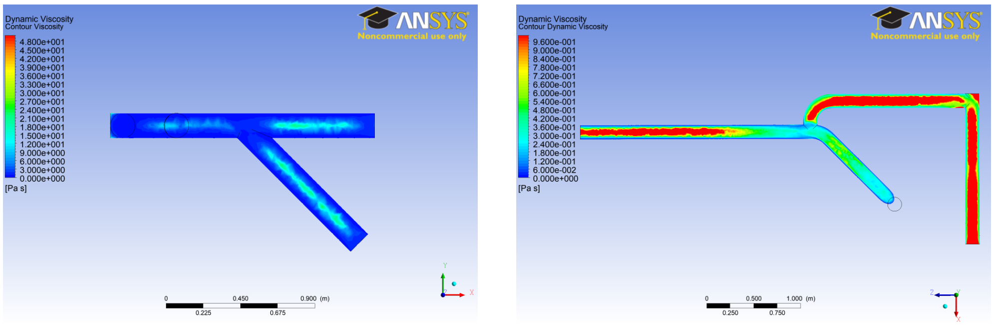

(c) Front view, XY-plane.

(d) Top view, ZX-plane, μ between $0-1$ Pa·s.

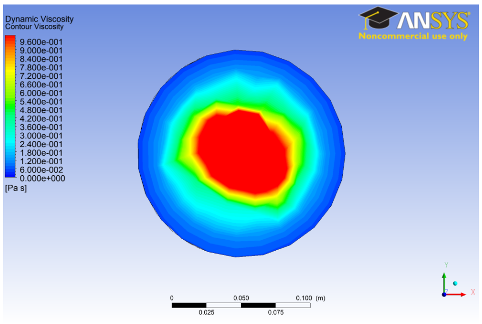

(e) Front view, XY-plane, outlet, μ between $0-1$ Pa·s.

Figure 4.2.5: Dynamic viscosity ranging from $0-50$ Pa·s for (a), (b) and (c), and from $0-1$ Pa ·s for (d) and (e), of the baseline model with digested sludge at $t = 6$ s.

Five views of the dynamic viscosity are displayed in figure 4.2.5. The viscosity took on values around 20 Pa·s in the middle of the pipes of primary and THP sludge. In the pipe containing digested sludge and a sludge mixture of all types, the viscosity was much lower. As the viscosity was an inverse function of the shear rate it could be concluded that the shear rate was relatively low in the pipes of primary and THP sludge, about $2{\cdot}10^{-2}$ s^{1}, and high in the pipes of digested sludge and a mixture of all three.

The maximum value of the viscosity was 146 Pa·s and this value was taken on in the corner of the dead end of the pipe containing both primary and THP sludge. This was to be expected as some of the sludge would get stuck in this corner and hence take on very low shear rates resulting in high values of the viscosity.

In figures 4.2.6 and 4.2.7 plots of the particle tracks are portrayed. The red particles were released at the THP inlet, the blue at the primary inlet and the yellow at the digested inlet.

The particles of primary and THP sludge did not intertwine when the two flows met. THP sludge stayed on top and the two flows continued flowing in two separate layers. At the junction of those two and digested sludge, THP revolved around digested sludge to the other side of the junction staying near the pipe wall, and primary sludge was pushed against the wall near the junction. At the outlet digested sludge was in the middle of the pipe, THP sludge near the pipe wall in positive x-direction and primary sludge near the pipe wall in negative x-direction. So based on the particle tracks no mixing was seen when simulating the baseline with digested sludge.

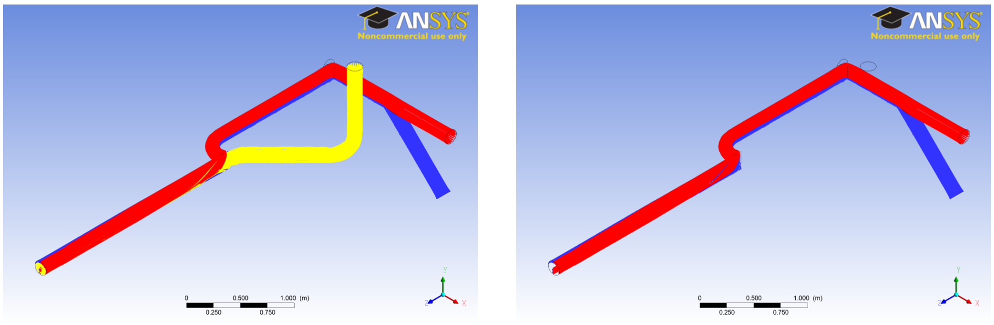

(a) Isometric view. (b) Isometric view of primary and THP sludge.

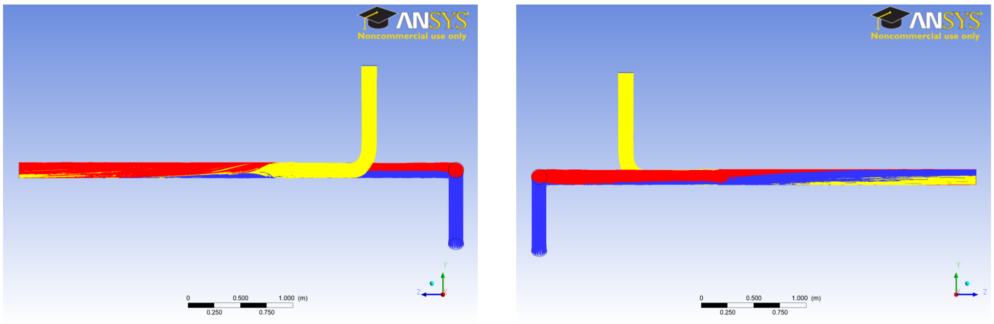

(c) Side view, YZ-plane. (d) Side view, YZ-plane.

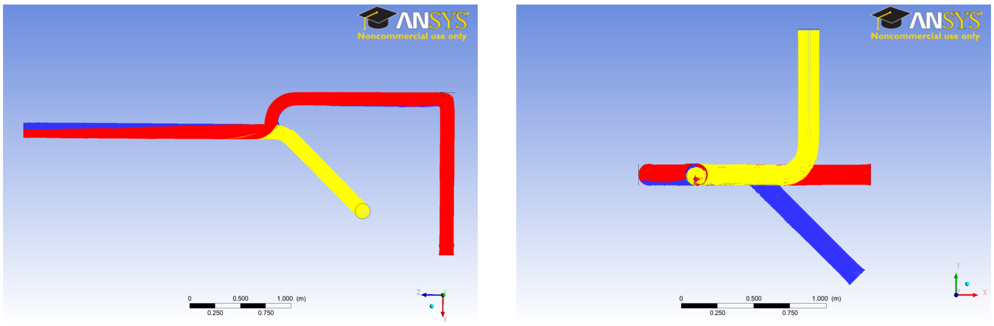

(e) Top view, ZX-plane. (f) Front view, XY-plane.

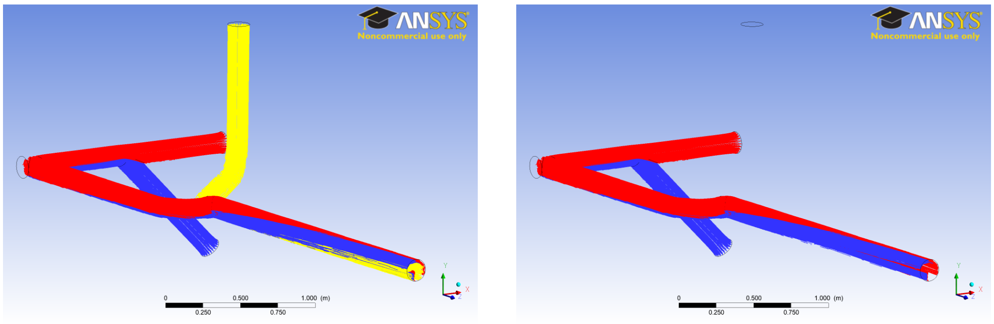

(g) Other view. (h) Other view with primary and THP sludge.

Figure 4.2.6: Particle tracks for the baseline model from $0 - 36$ s with digested sludge (yellow), primary sludge (blue) and THP sludge (red).

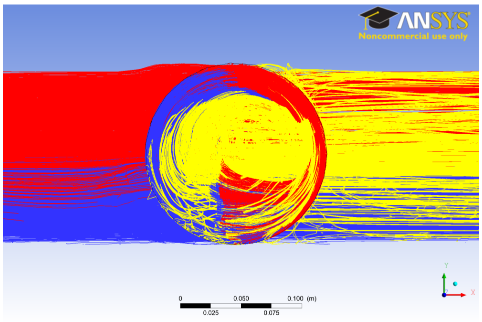

Figure 4.2.7: Zoom-in on the front view, XY-plane, of the particle tracks for the baseline model from $0-36$ *s with digested sludge (yellow), primary sludge (blue) and THP sludge (red).*

Species Transport

The second run of the baseline model was carried out using a sludge mixture. So in this case differences in density and viscosity were taken into account.

In figure 4.2.8 three views of the pressure field are shown. The overall pressure drop was higher compared to the baseline model run with digested sludge. High values of the pressure were now reached in the primary pipe, in contrast to the first run were higher pressures occurred in the digested pipeline. This could be explained by higher viscosity values of primary sludge for low shear rates in contrast with digested and THP sludge, hence more pressure was needed to let primary sludge flow through the pipe. Another contribution to the higher pressure values could be the higher density of primary sludge.

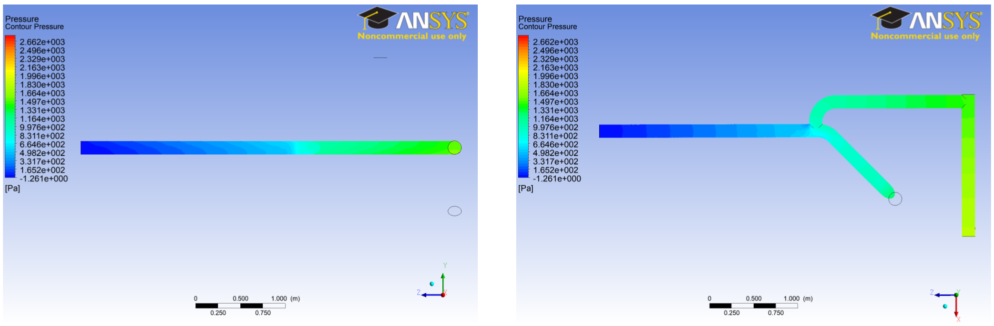

(a) Side view, YZ-plane. (b) Top view, ZX-plane.

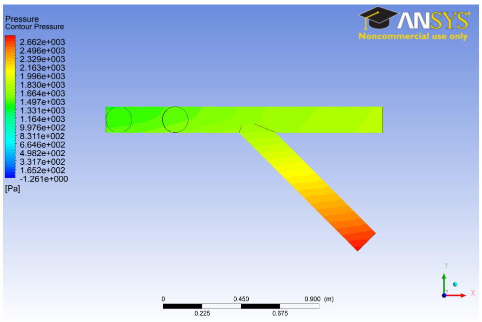

(c) Front view, XY-plane.

Figure 4.2.8: Pressure of the baseline model with a sludge mixture at $t = 40$ *s, with* ΔP *= 2.66 kPa.*

Four views of the velocity field are depicted in figure 4.2.9. The maximum velocity achieved in this case was slightly higher than in the first run with digested sludge. As can be seen in the side view and front view the velocity profile at the outlet was not axisymmetric any more. A larger region with a lower velocity was present in the bottom of the pipe than in top of the pipe. This could be the cause of the slightly larger maximum velocity. No further differences compared to the first run were noticed.

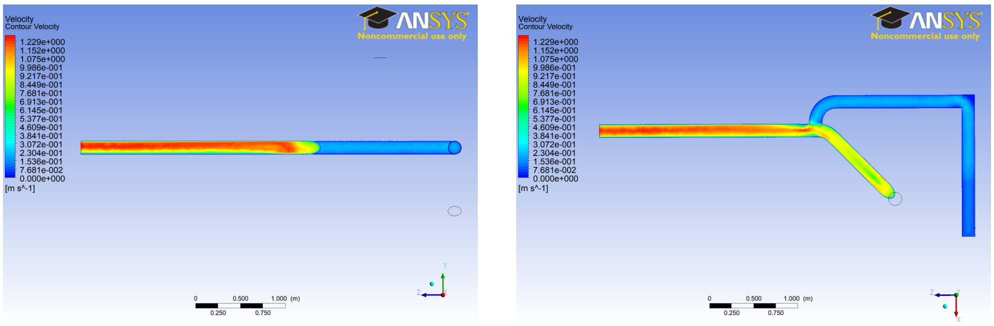

(a) Side view, YZ-plane.

(b) Top view, ZX-plane.

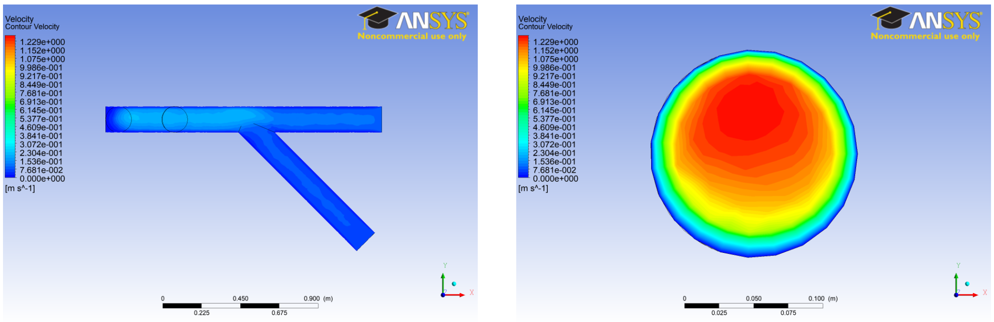

(c) Front view, XY-plane.

(d) Front view, XY-plane, outlet.

Figure 4.2.9: Velocity of the baseline model with a sludge mixture at $t = 40$ *s,* $\max(\vec{u}) = $ *1.23 m/s.*

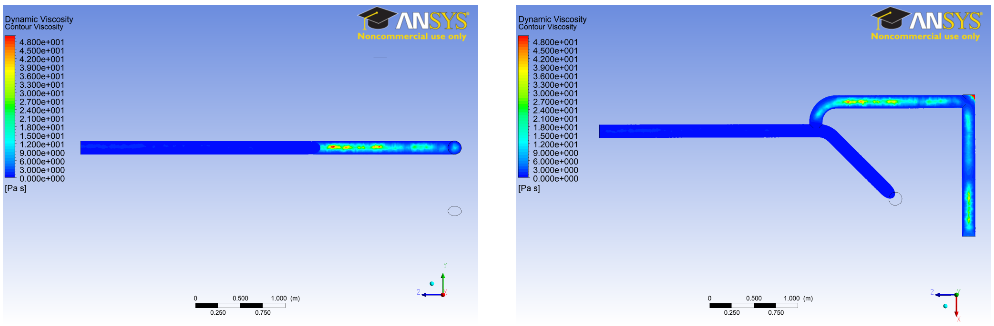

(a) Side view, YZ-plane.

(b) Top view, ZX-plane.

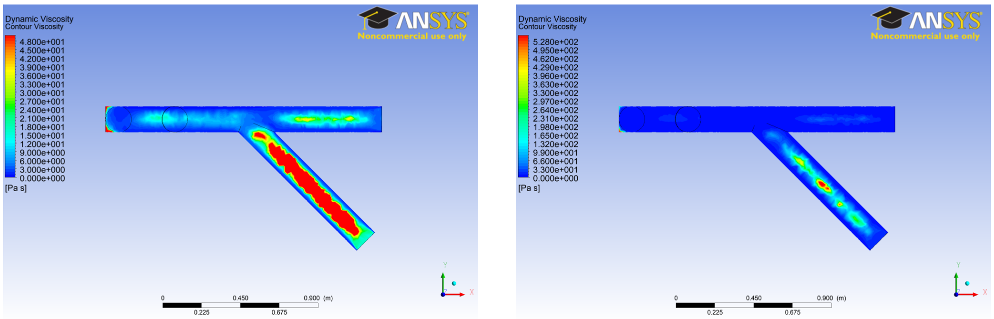

(c) Front view, XY-plane, μ between $0-50$ Pa·s..

(d) Front view, XY-plane, μ between $0-550$ Pa·s.

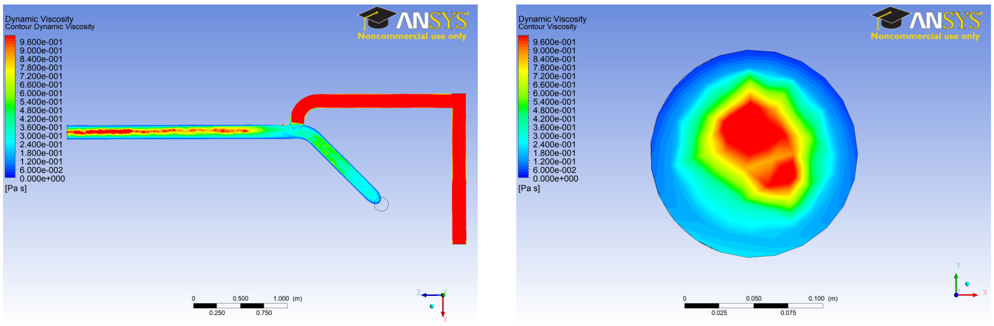

(e) Top view, ZX-plane, μ between $0-1$ Pa·s.

(f) Front view, XY-plane, outlet with μ between $0-1$ Pa·s.

Figure 4.2.10: Dynamic viscosity ranging from $0-50$ Pa·s for (a), (b) and (c), from $0-550$ Pa·s for (d), and from $0-1$ Pa·s for (e) and (f) of the baseline model with a sludge mixture at $t=40$ s.

Six contour plots of the dynamic viscosity are displayed in figure 4.2.10. Higher viscosity values were reached compared to the first simulation, with a maximum of 6057 Pa·s, which was incredibly high and physically not realistic. Values up to 550 Pa·s were taken on in the middle of the pipe containing primary sludge. This corresponded to shear rates of about $2{\cdot}10^{-2}$ s^{-1}. Behind the junction of digested sludge the viscosity of the mixture was of comparable size to the simulation with solely digested sludge.

The higher values could be explained by the fact that the fitted power law models of THP and primary sludge had a higher viscosity than the one of digested sludge over a range of shear rates from 10^{-3} to 10^{4} s^{-1}, see figure 4.1.19.

As the mass fractions sum up to 1 only the mass fractions of primary and THP sludge are discussed. The mass fractions of digested sludge for all models can be found in Appendix D.

In figure 4.2.11 the mass fraction of primary sludge is depicted. Because the mass fraction of primary sludge was relatively small compared to the mass fraction of digested scaled plots are included as well, with $0 \leq y_p \leq 0.1$. As can be seen in the front view, primary sludge remained mainly at the bottom of the pipe and little mixing took place with THP when those two came together. When they passed the dead end bend, primary sludge was not solely located at the bottom any more as can be seen in the side view. Some mixing might have taken place. However, behind the junction with digested sludge, primary sludge was mainly located at the bottom again and near the wall of the positive x-axis when it reached the outlet.

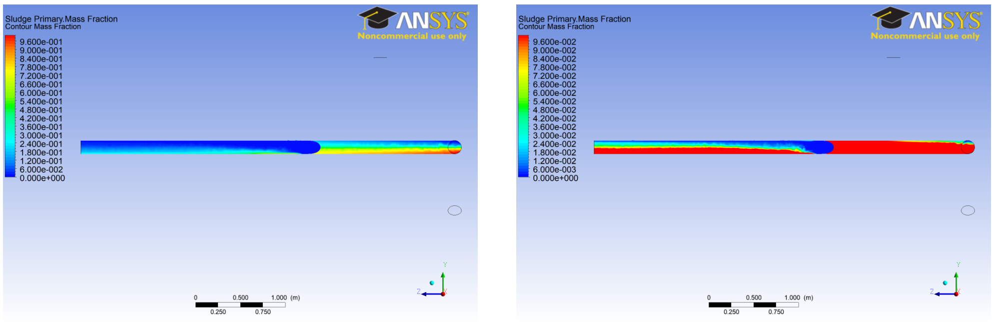

(a) Side view, YZ-plane.

(b) Side view, YZ-plane, $0 \leq y_p \leq 0.1$.

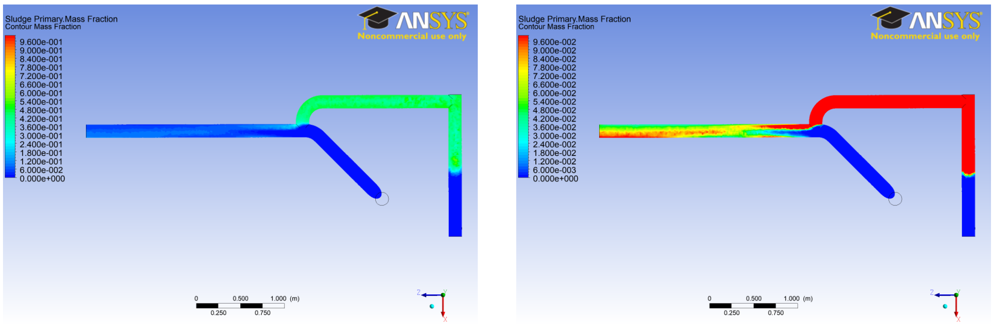

(c) Top view, ZX-plane.

(d) Top view, ZX-plane, $0 \leq y_p \leq 0.1$.

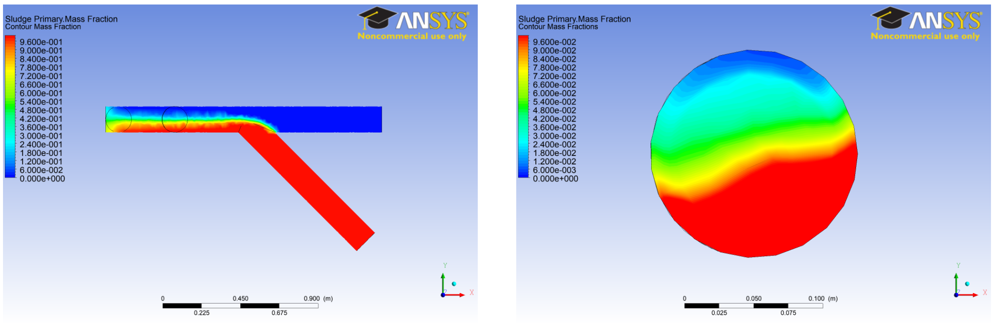

(e) Front view, XY-plane.

(f) Front view, XY-plane, outlet, $0 \leq y_p \leq 0.1$.

Figure 4.2.11: Mass fraction of primary sludge in the baseline model with a sludge mixture at $t = 40$ s.

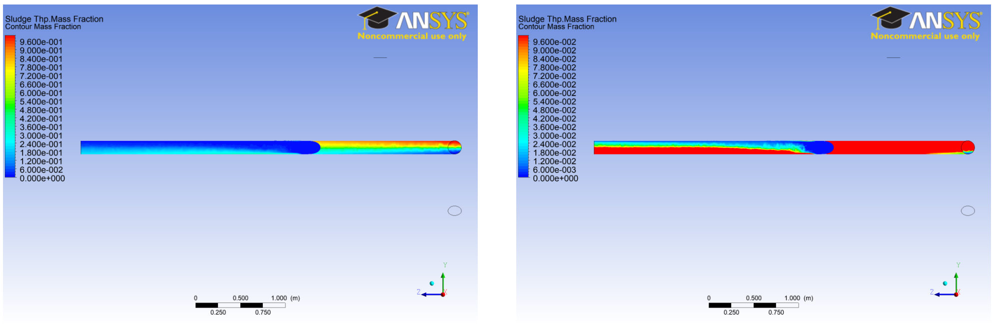

(a) Side view, YZ-plane. (b) Side view, YZ-plane, $0 \leq y_t \leq 0.1$.

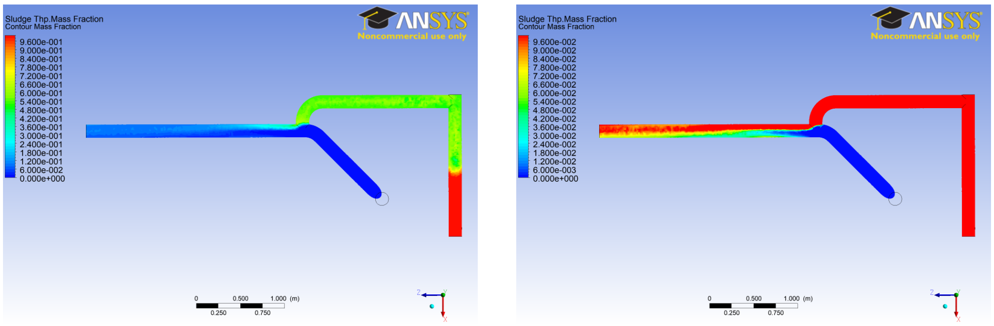

(c) Top view, ZX-plane. (d) Top view, ZX-plane, $0 \leq y_t \leq 0.1$.

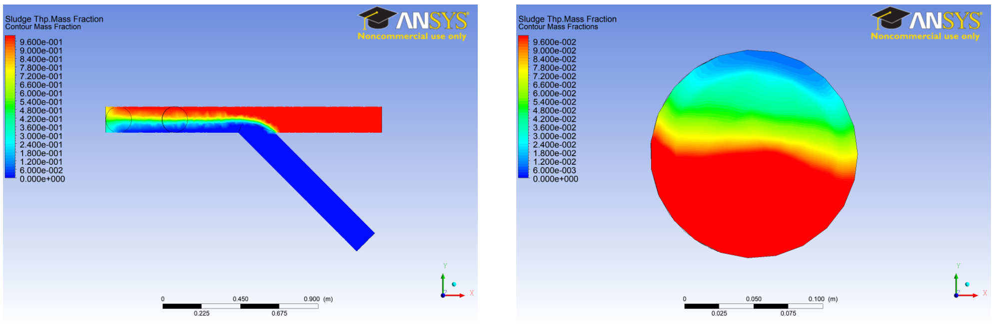

(e) Front view, XY-plane. (f) Front view, XY-plane, outlet, $0 \leq y_t \leq 0.1$.

Figure 4.2.12: Mass fraction of THP sludge in the baseline model with a sludge mixture at $t = 40$ s.

Similar notions as for the mass fraction of primary sludge before the junction with digested sludge could be made considering THP, see figure 4.2.12. After the junction the majority of THP sludge was located at the bottom of the pipe and near the wall in negative x-axis direction.

The density was closely correlated to the mass fractions, but was calculated using volume fractions. Plots of the density are shown in figure 4.2.13. Two regions of different densities could be discerned at the junction of primary and THP sludge, with the lower density on top of the other. In the side view two layers of different density were discerned behind the junction of digested sludge, with again the lower density on top. Actually, the differences in density counteract the mixing as for example primary sludge enters at the bottom and remains there partly due to its higher density.

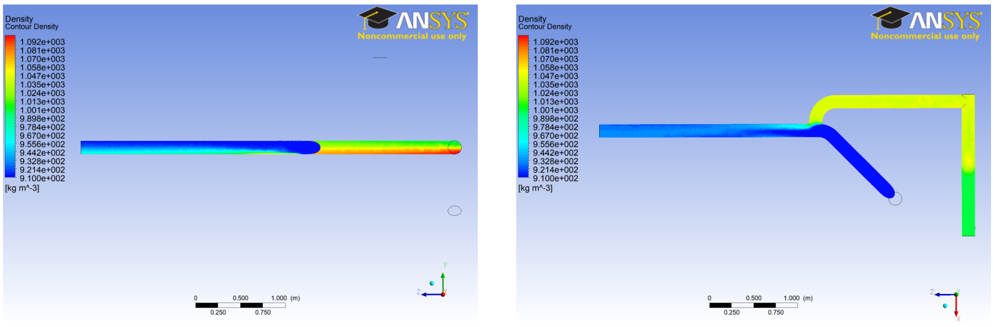

(a) Side view, YZ-plane.

(b) Top view, ZX-plane.

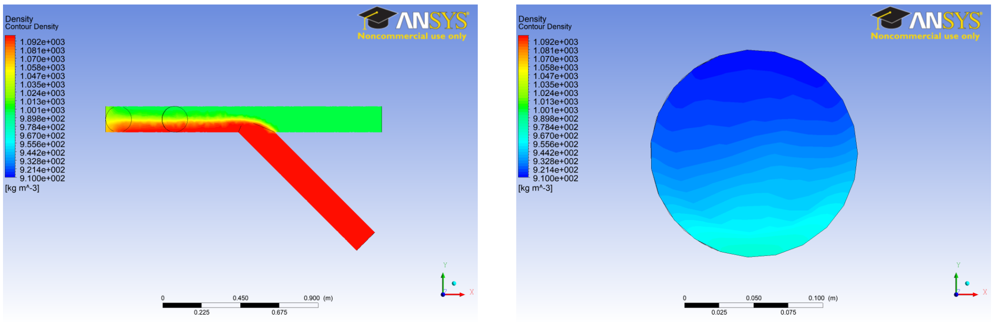

(c) Front view, XY-plane.

(d) Front view, XY-plane, outlet.

Figure 4.2.13: Density of the baseline model with a sludge mixture at $t = 40$ s.

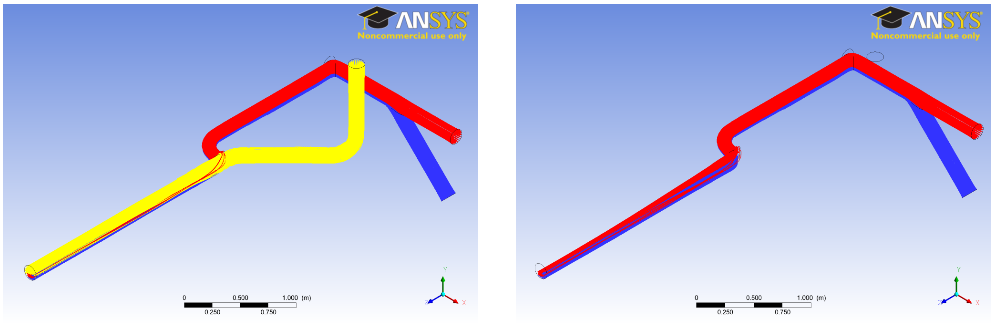

(a) Isometric view. (b) Isometric view of primary and THP sludge.

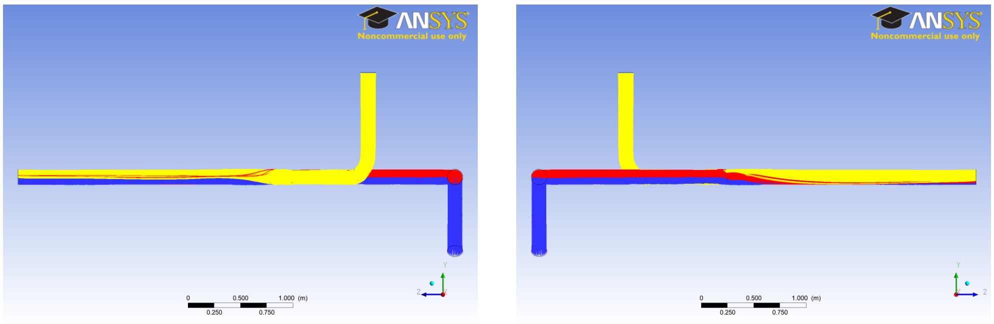

(c) Side view, YZ-plane. (d) Side view, YZ-plane.

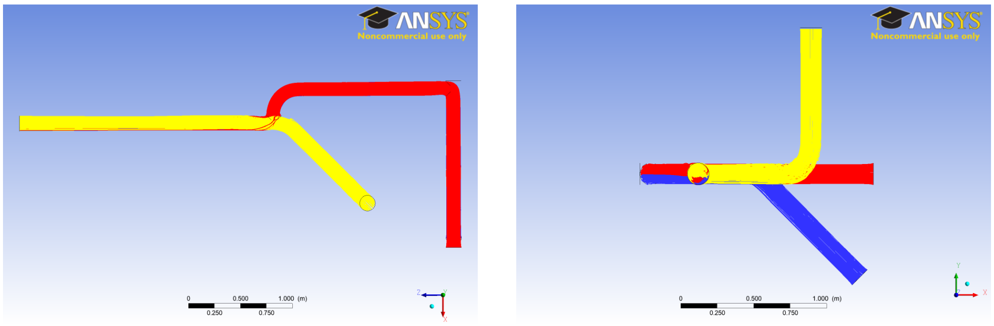

(e) Top view, ZX-plane. (f) Front view, XY-plane.

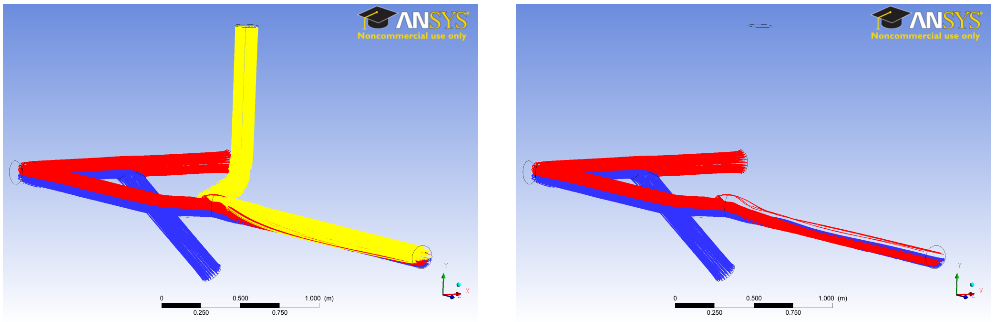

(g) Other view. (h) Other view with primary and THP sludge.

Figure 4.2.14: Particle tracks for the baseline model from $4 - 40$ *s with digested sludge (yellow), primary sludge (blue) and THP sludge (red).*

The particle tracks confirmed the results of the species transport, see figures 4.2.14 and 4.2.15. At the outlet roughly three layers of particles could be distinguished with primary sludge at the bottom, on top of that THP and on top of that digested sludge.

THP sludge was indeed located a bit more towards the wall in negative x-direction and primary sludge towards the positive x-direction. Comparing the particle tracks with the ones obtained in the first simulation with digested sludge, primary and THP sludge were not located on top of digested any more, but underneath it. The mixing of both simulations was not considered sufficient.

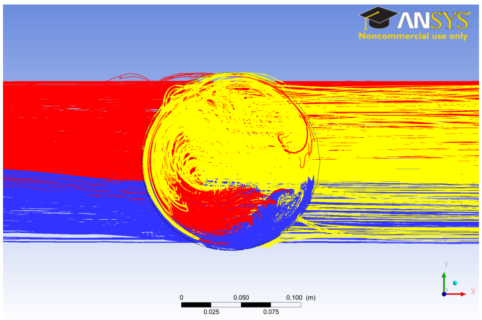

Figure 4.2.15: Zoom-in on the front view, XY-plane, of the particle tracks for the baseline model from $4-40$ *s with digested sludge (yellow), primary sludge (blue) and THP sludge (red).*

4.2.3 Model 2 - Venturi

Just as in the case of the baseline model, the venturi model was first simulated with only digested sludge. After that a second simulation was performed with a sludge mixture.

Digested sludge

Plots of the pressure field are depicted in figure 4.2.16. The overall pressure drop was $\Delta P = 24.0$ kPa, which was much higher than the in the baseline model as the sludge needed to pass a constriction, the venturi.

In figure 4.2.17 four plots of the velocity field are shown. The maximum velocity was reached at the narrowing of the venturi. Moreover, the jet flow behind the venturi showed some unsteady behaviour over time, with the angle of the flow direction shifting in time.

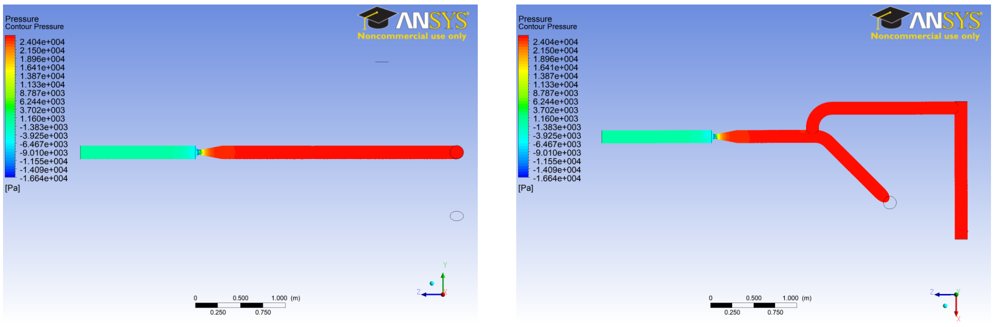

(a) Side view, YZ-plane.

(b) Top view, ZX-plane.

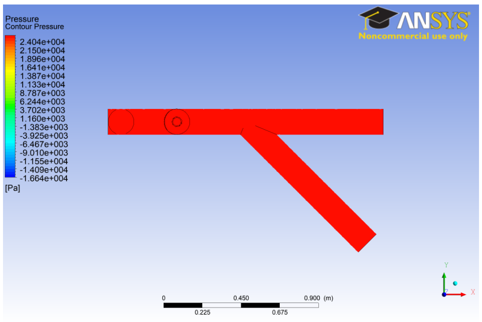

(c) Front view, XY-plane.

Figure 4.2.16: Pressure of the venturi model with digested sludge at $t = 36$ *s, with* ΔP *= 24.0 kPa.*

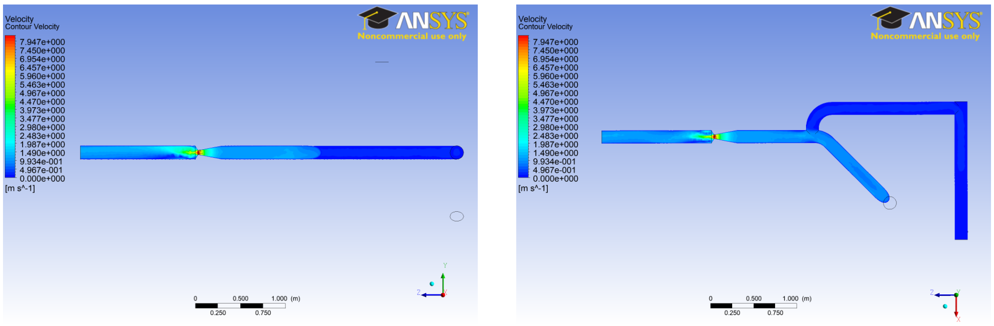

(a) Side view, YZ-plane.

(b) Top view, ZX-plane.

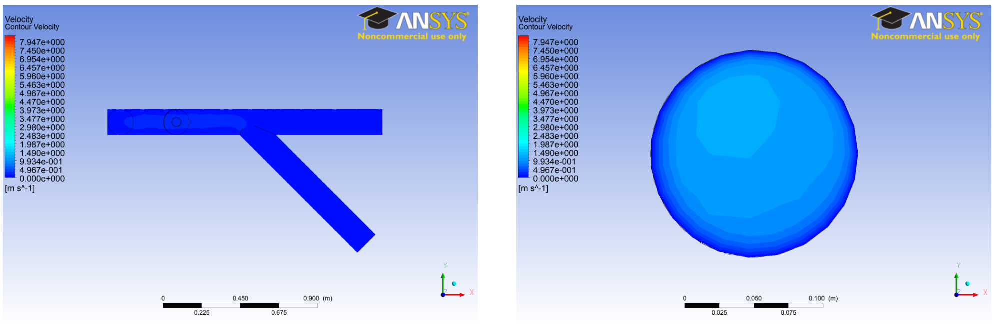

(c) Front view, XY-plane.

(d) Front view, XY-plane, outlet.

Figure 4.2.17: Velocity of the venturi model with digested sludge at $t = 36$ *s, with* $\max(\vec{u})$ *= 7.95 m/s.*

Plots of the dynamic viscosity are displayed in figure 4.2.18. Roughly the same notions could be made as in the case of the baseline model with digested sludge. The maximum viscosity reached in the venturi model was 149 Pa·s and was again taken on in the corner of the dead end of the pipe containing both primary and THP sludge.

Higher values of the viscosity, around 20 Pa·s which corresponded to a shear rate of approximately $2{\cdot}10^{-2}$ s^{-1}, were taken on in the middle of the pipes of primary and THP sludge. In the recirculation pipe and behind the junction where all three types of sludge met, the viscosity was much lower due to higher shear rates.

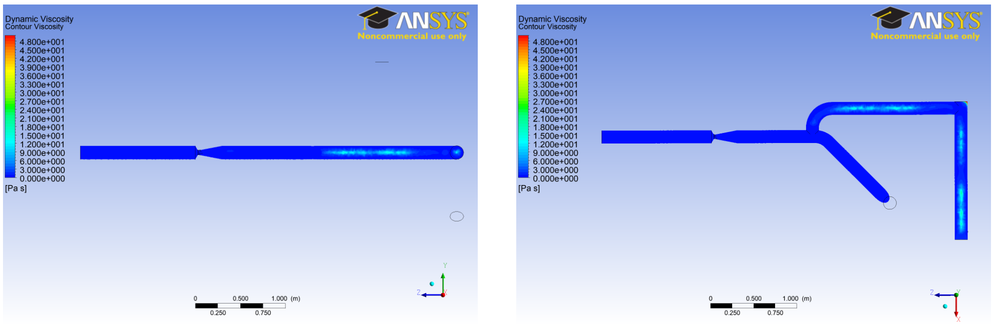

(a) Side view, YZ-plane.

(b) Top view, ZX-plane.

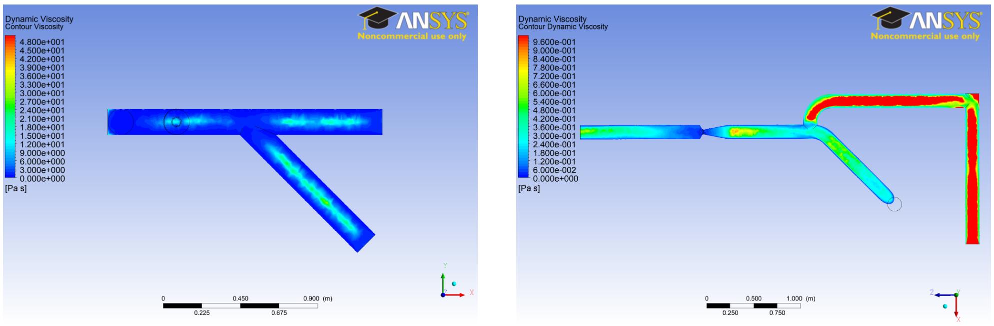

(c) Front view, XY-plane.

(d) Top view, ZX-plane, μ between $0 - 1$ Pa·s.

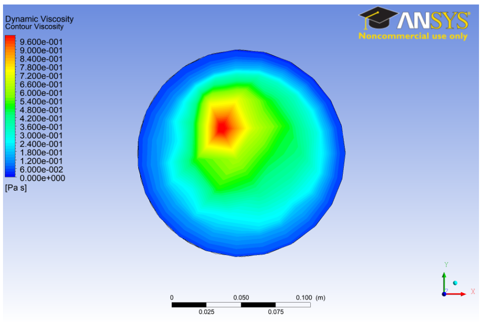

(e) Front view, XY-plane, outlet, μ between $0 - 1$ Pa·s.

Figure 4.2.18: Dynamic viscosity ranging from $0 - 50$ *Pa·s for (a), (b) and (c), and from* $0 - 1$ *Pa·s for (d) and (e), of the venturi model with digested sludge at* $t = 36$ *s.*

Particle tracks for the venturi model are displayed in figures 4.2.19 and 4.2.20. Ahead of the venturi the tracks of the particles were similar to the tracks of the first run of the baseline model, with THP near the pipe wall in positive x-direction on top of digested sludge and primary sludge pushed to the wall in negative x-direction. Behind the venturi at the outlet primary sludge was still found mainly near the wall in negative x-direction, THP near the wall in positive x-direction and digested sludge primarily in the middle of the pipe. However, a considerable amount of different sludge particles intertwined resulting in some mixing as can most clearly be seen in the front view of the outlet in figure 4.2.20. As primary regions of the different sludge types could still be distinguished, the mixing was not considered to be sufficient, but the results were better than in the baseline model.

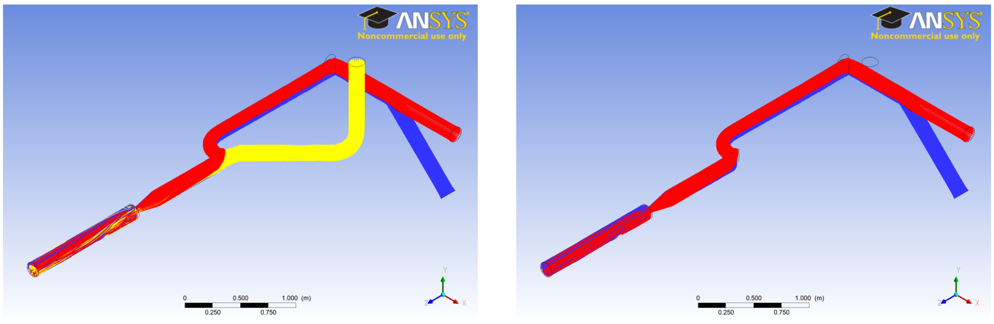

(a) Isometric view. (b) Isometric view of primary and THP sludge.

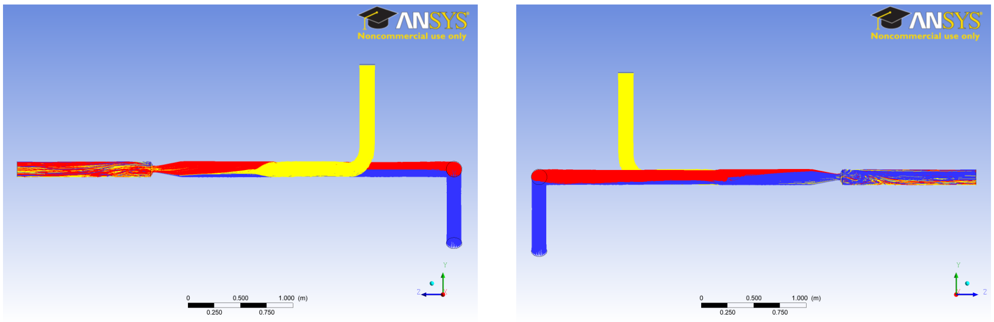

(c) Side view, YZ-plane. (d) Side view, YZ-plane.

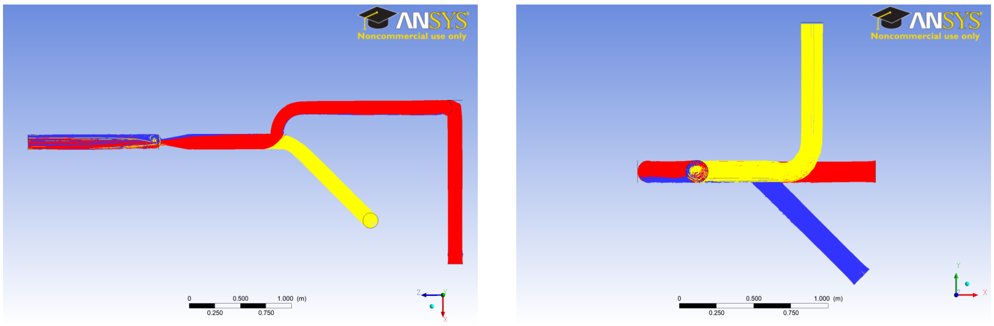

(e) Top view, ZX-plane. (f) Front view, XY-plane.

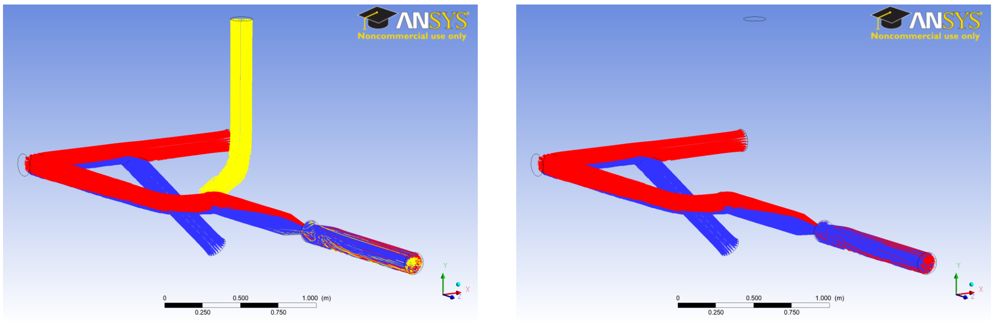

(g) Other view. (h) Other view with primary and THP sludge.

Figure 4.2.19: Particle tracks for the venturi model from $0 - 36$ *s with digested sludge (yellow), primary sludge (blue) and THP sludge (red).*

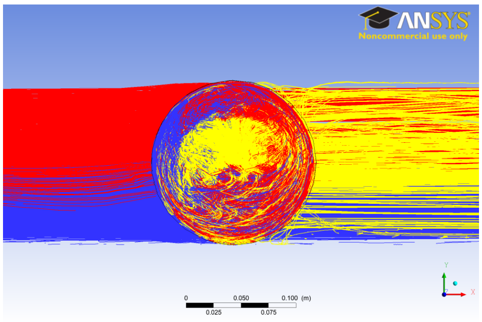

Figure 4.2.20: Zoom-in on the front view, XY-plane, of the particle tracks for the venturi model from $0 - 36$ *s with digested sludge (yellow), primary sludge (blue) and THP sludge (red).*

Species Transport

A second simulation of the venturi model was performed with a sludge mixture. Contours of the pressure field are shown in figure 4.2.21. Compared to the first simulation with digested sludge, the pressure drop was higher. This could be explained by the higher density of both primary sludge and THP sludge, which was now taken into account, and the higher viscosity values of these sludge types compared to digested sludge. Because these were higher, more pressure was needed to let both of them flow through the pipes.

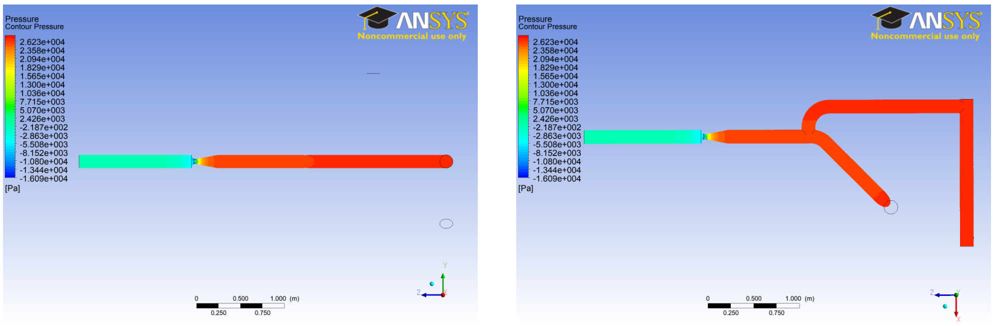

(a) Side view, YZ-plane. (b) Top view, ZX-plane.

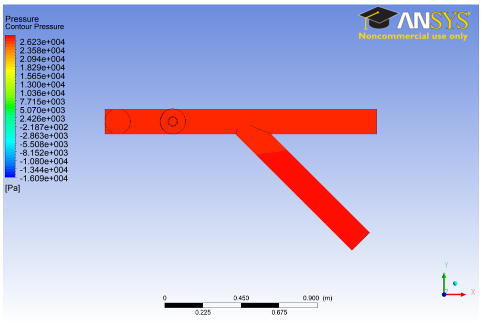

(c) Front view, XY-plane.

Figure 4.2.21: Pressure of the venturi model with a sludge mixture at $t = 40$ *s, with* ΔP *= 26.2 kPa.*

In figure 4.2.22 four views of the velocity field are shown. The maximum velocity was reached at the narrowing of the venturi. Moreover, the jet flow after the venturi showed some unsteady behaviour over time, with the angle of the flow direction shifting in time.

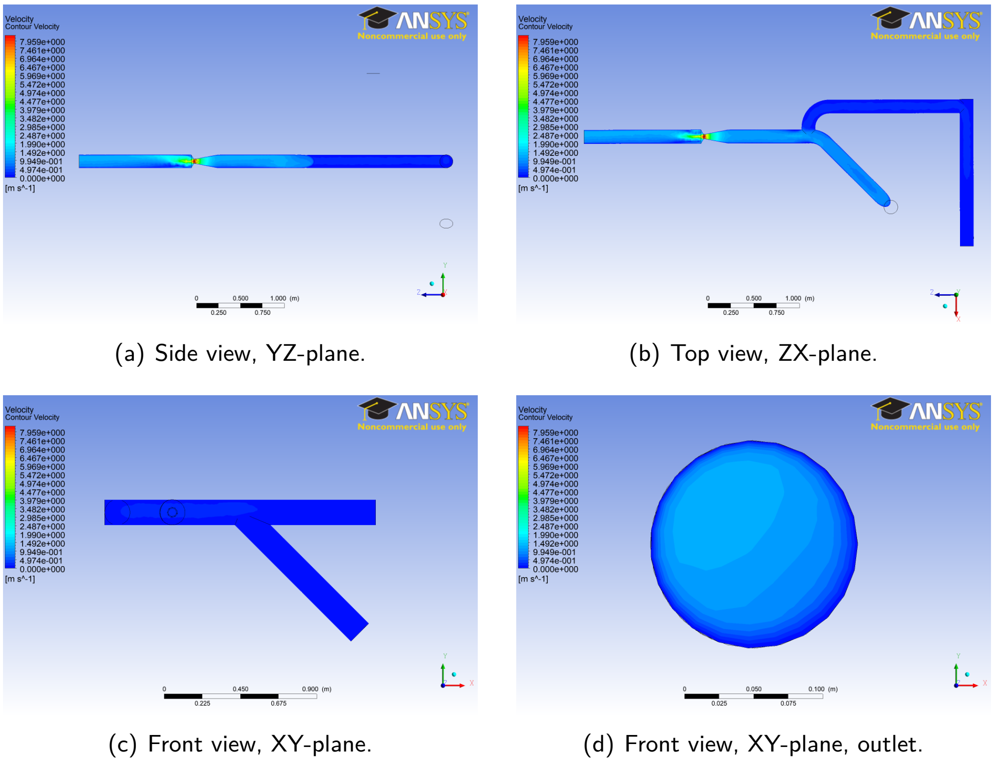

(a) Side view, YZ-plane. (b) Top view, ZX-plane.

(c) Front view, XY-plane. (d) Front view, XY-plane, outlet.

Figure 4.2.22: Velocity of the venturi model with a sludge mixture at $t = 40$ *s, with* $\max(\vec{u})$ = *7.96 m/s.*

Plots of the dynamic viscosity are portrayed in figure 4.2.23. The viscosity values in all pipes before the venturi should be roughly of the same size as in the baseline model, see figure 4.2.10. This was indeed the case with some small deviations which could be due to the effect of the venturi, numerical accuracy or a too coarse mesh.

A maximum value of 5075 Pa·s was reached, which was incredibly high and physically not realistic. Overall, higher values of the viscosity were reached, compared to the first run, in particular in the middle of the pipe of primary sludge with values up to 550 Pa·s. This corresponded to shear rates of about $2 \cdot 10^{-2}$ s^{-1}. Behind the junction where all sludge types met, the viscosity was about the same size as in the simulation with solely digested sludge.

The higher values could be explained by the fact that the fitted power law models of THP and primary sludge had a higher viscosity than the power law model of digested over a range of shear rates from 10^{-3} to 10^{4} s^{-1}, see figure 4.1.19.

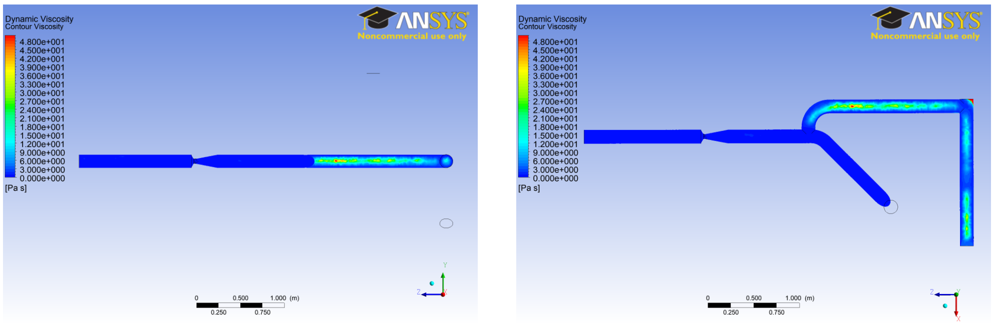

(a) Side view, YZ-plane.

(b) Top view, ZX-plane.

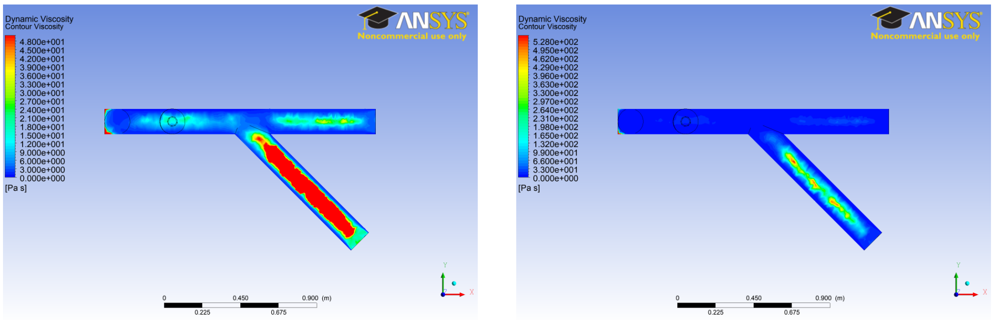

(c) Front view, XY-plane, μ between $0-50$ Pa·s..

(d) Front view, XY-plane, μ between $0-550$ Pa·s.

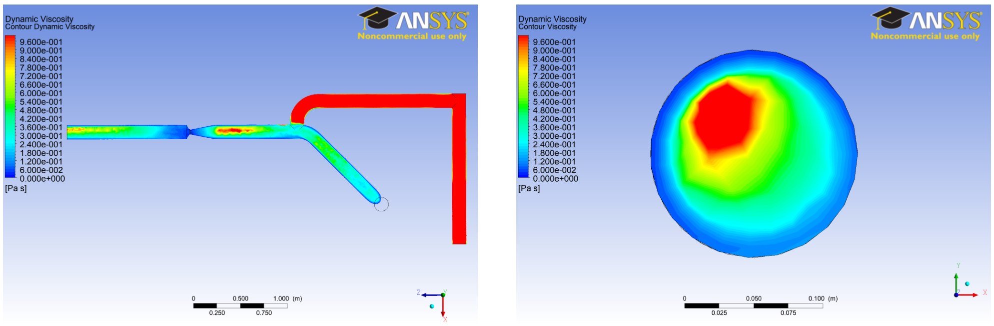

(e) Top view, ZX-plane, μ between $0-1$ Pa·s.

(f) Front view, XY-plane, outlet, μ between $0-1$ Pa·s.

Figure 4.2.23: Dynamic viscosity ranging from $0-50$ *Pa·s for (a), (b) and (c), from* $0-550$ *Pa·s for (d), and from* $0-1$ *Pa·s for (e) and (f), of the venturi model with a sludge mixture at* $t = 40$ *s.*

The mass fractions of primary sludge are displayed in figure 4.2.24. When primary and THP sludge came together, primary sludge was located at the bottom of the pipe and little mixing took place. Behind the junction with digested sludge primary sludge remained at the bottom and near the wall in negative x-direction. Especially just behind the venturi primary sludge was still primarily located in these regions, but a while behind the venturi primary sludge was located in other parts of the pipe as well. Only at the top there was little primary sludge. Compared to the baseline mixture simulation, more mixing had taken place.

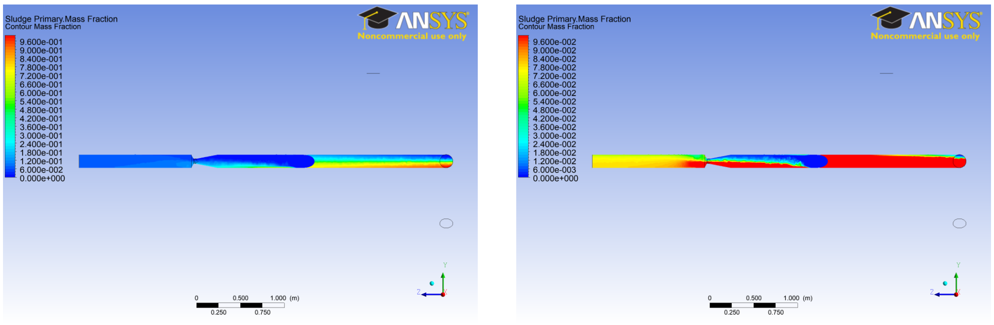

(a) Side view, YZ-plane.

(b) Side view, YZ-plane, $0 \leq y_p \leq 0.1$.

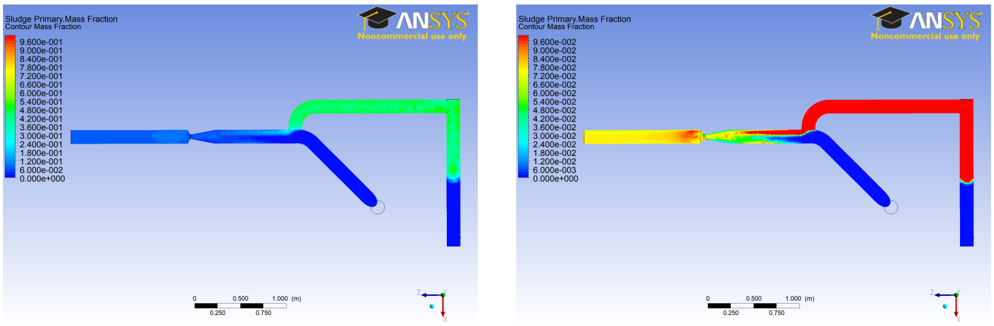

(c) Top view, ZX-plane.

(d) Top view, ZX-plane, $0 \leq y_p \leq 0.1$.

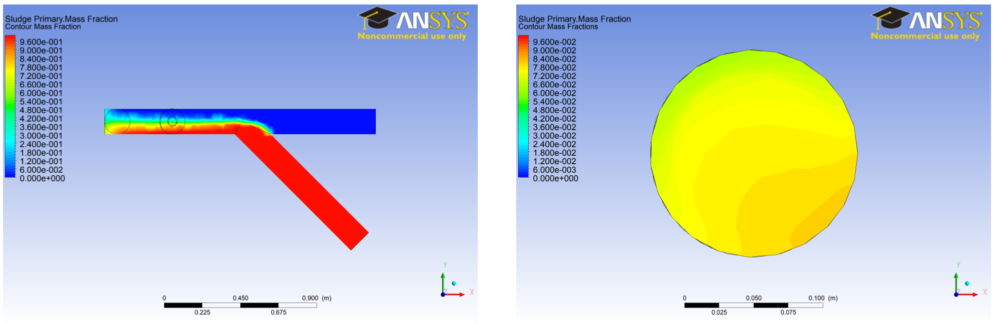

(e) Front view, XY-plane.

(f) Front view, XY-plane, outlet, $0 \leq y_p \leq 0.1$.

Figure 4.2.24: Mass fraction of primary sludge in the venturi model with a sludge mixture at $t = 40$ *s.*

Ahead of the junction with digested sludge when all three sludge types met, similar remarks could be made with respect to the mass fractions of THP sludge as to primary sludge, see figure 4.2.25. Ahead of the venturi THP sludge was located at the bottom and near the wall in negative x-direction. Shortly behind the venturi this tendency was still visible, but soon THP sludge was located at many more regions throughout the entire pipe, except for the top were little THP sludge was present.

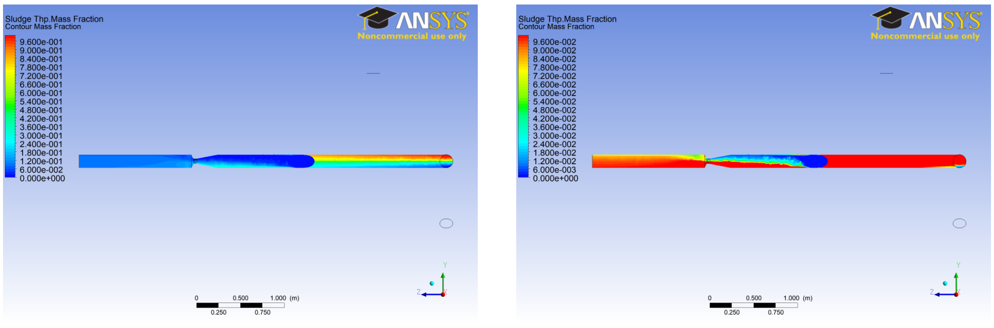

(a) Side view, YZ-plane. (b) Side view, YZ-plane, $0 \leq y_t \leq 0.1$.

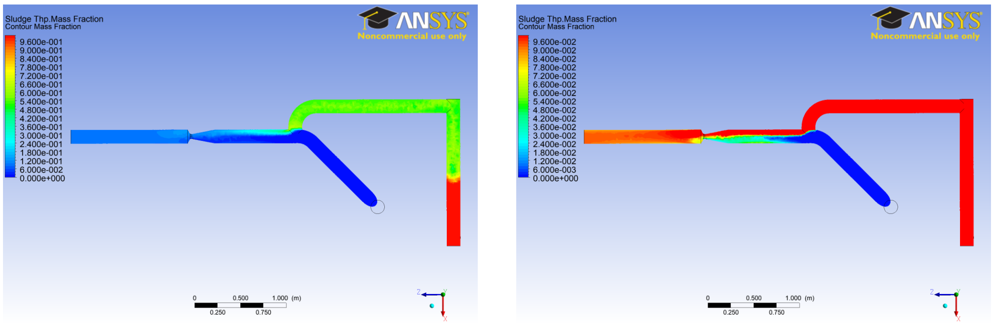

(c) Top view, ZX-plane. (d) Top view, ZX-plane, $0 \leq y_t \leq 0.1$.

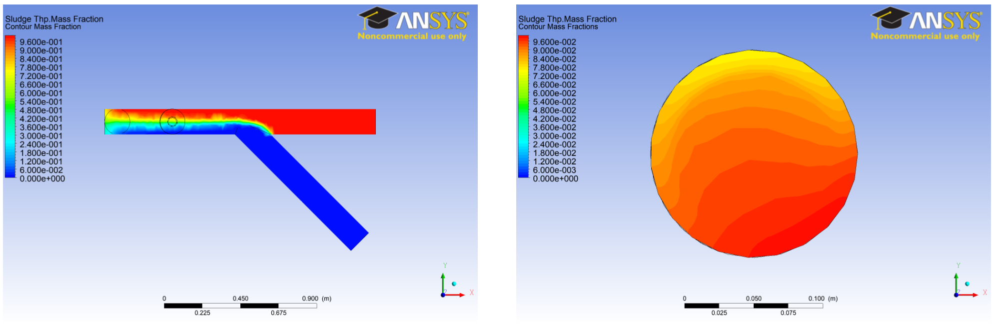

(e) Front view, XY-plane. (f) Front view, XY-plane, outlet, $0 \leq y_t \leq 0.1$.

Figure 4.2.25: Mass fraction of THP sludge in the venturi model with a sludge mixture at $t = 40$ s.

Plots of the density are shown in figure 4.2.26. Just as in the baseline model with a sludge mixture, two regions of different densities could be discerned at the junction of primary and THP sludge, with the lower density, of THP, on top of the other. In the side view two layers of different density could be discerned behind the junction of digested sludge and in front of the venturi, with again the lower density on top. Behind the venturi slight differences in density can be distinguished with for example a region of smaller density at top of the pipe.

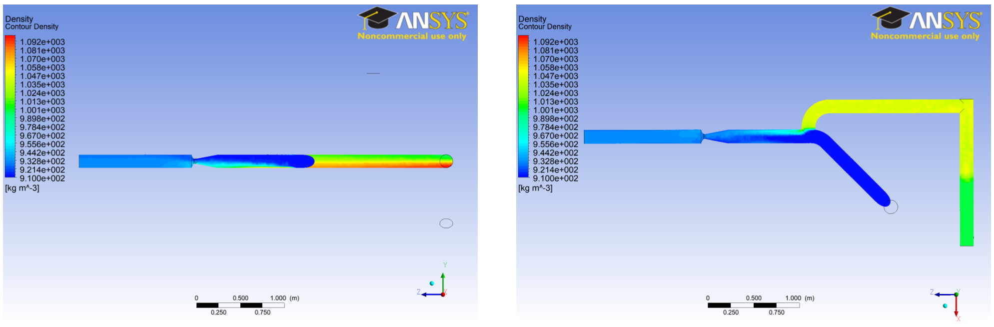

(a) Side view, YZ-plane.

(b) Top view, ZX-plane.

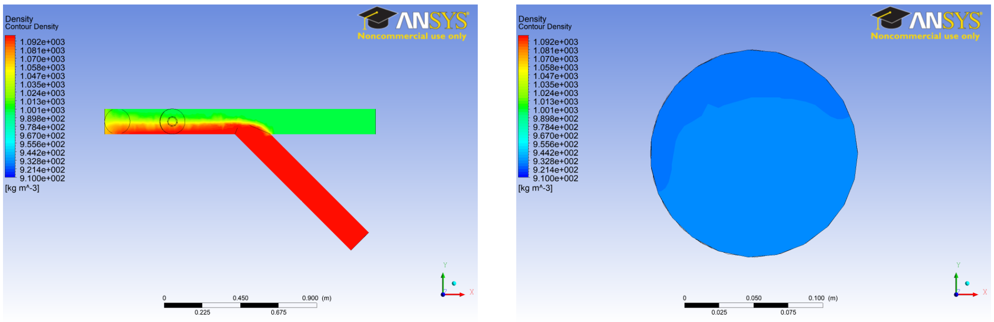

(c) Front view, XY-plane.

(d) Front view, XY-plane, outlet.

Figure 4.2.26: Density of the venturi model with a sludge mixture at $t = 40$ *s.*

In figures 4.2.27 and 4.2.28 plots of the particle tracks are displayed. The particle tracks of primary and THP particles showed no mixing ahead of the junction with digested sludge. Behind this junction THP and primary sludge flowed near the wall with primary sludge remaining at the bottom and THP sludge at the bottom and sidewards in negative x-direction. Behind the venturi THP sludge flowed over the bottom and primary sludge on top of that, near the wall in positive x-direction. Some sludge particles intertwined with another type of sludge, but this was to a far lesser extent than for the simulation of the venturi with one type of sludge. Hence, the mixing declined taking the differences in density and viscosity into account.

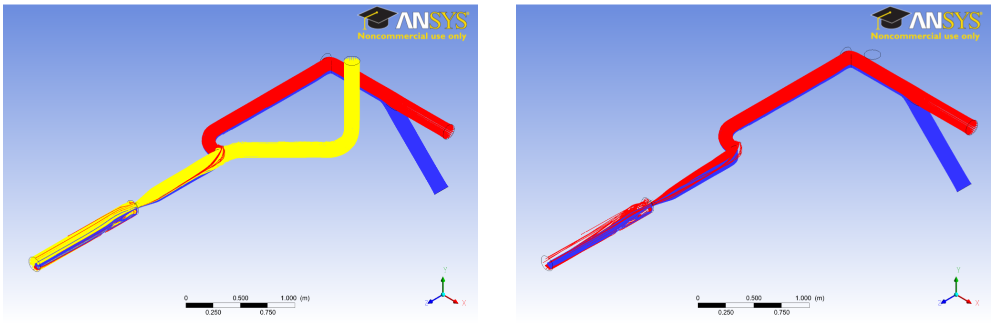

(a) Isometric view.

(b) Isometric view of primary and THP sludge.

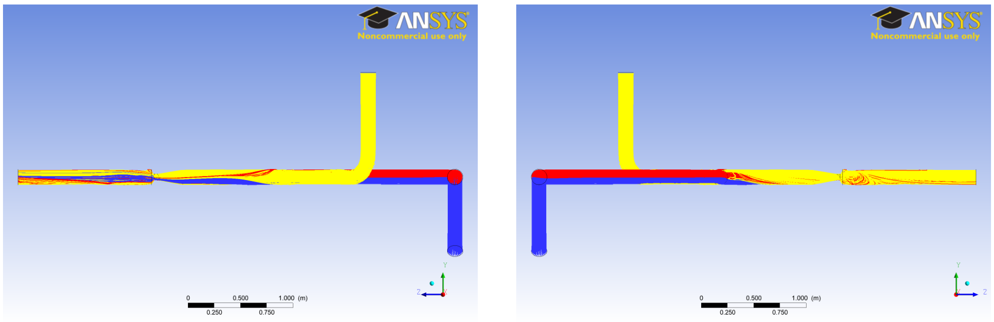

(c) Side view, YZ-plane.

(d) Side view, YZ-plane.

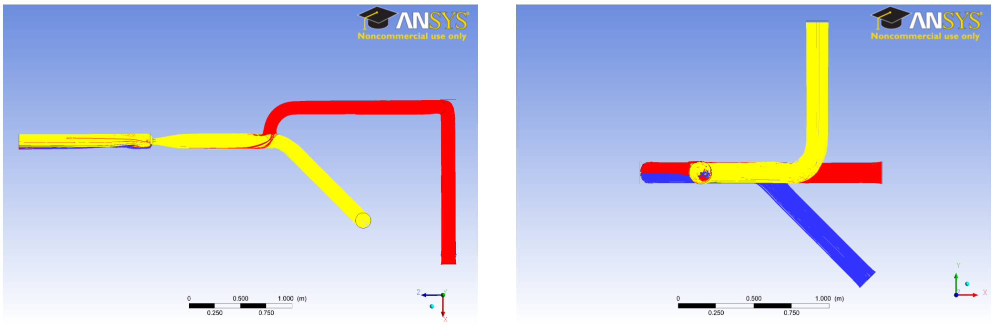

(e) Top view, ZX-plane.

(f) Front view, XY-plane.

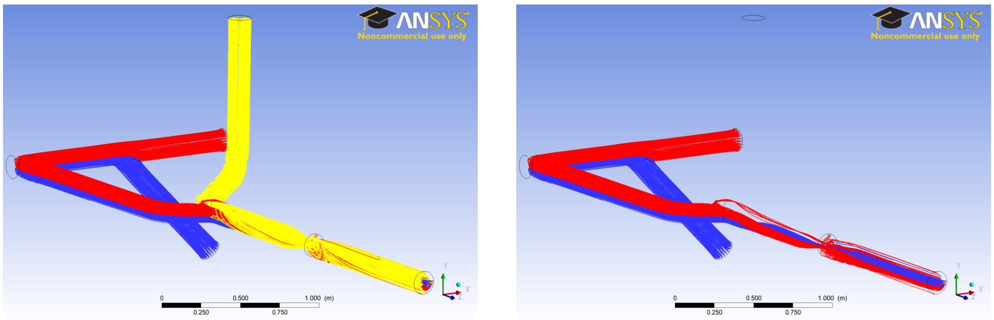

(g) Other view.

(h) Other view with primary and THP sludge.

Figure 4.2.27: Particle tracks for the venturi model from $4 - 40$ *s with digested sludge (yellow), primary sludge (blue) and THP sludge (red).*

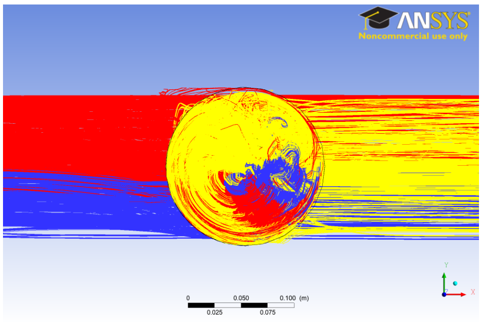

Figure 4.2.28: Zoom-in on the front view, XY-plane, of the particle tracks for the venturi model from $4-40$ *s with digested sludge (yellow), primary sludge (blue) and THP sludge (red).*

4.2.4 Model 3 - Static Mixer

The third model included one helical element of a static mixer. It was one of the two smaller models with an adjusted geometry which mixed most effectively compared to the other smaller models, see Appendix C. One simulation was carried out using a sludge mixture.

Species Transport

In figure 4.2.29 plots of the pressure field can be found. The pressure drop was slightly higher than that of the baseline mixture model, but much smaller than the drop over the venturi. High values of the pressure were reached in the pipe containing primary sludge. Both the higher viscosity of primary sludge and the higher density compared to digested sludge might have contributed to this, as more power was needed to let primary sludge flow through the pipe.

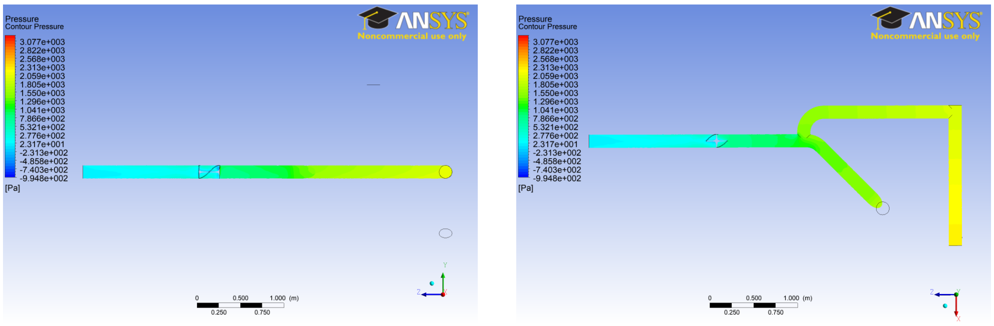

(a) Side view, YZ-plane. (b) Top view, ZX-plane.

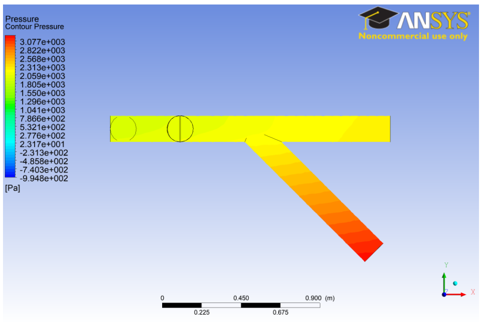

(c) Front view, XY-plane.

Figure 4.2.29: Pressure of the static mixer model with a sludge mixture at $t = 40$ *s, with* $\Delta P = 3.08$ *kPa.*

Contour plots of the velocity field are shown in figure 4.2.30. The maximum velocity was reached near the helical element. Behind the helical element the velocity profile was not axisymmetric yet, but before the flow reached the outlet it appeared almost axisymmetric, but taking the results of the mass fractions and particle tracks into account this turned out not to be the case.

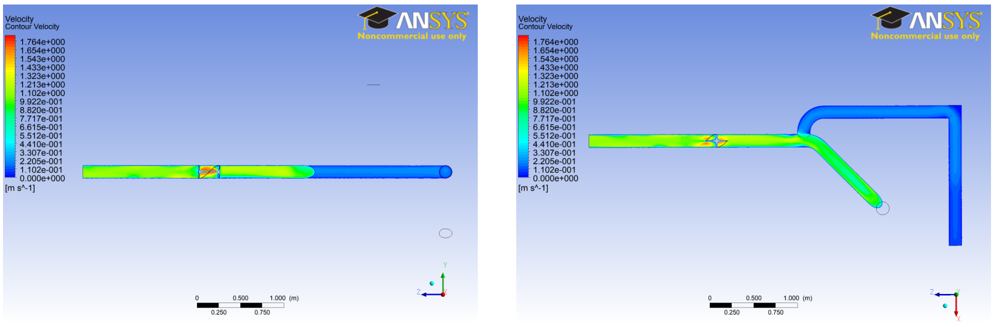

(a) Side view, YZ-plane.

(b) Top view, ZX-plane.

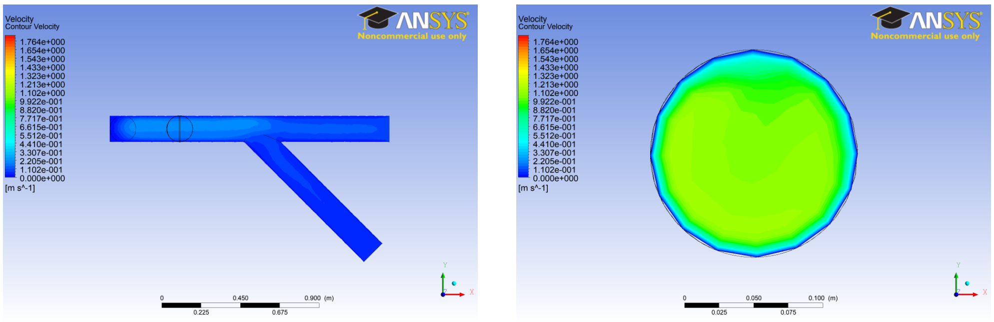

(c) Front view, XY-plane.

(d) Front view, XY-plane, outlet.

Figure 4.2.30: Velocity of the static mixer model with a sludge mixture at $t = 40$ *s, with* $\max(\vec{u}) =$ *1.76 m/s.*

Compared to the baseline and venturi mixture models a larger region of high viscosity was present in the primary and THP pipelines, see the plots in figure 4.2.31. However, the maximum viscosity was lower, namely 4146 Pa·s. Behind the junction with digested sludge, the viscosity was of roughly the same size as in the case of the baseline and venturi mixture models. The high viscosity values related to a shear rate of about $1 - 2 \cdot 10^{-2}$ s^{-1} and the low viscosity values around the helical element to shear rates of about $100 - 250$ s^{-1}.

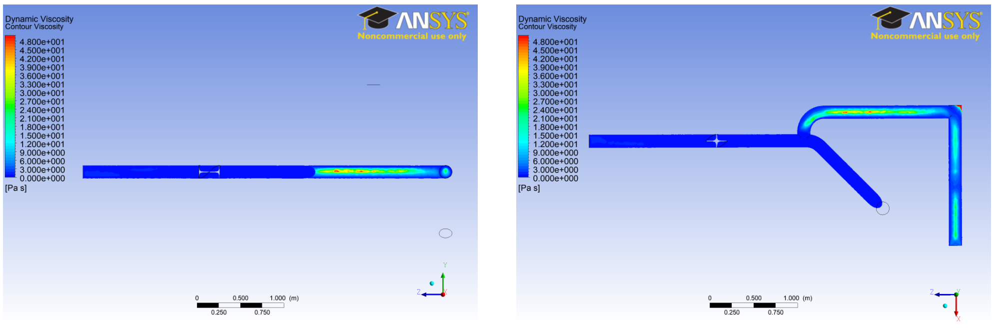

(a) Side view, YZ-plane. (b) Top view, ZX-plane.

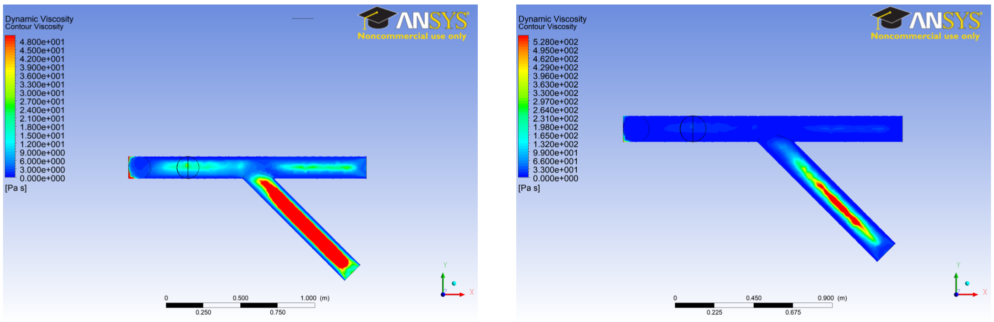

(c) Front view, XY-plane, μ between $0 - 50$ Pa·s.. (d) Front view, XY-plane, μ between $0 - 550$ Pa·s.

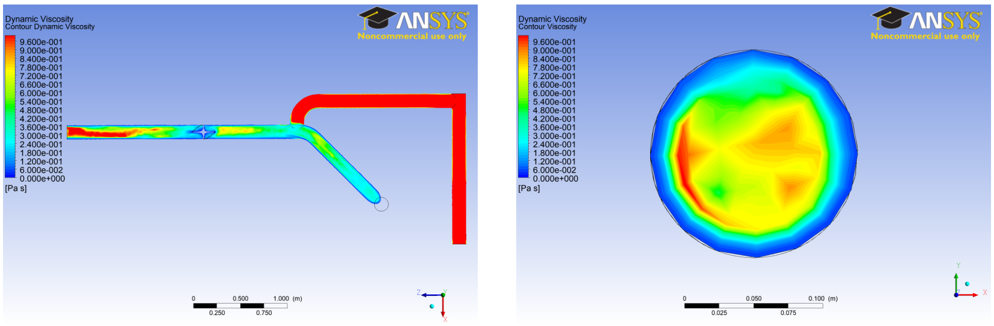

(e) Front view, XY-plane, μ between $0 - 1$ Pa·s. (f) Front view, XY-plane, outlet with μ between $0 - 1$ Pa·s.

Figure 4.2.31: Dynamic viscosity ranging from $0 - 50$ *Pa·s for (a), (b) and (c), from* $0 - 550$ *Pa·s for (d), and from* $0 - 1$ *Pa·s for (e) and (f), of the static mixer model with a sludge mixture at* $t = 40$ *s.*

Ahead of the helical element primary sludge followed roughly the same path as in the mixture models before, see the mass fractions in figure 4.2.32. However, there seemed to be more mixing between primary and THP sludge in the previous two mixture models compared to this model which was peculiar as only the geometry and mesh of the model should be different, but all the other settings the same.

Behind the helical element distinct alternating regions of high and low mass fractions were visible. Hence, some mixing took place, but not sufficient as primary sludge was not evenly distributed.

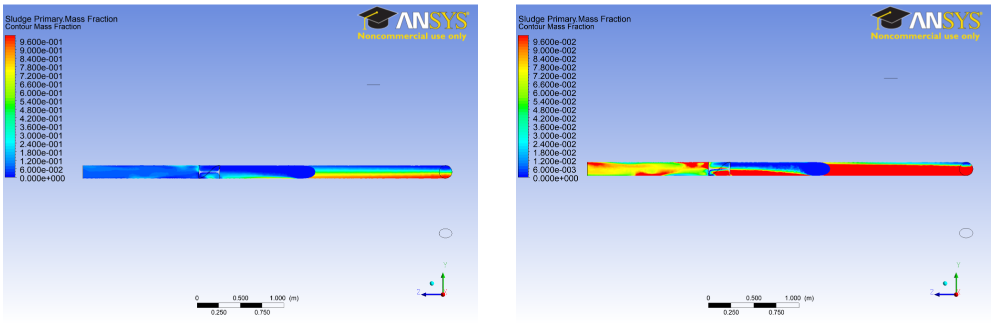

(a) Side view, YZ-plane. (b) Side view, YZ-plane, $0 \leq y_p \leq 0.1$.

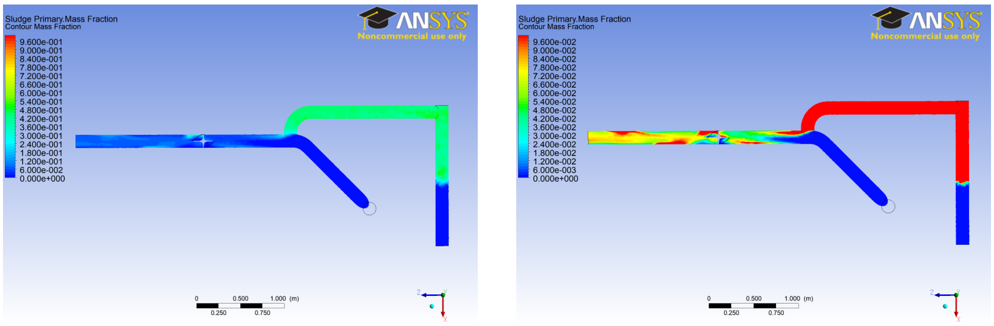

(c) Top view, ZX-plane. (d) Top view, ZX-plane, $0 \leq y_p \leq 0.1$.

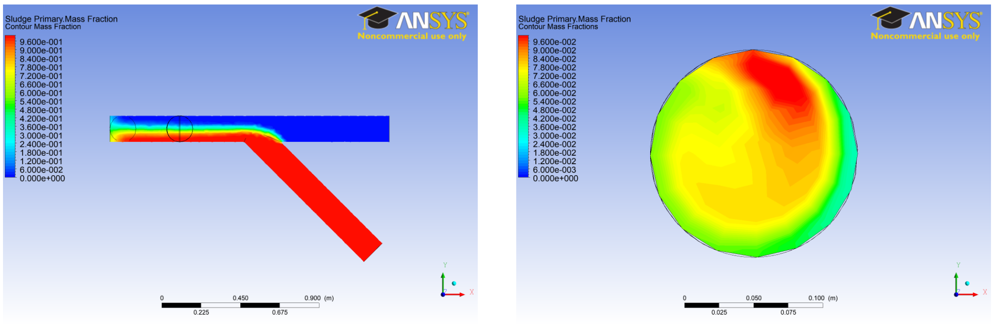

(e) Front view, XY-plane. (f) Front view, XY-plane, outlet, $0 \leq y_p \leq 0.1$.

Figure 4.2.32: Mass fraction of primary sludge in the static mixer model with a sludge mixture at $t = 40$ *s.*

The same could be said of the mass fractions of THP, see figure 4.2.33. Ahead of the helical element THP followed roughly the same path as in the other mixture models and behind the element distinct alternating regions were visible of higher and lower mass fractions. This indicated that some mixing took place, but not sufficient as THP was not uniformly distributed along the entire pipe behind the element.

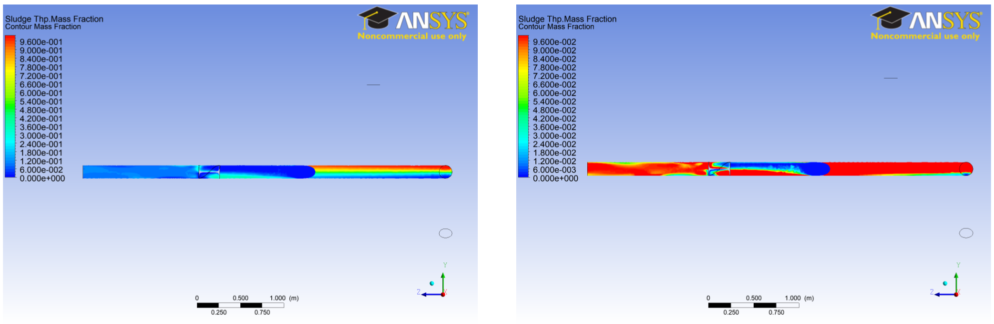

(a) Side view, YZ-plane. (b) Side view, YZ-plane, $0 \leq y_t \leq 0.1$.

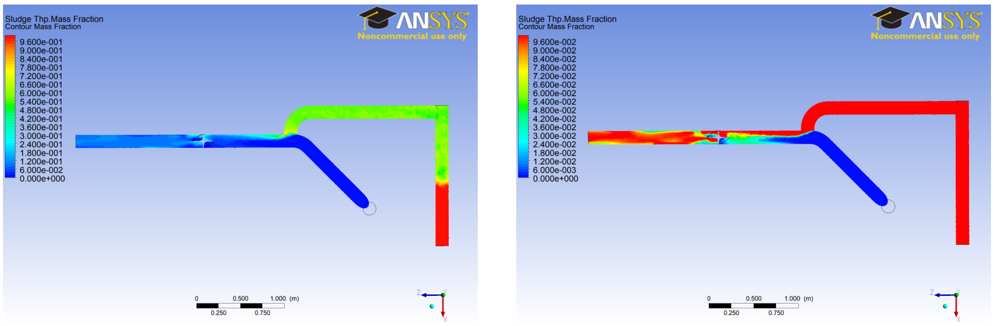

(c) Top view, ZX-plane. (d) Top view, ZX-plane, $0 \leq y_t \leq 0.1$.

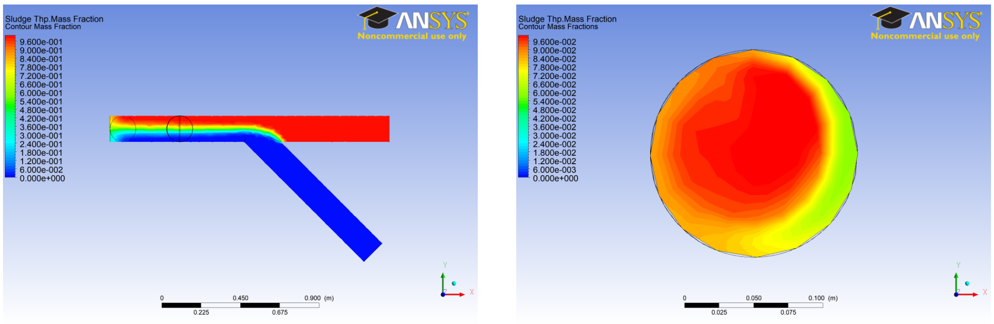

(e) Front view, XY-plane. (f) Front view, XY-plane, outlet, $0 \leq y_t \leq 0.1$.

Figure 4.2.33: Mass fraction of THP sludge in the static mixer model with a sludge mixture at $t = 40$ *s.*

The density showed a similar pattern as the mass fractions, see figure 4.2.34. The density ahead of the helical element was divided into two layers and behind the element distinct alternating regions of higher and lower density could be discerned.

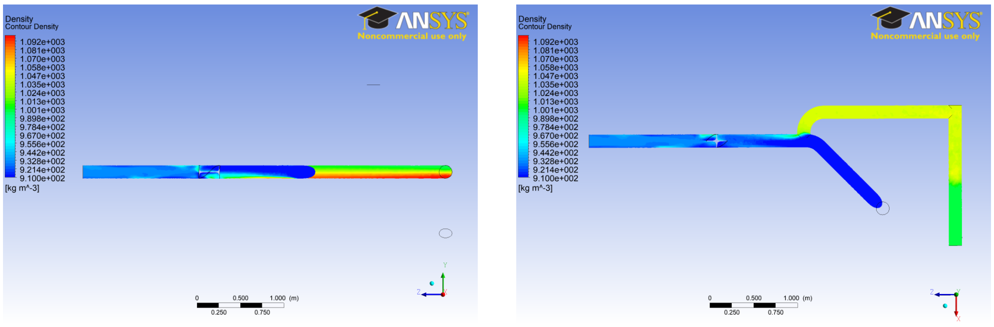

(a) Side view, YZ-plane. (b) Top view, ZX-plane.

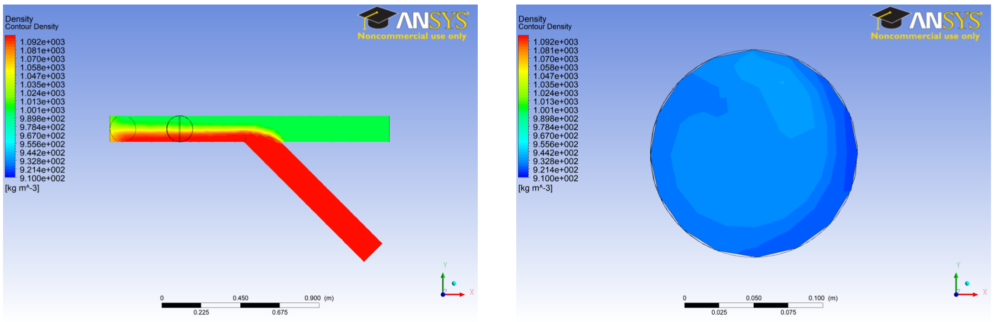

(c) Front view, XY-plane. (d) Front view, XY-plane, outlet.

Figure 4.2.34: Density of the static mixer model with a sludge mixture at $t = 40$ *s.*

In figures 4.2.35 and 4.2.36 plots of the particle tracks are depicted. The helical element caused a swirling motion of the sludge and because of this some mixing took place. The flow behind the helical element was unsteady. Still, streams of different sludge types were visible and hence the mixture could not be considered to be sufficiently mixed.

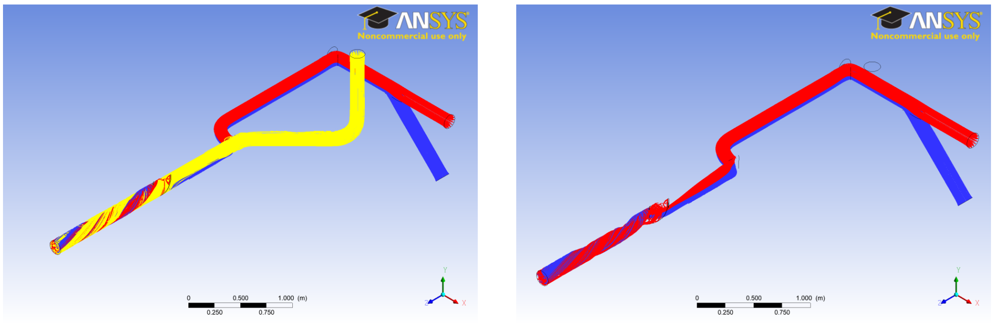

(a) Isometric view.

(b) Isometric view of primary and THP sludge.

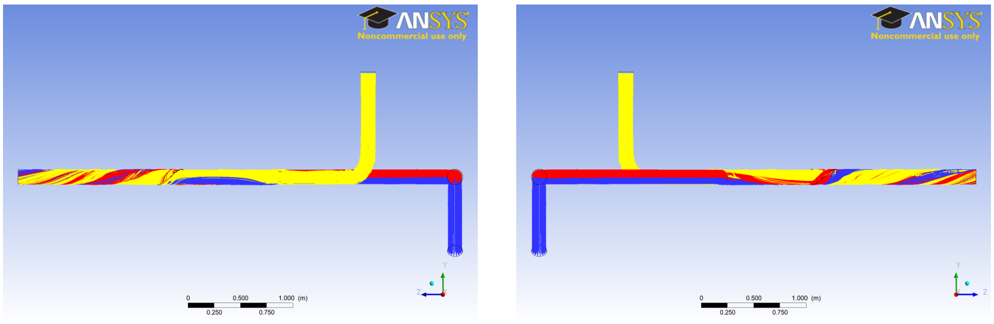

(c) Side view, YZ-plane.

(d) Side view, YZ-plane.

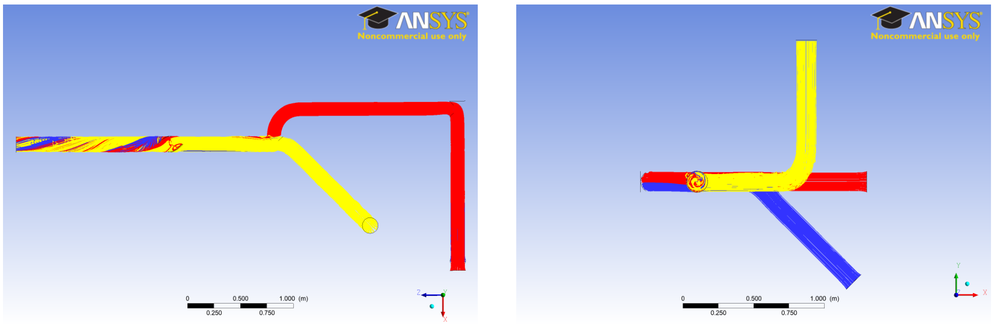

(e) Top view, ZX-plane.

(f) Front view, XY-plane.

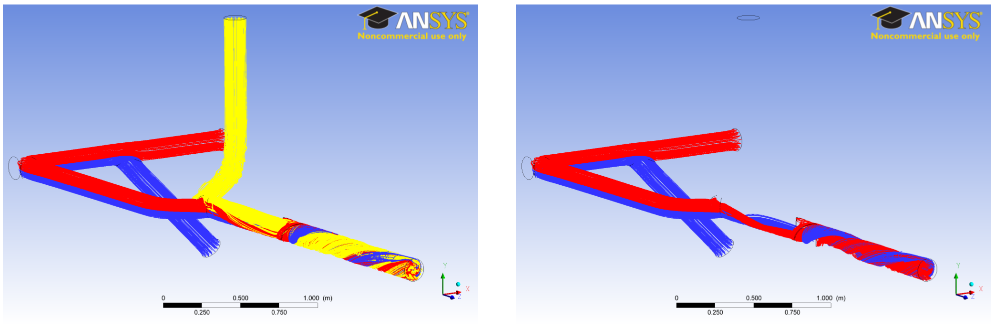

(g) Other view.

(h) Other view with primary and THP sludge.

Figure 4.2.35: Particle tracks for the static mixer model from $4 - 40$ *s with digested sludge (yellow), primary sludge (blue) and THP sludge (red).*

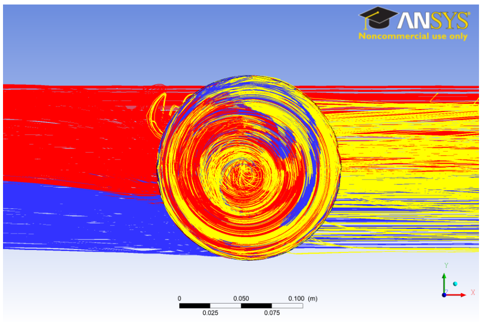

Figure 4.2.36: Zoom-in on the front view, XY-plane, of the particle tracks for the static mixer model from $4 - 40$ *s with digested sludge (yellow), primary sludge (blue) and THP sludge (red).*

4.2.5 Model 4 - Corkscrew

The fourth model included a corkscrew. It was the second of the two smaller models with an adjusted geometry which mixed most effectively compared to the other smaller models, see Appendix C. One simulation was carried out using a sludge mixture.

Species Transport

Contours of the pressure field are depicted in figure 4.2.37. The pressure drop in this model was larger than for the baseline and static mixer models. Two possible causes could be that a smaller diameter was used in the corkscrew and that the fluid had to travel a larger distance in this model. The highest pressure was achieved at the inlet of primary sludge. Both the higher viscosity of primary sludge and the higher density compared to digested sludge might have contributed to this, as more power was needed to let primary sludge flow through this pipe.

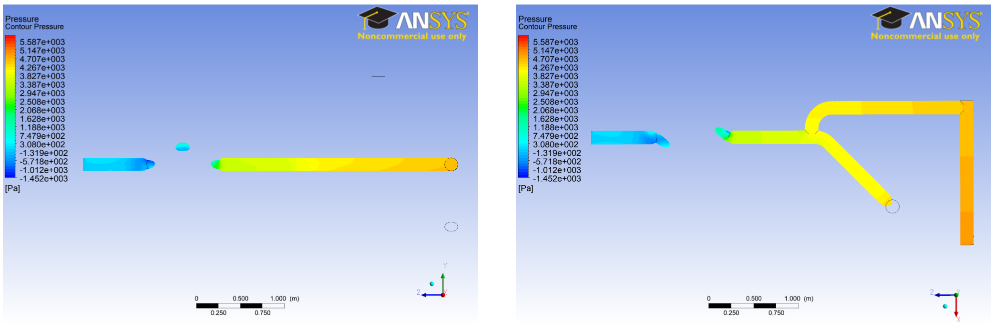

(a) Side view, YZ-plane.

(b) Top view, ZX-plane.

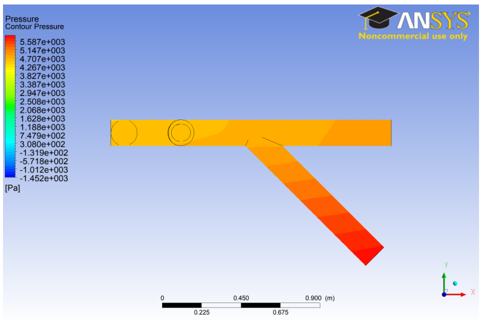

(c) Front view, XY-plane.

Figure 4.2.37: Pressure of the corkscrew model with a sludge mixture at $t = 40$ *s, with* ΔP *= 5.59 kPa.*

In figure 4.2.38 three plots of the velocity field are displayed. The maximum velocity was reached inside the corkscrew and was partly due to the smaller diameter used. The velocity field behind the corkscrew was still influenced by it and was not axisymmetric.

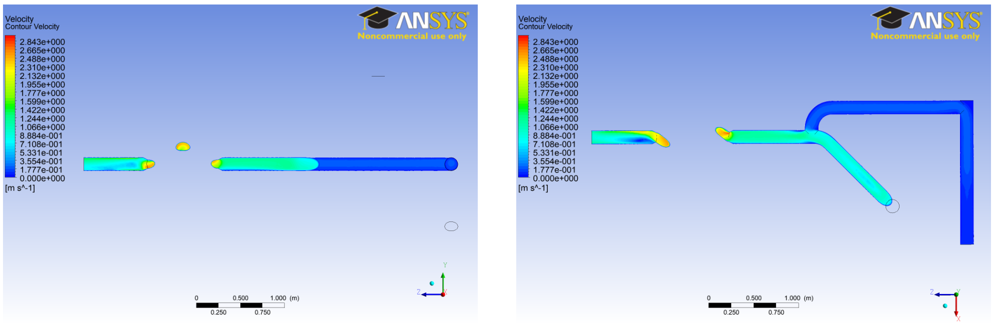

(a) Side view, YZ-plane.

(b) Top view, ZX-plane.

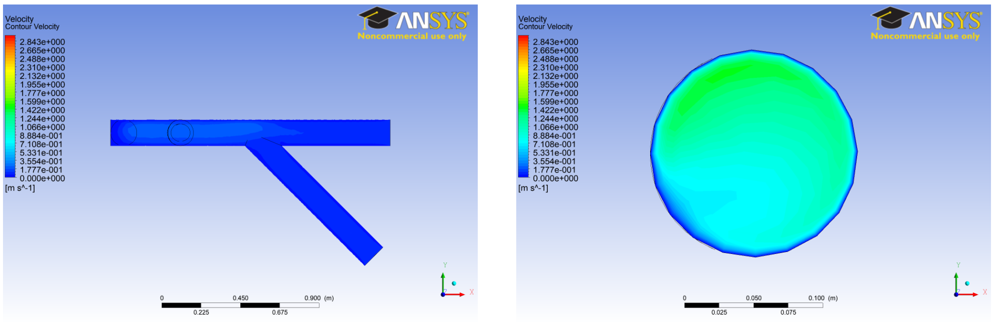

(c) Front view, XY-plane.

(d) Front view, XY-plane, outlet.

Figure 4.2.38: Velocity of the corkscrew model with a sludge mixture at $t = 40$ *s, with* $\max(\vec{u}) =$ *2.84 m/s.*

In figure 4.2.39 plots of the dynamic viscosity are portrayed. The viscosity values ahead of the corkscrew were quite similar to the previous models, although the region of higher viscosity was slightly larger than in the other models, which could be due to the upstream influence of the corkscrew, the numerical accuracy or the mesh quality. The highest value of the viscosity was 6588 Pa·s, which was physically not realistic. Behind the junction with digested sludge, the viscosity was of roughly the same size as in the previous mixture models. The high viscosity values related to a shear rate of about $1 - 2 \cdot 10^{-2}$ s^{-1}.

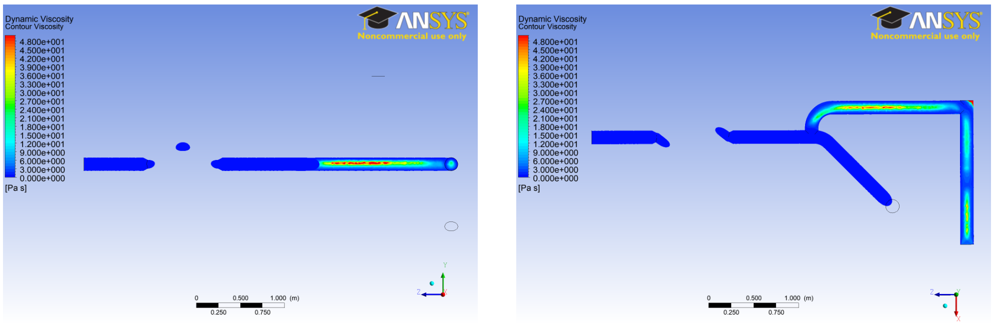

(a) Side view, YZ-plane.

(b) Top view, ZX-plane.

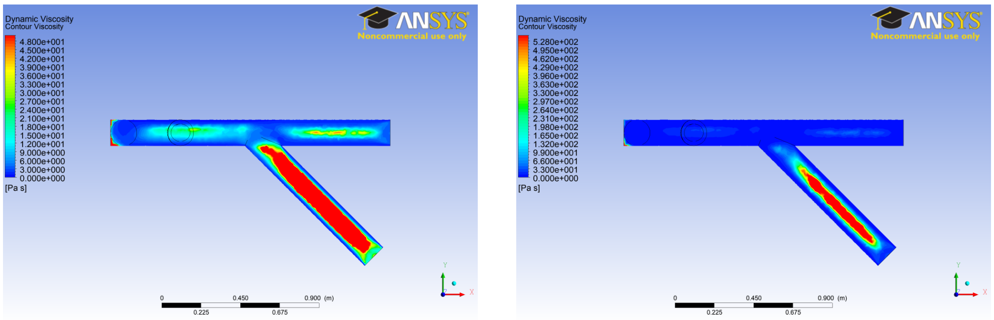

(c) Front view, XY-plane, μ between $0-50$ Pa·s..

(d) Front view, XY-plane, μ between $0-550$ Pa·s.

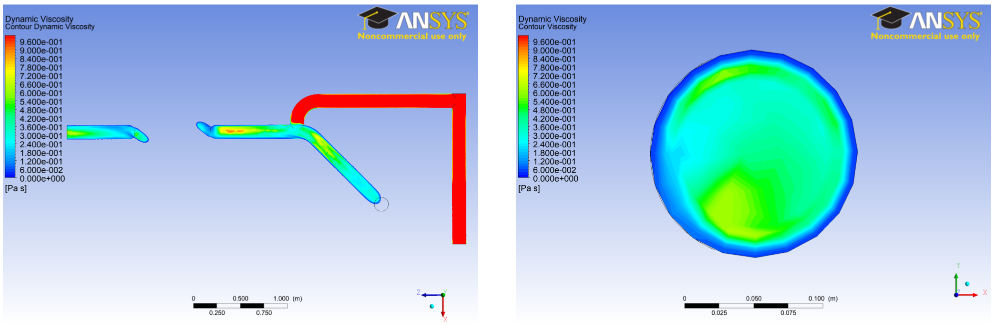

(e) Top view, ZX-plane, μ between $0-1$ Pa·s.

(f) Front view, XY-plane, outlet, μ between $0-1$ Pa·s.

Figure 4.2.39: Dynamic viscosity ranging from $0-50$ Pa·s for (a), (b) and (c), from $0-550$ Pa·s for (d), and from $0-1$ Pa·s for (e) and (f), of the corkscrew model with a sludge mixture at $t=40$ s.

Ahead of the corkscrew the path of primary sludge was roughly similar to the previous mixture models, see the mass fractions of figure 4.2.40. However, as already noted in the analysis of the primary mass fractions in the static mixer model, there seemed to be more mixing between primary and THP sludge in the baseline and venturi mixture models compared to this model. The mixing of this model was comparable with the static mixer model. This difference in mixing was peculiar as only the geometry and mesh of the model should be different, but all the other settings the same.

Behind the corkscrew primary sludge was more evenly distributed along the pipe, but near the walls there was less primary sludge present.

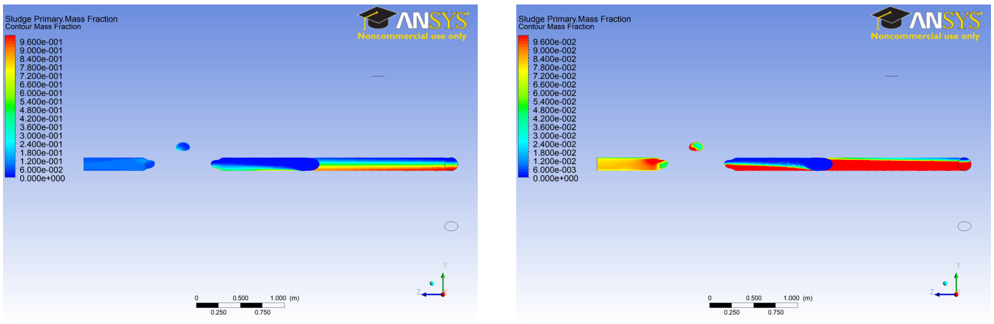

(a) Side view, YZ-plane.

(b) Side view, YZ-plane, $0 \leq y_p \leq 0.1$.

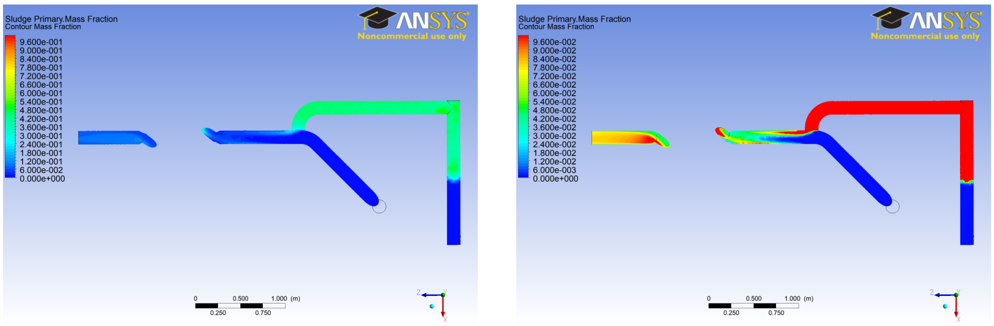

(c) Top view, ZX-plane.

(d) Top view, ZX-plane, $0 \leq y_p \leq 0.1$.

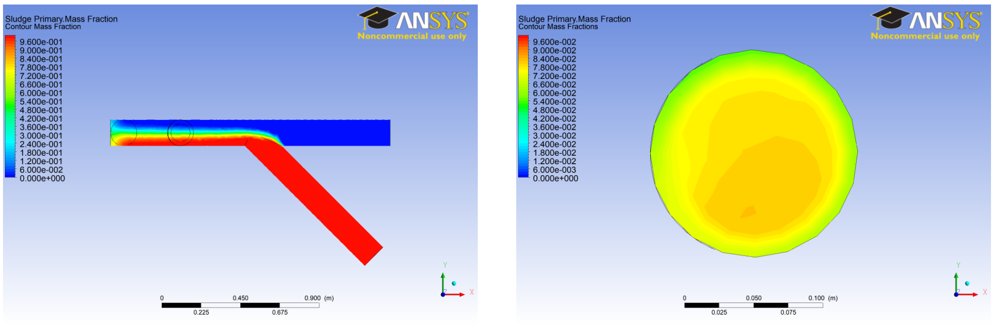

(e) Front view, XY-plane.

(f) Front view, XY-plane, outlet, $0 \leq y_p \leq 0.1$.

Figure 4.2.40: Mass fraction of primary sludge in the corkscrew model with a sludge mixture at $t = 40$ *s.*

Similar remarks could be made with respect to the mass fractions of THP, see figure 4.2.41. In front of the corkscrew the path of THP sludge was roughly similar to the previous mixture models. Behind the corkscrew THP was more evenly distributed along the pipe, but less THP sludge appeared to be present at the top.

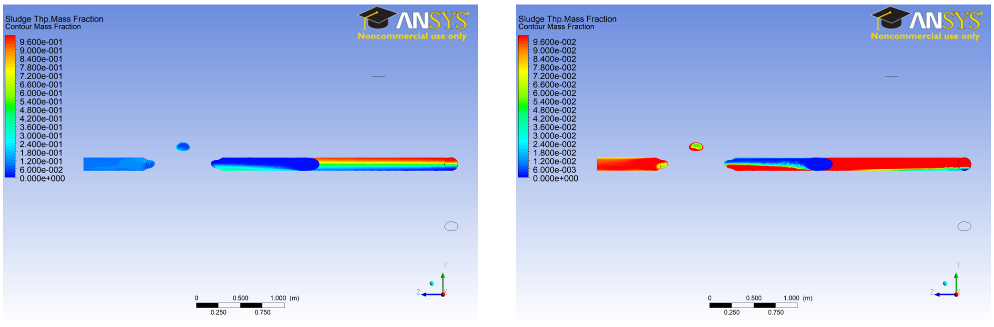

(a) Side view, YZ-plane. (b) Side view, YZ-plane, $0 \leq y_t \leq 0.1$.

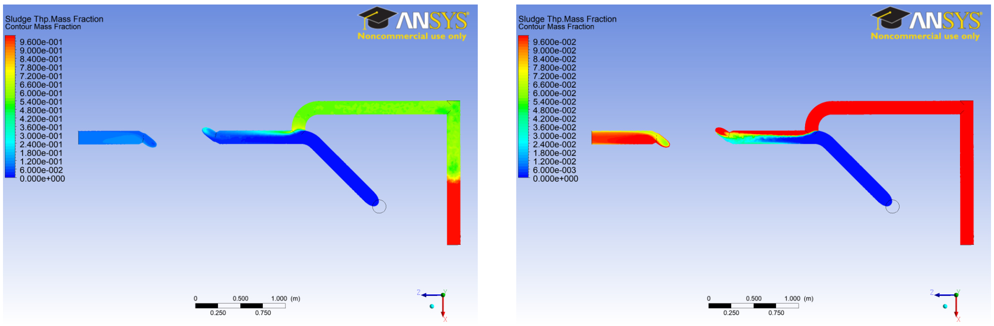

(c) Top view, ZX-plane. (d) Top view, ZX-plane, $0 \leq y_t \leq 0.1$.

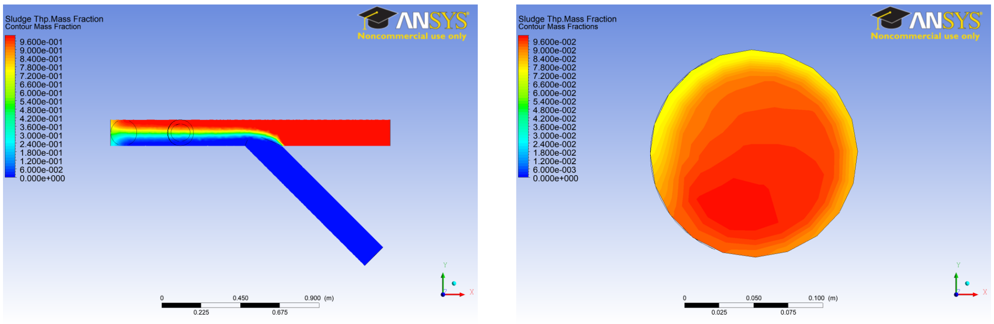

(e) Front view, XY-plane. (f) Front view, XY-plane, outlet, $0 \leq y_t \leq 0.1$.

Figure 4.2.41: Mass fraction of THP sludge in the corkscrew model with a sludge mixture at $t = 40$ *s.*

The density ahead of the corkscrew showed a similar pattern as in the previous models, see figure 4.2.42. Behind the corkscrew slight variations in density were visible.

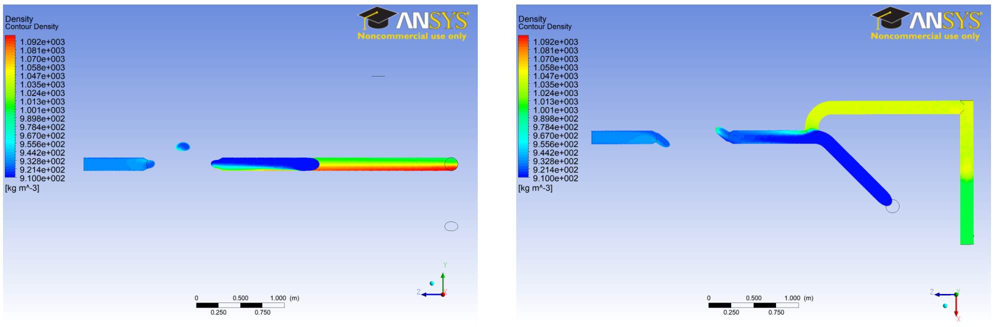

(a) Side view, YZ-plane.

(b) Top view, ZX-plane.

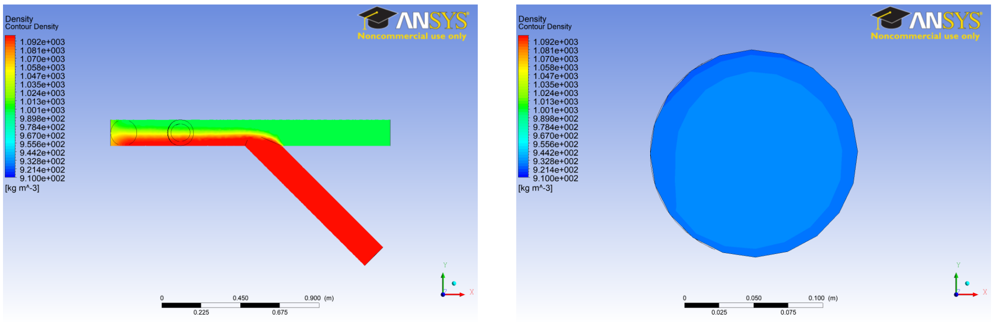

(c) Front view, XY-plane.

(d) Front view, XY-plane, outlet.

Figure 4.2.42: Density of the corkscrew model with a sludge mixture at $t = 40$ s.

In figures 4.2.43 and 4.2.44 the particle tracks are shown. Ahead of the corkscrew the behaviour of the particles was similar to the other mixture models. The corkscrew initiated some swirling motion, but to a lesser extent than in the static mixer model. At the outlet primary and THP sludge were not located at the walls any more, as in the baseline model, but were located more in the middle of the pipe. Just as in the static mixer model still separate streams of sludge could be distinguished. For this reason the sludge could not be considered to be sufficiently mixed.

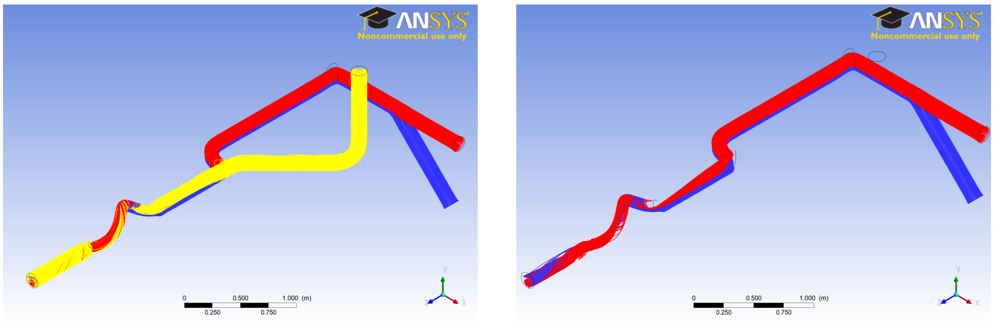

(a) Isometric view. (b) Isometric view of primary and THP sludge.

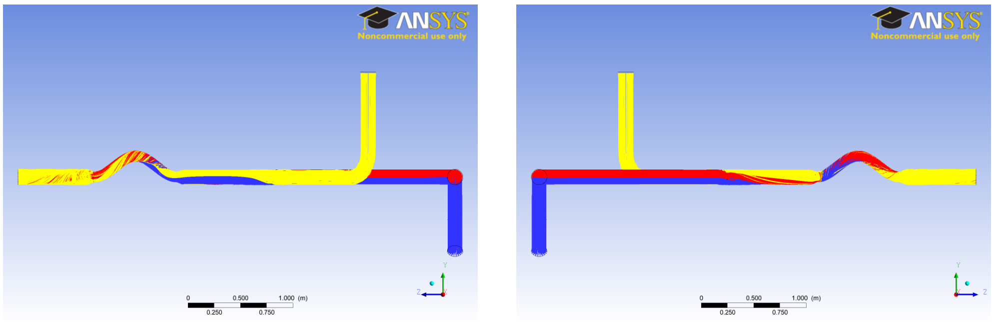

(c) Side view, YZ-plane. (d) Side view, YZ-plane.

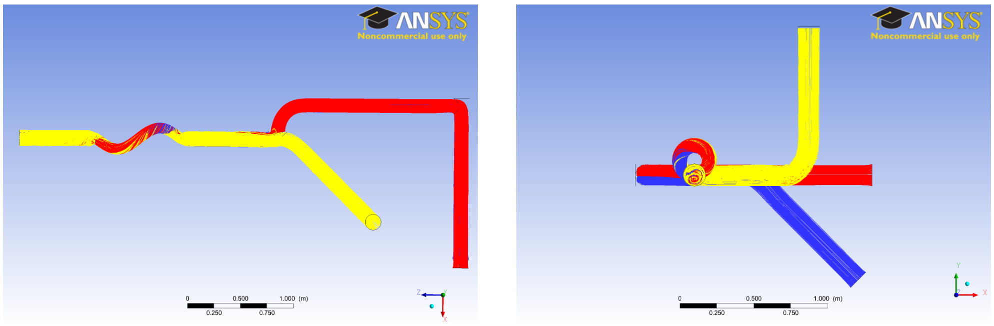

(e) Top view, ZX-plane. (f) Front view, XY-plane.

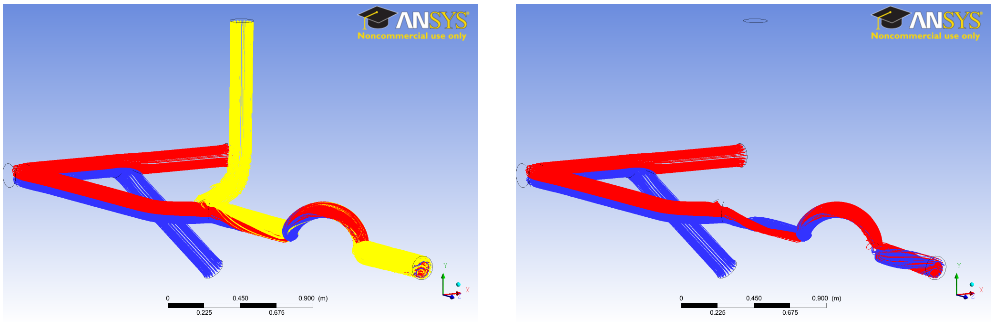

(g) Other view. (h) Other view with primary and THP sludge.

Figure 4.2.43: Particle tracks for the corkscrew model from $4 - 40$ *s with digested sludge (yellow), primary sludge (blue) and THP sludge (red).*

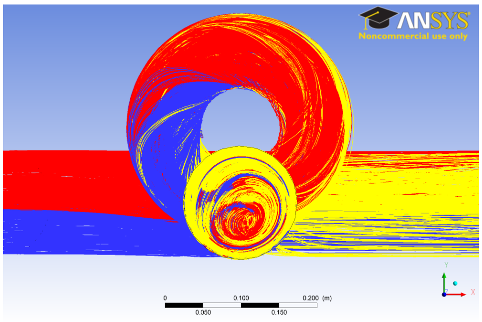

Figure 4.2.44: Zoom-in on the front view, XY-plane, of the particle tracks for the corkscrew model from $4-40$ *s with digested sludge (yellow), primary sludge (blue) and THP sludge (red).*

4.2.6 Model 5 - Venturi D40

When calculating the pressure drop over two geometries of the venturi for validation purposes, the mixing with a venturi with an inner diameter of constriction of 40 mm appeared to be very good. Hence, a fifth model was run including particles. Because this model was intended for validation, the inlet velocities of primary and THP sludge were different.

Species Transport

The pressure field is captured in three views as shown in figure 4.2.45. The pressure drop over the venturi D40 was approximately 1.3 bar which is high. The pumps could still manage this pressure drop, but the effect on their life cycle is not yet known. The higher pressure compared to the venturi model could be due to the higher flow values and the narrower constriction.

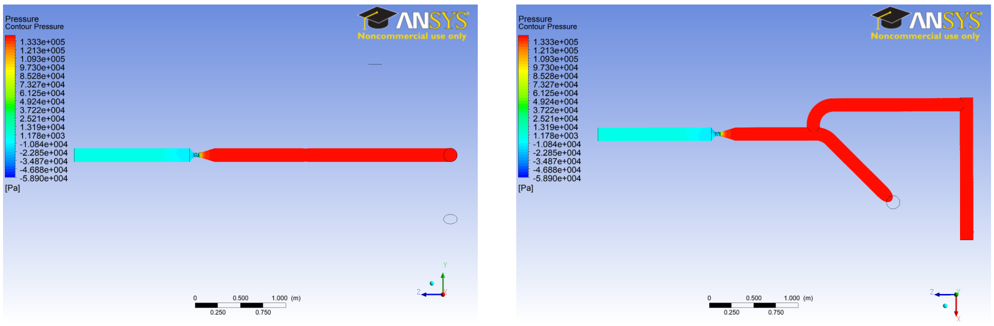

(a) Side view, YZ-plane.

(b) Top view, ZX-plane.

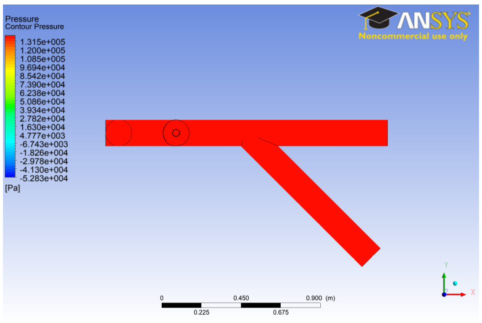

(c) Front view, XY-plane.

Figure 4.2.45: Pressure of the venturi D40 model with a sludge mixture at $t = 8$ *s, with* ΔP = *133.3 kPa.*

The velocity field is depicted in figure 4.2.46. The maximum velocity was reached at the venturi and was more than twice as large as in the venturi model with a narrowing of 50 mm. The jet flow behind the venturi showed again some unsteady behaviour over time, with the angle of the flow direction shifting in time.

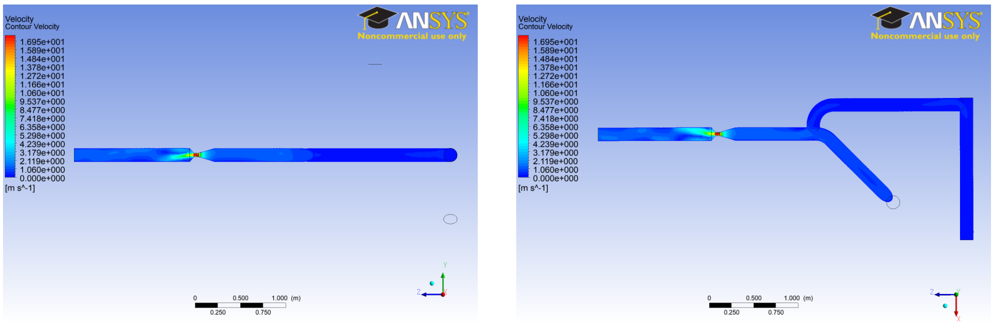

(a) Side view, YZ-plane.

(b) Top view, ZX-plane.

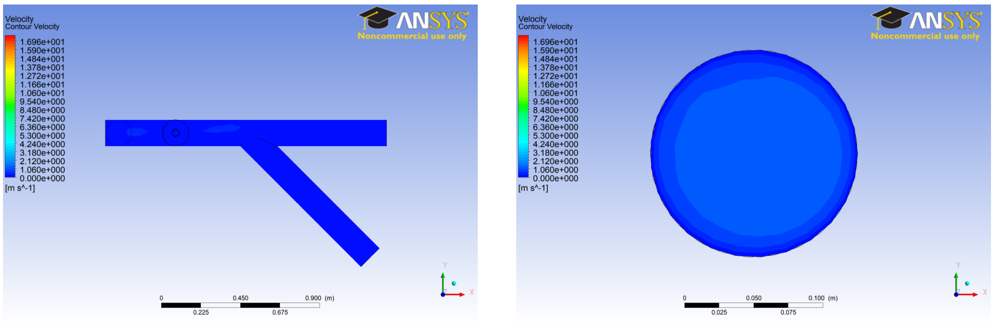

(c) Front view, XY-plane.

(d) Front view, XY-plane, outlet.

Figure 4.2.46: Velocity of the venturi D40 model with a sludge mixture at $t = 8$ *s, with* $\max(\vec{u}) =$ *16.95 m/s.*

In figure 4.2.47 contours of the dynamic viscosity are shown. The values in front of the junction with digested sludge were quite similar to the other mixture models. An incredibly high and physically not realistic value of the maximum viscosity was achieved, namely of 8063 Pa·s, which was highest of all models analysed. High shear rates were reached at the narrowing of the venturi resulting in a very low viscosity in that region.

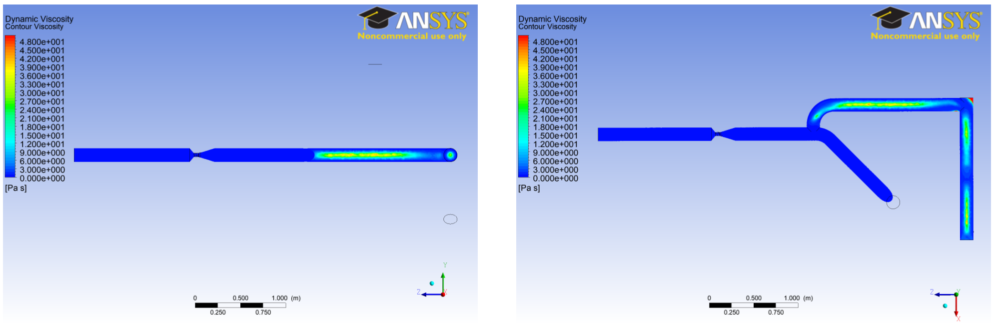

(a) Side view, YZ-plane.

(b) Top view, ZX-plane.

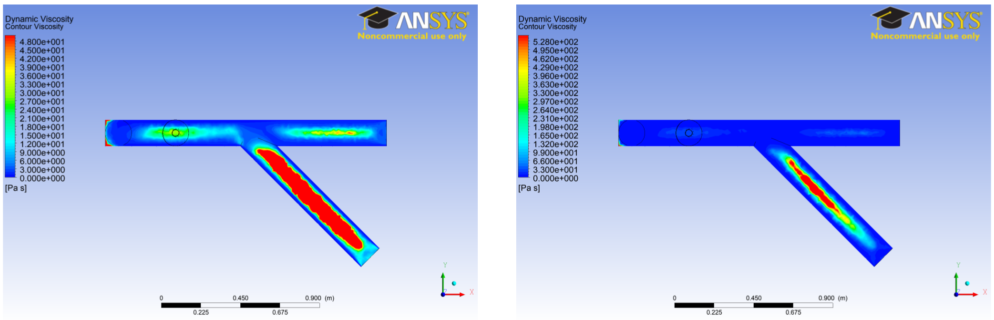

(c) Front view, XY-plane, μ between $0 - 50$ Pa·s..

(d) Front view, XY-plane, μ between $0 - 550$ Pa·s.

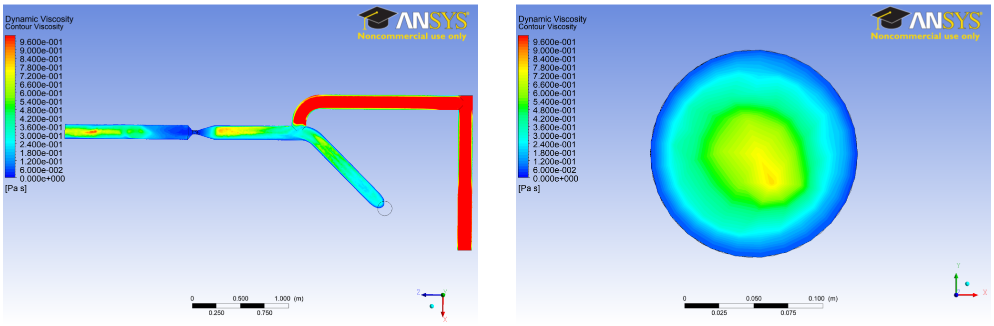

(e) Front view, XY-plane, μ between $0-1$ Pa·s.

(f) Front view, XY-plane, outlet with μ between $0 - 1$ Pa·s.

Figure 4.2.47: Dynamic viscosity ranging from $0 - 50$ *Pa·s for (a), (b) and (c), from* $0 - 550$ *Pa·s for (d), and from* $0 - 1$ *Pa·s for (e) and (f), of the venturi D40 model with a sludge mixture at* $t = 8$ *s.*

Plots of the mass fractions of primary sludge can be found in figure 4.2.48. From the front view it can be noticed that a primary sludge had a higher flow rate than THP sludge. Untill the junction with digested sludge the path primary sludge followed was roughly the same as in the previous models. Behind the junction primary sludge revolved around digested sludge over the bottom of the pipe, flowing from the wall in negative x-direction to the wall in positive x-direction. Behind the venturi primary sludge appeared to be almost uniformly distributed along the entire pipe.

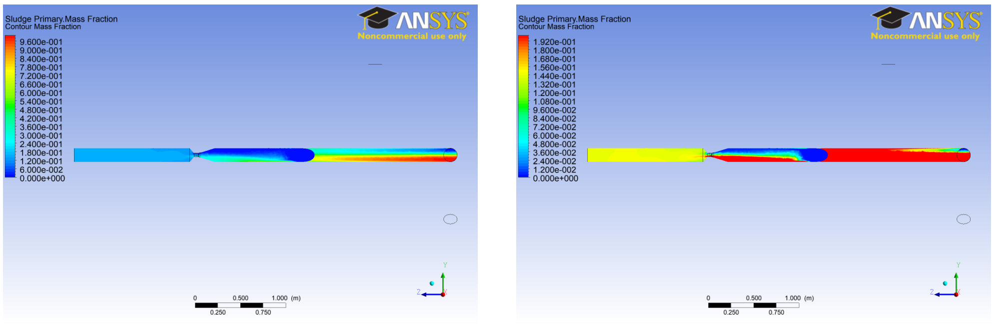

(a) Side view, YZ-plane. (b) Side view, YZ-plane, $0 \leq y_p \leq 0.2$.

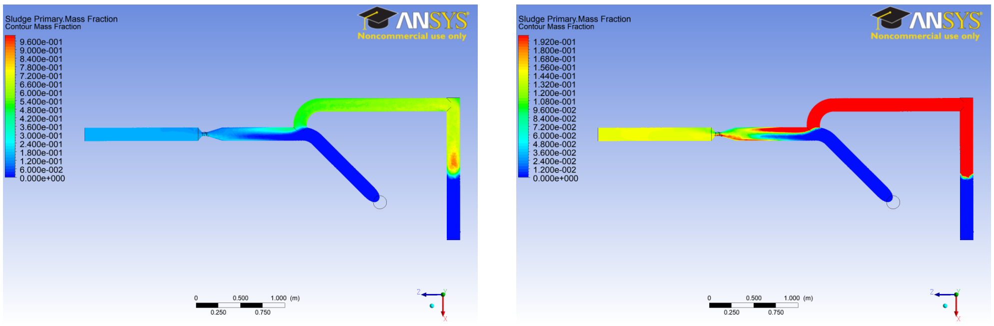

(c) Top view, ZX-plane. (d) Top view, ZX-plane, $0 \leq y_p \leq 0.2$.

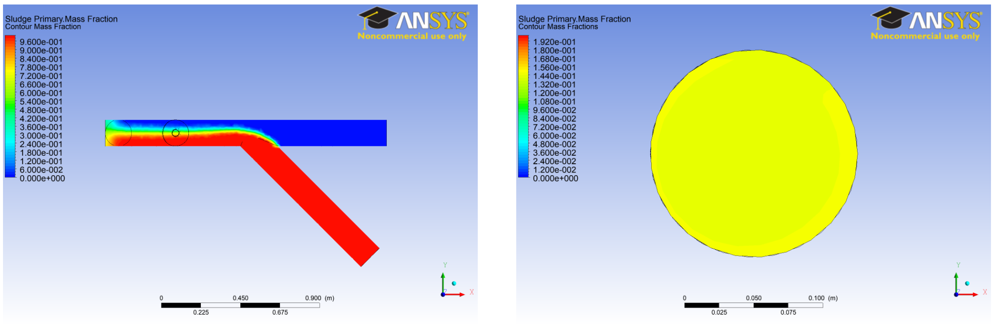

(e) Front view, XY-plane. (f) Front view, XY-plane, outlet, $0 \leq y_p \leq 0.2$.

Figure 4.2.48: Mass fraction of primary sludge in the venturi D40 model with a sludge mixture at $t = 8$ *s.*

In figure 4.2.49 plots of the mass fractions of THP sludge can be found. Until the junction with digested sludge THP followed roughly the same path as in the previous models. Behind the junction THP sludge remained near the wall in negative x-direction and flows over the bottom. Behind the venturi THP sludge also appeared to be almost uniformly distributed along the entire pipe.

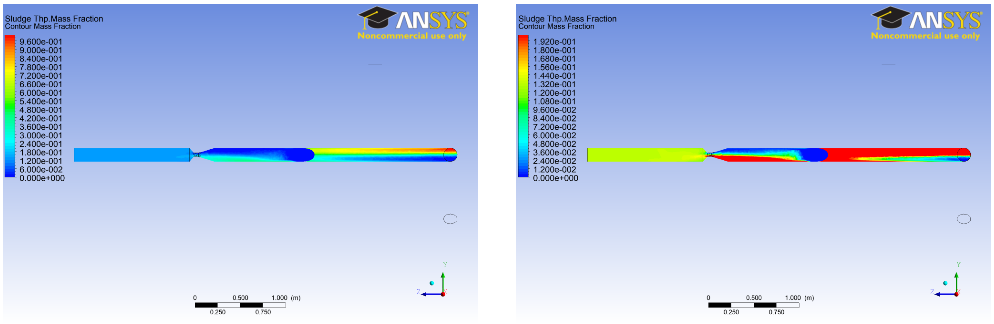

(a) wastewater, YZ-plane.

(b) wastewater, YZ-plane, $0 \leq y_t \leq 0.2$.

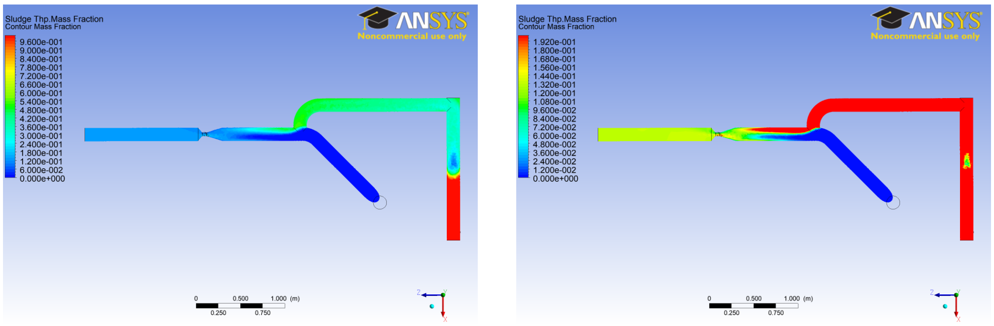

(c) Top view, ZX-plane.

(d) Top view, ZX-plane, $0 \leq y_t \leq 0.2$.

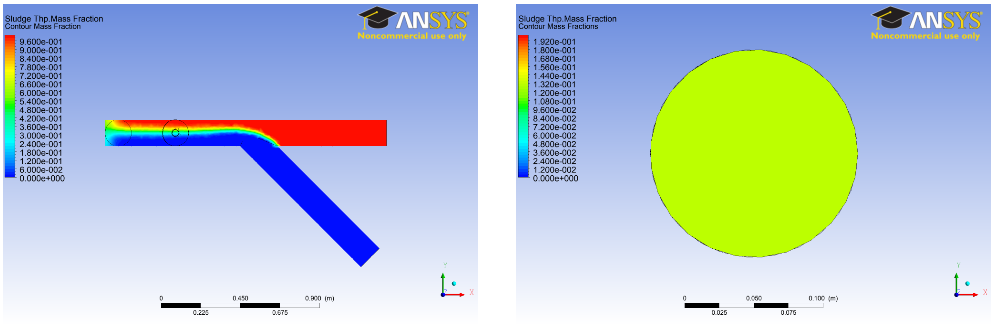

(e) Front view, XY-plane.

(f) Front view, XY-plane, outlet, $0 \leq y_t \leq 0.2$.

Figure 4.2.49: Mass fraction of THP sludge in the venturi D40 model with a sludge mixture at $t = 8$ *s.*

Contours of the density are displayed in figure 4.2.50. In front of the junction with digested sludge the regions of high and low density were roughly the same as in the previous models, taking into account that different inlet velocities were used in this model. Behind the venturi the density was almost uniform along the entire pipe.

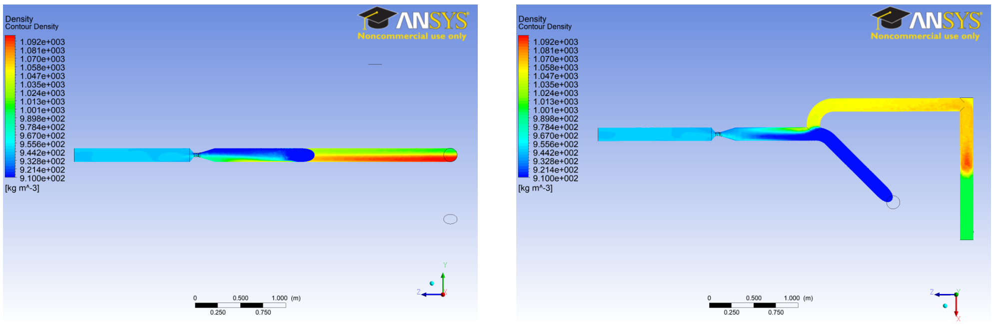

(a) Side view, YZ-plane.

(b) Top view, ZX-plane.

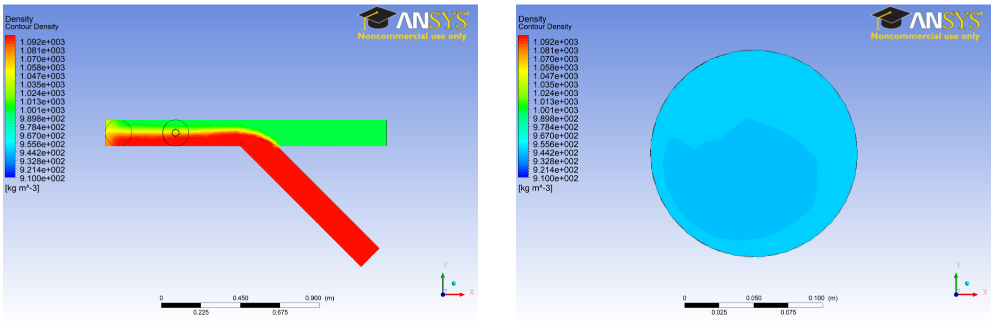

(c) Front view, XY-plane.

(d) Front view, XY-plane, outlet.

Figure 4.2.50: Density of the venturi D40 model with a sludge mixture at $t = 8$ *s.*

The particle tracks in figures 4.2.51 and 4.2.52 confirmed the remarks and the conclusion that the mixing was sufficient. The remarks made about the mass fractions of primary and THP sludge ahead of and behind the venturi were confirmed by the particle tracks. At the outlet a well mixed sludge mixture could be seen.

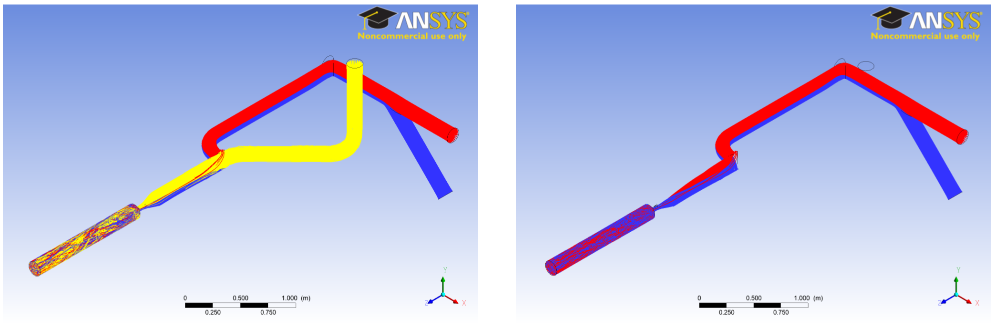

(a) Isometric view.

(b) Isometric view of primary and THP sludge.

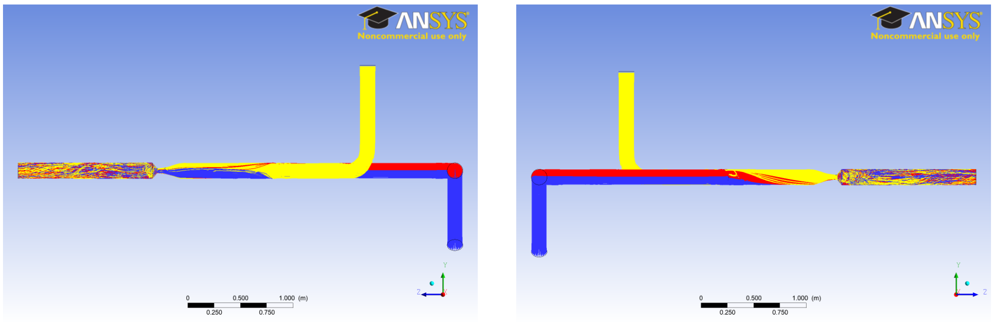

(c) Side view, YZ-plane.

(d) Side view, YZ-plane.

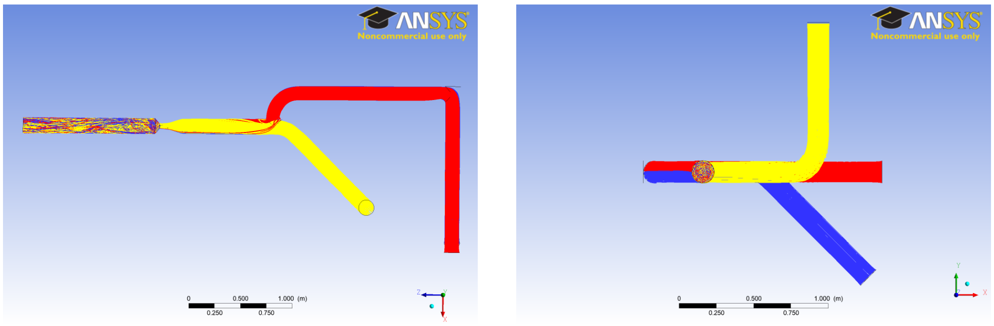

(e) Top view, ZX-plane.

(f) Front view, XY-plane.

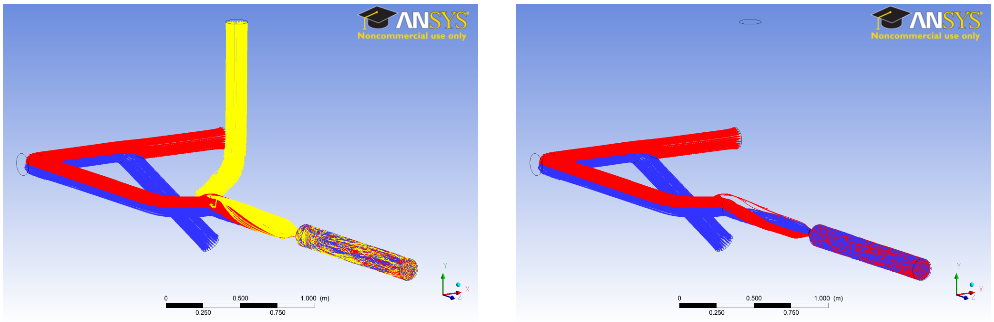

(g) Other view.

(h) Other view with primary and THP sludge.

Figure 4.2.51: Particle tracks for the venturi D40 model from $4-32$ s with digested sludge (yellow), primary sludge (blue) and THP sludge (red).

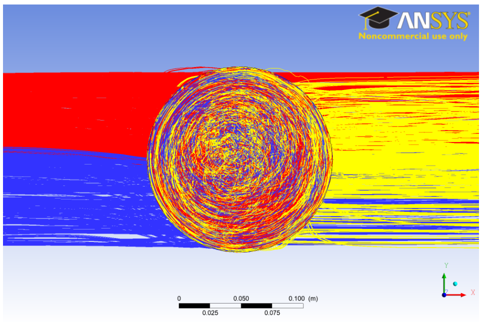

Figure 4.2.52: Zoom-in on the front view, XY-plane, of the particle tracks for the venturi D40 model from $4 - 32$ s with digested sludge (yellow), primary sludge (blue) and THP sludge (red).

4.2.7 Estimation of the Discretization Error

For 25 points along the y-axis near the outlet the local order of convergence p was determined solving equation (2.4.34). For many points Matlab was unable to solve for p. In tables 4.2.53 and 4.2.54 the minimum, average and maximum order of convergence and the number of unsolved points are shown for respectively the baseline and venturi D40 model.

As can be seen the order of convergence was high, much higher than the expected order of convergence of 2 as second order schemes were used to calculate the solution.

Baseline	ρ	μ	y_p	y_t	P	$\lvert\vec{u}\rvert$
p_{min}	2.9715	3.0375	4.0760	1.7312	3.5077	2.3952
p_{avg}	12.9646	6.2210	7.6890	5.8295	10.2918	4.8673
p_{max}	19.5559	16.3978	12.6249	11.3065	18.3272	9.3393
# NaN	21	16	17	18	7	20

Table 4.2.53: Minimum, average and maximum values of the local order of convergence p for key variables along the y-axis near the outlet of the baseline model, including the number of unsolved points.

Venturi D40	ρ	μ	y_p	y_t	P	$\lvert\vec{u}\rvert$
p_{min}	4.0556	3.6848	1.3922	1.1716	3.0056	1.4146
p_{avg}	7.6325	8.5010	2.8025	2.4201	9.6852	8.6159
p_{max}	17.6363	17.9895	4.1056	4.3838	12.0336	15.8210
# NaN	13	12	13	10	18	19

Table 4.2.54: Minimum, average and maximum values of the local order of convergence p for key variables along the y-axis near the outlet of the venturi D40 model, including the number of unsolved points.

Considering the plots of the key variables along the y-axis odd behaviour was noticed for both models, see figures 4.2.56 and 4.2.57. Of all key variables only the pressure behaved as expected, converging for a finer grid, and the viscosity to a lesser extent. However the other key variables, the density, the mass fractions of primary and THP sludge, and the velocity, behaved strange.

As can be seen the density and mass fractions were closely related. For positive y-values the convergence of the density and mass fractions of the baseline model was according to what would be expected, but for negative y-values the convergence was odd as the fine mesh showed different results for the mass fractions than what would be expected from the convergence of the coarse to the medium grid. The velocity showed this behaviour as well, with the coarse grid approximation of the velocity being closer to the fine grid than the medium grid was to the fine grid.

These results could be explained by bad convergence on the coarse and medium grid, which could be due to a too coarse grid.

The velocity profiles of the different meshes in the venturi D40 model differed quite a lot, just as the profiles of the viscosity. However, the profiles of the density and mass fractions showed even stranger behaviour. The mass fractions of primary and THP sludge were roughly the same over the entire y-axis for the medium grid, but for the coarse and the fine grid they showed variations along the y-axis. The average of the mass fractions seemed to differ among the grids. This was confirmed when calculating the average mass fractions at the outlet, see table 4.2.55. The expected mass fraction was calculated by multiplying the volume flow with the density of that sludge type and computing the ratios of the mass flows.

These differences in average mass fractions could be explained by a not well enough mixed mixture or by an unsteady solution in which bulks of one sludge type flowed trough the outlet.

Especially the results of the Venturi D40 model were grid dependent with the key variables showing great variation between the different meshes. Whereas in the baseline model convergence for the density and viscosity was visible with smaller mesh size, no consistent development could be distinguished for smaller mesh sizes in the venturi D40 model. It was expected that more turbulence was generated in the venturi D40 model by the venturi than in the baseline model, hence these mesh dependent results could be due to the sensitivity of the $k - \varepsilon$ model to disturbances. However, these results could also be caused by using a too coarse mesh or a mesh of poor quality. Another cause could be that no steady solution existed. This was investigated by accessing the key variables at different time steps and found to be a likely option. These plots were not included.

Because of the differences between the meshes the reliability of the results of the models discussed before was questionable. They may serve as an indication of the flow behaviour but could and should not be considered as good solutions.

	Baseline		Venturi D40	
Grid	y_p	y_t	y_p	y_t
Coarse	0.1020	0.0935	0.1476	0.1317
Medium	0.0934	0.0998	0.1624	0.1079
Fine	0.0985	0.0903	0.1447	0.1288
Expected	0.1751	0.1095	0.1751	0.1095

Table 4.2.55: Average mass fractions of primary and THP sludge at the outlet of the baseline and venturi D40 models.

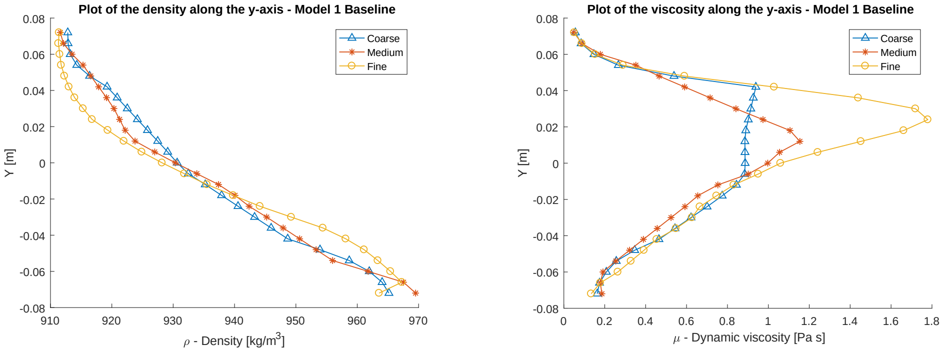

(a) Density.

(b) Viscosity.

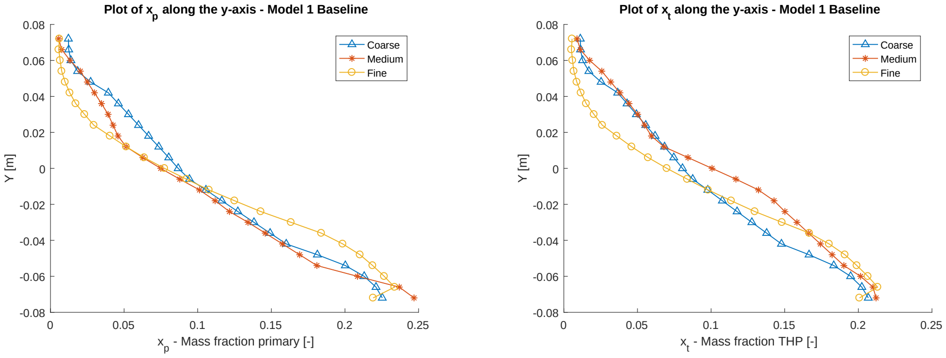

(c) Mass fraction primary sludge.

(d) Mass fraction THP sludge.

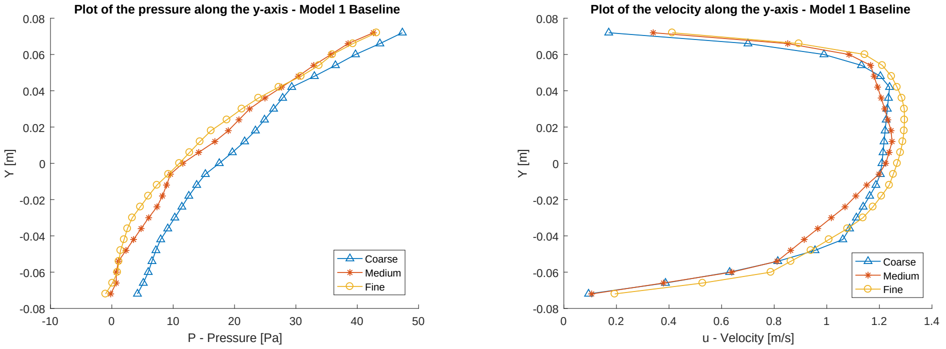

(e) Pressure.

(f) Velocity.

Figure 4.2.56: Plots of the key variables along the y-axis for the baseline model with different meshes.

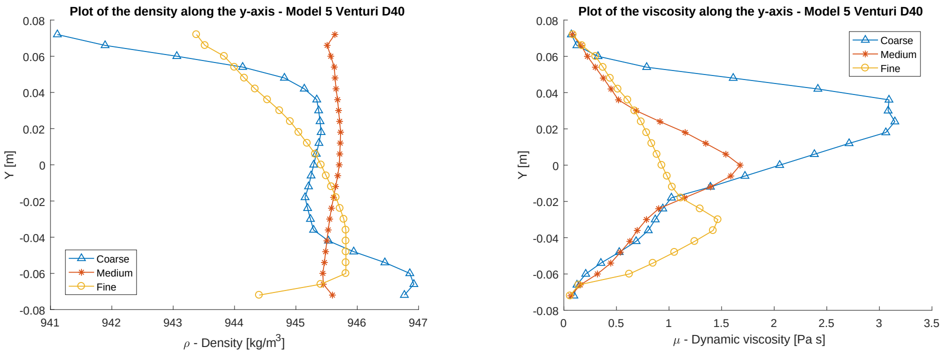

(a) Density. (b) Viscosity.

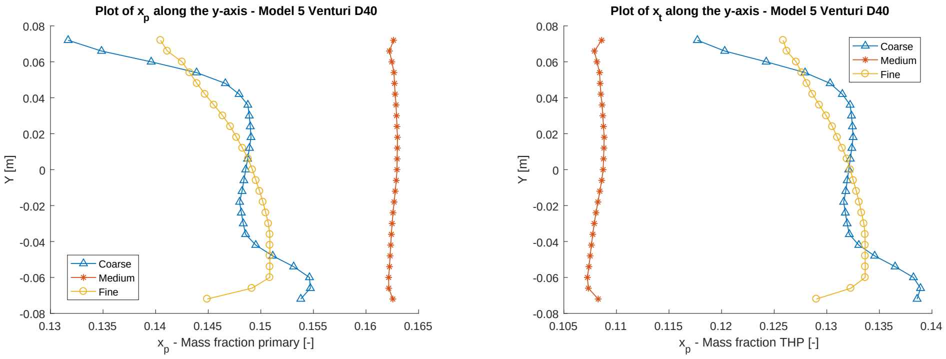

(c) Mass fraction primary sludge. (d) Mass fraction THP sludge.

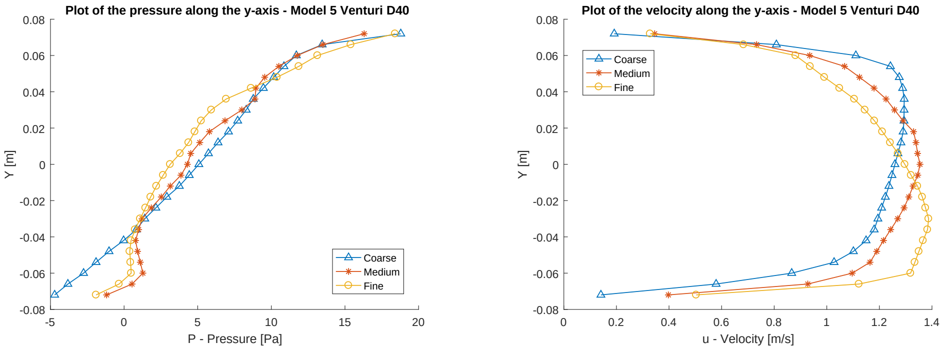

(e) Pressure. (f) Velocity.

Figure 4.2.57: Plots of the key variables along the y-axis for the venturi D40 model with different meshes.

4.3 Validation of the CFD Model

The CFD model of the venturi D40 was validated by measuring the pressure drop over the venturi. An additional indication of the mixing was given by measuring the dry solids content of five samples behind the venturi.

4.3.1 Pressure

The CFD model was validated by measuring the pressure drop over a venturi with a 40 mm narrowing. The calculated pressure drop in the model was $\Delta P = 133.3$ kPa, see figure 4.2.45. The measured pressure drop was ΔP = 100 kPa. So there was some deviation between the model and practice.

Because of the variations in the venturi D40 model between the different meshes, the pressure drop of these meshes are mentioned as well. In case of the coarse mesh the calculated pressure drop was ΔP = 54.7 kPa, and in case of the fine mesh ΔP = 92.5 kPa. Hence, the pressure drop of the fine mesh approached practice closest. However, as can be seen there was also a large deviation present among the pressure drops of the different meshes for the same geometry. This should certainly not be the case. Therefore, the reliability and accuracy of the model is under discussion.

4.3.2 Dry Solids Content

On the 21th of June 2017 five samples over the diameter of the pipe, behind the venturi with a narrowing of 40 mm, were taken and the average dry solids content of these samples was determined. In table 4.3.1 the flow rates and the dry solids content of the sludge streams at the time of measuring are summarized. The mass fractions were calculated assuming the densities measured at the TU Delft in June 2017, see table 4.1.20.

The results of the dry solids content measurements are presented in table 4.3.2 with the sampling points depicted in figure 3.3.1. There was a slight variation visible in the measured dry solids content over the diameter, but this could be due to measuring errors. Overall, the sludge could be considered to be sufficiently mixed.

The measured dry solids content differed from the expected average dry solids contents This could be caused by the values of the flow. The values were pump flow values and were measured, in case of primary and THP sludge, before the pipe branched to the different digesters. The operators explained that pump flows differed from usual flow values and that this pump flow should not be divided over the number of digesters in use. However, if this would be done, although the ratio between the digesters might be different, the average dry solid contents would be 5.43 which was closer to the measured average values behind the venturi.

Sludge	Flow (m^3/h)	y_i	ds (%)
Digested	48.8	0.80	5.093
Primary	5	0.082	4.86
THP	7	0.12	12.72
Average			5.96

Table 4.3.1: Flows and average dry solids content of the three sludge streams when sampling on the 21th of June 2017.

Point	ds %
Wall 1	5.1
Quarter 2	5.11
Centre 3	5.15
Quarter 4	5.15
Wall 5	5.23

Table 4.3.2: Measured average dry solids content on the 21th of June 2017.

Chapter 5

Conclusion & Discussion

The goal of this assignment was to improve the mixing of sludge in the pipeline entering the digester. Based on the dry solids content measurements and the CFD modelling the Venturi D40 appeared to mix best. However, as CFD modelling was found to be a very delicate matter this conclusion was drawn with a great deal of caution.

Conclusions of and remarks on several parts of the assignment are treated.

Viscosity measurements

Two viscosity data sets were considered for fitting a non-Newtonian model to describe the viscosity of the three sludge types, one measured by the TU Delft and another one measured at WVS. The measurements of the TU Delft were chosen for fitting as the viscosity was measured over a broad shear rate range, encompassing both the laminar and turbulent flow regimes, and the rheometer measured absolute values of the viscosity which did not have to be converted.

A power law model was assumed as non-Newtonian model for the three sludge types and was fitted on the viscosity measurements of the TU Delft of December 2016, see table 4.1.18 for the fitted values of the parameters k and n and the fitted models and data points in the plot of figure 4.1.19. It should be noted that the viscosity measurements for higher shear rates of primary sludge showed a large fluctuation due to its inhomogeneous structure. The power law model was chosen as the whole bandwidth of shear rates had to be taken into account because of both laminar and turbulent flow regimes, no distinct upper or lower limit of the viscosity was visible and the yield stress was not relevant as a function of the viscosity was required as input of the CFD model.

Using the fitted power law models as a prediction for more recent viscosity measurements of the TU Delft of June 2017 they gave a good prediction of these data points. Hence, the predictability of the fitted power law models was satisfactory.

The samples of the two measurements performed by the TU Delft differed slightly in dry solids content. As the fitted power law model of the first measurements was able to describe the second data set well, this formed an indication that the variation in dry solids content might be of lesser influence on the viscosity.

All measurements of the TU Delft were done at 40 °C and the influence of temperature on viscosity was neglected in fitting a non-Newtonian model. Because of the measurements at constant speed performed at WVS, see figure 4.1.8, the validity of this assumption is questioned. The viscosity measured at constant speed showed quite some difference for primary sludge at two different temperatures.

Physically unrealistic values of the viscosity in the CFD model were achieved such as 8063 Pa·s in the venturi D40 model. Hence, a model such as the Cross or Carreau model with an upper limit of the viscosity would possible describe the physics in the CFD model better.

The volume-weighted-mixing law was assumed for the mixing of the densities of the sludge mixture in the species transport model and the mass-weighted-mixing law for the mixing of the viscosity. Using the second data set of the TU Delft measured in June 2017 these mixing laws were successfully validated. Note however that the sample taken behind the venturi, which was not used for validation, showed a lower viscosity which hinted at a memorised history of shear rates by the sludge.

Geometry

The geometry of the models was based on the second situation described in section 3.2.1. The adjustments of the third situation were not taken into account. These encompassed pipes of another material with a larger diameter, and another arrangement with some other junctions.

A broader diameter would result in a lower velocity of the streams if the flow values are kept constant. Because of the different outcomes of the venturi models (Model 2 and Model 5), this lower velocity might result in a decline of the mixing after the venturi. However, the flow of the sludge streams fluctuated somewhat over time and some indistinctness existed about what inlet values should be assumed regarding the flow values, see section 4.3.2 and table 3.2.13. So caution is recommended with respect to the flow values and the geometry of the venturi.

The 90 degree junction between the combination of primary and THP sludge, and digested sludge was replaced by a 45 degree junction. As, also for higher flow speeds, hardly any mixing took place between primary and THP sludge after the 45 degree junction, it is expected that the replacement of the 90 degree junction will not improve the mixing. Nevertheless, if the venturi D40 mixes the sludge indeed satisfactory, this should not be of importance.

Mesh

Because of the limitations on computational time and effort and the limited number of cells which could be solved using the academic license of ANSYS, a coarser mesh with lower quality was used. Although the quality was still considered acceptable compared to the recommended values of the skewness and orthogonal quality by ANSYS, it is plausible that the quality was not sufficient for the geometry and models used to ensure good convergence and a numerical solution with enough accuracy.

Physical Models

Determining the discretization error of the baseline and venturi D40 model, the numerical solution appeared to be to some extent mesh dependent, in particular for the venturi D40 model. This might be due to the $k-\varepsilon$ model being too sensitive for the turbulence generated behind the venturi D40 and therefore not able to resolve the turbulent flow well.

It was not possible to include the virtual mass force and the pressure gradient force in the discrete model. This might be caused by the academic license of ANSYS. Because the densities of the sludge streams and the solid sludge particles were of the same order, it was recommended to include these forces. Henceforth, the particle tracks might be different to some extent when these forces were included.

Considering the results of the mass fractions, which were used in the species transport to model the mixing, and the particle tracks a good resemblance was noticed between the two. Many particles of one sludge type being present in regions with high mass fractions of that particular type and few particles present in regions with a low mass fraction. So the species transport model and the discrete model were in good agreement.

The wall roughness was not taken into account. A short run was done with Model 2 - Venturi, digested sludge and a wall roughness height of 0.3 mm and a constant of 0.5 to see what the influence would be. The wall roughness seemed in this case to be of hardly any influence. As the surface finishing and roughness of the pipes on site were unknown it was neglected. Wall roughness would likely enhance the mixing, so the predicted mixing by the models might be lower than the actual mixing in practice.

Results of Models

Strange differences were noticed between the mass fractions of THP and primary after the 45 degree junction in the first two models and the last three models. The same settings were used and it was expected that the mass fractions would be the same at that point as the geometry was the same for all models ahead of and behind that junction. However, there appeared to be more mixing in the first two models than in the other models.

The average mass fractions of the three sludge streams at the outlet differed from the expected average based on the inlet flows. This might be because the solution was time-dependent and hence at some moments in time more sludge of a certain type exited the outlet than at other moments in time. A large difference between the average mass fraction and the expected average might be an indication that the sludge was not mixed sufficiently.

Based on the particle tracks and mass fractions the venturi D40 model seemed to achieve sufficient mixing, whereas all the other models did not. However, the pressure drop was very high and this has a negative influence on the durability of the pumps.

Discretization Error

The discretization error was determined using a coarser and finer mesh for both the baseline and venturi D40 model. The flow of the baseline model exhibited some change between the different meshes, but convergence was visible with smaller mesh size for the density and viscosity.

However, for the venturi D40 model the solution was grid dependent and the key variables showed great variation between the different meshes. No consistent development could be distinguished for smaller mesh sizes. Several factors might have contributed to this.

As already stated, the $k-\varepsilon$ turbulence model might be too sensitive for the turbulence generated in the models. More turbulence was generated by the venturi than in the baseline model and hence the sensitivity of the $k-\varepsilon$ model had more impact on the solution of the venturi D40 model.

Another possibility could be that no steady solution exists, in particular behind the venturi.

The discretization error was not determined for the other models. Because of the mixed results of the baseline and venturi D40 model, it could not be said beforehand how reliable and accurate the solutions of the other models were.

Other Errors

User errors could not be excluded. In spite of careful checking all the settings and parameters in each simulation, a setting could be missed due too the many settings and acts which need to be set and performed for every simulation. This might explain the different mixing of THP and primary sludge in the first two and last three models, although the settings were checked retrospectively and found to be the same.

Validation

The pressure drop over the venturi D40 was measured on site and compared to the model. The pressure drop on site was about 1.0 bar and in the model 1.33 bar. However, taking the results of the other meshes of the venturi D40 model into account, which were calculated in order to determine the discretization error, the pressure drop was about 0.55 bar for the coarse mesh and 0.93 bar for the fine mesh. The differences between the meshes were great and hence the model could not be validated on pressure.

The dry solids content of five samples taken over the diameter behind the venturi were measured. These varied between 5.1 and 5.23 %, which would indicate a sufficiently mixed sludge mixture. However, the measuring error was not known, so it could not be said with certainty whether these measurements indeed showed that the mixture is sufficiently mixed.

Chapter 6

Recommendations

Some recommendations are made to improve the CFD model and hence the accuracy of the solutions of the mixing achieved by the models. Other recommendations are made on alternatives to improve the mixing.

Viscosity Measurements

Because the temperature seemed to be of significant influence on the viscosity, see figure 4.1.8, it is recommended to take it into account when fitting a non-Newtonian model. In order to do so more viscosity measurements should be performed over a range of shear rates at different temperatures.

In a future phase a strain press might be placed to filter the primary sludge before it is mixed with THP and digested sludge. This sieving will likely have the result that less maintenance is needed for the equipment but it will also affect the viscosity of primary sludge. Hence, it is recommended to measure the viscosity of primary sludge again when this strain press is realized.

Geometry

A sensitivity analysis on the influence of the inlet velocities on the mixing after the venturi might give relevant results and form a benchmark. Furthermore, small adjustments of the venturi, such as the length or the diameter of the narrowing, seemed to greatly influence the mixing behind the venturi. Therefore an analysis on the dimensions of the venturi is recommended.

The corkscrew and static mixer models gave a swirl to the flow. However, it seemed not enough to achieve sufficient mixing. Usually two helical elements with opposite orientation are used in a static mixer. Therefore, if one of these alternatives would be implemented or further investigated it is recommended to use two loops for the corkscrew with opposite orientation and at least two helical elements.

Mesh

To achieve more accurate results simulations with a finer mesh are advised.

Physical Models

The most important recommendation would probably be to choose a more suitable turbulence model, as the $k-\varepsilon$ model did not seem able to fully resolve the generated turbulence behind the venturi D40.

Because the virtual mass force and pressure gradient force were recommended to include in the discrete model, but these were not available, it would be advised to do so in another CFD package or with another ANSYS license to see whether this has a significant impact on the particle tracks.

The wall roughness might enhance mixing, although it is expected that the effect is small. To determine whether this really is the case the wall roughness should be measured on site and included in the model.

Numerical Methods

The pressure-based solver with the PISO algorithm and under-relaxation factors seemed to give sufficient convergence. However, the density-based solver or the pressure-based solver using the 'Coupled' algorithm might give better convergence. This could be investigated, together with the influence of a smaller time step and more iterations per time step using a greater computational power.

The model needs to be initialized. Hybrid initialization was used together with higher velocities during a short time period to speed up the computation. However, it cannot be guaranteed that this will not affect the results.

Alternatives

At another WWTP which also uses THP a pump is used to mix and pump the different sludge streams. This could be an option but would require a reconstruction of current pipelines and pumps.

Another option would be to create a small mixing tank with a mechanical mixer. However, this requires a lot of energy.

References

Ancheyta, J. (2013). *Modeling of processes and reactors for upgrading of heavy petroleum.* CRC Press.

ANSYS. (2013a). *Ansys fluent theory guide, release 15.0.* Inc. ANSYS.

ANSYS. (2013b). *Ansys fluent user's guide, release 15.0.* Inc. ANSYS.

ANSYS. (2014). *Ansys convergence monterrey.* (`http://www.grupossc.com/ponencias/ponencia_39114164442.pdf`, Presentation of Ansys Inc. on Best Practices for Meshing. Retrieved at 2017-06-14.)

Bakker, A. (2006). *Lecture 10 - turbulence models.* (`http://www.bakker.org/dartmouth06/engs150/10-rans.pdf`, Presentation of Lecture 10 of Applied Computational Fluid Dynamics at Dartmouth College. Retrieved at 2017-06-08.)

Barnes, H., Hutton, J., & Walters, K. (1989). *An introduction to rheology.* Elsevier.

Baroutian, S., Eshtiaghi, N., & Gapes, D. (2013). Rheology of a primary and secondary sewage sludge mixture: Dependency on temperature and solid concentration. *Biosource Technology*, *140*, 227-233.

Bechtel, T. (2003). Laminar pipeline flow of wastewater sludge: Computational fluid dynamics approach. *Journal of Hydraulic Engineering*, *129(2)*, 153-158.

Cao, X., Jiang, Z., Cui, W., Wang, Y., & Yang, P. (2016). Rheological properties of municipal sewage sludge: dependency on solid concentration and temperature. *Procedia Environmental Sciences*, *31*, 113-121.

Celik, I., Ghia, U., Roache, P., & Freitas, C. J. (2008). Procedure for estimation and reporting of uncertainty due to discretization in cfd applications. *Journal of Fluids Engineering*, *130*, 7.

Chhabra, R., & Richardson, J. (2008). *Non-newtonian flow and applied rheology (2nd ed.).* Elsevier.

Dammel, E., & Schroeder, E. (1991). Density of activated sludge solids. *Water Research*, *25(7)*, 841-846.

Delft, T. (2008). *Afvalwaterbehandeling - civiele gezondheidstechniek - ct3420.* Author.

Endress+Hauser. (2017). *Flow measuring technology for liquids, gases and steam - products and services at a glance.* Author.

Eshtiaghi, N., Markis, F., Yap, S., Baudez, J., & Slatter, P. (2013). Rheological characterisation of municipal sludge: A review. *Water Research*, *47*, 5493-5510.

Flexim. (2017a). *Flexim flowmeter fluxus f601 - arrangement on site.* (`http://www.introl.pl/upload/catalog/gallery/GAL3e7ba70a1099903f988b0fd5dfb90310.jpg`. Retrieved at 2017-07-07.)

Flexim. (2017b). *Technical specification of fluxus f601.* Author.

Garakani, A. K., Mostoufi, N., Sadaghi, F., Hosseinzadeh, M., Fatourechi, H., Sarrafzadeh, M., & Mehrnia, M. (2011). Comparison between different models for rheological characterization of activated sludge. *Iran Journal Environmental Health Science and Engineering*, *8*(3), 255-264.

Isco. (2017a). *Hot tap - pulse doppler insertion flow meter.* TELEDYNE ISCO.

Isco. (2017b). *Isco hot tap - 3d picture.* (`http://img.directindustry.com/images_di/photo-g/22360-2842677.jpg`. Retrieved at 2017-07-07.)

Isco. (2017c). *Isco hot tap - sensor.* (`http://www.technoaqua.cz/cache/images/senzor-prutokomeru-hottap_resize_600_600.jpg`. Retrieved at 2017-07-07)

ITS. (2017). *Dens-itometer for dredging - product brochure.* Industrial Tomography Systems.

Kundu, P., Cohen, I., & Dowling, D. (2012). *Fluid mechanics (5th ed.).* Elsevier.

Kuzmin, D. (2010). *Introduction to computational fluid dynamics.* (`http://www.mathematik.uni-dortmund.de/~kuzmin/cfdintro/lecture1.pdf`, Presentation of Lecture 1 at University of Dortmund. Retrieved at 2017-06-07.)

Marshall, E., & Bakker, A. (2002). *Computational fluid mixing.* Fluent Inc.

MathWorks. (2017). *Evaluating goodness of fit.* (`https://nl.mathworks.com/help/curvefit/evaluating-goodness-of-fit.html`. Retrieved at 2017-07-03.)

Mitschka, P. (1982). Simple conversion of brookfield r.v.t. readings into viscosity functions. *Rhologica Acta*, *21*, 207-209.

Patil, K. (2009). *Mechanical operations fundamental principles and applications (enlarged and revised 2nd edition.* Nirali Prakashan.

Pharmacopoeia, E. (2008). *European pharmacopoeia (6th edition).* European Union.

Primix. (2017). *Primix bv - pms mixing element.* (`https://www.primix.com/images/products/static_mixers/pms_mengelement.jpg`. Retrieved at 2017-06-27.)

Rudman, M., Graham, L., Blackburn, H., & Pullum, L. (2002). *Non-newtonian turbulent and transitional pipe flow.* (`http://users.monash.edu.au/~bburn/pdf/Hy15.pdf`, 15th International Conference Hydrotransport, Banff)

Sahin, S., & Sumnu, S. (2006). *Physical properties of food.* Springer.

Sanin, F., Clarkson, W., & Vesilind, P. (2011). *Sludge engineering: The treatment and disposal of wastewater sludges.* DEStech Publications.

Singh, R., & Heldman, D. (2014). *Introduction to food engineering (5th edition).* Elsevier.

Slater, J. (2008). *Uncertainty and error in cfd simulations.* (`https://www.grc.nasa.gov/www/wind/valid/tutorial/errors.html`. Retrieved at 2017-06-15.)

Turovskiy, I., & Mathai, P. (2006). *Wastewater sludge processing.* Wiley-Interscience.

Vechtstromen, W. (2013). *Luchtfoto waterberging westermaat rwzi hengelo.* (`https://www.vechtstromen.nl/publish/pages/17949/20130701_luchtfoto_waterberging_westermaat_rwzi_hengelo_bijgesneden.jpg`. Retrieved at 2017-05-18.)

Appendix A

Assignment in a Context

This appendix contains my experiences as trainee with Witteveen+Bos.

A.1 Witteveen+Bos

Witteveen+Bos is an engineering and consultancy firm with its head offices located in Deventer, the Netherlands. It was founded in 1946 by Sir Witteveen and Sir Bos in Deventer where their first project was located, namely the construction of the Prins Bernhard lock. Its attributes are: expert, reliable and committed. Witteveen+Bos now operates in countries all around the world with more than 1000 employees working at offices located in the Netherlands, Belgium, Latvia, United Kingdom, Ghana, Kazakhstan, Russia, Dubai, Indonesia, Singapore and Vietnam.

The firm is divided in four business lines, or sectors in Dutch, namely 'Built environment', 'Deltas, coasts and rivers', 'Energy, water and environment' and 'Infrastructure and mobility'. These sectors are divided in so called Product Market Combinations (PMCs) for example Wastewater, Urban Development, Smart Infra Systems and Ecology. These PMCs are again divided in several groups. Each sector, PMC and group has a leader who manages but works on projects as well to keep in touch with the work done by employees. The ownership of Witteveen+Bos is in hands of its employees as shareholders. In this way it is aimed to stimulate entrepreneurship and commitment.

Mechanical engineers work in several sectors of Witteveen+Bos. In the sector 'Infrastructure and mobility' they work at ventilation, steel structures, locks, bridges and pumping stations. In the sector 'Built environment' they work at heating, ventilation and cooling. Most mechanical engineers work in the Drinking and Wastewater groups of the sector 'Energy, water and environment'. Currently the drinking and wastewater groups have about seventeen employees of which most are located in Deventer at the Van Twickelostraat and some are detached, for example at the WWTP in Utrecht which is currently under construction. The work consists for example of drawing Process & Information Diagrams (P&IDs) for adaptations of drinking water facilities, making offers to win new projects such as designing a new WWTP and consulting with suppliers to see which boiler would be best to place at a plant.

A.2 My Experience at Witteveen+Bos

In January 2017 I contacted Mark van der Werf, group leader of Wastewater, to see whether there was an opportunity to do my internship at Witteveen+Bos. The impact of its projects on society and the environment motivated me to do this. In a few weeks I was able to begin with my internship.

Contact with Colleagues

The first day I had a tour in the Van Twickelostraat to meet my new colleagues. I had a warm welcome! A lot of people were interested in my assignment, were already informed to some extent about the contents and offered help. My mechanical engineering colleagues also assisted in matters such as arranging a laptop standard and access to internet or whom to contact when the power box burned out when I plugged my laptop into it.

My desk was located in a room, or hallway, called the 'Tussenzaal' with about ten other desks. So I learned quite a lot about what my colleagues did by overhearing their conversations and phone calls. And during the daily lunch walk I had time to get to know them better.

In addition, I joined activities such as the family day of Witteveen+Bos to the zoo in Emmen together with my husband and a BBQ with the mechanical engineers of the waste and drinking watergroups.

Content of the Assignment

At the start my focus was at searching a suitable validation instrument and learning to use the CFD software. It was important that the measuring instrument was determined in the first part of my internship because it was expected that some time would be spend on making an application for the water board, having it approved, installing the instrument and performing measurements. Therefore it turned out for the better that I worked four days a week for a longer period of time than five days a week.

Because I had to contact suppliers I was given a mobile phone. With one supplier I arranged a meeting to explain the problem and investigate whether they had the right material to offer. Finally, an ultrasonic flow meter of Flexim seemed to be best suitable and hence I wrote an application for the water board. A meeting was arranged and together with the operators and the employees of the water board it was decided to make a sampling point instead.

One of my biggest struggles was to learn to use a CFD software package. Knowledge of CFD was hardly present in the group, so I had to contact Arie de Niet who used CFD modelling in the sector 'Deltas, coasts and rivers'. He could help me to some extent, but was during that period busy with other projects.

I struggled with communication and decision making between me, the water board and the operators. It took a long time to decide whether additional viscosity measurements would take place and whether this would be done by WVS or TU Delft. Also it took a long time till the validation measurements could be done and only one of the venturi geometries could be validated. The operators were very busy at that time because many processes and adjustments were going on. In communication I had trouble finding the right person to tell me the right parameter values for the model, such as the flow values. Also the geometry on site was changed multiple times.

It was surprising for me that I could finish my internship in time, including a validation measurement and analysing the additional viscosity measurements.

Other Things I did at Witteveen+Bos

I visited the WWTP in Hengelo several times to see the situation myself, to measure the viscosity of sludge with the viscometer of WVS, to join an excursion of UT students and give a presentation on my internship. Two digesters were empty and one was cleaned. I entered this one twice, once from the top and once from the bottom wearing a special protective suit.

Furthermore I joined an excursion to the ultra pure water factory in Emmen were Witteveen+Bos designed an installation to produce ultra pure water for the collection of oil. And I joined an excursion to Utrecht were Witteveen+Bos cooperates in the building of a new WWTP next to the existing one. Also, I attended meetings of the wastewater group.

Moreover, I attended lunch lectures and I gave a lunch lecture after my internship about the results. Additionally, I gave a teaser at a meeting of the technology group to stimulate people to come to my presentation.

At the moment the water board was investigating several mixing options for the digester in cooperation with Tauw, who performed CFD modelling of these options in the digester. I attended several meetings and was able to give some input. During one of the last weeks I gave a presentation to inform the water board of the preliminary results.

My Working Experience at Witteveen+Bos

My research was quite stand-alone and in that view exceptional for how they work and what they do as mechanical engineers at Witteveen+Bos. There was nobody else who did literature study and research in this group.

I would describe the ambiance in the group as open and friendly. The working atmosphere is good: there is time for a short personal talk, for example during birthday treats, but quite quickly everyone goes back to work. There is a lot of cooperation between colleagues and so far I have not experienced competition within the group, which I really appreciate. Managers and leaders of groups also work on projects, and do not just do paper work and delegation.

Short connections are important. Working from home was discouraged as face-to-face contact was preferred above e-mail. I noticed the importance of personal contact also in the high amount of phone calls. As a commercial company it is very important to obtain offers and work as much claimable hours as possible.

A positive thing at Witteveen+Bos I found that there are bikes and cars available for borrowing. I borrowed a car several times because the WWTP in Hengelo is not easily reached by public transport.

The company is internationally oriented. We had a colleague from Kazachstan visiting for a project and also joining the excursions to Utrecht and Emmen.

For now I would like to continue doing research, but I truly recommend Witteveen+Bos as employer!

Appendix B

Analysis of Viscosity Measurements

In this chapter the mathematical procedure for converting relative viscosity values to absolute viscosity values is presented. Furthermore, fits of the non-Newtonian power law model on the WVS measurements are given and compared to the fits of the TU Delft.

B.1 Converting Relative Viscosity to Absolute Viscosity

In subsection 3.1.3 the mathematical procedure for converting relative apparent viscosity values to absolute viscosity values as presented in Mitschka (1982) was outlined. In this section it is applied to the measurements done at the Brookfield viscometer DV2T at WVS.

The first step was to measure the torque α_i (%) at different rotational speeds N_i (rpm). This data is depicted in figure B.1.1.

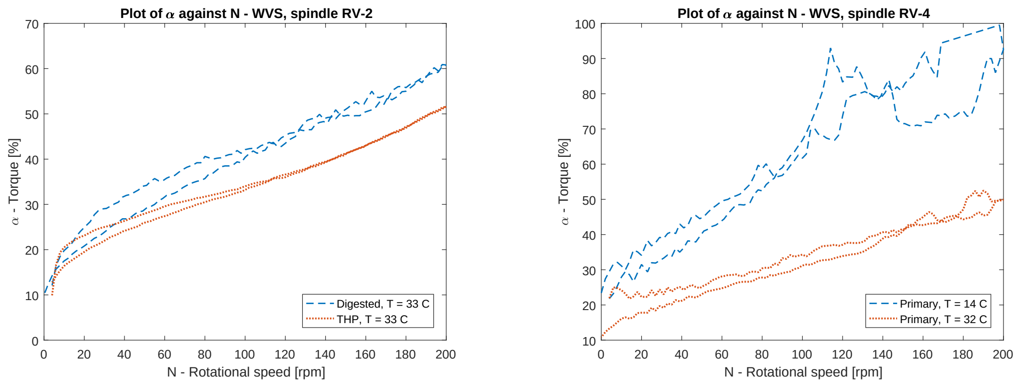

(a) RV-2: Digested (5.7 % ds, 33 °C), THP (9.5 % ds, 33 °C)

(b) RV-4: Primary (6.3 % ds, 14 °C), Primary (6.3 % ds, 32 °C)

Figure B.1.1: Plots of the torque α against the rotational speed N measured at WVS.

The next step was to multiply the torque with a constant $k_{\alpha\tau}$ to convert it to shear stress (Pa). The values of $k_{\alpha\tau}$ for the spindles used can be found in table B.1.4. In figures 4.1.10, 4.1.11 and B.1.2 respectively loglog plots of the shear stress and the viscosity against the rotational speed and a plot of the viscosity against the rotational speed are displayed.

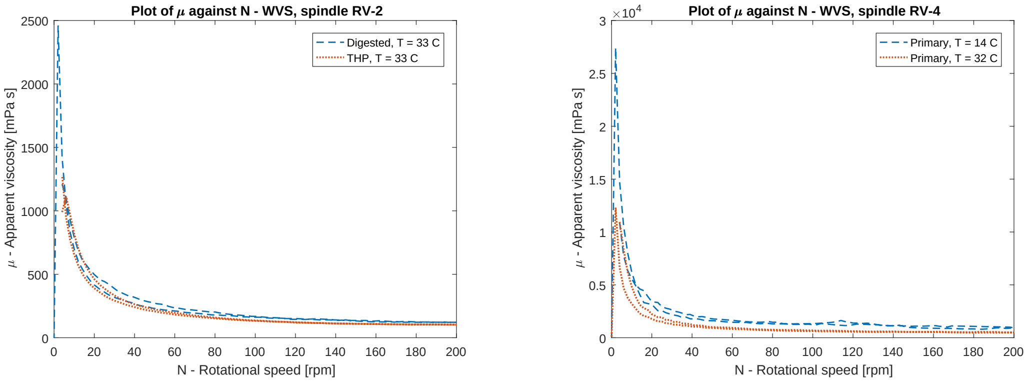

(a) RV-2: Digested (5.7 % ds, 33 °C), THP (9.5 % ds, 33 °C)

(b) RV-4: Primary (6.3 % ds, 14 °C), Primary (6.3 % ds, 32 °C)

Figure B.1.2: Plots of the apparent viscosity μ against the rotational speed N measured at WVS.

The third step was to convert the rotational speed to shear rate. In order to do this the relation between the shear stress τ and the rotational speed N must be determined on a loglog scale. Only the first part of the speed ramp was taken into account, namely the viscosity and shear stress measured when turning up the speed. For all types of sludge a linear relation was assumed by fitting a polynomial of order one, and a non-linear relation by fitting a smoother curve, namely a polynomial of order three, see figure B.1.3.

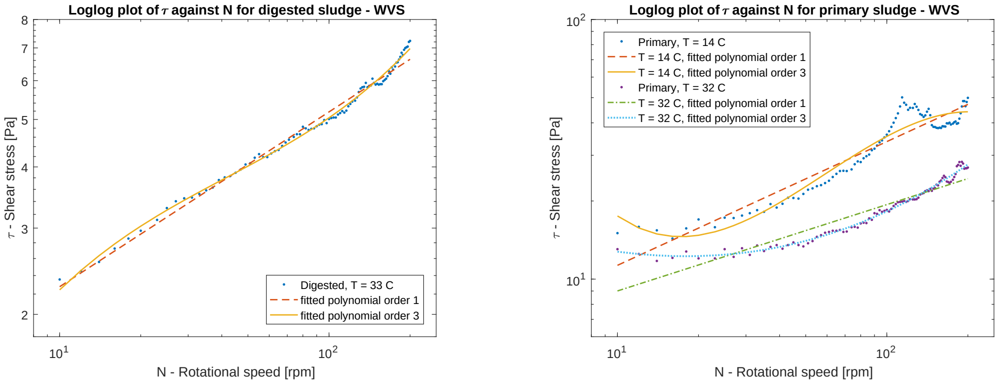

(a) RV-2: Digested (5.7 % ds, 33 °C)

(b) RV-4: Primary (6.3 % ds, 14 °C), Primary (6.3 % ds, 32 °C)

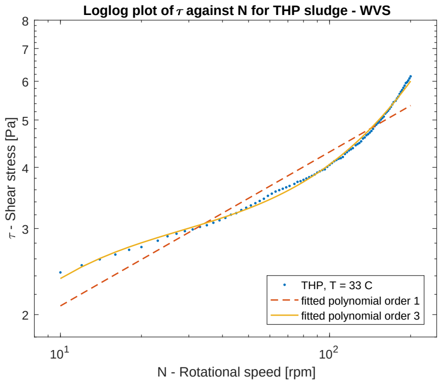

(c) RV-2: THP (9.5 % ds, 33 °C)

Figure B.1.3: Loglog plots of the shear stress τ against the rotational speed N with two fitted polynomials for all types of sludge.

Spindle		RV-2	RV-4
$k_{\alpha\tau}$		0.119	0.539
$k = N\gamma$	$n =$ 0.1	1.431	1.492
	0.2	0.875	0.892
	0.3	0.656	0.658
	0.4	0.535	0.529
	0.5	0.458	0.445
	0.6	0.404	0.387
	0.7	0.365	0.343
	0.8	0.334	0.310
	0.9	0.310	0.283
	1.0	0.291	0.262

Table B.1.4: Conversion factors for the spindles of the Brookfield viscometer DV2T Mitschka (1982).

The shear rate γ_i was calculated by multiplying the rotational speed N_i with a constant $k_{N\gamma}$. This constant depended on the spindle used and the direction coefficient n'_i of the curve at point i. Values for this constant can be found in table B.1.4. Because there are only values of the constant given for multiples of 0.1 an interpolation was done.

A power law function was fitted on the values of n, see figure B.1.5 for the plots and table B.1.6 for the values of the parameters of the power function.

The shear rate γ_i could now be determined by calculating the slope of the first and third order polynomial, n_i', fitted on the loglog scale of τ and N, substituting this in the power function of $k_{N\gamma}(n_i) = an_i^b$ and multiplying the rotational speed N_i with this constant. The pairs of $\tau_i - \gamma_i$ and $\mu_i - \gamma_i$ were now assumed to be of the viscosity function. Plots of these pairs can be found in section 4.1.3.

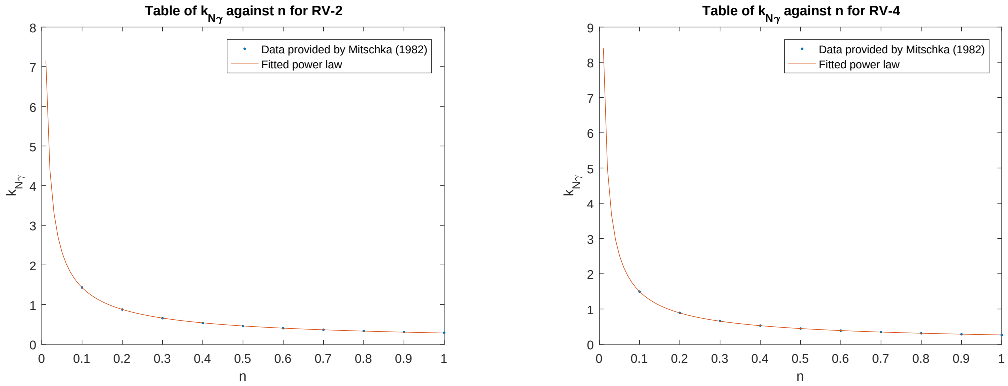

(a) Power law for RV-2.

(b) Power law for RV-4.

Figure B.1.5: Plots of the power law fitted on the values of $k_{N\gamma}$ and n as provided in table B.1.4.

$k_{N\gamma} = an^b$	RV-2	RV-4
a	0.2833	0.2642
b	-0.7026	-0.7527

Table B.1.6: Values of the parameters of the power law fitted on $k_{N\gamma}$ and n.

B.2 Fitting a non-Newtonian Model on the WVS Measurements

In figures B.2.2, B.2.3 and B.2.4 fits of the non-Newtonian power law model are displayed for both the TU Delft and WVS measurements for respectively digested, primary and THP sludge. In table B.2.1 fitted values for the parameters k and n of the power law model are displayed for all types of sludge.

Sludge	Origin	k	n
Digested	Poly. Order 1	2.4480	0.3451
	Poly. Order 3	2.1770	0.3741
	TU Delft	1.2987	0.3155
Primary	Poly. Order 1, 14 °C	9.3465	0.4765
	Poly. Order 1, 32 °C	3.6111	0.7396
	Poly. Order 3, 14 °C	11.0232	0.3326
	Poly. Order 3, 32 °C	19.5896	0.1366
	TU Delft	7.8853	0.1280
THP	Poly. Order 1	2.4540	0.3149
	Poly. Order 3	9.6697	-0.0620
	TU Delft	3.5219	0.3379

Table B.2.1: Fitted values for k and n of the non-Newtonian power law model for digested, primary and THP sludge for measurements of the TU Delft and WVS.

For digested sludge the fits of the TU Delft and WVS resembled each other closely as can be seen both in table B.2.1 and in figure B.2.2. The slope of the fits $n - 1$ was roughly equal, but the height k differed.

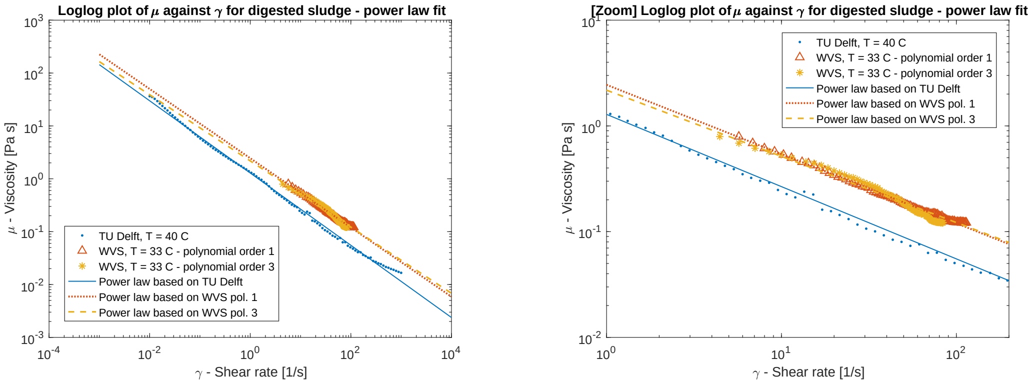

(a) Digested TU Delft: T = 40 °C, 5.3% ds. Digested WVS: T = 33.5 °C, 5.7% ds.

(b) Digested TU Delft: T = 40 °C, 5.3% ds. Digested WVS: T = 33.5 °C, 5.7% ds.

Figure B.2.2: Loglog plots of the power law fitted to the measurements of the TU Delft and WVS for digested sludge.

The fits for primary sludge showed a large deviation in both k and n values among all measurements, see table B.2.1 and figure B.2.3. This was due to the inhomogeneity of primary sludge and a varying composition. The reliability of the measurements was hence restricted.

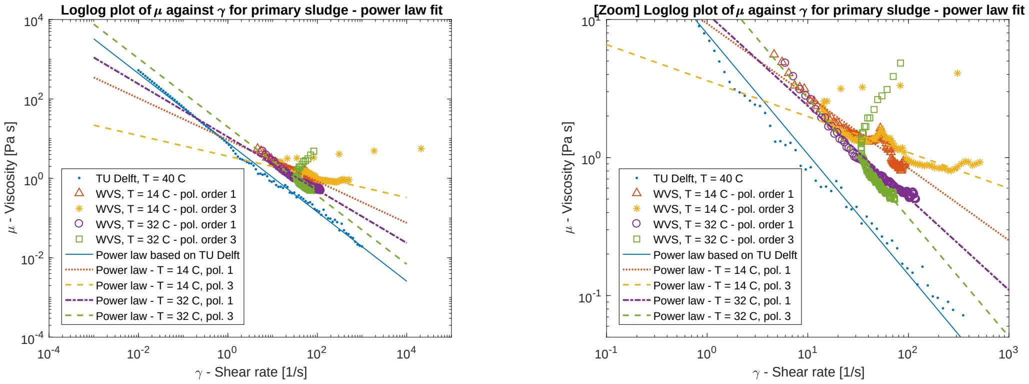

(a) Primary TU Delft: T = 40 °C, 4.2% ds. Primary WVS: T = 14.4 °C, 6.3% ds, and T = 32.0 °C, 6.3% ds.

(b) Primary TU Delft: T = 40 °C, 4.2% ds. Primary WVS: T = 14.4 °C, 6.3% ds, and T = 32.0 °C, 6.3% ds.

Figure B.2.3: Loglog plots of the power law fitted to the measurements of the TU Delft and WVS for primary sludge.

For THP sludge the fits of the first order polynomial of WVS and the TU Delft were quite similar, with the height of the fit k of the TU Delft being slightly larger than the height of WVS, see table B.2.1 and figure B.2.4. However, the third order polynomial of WVS showed large deviations with even a negative value for n.

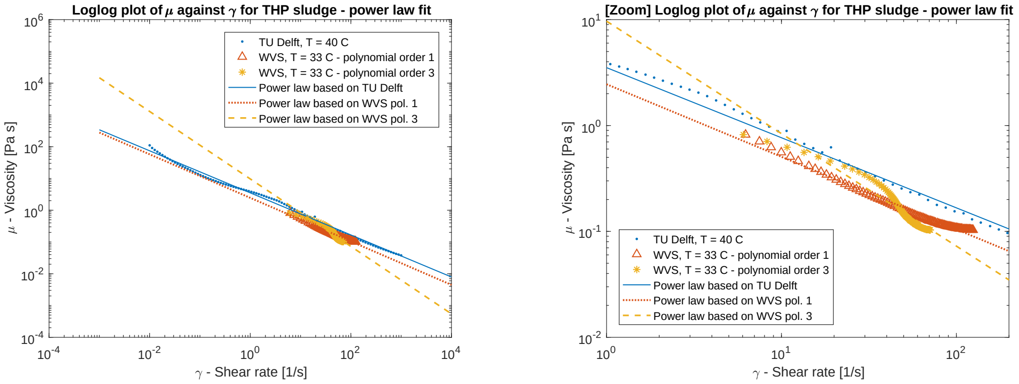

(a) THP TU Delft: T = 40 °C, 11.0% ds. THP WVS: T = 33.4 °C, 9.5% ds.

(b) THP TU Delft: T = 40 °C, 11.0% ds. THP WVS: T = 33.4 °C, 9.5% ds.

Figure B.2.4: Loglog plots of the power law fitted to the measurements of the TU Delft and WVS for THP sludge.

Appendix C

Alternative Geometries

To determine which adjustments of the geometry would result in the best mixing, nine smaller models were simulated. The best two based on effectiveness and realizability were chosen. The models were divided into two categories. The first category contained four models based on adjustments in the arrangement of the pipe geometry, such as bends. These models were all non-invasive. The second category contained five models based on the operation of a static mixer. These models were made non-invasive to prevent clogging, except for one model which is a static mixer element and hence invasive.

C.1 Geometry

All models started with a 0.5 m straight pipeline in order to let the flow develop somewhat in fully developed flow instead of uniform flow.

The first two cases included respectively one and two bends to induce mixing. Their Solidworks models and drawings are depicted in figure C.1.1. It was expected that these were easy to produce and relatively inexpensive. Furthermore, the frequency for which these bends would need maintenance, for example cleaning, was considered to be minimal.

The third case injected the combination of THP and primary sludge downstream in the pipe containing digested sludge. As other geometries comparable to this injection are made more often, it would be a bit more expensive than the bends, but still affordable. The risk of sludge sticking to the stream downwards side of the injection pipe was assumed to be small and hence the frequency of maintenance was assumed to be minimal.

The fourth case was based on a corkscrew. The internal diameter of the corkscrew of the fourth case followed the path of a helix. This helix could be described mathematically by $x = r \cos a, y = r \cos a$ and $z = ct$ with the radius $r = 150$ mm and as one turn is made $0 \leq a \leq 2\pi$, and $c = \frac{1260}{2\pi}$ mm. The Solidworks models and drawings of the third and fourth case are depicted in figure C.1.2. The corkscrew could be produced by welding 45 degree bends, hence it was assumed that it could be realized, but the costs would probably be a bit higher than for the bends and also for the injection case, as pipes like this corkscrew are not often made. The frequency for which the corkscrew would need maintenance was assumed to be minimal.

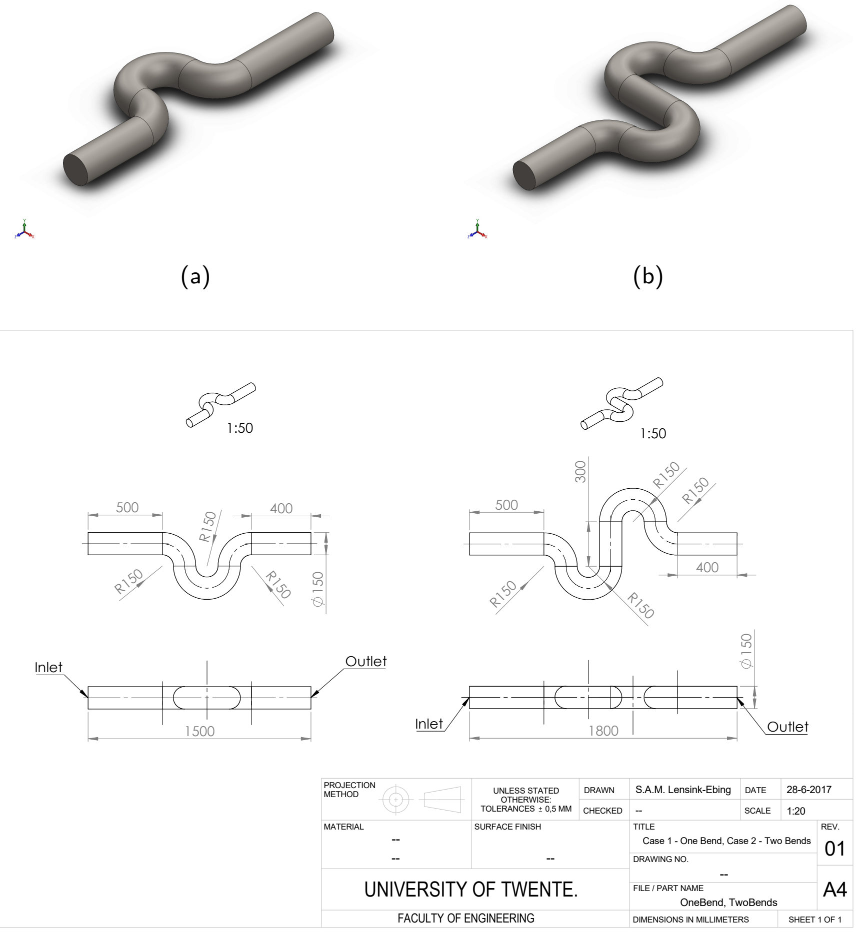

(a)

(b)

(c)

Figure C.1.1: Solidworks model and drawing of Case 1 - One Bend and Case 2 - Two Bends.

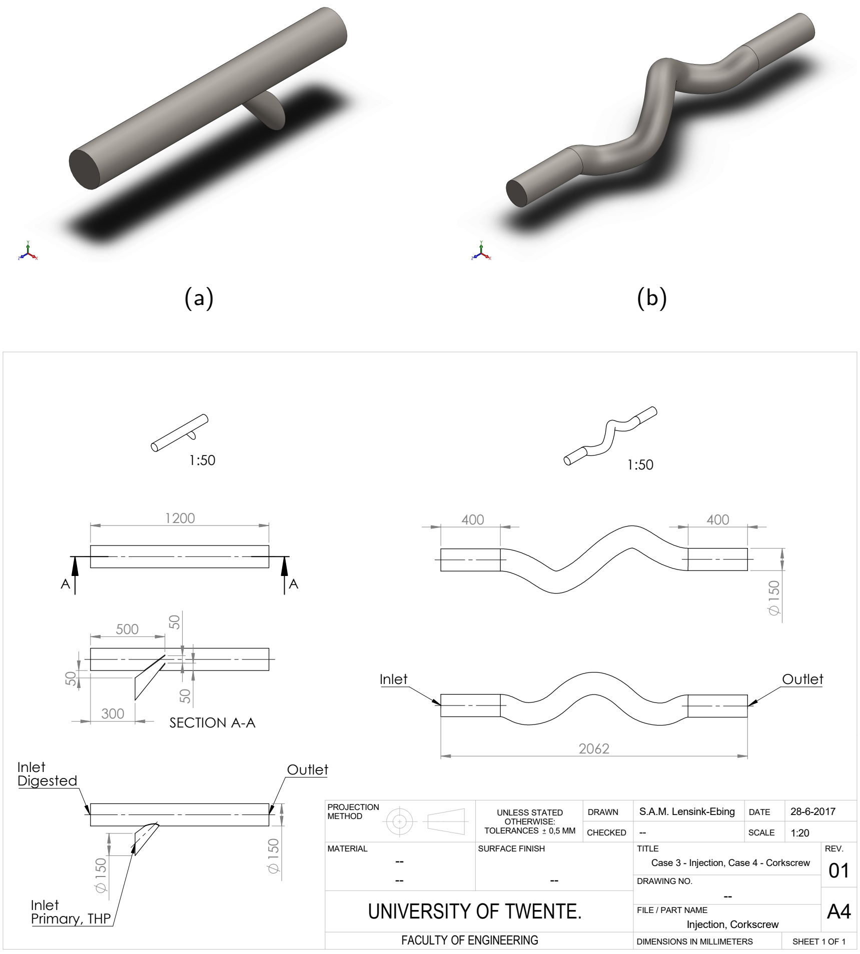
(a)

(b)

(c)

Figure C.1.2: Solidworks model and drawing of Case 3 - Injection and Case 4 - Corkscrew.

The fifth case had notches on its sides to disturb the flow and induce mixing. It was assumed that this one could be realized using a standard pipe and adjusting it. However, the costs would probably be higher than in the case of bends and also higher than the injection pipe of case 3, as notches like these in pipes are not often made. Sludge might stick between the notches, but for now it was assumed that this would be minimal and hence the pipe would not need maintenance often.

Case six had carved curves on the pipe wall to induce swirling of the flow. The Solidworks models and drawings of case five and six are shown in figure C.1.3. The production of this case would probably be difficult and expensive as it might need to be cast as a single piece. The maintenance however was assumed to be minimal as the carving starts and ends smooth and no sharp edges were present for sludge to stick to.

Case seven also had carved curves on its side, but then two in a row with opposite orientation. The production and maintenance were assumed to be of the same kind as Case 6 - Streamlines.

Case eight had one deeper carved curve to disturb the midst of the flow. In figure C.1.4 the Solidworks models and drawings of the seventh and eighth case are depicted. For this case the production and maintenance were also assumed to be of the same kind as Case 6 - Streamlines.

The last case, case nine, was based on a helical element produced by Primix. See for more information section 3.2.2. In figure C.1.4 the Solidworks model and drawing of the ninth case is displayed. The helical element could be produced, but is likely to be more expensive than just bended pipes, but less expensive than single piece cast pipes. The maintenance might be a problem. Primix told that sludge would stick to the element but that it depended on the type of sludge and flow how often the element needed cleaning. The element would be placed on a string which can be taken out, which would make cleaning easier. Because of the inhomogeneity of primary sludge and the high dry solids content it was expected that the element needed to be cleaned quite often to prevent clogging of the pipe. As in the future situation a strain press will most likely be installed to clean and filter the primary sludge, the helical element was still taken into account despite the maintenance problems.

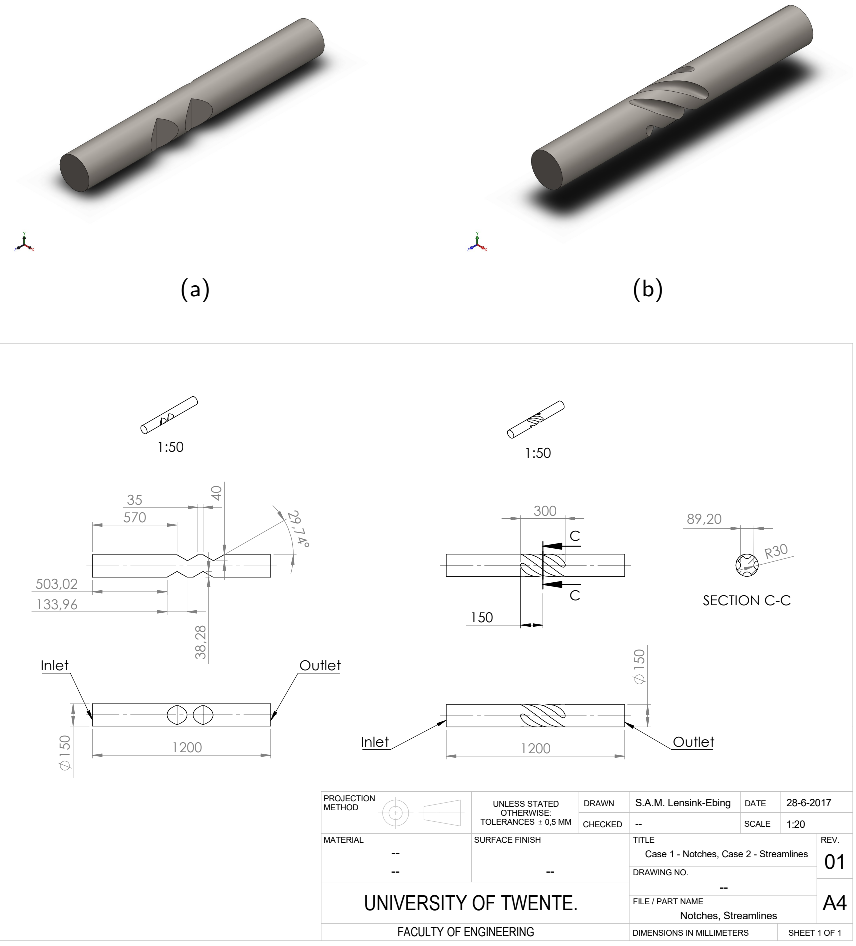

(a) (b)

(c)

Figure C.1.3: Solidworks model and drawing of Case 5 - Notches and Case 6 - Streamlines.

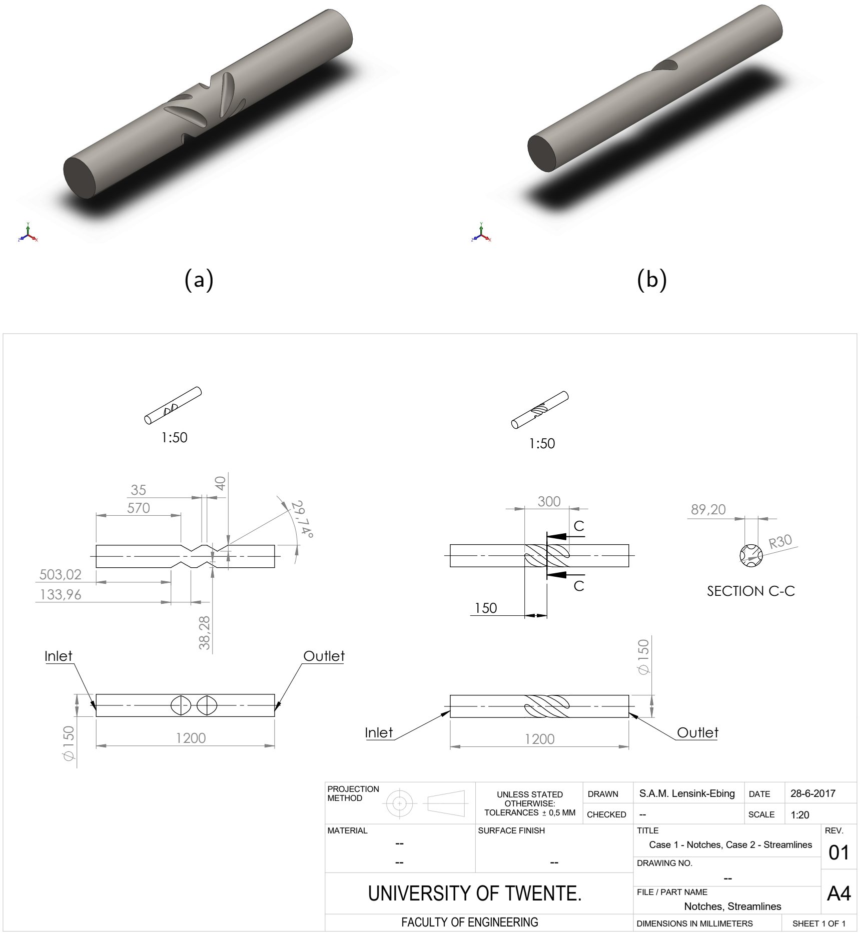

(a) (b)

(c)

Figure C.1.4: Solidworks model and drawing of Case 7 - Opposite Streamlines and Case 8 - One Streamline.

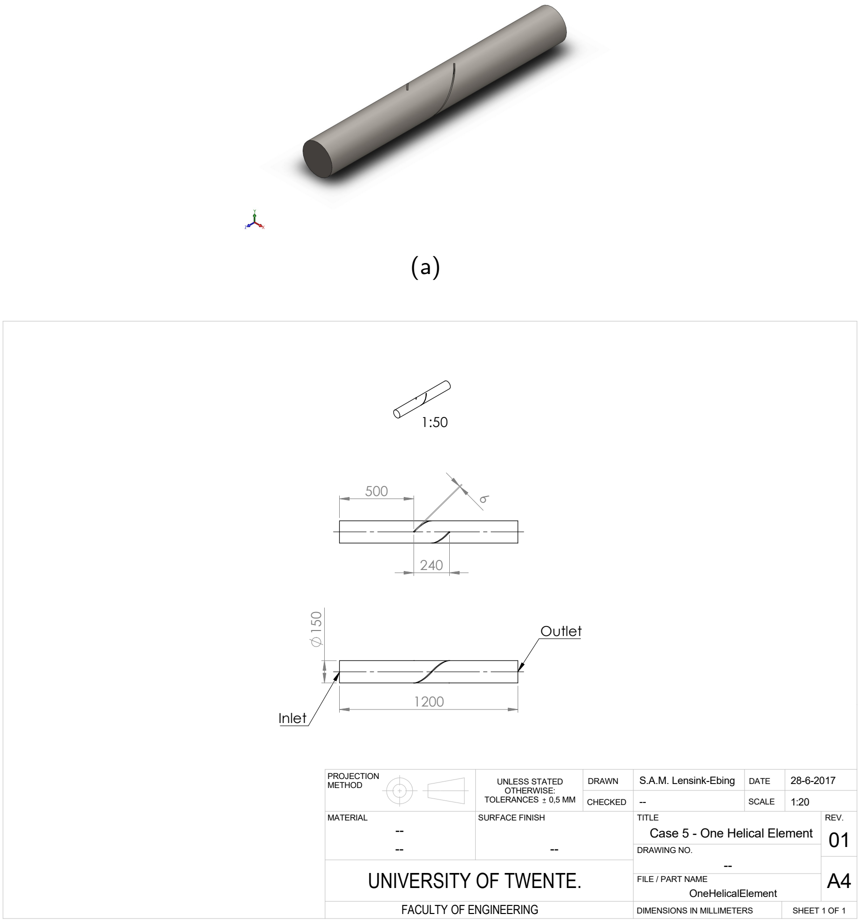

PROJECTION METHOD
UNLESS STATED OTHERWISE: TOLERANCES ± 0,5 MM
DRAWN S.A.M. Lensink-Ebing
DATE 28-6-2017
CHECKED --
SCALE 1:20
MATERIAL -- --
SURFACE FINISH --
TITLE Case 5 - One Helical Element
REV. 01
DRAWING NO. --
FILE / PART NAME OneHelicalElement
A4
UNIVERSITY OF TWENTE.
FACULTY OF ENGINEERING
DIMENSIONS IN MILLIMETERS
SHEET 1 OF 1

(a)

(b)

Figure C.1.5: Solidworks model and drawing of Case 9 - One Helical Element.

C.2 Mesh

Information about the mesh quality is displayed in table C.2.1. These values were obtained from FLUENT with one exception being the skewness, as these values were retrieved from ANSYS Meshing. The maximum values of skewness and the minimum values of the orthogonal quality could be compared with the recommended values by ANSYS described in section 2.4.2. Comparing these it was concluded that the meshes were generally of acceptable to good quality.

Models	# elements	V (m^3)	Orth. Q.	Asp. R.	Skew.
Case 1 - One Bend	32710	$3.217 \cdot 10^{-2}$	0.1784	21.899	0.8920
Case 2 - Two Bends	46375	$4.564 \cdot 10^{-2}$	0.2105	18.095	0.8719
Case 3 - Injection	52983	$2.227 \cdot 10^{-2}$	0.1861	81.125	0.9225
Case 4 - Corkscrew	45343	$4.101 \cdot 10^{-2}$	0.1489	23.491	0.8693
Case 5 - Notches	23646	$2.016 \cdot 10^{-2}$	0.3755	19.566	0.7597
Case 6 - Streamlines	47406	$1.981 \cdot 10^{-2}$	0.2219	33.530	0.8975
Case 7 - Opposite Streamlines	170865	$2.015 \cdot 10^{-2}$	0.2116	24.271	0.8819
Case 8 - One Streamline	39074	$1.987 \cdot 10^{-2}$	0.1805	35.513	0.9749
Case 9 - One Helical Element	133573	$2.074 \cdot 10^{-2}$	0.2582	18.879	0.7920

Table C.2.1: Relevant information about the mesh of the nine smaller models. From left to right the number of elements, the volume of the mesh, the minimum value of the orthogonal quality, the maximum value of the aspect ratio and the maximum value of the skewness.

C.3 Physical Models

Deviations from the physical models discussed in section 3.2.4 are mentioned here. The mean velocity was taken to be 0.89 m/s as it was assumed that the velocities of primary and THP sludge would be around 0.10 m/s and the one of digested sludge would remain 0.79 m/s. For Case 3 - Injection the inlet velocity of primary and THP sludge was 0.10 m/s and the inlet velocity of digested sludge was 0.79 m/s. All models were run with digested sludge, hence no species transport model was used. The discrete model was used as particle tracking was important to determine the quality of mixing.

C.4 Numerical Methods

Deviations from the numerical methods discussed in section 3.2.5 are mentioned here. The settings displayed in table 3.2.16 were used, but the number of time steps differed as the average distance the particles should cover was different between the models.

Final Solution	Number of Time Steps
Case 1 - One Bend	180
Case 2 - Two Bends	580
Case 3 - Injection	580
Case 4 - Corkscrew	380
Case 5 - Notches	180
Case 6 - Streamlines	180
Case 7 - Opposite Streamlines	180
Case 8 - One Streamline	180
Case 9 - One Helical Element	280

Table C.4.1: Deviating number of time steps in the calculation of the final solution from table 3.2.16.

C.5 Analysis & Results

The results were analysed on pressure, velocity and particle tracks. Because of the pump capacity the pressure drop ΔP from inlet to outlet should not be too high. The velocity gave an indication whether the flow was sufficiently disturbed for mixing to take place. Tracking the particles coloured by their ID numbers gave the best indication for mixing.

C.5.1 Case 1 - One Bend

The contours of the pressure and velocity field are displayed in figure C.5.1. The pressure drop in case 1 was 1.06 kPa, which was relatively small and doable for the pumps. A large force was exerted at the pipe wall before the bend and a small area of negative pressure near the wall was present at the end of the bend. As could be seen in the velocity field, the velocity in the inside bend was higher and behind the bend the flow was pushed sidewards.

The particle tracks are shown in figure C.5.2. The particles were coloured by ID and were numbered in concentric circles at the inlet where they were released with light blue particles in the middle, then to the outside light green, yellow, red and dark blue at the wall. It was assumed that for a good mixing the particle colours should be well mixed at the outlet.

In pictures (a) and (b) it could be seen that particles near the wall of the pipe shear over the other particles in the middle and take another path in the first part of the bend. In picture (c) it is clearly noticed that there was symmetry in the ZX-plane. The results of the mixture of the baseline in section 4.2.2 showed that heavier sludge, primary and THP, remained to a great extent at the bottom of the pipe. If there is symmetry in the ZX-plane and those sludges remain below the ZX-plane, no mixing is expected. Furthermore, groups of coloured particles could be distinguished at the outlet, such as a light blue group of particles left, dark blue at the right wall, and red in the middle of the top and bottom. Hence, the sludge was not well enough mixed.

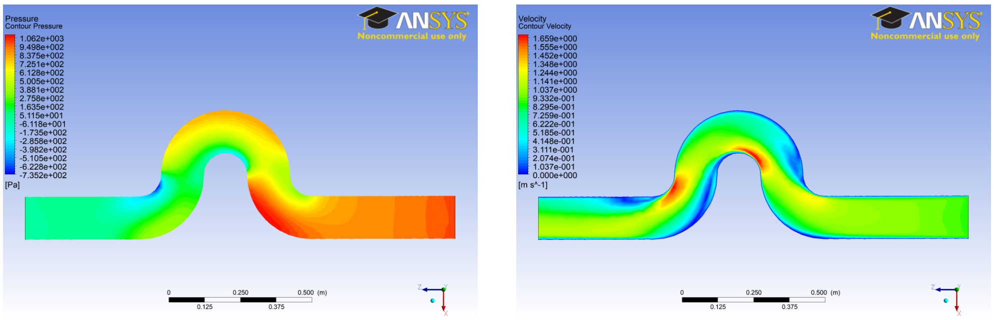

(a) Top view, ZX-plane, $\Delta P = 1.06$ kPa. (b) Top view, ZX-plane, $\max(\vec{u}) = 1.66$ m/s.

Figure C.5.1: Pressure and velocity fields of Case 1 - One Bend.

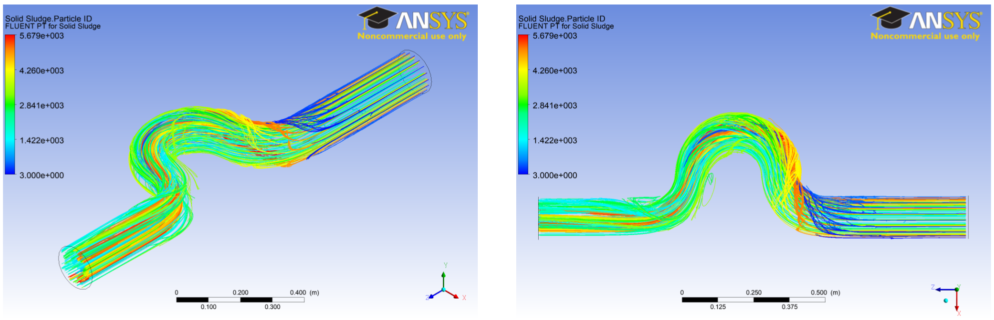

(a) Isometric view. (b) Top view, ZX-plane.

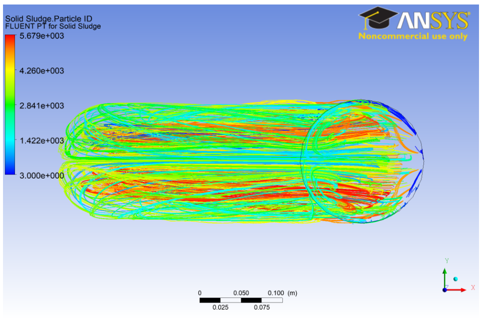

(c) Front view, XY-plane.

Figure C.5.2: Particle tracks coloured by particle ID number of Case 1 - One Bend.

C.5.2 Case 2 - Two Bends

The pressure drop in the case of two bends was a bit higher than with one bend, namely $\Delta P = 1.32$ kPa, but the pipe was also longer, see figure C.5.3 (a). Still the pressure drop was relatively small. A large force was exerted on the pipe wall starting the first bend. The forces on the walls in the two bends were smaller. A small area of negative pressure was present at the end of the last bend. As can be seen in figure C.5.3 (b) the flow was bended by the bends, and was pushed sidewards before the outlet, to the other side compared to the case of one bend.

Just as in the case of one bend, particles near the wall sheared over the particles in the middle to another path, see the pictures in figure C.5.4. There was again a symmetry in the ZX-plane and at the outlet likewise coloured particle groups could be discerned, although a little more mixed than with one bend. However, the sludge was not sufficiently mixed.

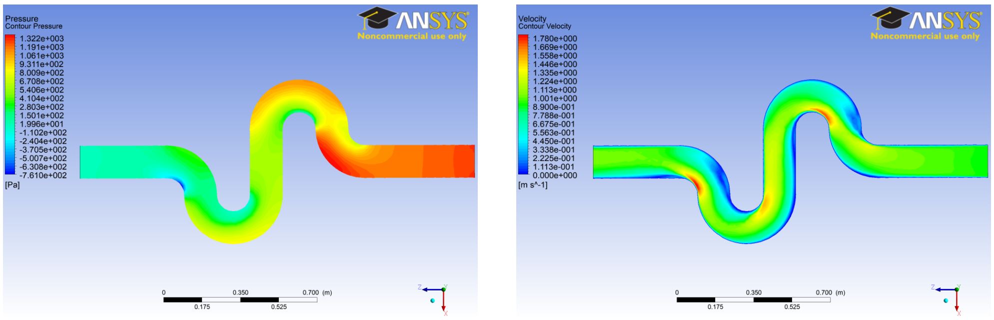

(a) Top view, ZX-plane, $\Delta P = 1.32$ kPa. (b) Top view, ZX-plane, $\max(\vec{u}) = 1.66$ m/s.

Figure C.5.3: Pressure and velocity fields of Case 2 - Two Bends.

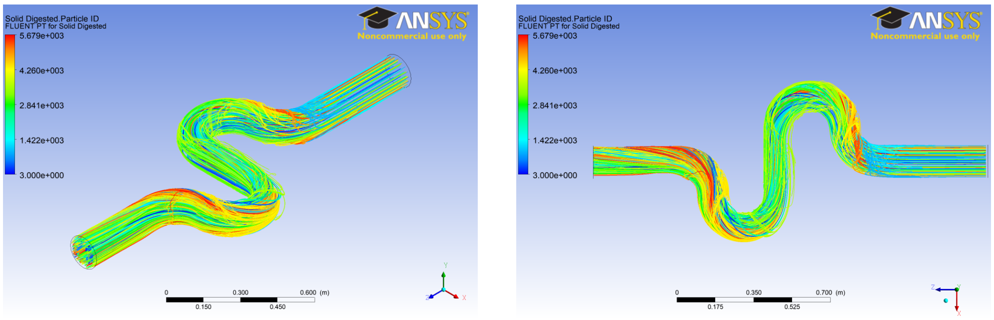

(a) Isometric view. (b) Top view, ZX-plane.

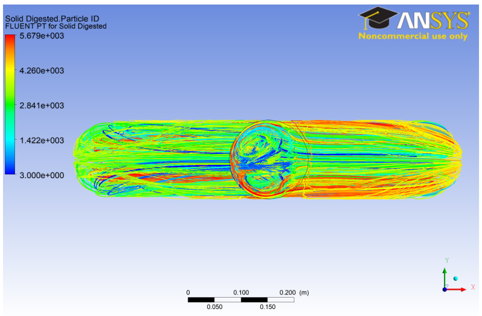

(c) Front view, XY-plane.

Figure C.5.4: Particle tracks coloured by particle ID number of Case 2 - Two Bends.

C.5.3 Case 3 - Injection

The pressure drop in the third case was small, namely $\Delta P = 0.688$ kPa, see figure C.5.5 (a). Stream downwards, after the injection pipe, there was an area of negative pressure. The flow of digested sludge was pushed around the injection pipe, see figure C.5.5 (b), but at the bottom of the straight pipe, after the injection pipe, the velocity dropped. This might be a point where sludge would stick, but it was expected that this risk would be low and that the sludge would flow nicely around the injection pipe. After the injection the flow developed towards a fully developed flow.

The particle tracks are depicted in figure C.5.6 with the digested sludge particles coloured yellow and the combination of primary and THP red. There was symmetry in the ZY-plane and it was clear from the three pictures that the two types of sludge did not mix well.

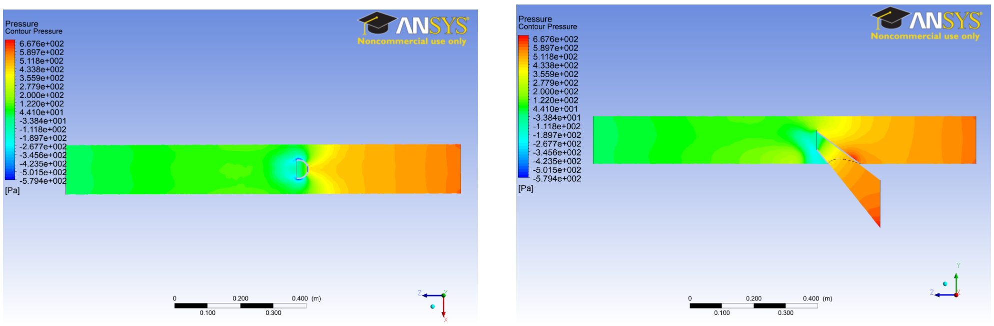

(a) Top view, ZX-plane, ΔP = 0.668 kPa. (b) Side view, YZ-plane, ΔP = 0.668 kPa.

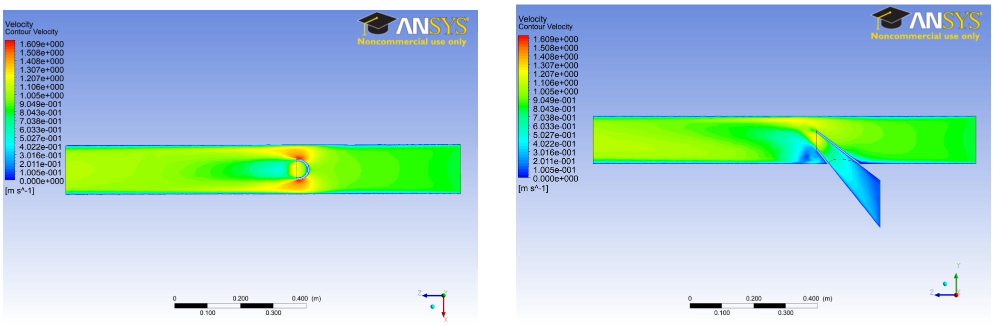

(c) Top view, ZX-plane, $\max(\vec{u})$ = 1.66 m/s. (d) Side view, ZX-plane, $\max(\vec{u})$ = 1.66 m/s.

Figure C.5.5: Pressure and velocity fields of Case 3 - Injection.

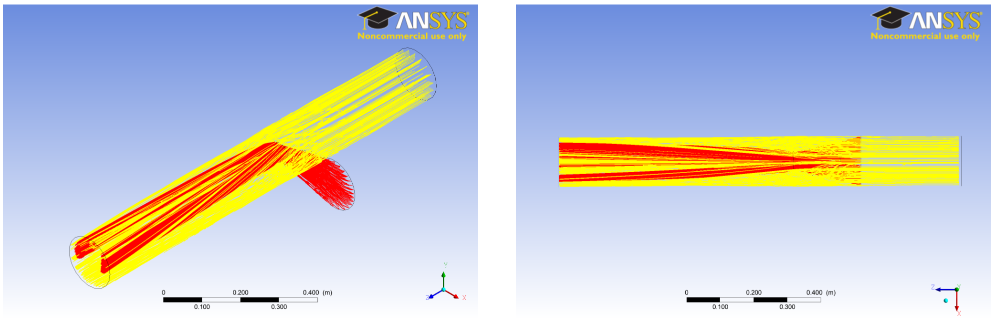

(a) Isometric view.

(b) Top view, ZX-plane.

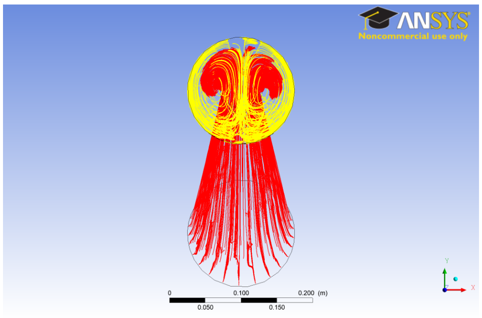

(c) Front view, XY-plane.

Figure C.5.6: Particle tracks coloured red (primary and THP) and yellow (digested) of Case 3 - Injection.

C.5.4 Case 4 - Corkscrew

The pressure drop for the corkscrew of the fourth case, see figure C.5.7 (a), was $\Delta P = 0.774$ kPa and did not pose a problem for the pump capacity. The pressure field was more complex than in the previous cases and there were areas of negative pressure. The velocity field was also more complex than in the cases before, see figure C.5.7 (b). This made it more likely that the sludge would be mixed to some extent.

In the pictures of figure C.5.8 it was noticed that the particles were swirled by the geometry of the corkscrew. At the outlet still a swirling motion was observed. The coloured particles grouped somewhat in cylindrical shells. The sludge was therefore said to be sufficiently mixed. It should be noted however that due to the centrifugal forces in the swirl the sludge might be separated on density differences if these would be present.

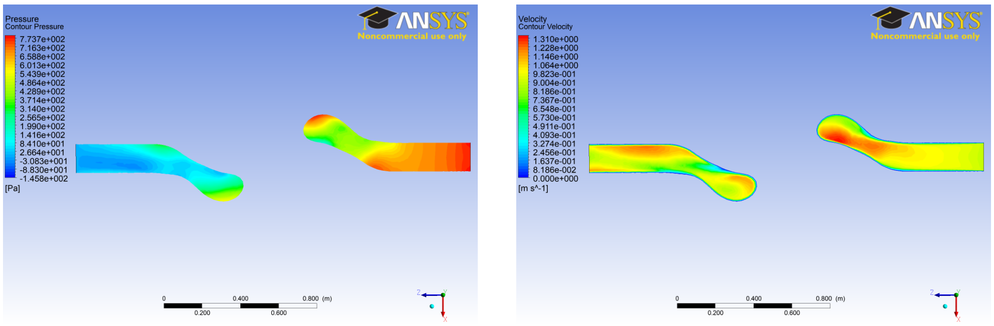

(a) Top view, ZX-plane, $\Delta P = 0.774$ kPa.

(b) Top view, ZX-plane, $\max(\vec{u}) = 1.31$ m/s.

Figure C.5.7: Pressure and velocity fields of Case 4 - Corkscrew.

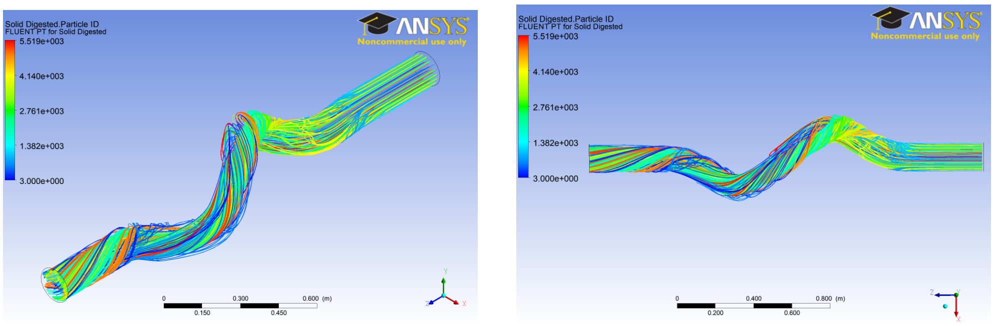

(a) Isometric view.

(b) Top view, ZX-plane.

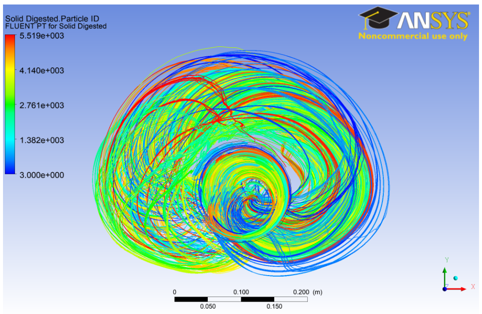

(c) Front view, XY-plane.

Figure C.5.8: Particle tracks coloured by particle ID number of Case 4 - Corkscrew.

C.5.5 Case 5 - Notches

The pressure and velocity field of case five are depicted in figure C.5.9. The pressure drop, $\Delta P = 0.899$ kPa, was relatively small. After the last notches, there was a region of negative pressure. The velocity increased due to the notches, but soon after the flow passed the notches it developed towards fully developed flow. The velocity between the notches dropped to zero, which could result in sludge sticking in the cavities between the notches. This could narrow the pipe, which might not on itself impose a big problem, but clogging could also take place, which would be a bigger problem.

The particle tracks are shown in figure C.5.10. The flow in the middle of the pipe was hardly disturbed by the notches and was still in the middle of the pipe at the outlet.

Again the ZX-plane was a symmetry plane. Thus, the sludge was not well enough mixed by these vertical notches.

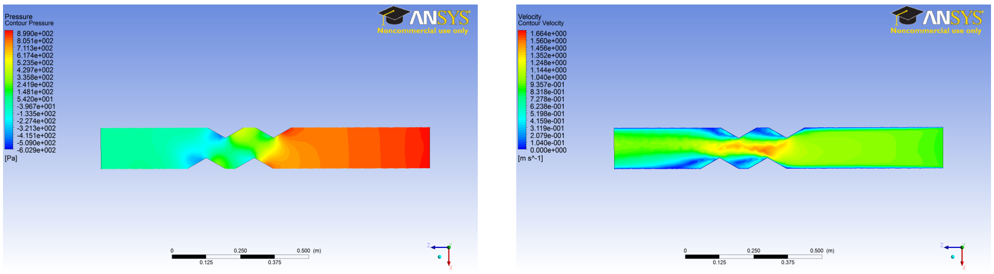

(a) Top view, ZX-plane, $\Delta P = 0.899$ kPa. (b) Top view, ZX-plane, $\max(\vec{u}) = 1.66$ m/s.

Figure C.5.9: Pressure and velocity fields of Case 5 - Notches.

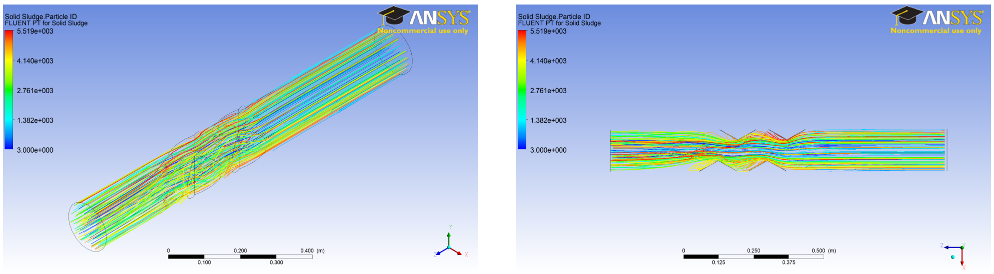

(a) Isometric view. (b) Top view, ZX-plane.

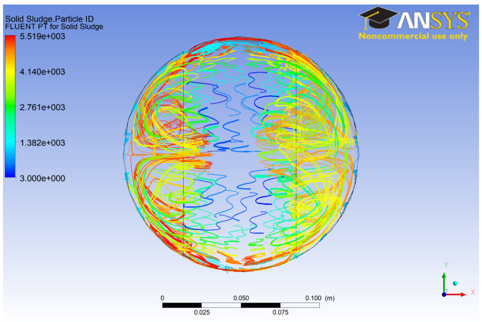

(c) Front view, XY-plane.

Figure C.5.10: Particle tracks coloured by particle ID number of Case 5 - Notches.

C.5.6 Case 6 - Streamlines

The pressure drop in the sixth case, see figure C.5.11 (a), was $\Delta P = 0.648$ kPa, which was relatively small. In the region where the streamlines were there was an area of negative pressure. When the sludge entered the region of the streamlines, the velocity was higher, which was due to the smaller area the sludge was pushed through, see figure C.5.11 (b). The velocity in the middle of the stream was still higher when the flow reached the outlet.

The streamlines swirled the flow near the wall pipe, but the flow in the middle of the pipe remained unaffected by the streamlines, see the particle tracks in figure C.5.12. Hence, the flow was not sufficiently mixed.

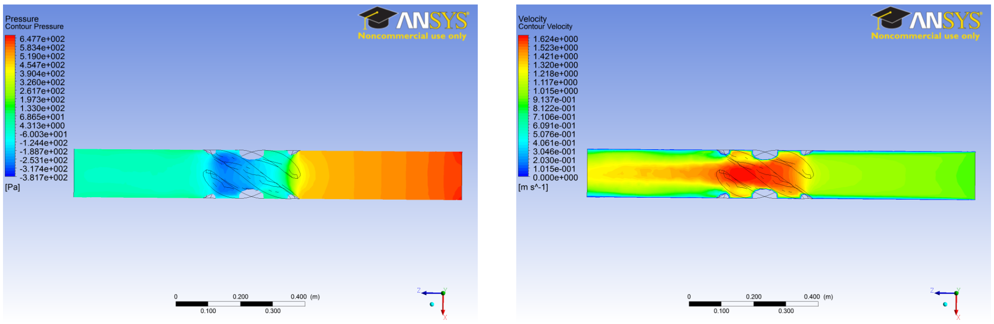

(a) Top view, ZX-plane, ΔP = 0.648 kPa. (b) Top view, ZX-plane, $\max(\vec{u})$ = 1.62 m/s.

Figure C.5.11: Pressure and velocity fields of Case 6 - Streamlines.

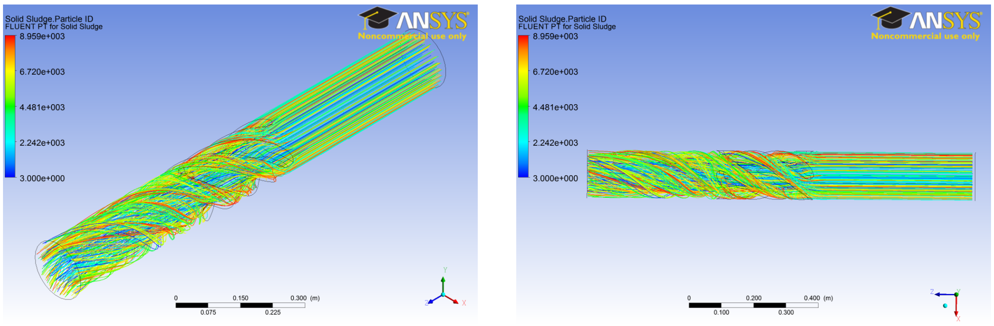

(a) Isometric view. (b) Top view, ZX-plane.

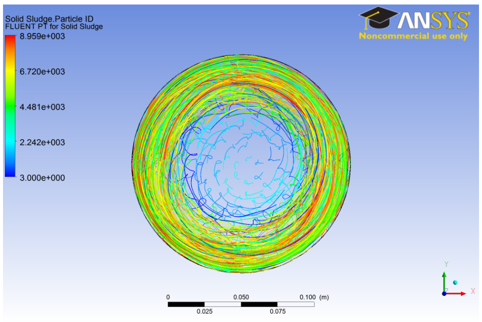

(c) Front view, XY-plane.

Figure C.5.12: Particle tracks coloured by particle ID number of Case 6 - Streamlines.

C.5.7 Case 7 - Opposite Streamlines

For the opposite streamlines of case seven the pressure drop was $\Delta P = 0.827$ kPa and only a small area of a slight negative pressure was present in the second part of the streamlines, see figure C.5.13 (a). The maximum velocity achieved by the opposite streamlines was higher than for the single streamlines of Case 6, but the velocity in the middle of the flow was roughly the same, see figure C.5.13 (b).

Considering the particle tracks in figure C.5.14, it was noticed that the flow near the wall was again well mixed by the carved curves on the pipe wall, but the flow in the middle of the pipe remained relatively unaffected, but to a slightly lesser extent than with one pair of streamlines as in Case 6. Because of the straight flow stream in the middle, the sludge was not said to be well enough mixed.

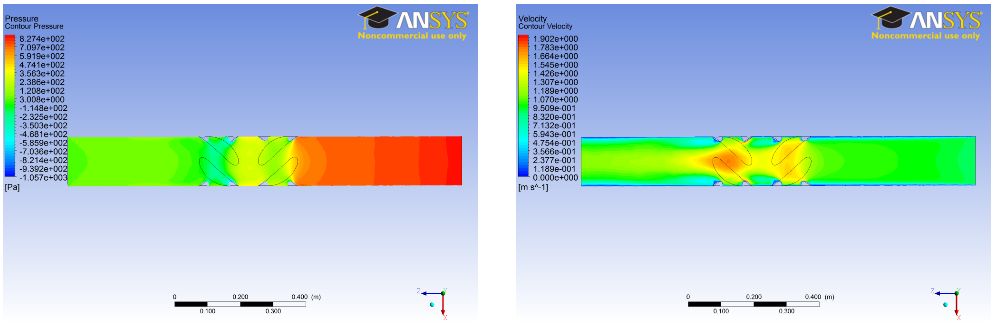

(a) Top view, ZX-plane, $\Delta P = 0.827$ kPa. (b) Top view, ZX-plane, $\max(\vec{u}) = 1.90$ m/s.

Figure C.5.13: Pressure and velocity fields of Case 7 - Opposite Streamlines.

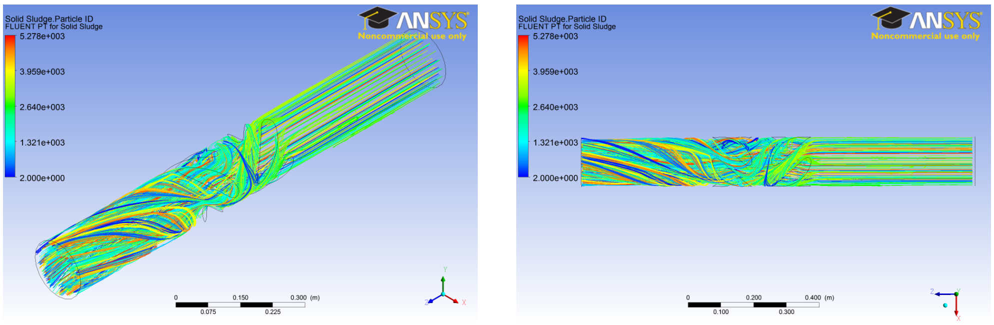

(a) Isometric view. (b) Top view, ZX-plane.

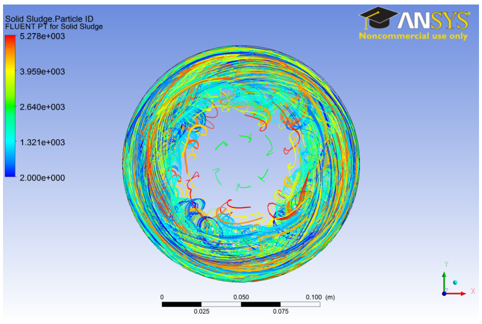

(c) Front view, XY-plane.

Figure C.5.14: Particle tracks coloured by particle ID number of Case 7 - Opposite Streamlines.

C.5.8 Case 8 - One Streamline

The pressure drop of Case 8 was $\Delta P = 0.716$ kPa and relatively small. Near the carved curve on the pipe wall a region of negative pressure was present, see figure C.5.15 (a). As the area through which the flow passed narrowed, the velocity increased, see figure C.5.15 (b). The flow was pushed sidewards to one side after the streamline.

A swirling motion was induced by the carved curve which also affected the middle of the flow, see figure C.5.16. Considering the Isometric view, it could be seen that at the outlet groups of coloured particles could be distinguished, for example in the negative x-direction were more yellow coloured particles whereas in the positive x-direction more light blue and green particles were present. However, because of the swirling motion which affected the centre of the pipe, the sludge was said to be mixed to some extent.

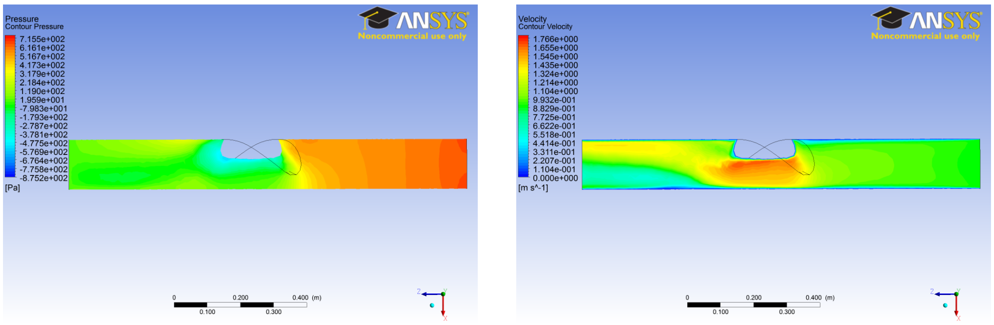

(a) Top view, ZX-plane, $\Delta P = 0.716$ kPa. (b) Top view, ZX-plane, $\max(\vec{u}) = 1.77$ m/s.

Figure C.5.15: Pressure and velocity fields of Case 8 - One Streamline.

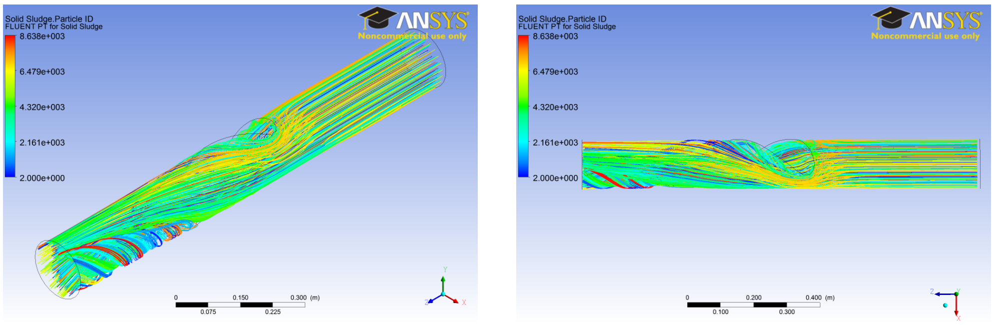

(a) Isometric view. (b) Top view, ZX-plane.

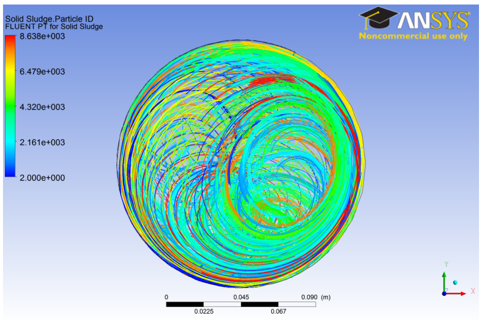

(c) Front view, XY-plane.

Figure C.5.16: Particle tracks coloured by particle ID number of Case 8 - One Streamline.

C.5.9 Case 9 - One Helical Element

In the ninth case the pressure drop was $\Delta P = 0.971$ kPa, see figure C.5.17 (a). The velocity field looked symmetric considering figure C.5.17 (b), with higher velocities near the helical element, which obstructed the flow.

A swirling motion induced by the helical element was observed examining the particle tracks in figure C.5.18. The sludge seemed to be pretty well mixed at the outlet regarding the particle colours.

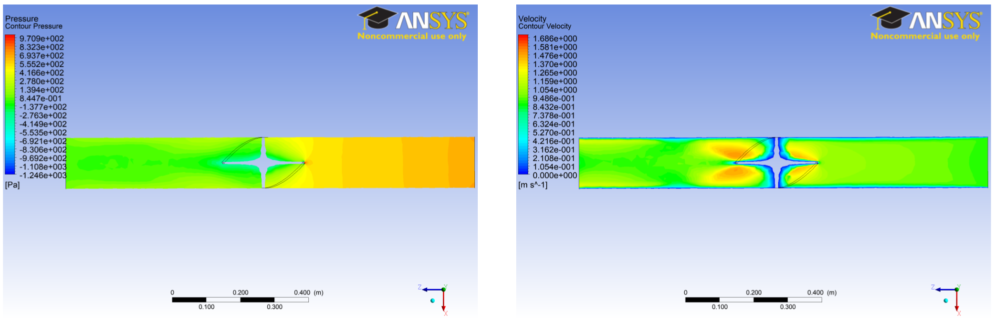

(a) Top view, ZX-plane, $\Delta P = 0.971$ kPa. (b) Top view, ZX-plane, $\max(\vec{u}) = 1.69$ m/s.

Figure C.5.17: Pressure and velocity fields of Case 9 - One Helical Element.

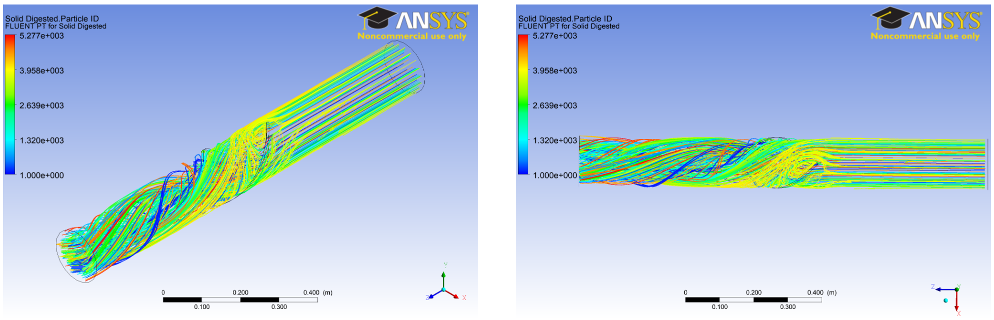

(a) Isometric view. (b) Top view, ZX-plane.

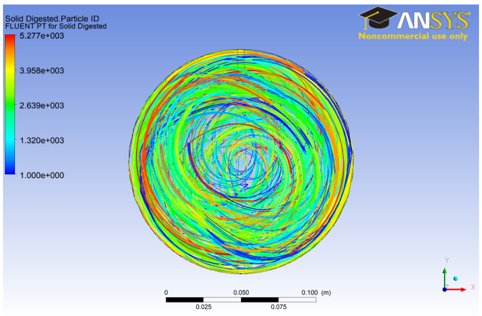

(c) Front view, XY-plane.

Figure C.5.18: Particle tracks coloured by particle ID number of Case 9 - One Helical Element.

C.6 Conclusion

The nine cases were compared in effectiveness of mixing the sludge, how easy and inexpensive they could be produced, and the frequency with which maintenance would be required. The effectiveness of mixing the sludge well was considered more important than the other aspects. The results of this comparison are summarized in table C.6.1.

As can be seen it was expected that the corkscrew of case four and the helical element of case nine would yield sufficient mixing of the sludge. Case 8 - One Streamline would need further optimization to induce better mixing. Despite the possible problems in maintenance of the helical element, this one was chosen as well as the corkscrew of case four to be incorporated in the total piping system and simulated with a mixture of sludge.

	Mixing	Production	Maintenance	Netto rating
Case 1 - One Bend	−	+	+	−
Case 2 - Two Bends	−	+	+	−
Case 3 - Injection	−	+	+	−
Case 4 - Corkscrew	+	O	+	+
Case 5 - Notches	−	O	O	−
Case 6 - Streamlines	−	−	+	−
Case 7 - Opposite Streamlines	−	−	+	−
Case 8 - One Streamline	O	−	+	O
Case 9 - One Helical Element	+	O	−	+

Table C.6.1: Comparison of the nine cases of alternative geometries on basis of effectiveness in mixing, realizability and costs of production, and frequency of maintenance. With '−' a negative rating, '+' a positive rating and 'O' a rating in between.

Appendix D

Additional CFD Models and Results

In this appendix additional CFD results are presented. The first section contains plots of the mass fractions of digested sludge for all models. Also a description and the results of Model 6 - Venturi D50 are given. This model was intended to be validated, but this did not take place.

D.1 Digested Mass Fractions

This section contains plots of the digested mass fractions of all models. These were left out as the mass fractions sum up to 1 and hence the mass fractions of primary and THP sludge gave already all information. However, they are provided in this appendix for the ease of readers. The analysis of the plots is left to the reader.

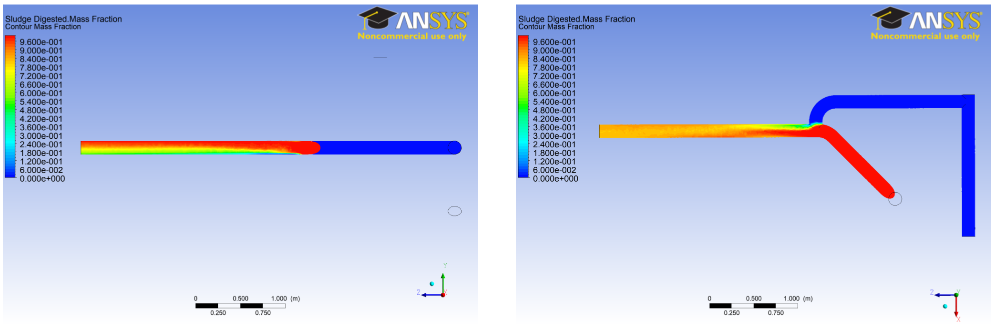

(a) Side view, YZ-plane.

(b) Top view, ZX-plane.

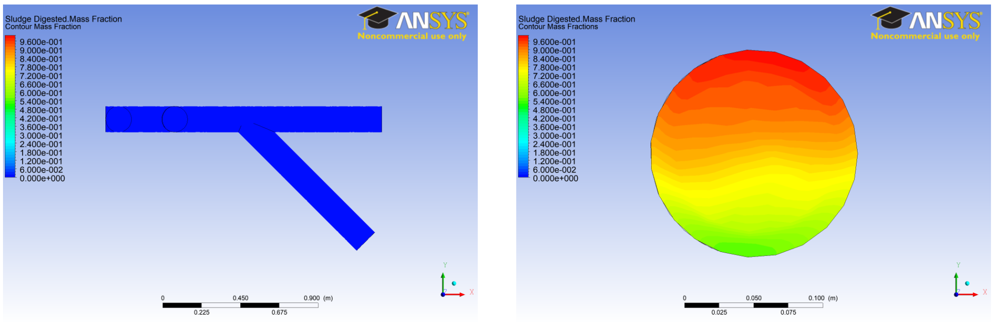

(c) Front view, XY-plane.

(d) Front view, XY-plane, outlet.

Figure D.1.1: Mass fraction of digested sludge in the baseline model with a sludge mixture at $t = 40$ *s.*

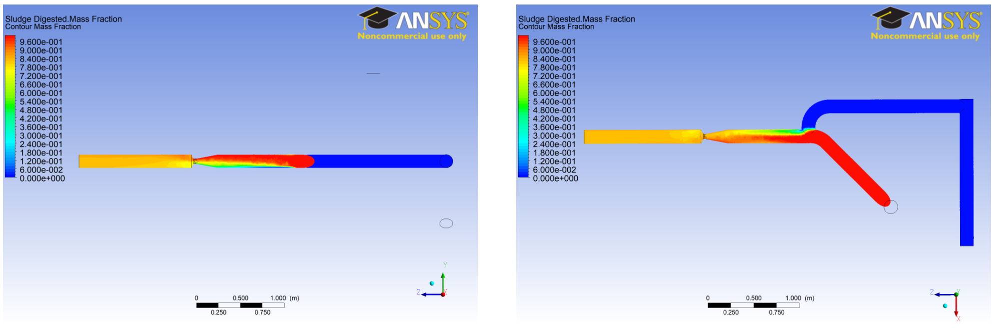

(a) Side view, YZ-plane. (b) Top view, ZX-plane.

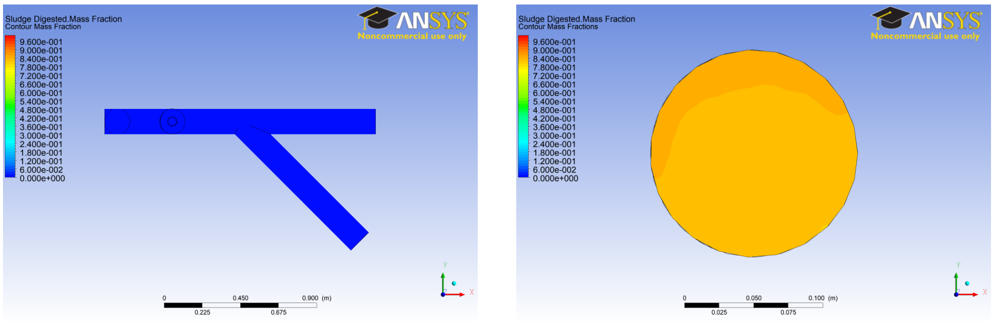

(c) Front view, XY-plane. (d) Front view, XY-plane, outlet.

Figure D.1.2: Mass fraction of digested sludge in the venturi model with a sludge mixture at $t = 40$ *s.*

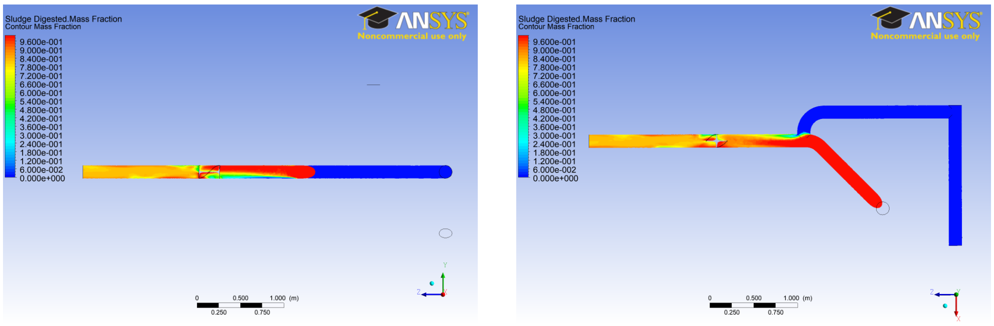

(a) Side view, YZ-plane. (b) Top view, ZX-plane.

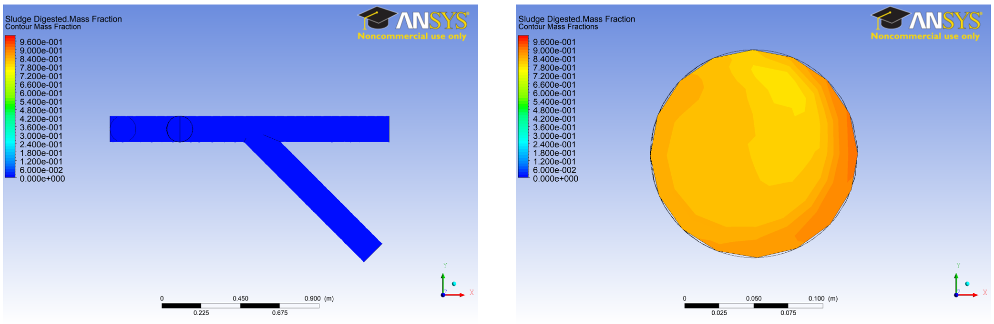

(c) Front view, XY-plane. (d) Front view, XY-plane, outlet.

Figure D.1.3: Mass fraction of digested sludge in the static mixer model with a sludge mixture at $t = 40$ *s.*

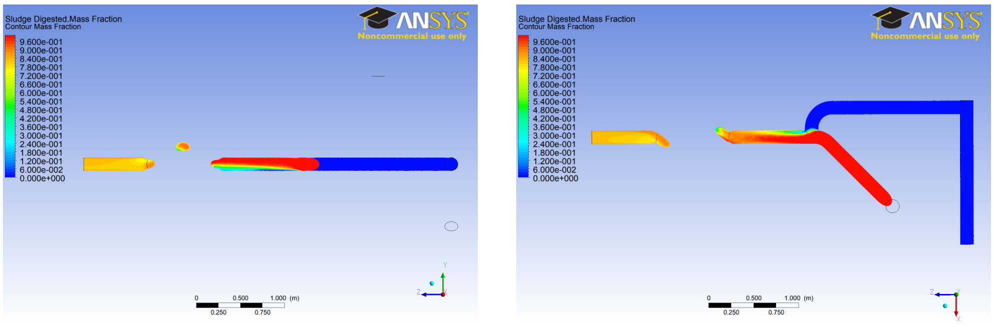

(a) Side view, YZ-plane.

(b) Top view, ZX-plane.

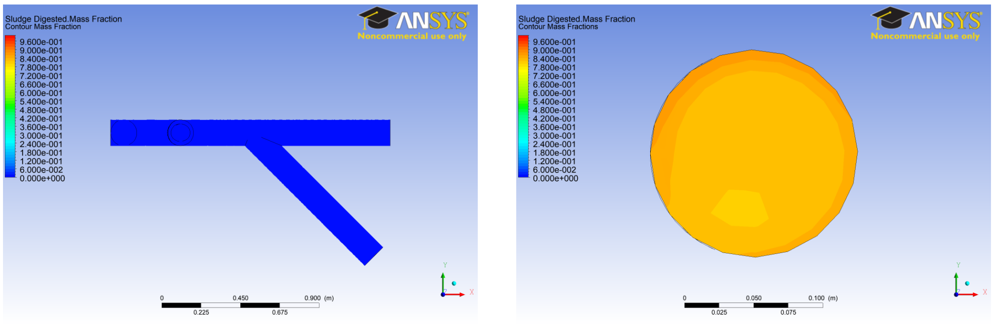

(c) Front view, XY-plane.

(d) Front view, XY-plane, outlet.

Figure D.1.4: Mass fraction of digested sludge in the corkscrew model with a sludge mixture at $t = 40$ *s.*

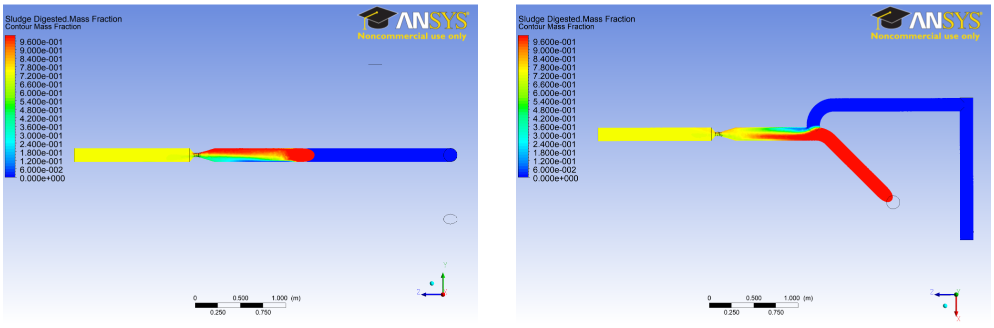

(a) Side view, YZ-plane.

(b) Top view, ZX-plane.

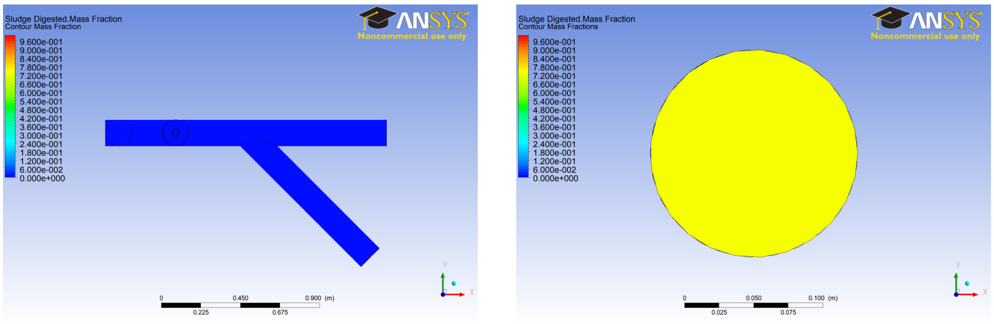

(c) Front view, XY-plane.

(d) Front view, XY-plane, outlet.

Figure D.1.5: Mass fraction of digested sludge in the venturi D40 model with a sludge mixture at $t = 8$ *s.*

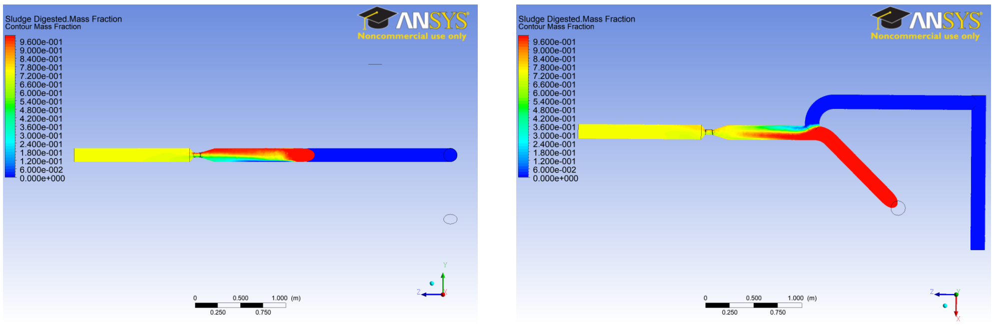

(a) Side view, YZ-plane.

(b) Top view, ZX-plane.

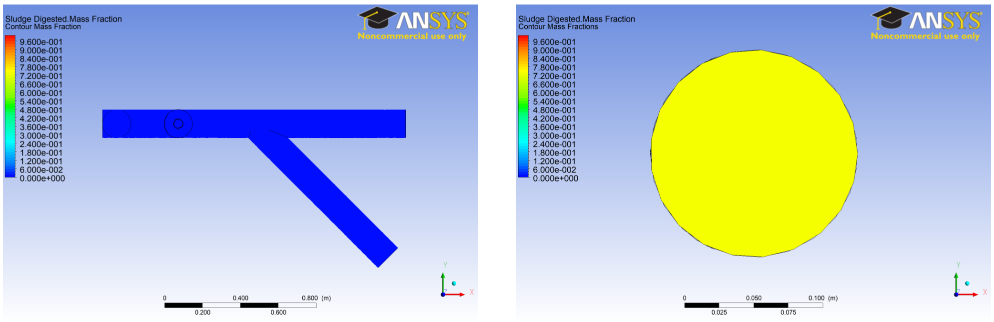

(c) Front view, XY-plane.

(d) Front view, XY-plane, outlet.

Figure D.1.6: Mass fraction of digested sludge in the venturi D50 model with a sludge mixture at $t = 8$ *s.*

D.2 Model 6 - Venturi D50

The sixth model had a venturi with a narrowing of 50 mm. The dimensions were measured at the workshop of the WWTP in Hengelo. This model was build in order to validate the CFD model on pressure. However, in the end, this did not take place. The results are shown, but the analysis is left to the reader.

The Solidworks model and drawing are shown in figure D.2.1. Relevant information about the mesh can be found in table D.2.2. The mesh was considered to be of acceptable quality.

In the calculation of the solution the same settings and physical models were used as for the other models with one exception, namely that the discrete model was not included as it only served for validation of the pressure. Therefore, it ran for a shorter period of time, with the number of time steps of the final solution being 650.

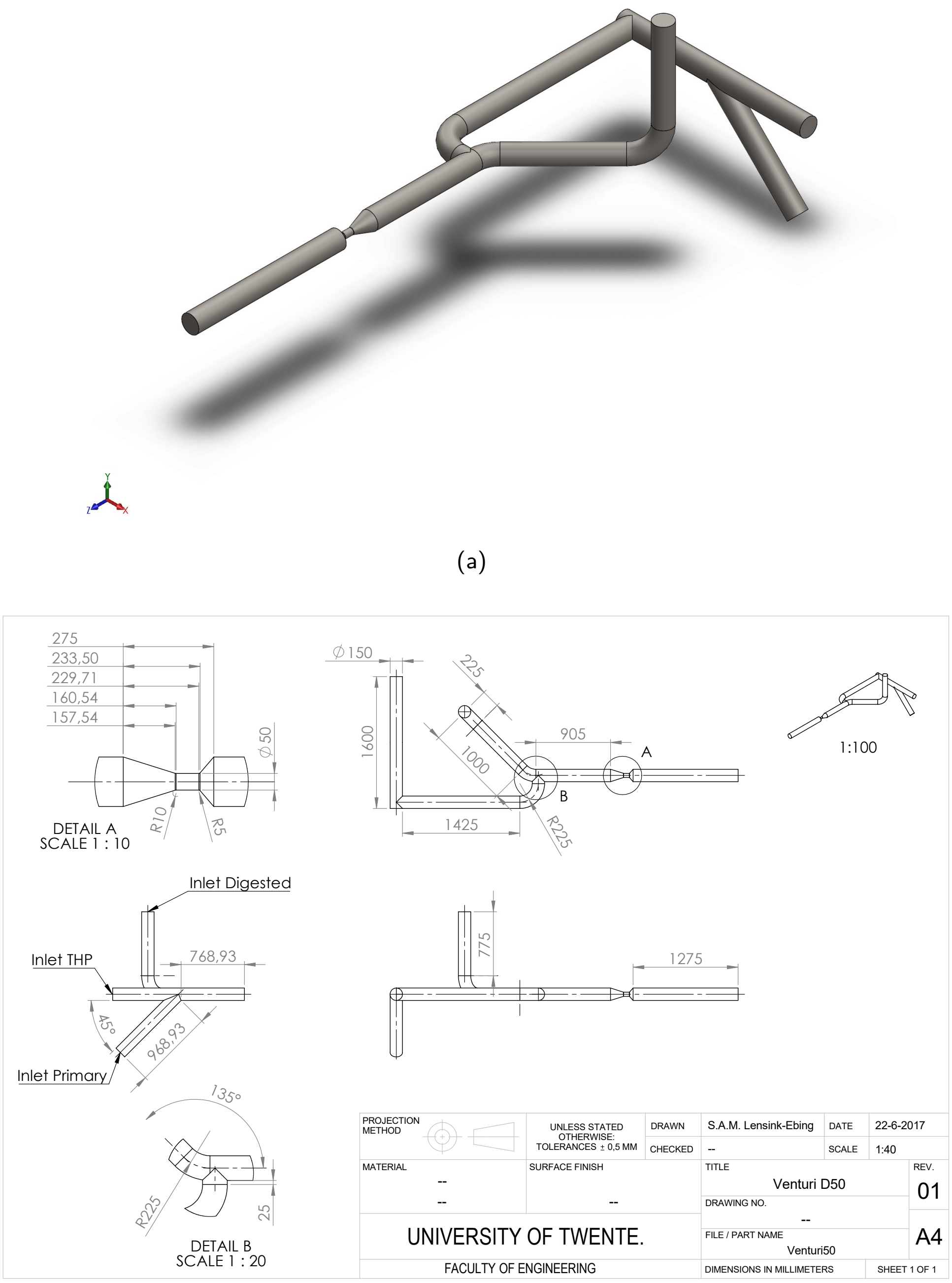

(a)

(b)

Figure D.2.1: Solidworks model and drawing of model 6 - Venturi D50.

Model	# elements	V (m^3)	Orth. Q.	Asp. R.	Skew.
Model 6 - Venturi D50	164984	0.1522	0.1846	54.409	0.8986

Table D.2.2: Relevant information about the meshes used. From left to right the number of elements, the volume of the mesh, the minimum value of the orthogonal quality, the maximum value of the aspect ratio and the maximum value of the skewness.

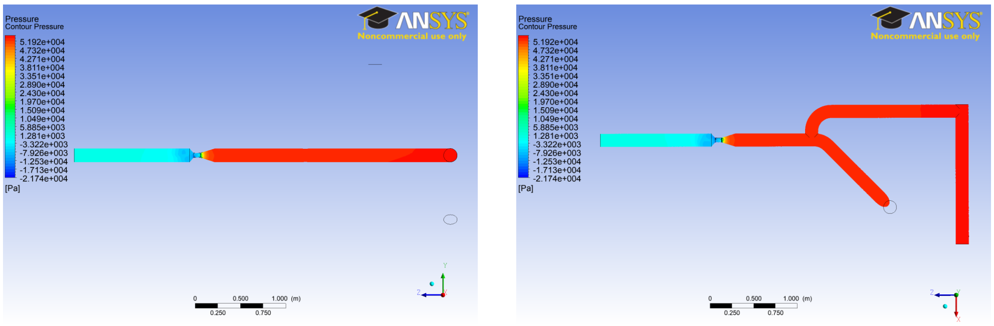

(a) Side view, YZ-plane.

(b) Top view, ZX-plane.

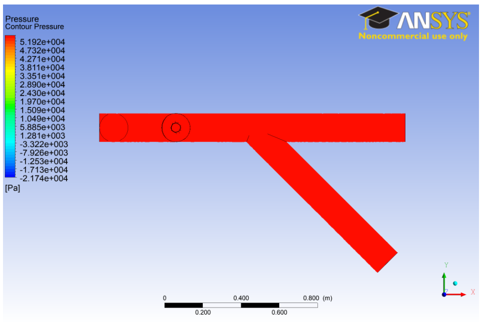

(c) Front view, XY-plane.

Figure D.2.3: Pressure of the venturi D50 model with a sludge mixture at $t = 8$ *s, with* ΔP *= 133.3 kPa.*

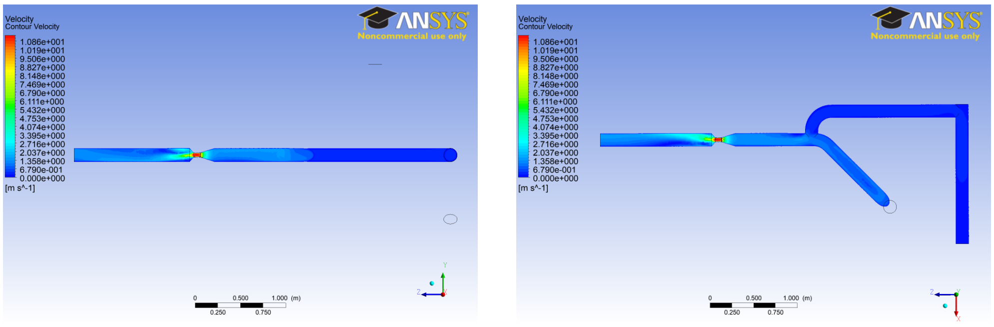

(a) Side view, YZ-plane.

(b) Top view, ZX-plane.

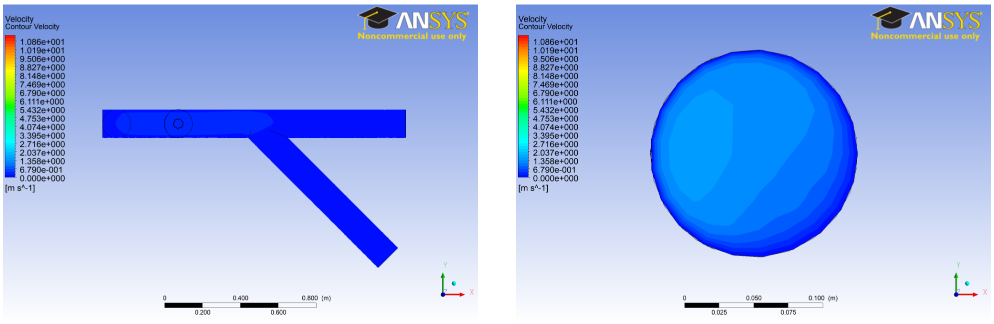

(c) Front view, XY-plane.

(d) Front view, XY-plane, outlet.

Figure D.2.4: Velocity of the venturi D50 model with a sludge mixture at $t = 8$ *s, with* $\max(\vec{u}) =$ *16.95 m/s.*

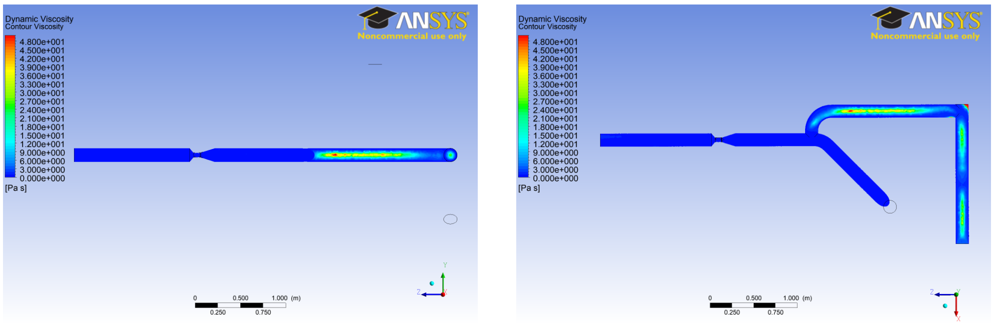

(a) Side view, YZ-plane.

(b) Top view, ZX-plane.

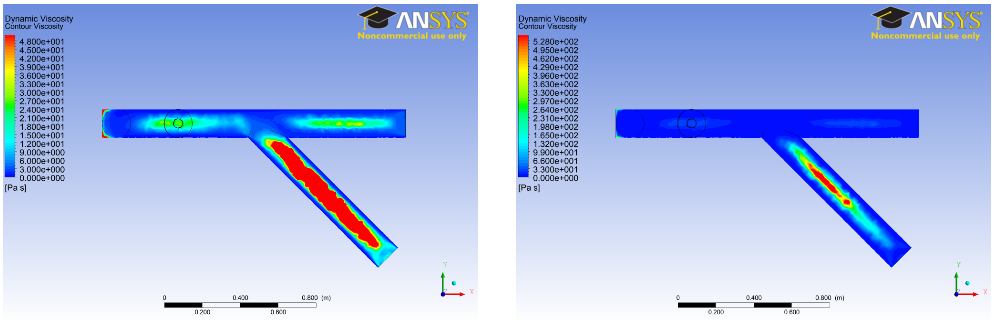

(c) Front view, XY-plane, μ between $0 - 50$ Pa·s..

(d) Front view, XY-plane, μ between $0 - 550$ Pa·s.

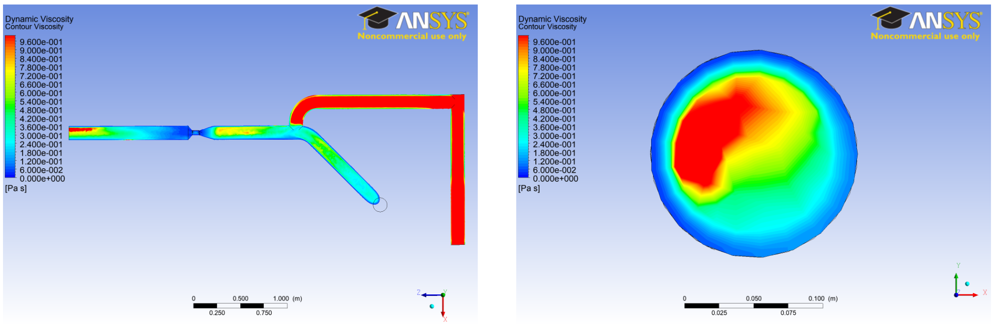

(e) Front view, XY-plane, μ between $0 - 1$ Pa·s.

(f) Front view, XY-plane, outlet with μ between $0 - 1$ Pa·s.

Figure D.2.5: Dynamic viscosity ranging from $0 - 50$ Pa·s for (a), (b) and (c), from $0 - 550$ Pa·s for (d), and from $0 - 1$ Pa·s for (e) and (f), of the venturi D50 model with a sludge mixture at $t = 8$ s.

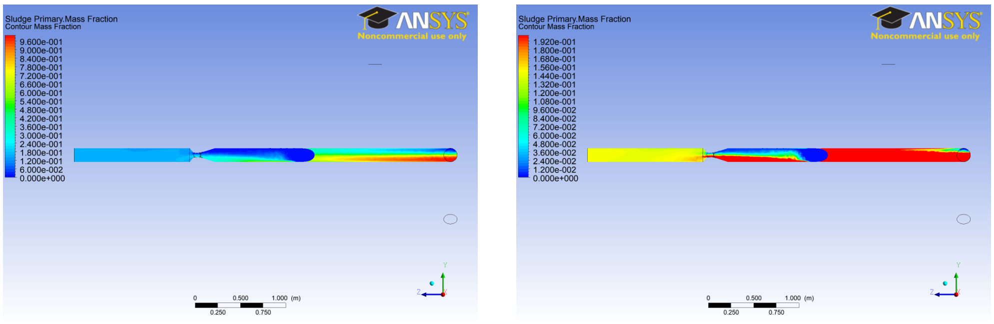

(a) Side view, YZ-plane. (b) Side view, YZ-plane, $0 \leq y_p \leq 0.2$.

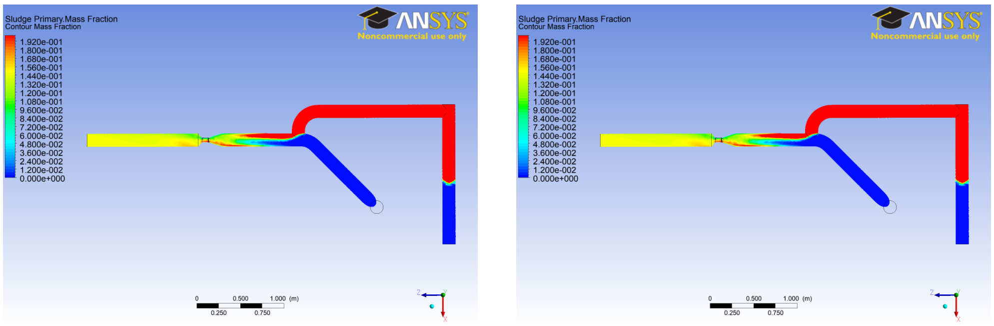

(c) Top view, ZX-plane. (d) Top view, ZX-plane, $0 \leq y_p \leq 0.2$.

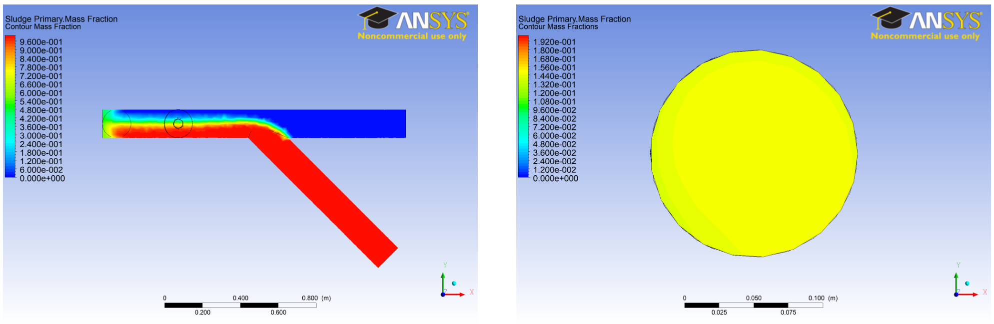

(e) Front view, XY-plane. (f) Front view, XY-plane, outlet, $0 \leq y_p \leq 0.2$.

Figure D.2.6: Mass fraction of primary sludge in the venturi D50 model with a sludge mixture at $t = 8$ s.

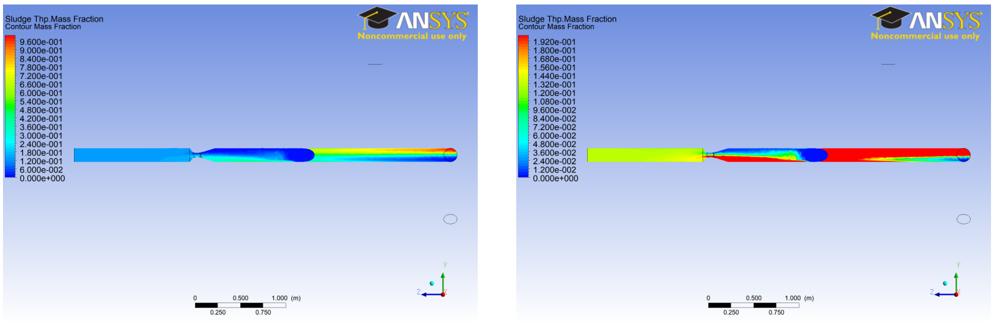

(a) wastewater, YZ-plane.

(b) wastewater, YZ-plane, $0 \le y_t \le 0.2$.

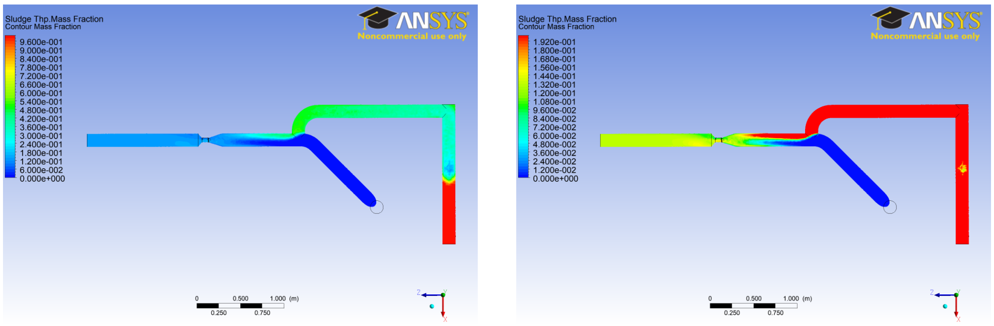

(c) Top view, ZX-plane.

(d) Top view, ZX-plane, $0 \le y_t \le 0.2$.

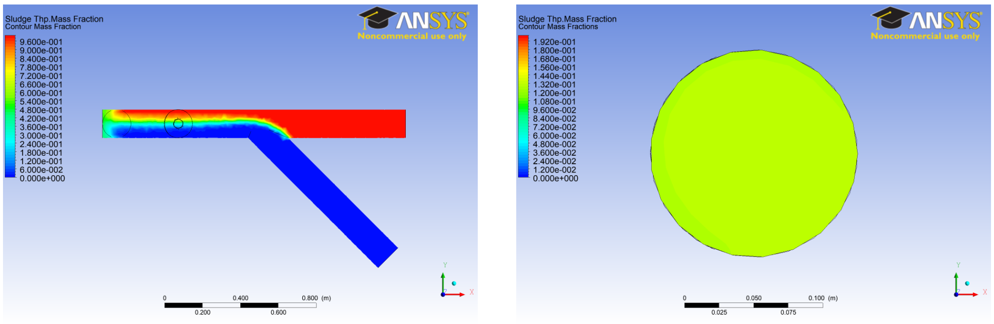

(e) Front view, XY-plane.

(f) Front view, XY-plane, outlet, $0 \le y_t \le 0.2$.

Figure D.2.7: Mass fraction of THP sludge in the venturi D50 model with a sludge mixture at $t = 8$ *s.*

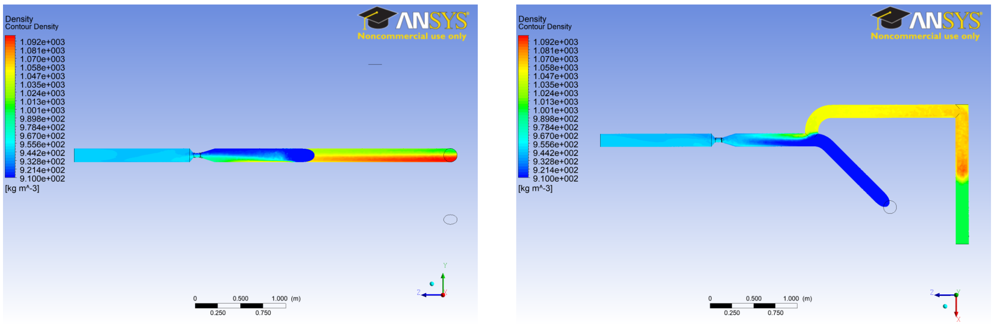

(a) Side view, YZ-plane.

(b) Top view, ZX-plane.

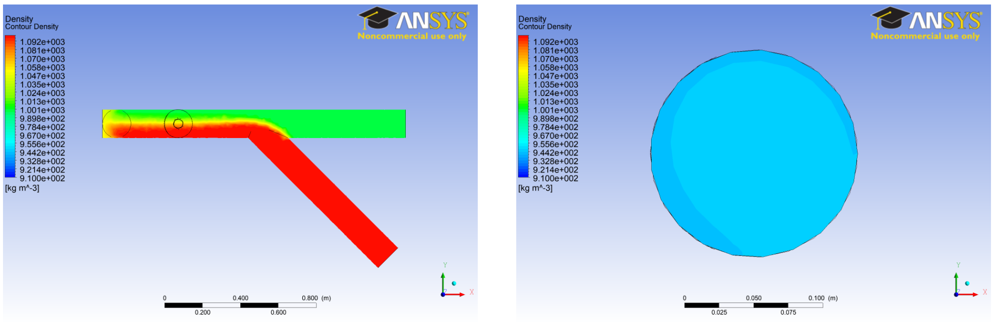

(c) Front view, XY-plane.

(d) Front view, XY-plane, outlet.

Figure D.2.8: Density of the venturi D50 model with a sludge mixture at $t = 8$ *s.*

Appendix E

Quest for a Suitable Validation Instrument

In order to find a suitable validation instrument many issues had to be tackled. The high operational temperature and pressure and the high dry solids content formed a huge challenge. Non-invasive instruments were therefore preferred.

The quest focused first on validating the turbulent nature of the flow as the idea in installing a venturi was to generate turbulence and in this way improve the mixing. A turbulent flow is characterised by chaotic behaviour in time. This is seen in local fluctuations such as eddies, but the average of variables such as the velocity remain roughly constant over time. To measure these fluctuations local measurements in time were needed.

As it appeared to be very hard to find an instrument which was able to do this in the limited time of this internship, within the budget and providing valuable results, the focus shifted towards measuring the quality of mixing.

E.1 Velocity

Mainstream flowmeters measure the average velocity over the diameter of a pipe. Examples of these instruments are Coriolis, electromagnetic and ultrasonic flowmeters.

Coriolis Flowmeter

The Coriolis mass flowmeter consists of two or more tubes which are subjected to an artificial oscillation. This oscillation changes in time and place when fluid enters these tubes. Based on this difference in oscillation the mass flow is calculated. From this calculation no information about local fluctuations in the diameter could be extracted (Endress+Hauser, 2017).

Electromagnetic Flowmeter

An electromagnetic flowmeter is based on Faraday's law of induction. A magnetic field is applied across the diameter. When electrically charged particles pass this field, an electrical voltage is induced, which is proportional to the velocity of the flow. Because of this measuring principle, the fluid should be conductive. However, an electromagnetic flowmeter could not be used as validation because no information about local fluctuations could be extracted from this measurement (Endress+Hauser, 2017).

Ultrasonic Flowmeter

Ultrasonic flowmeters use the Doppler principle. They are produced in different arrangements. In case of two clamp-on sensors an ultrasonic signal is send by the first sensor downstream to the second, bouncing off the wall, and the second sends a signal upstream to the first. The difference in time of arrival between these signals is directly proportional to the velocity of the flow. This measurement gives an average of the flow velocity (Flexim, 2017b).

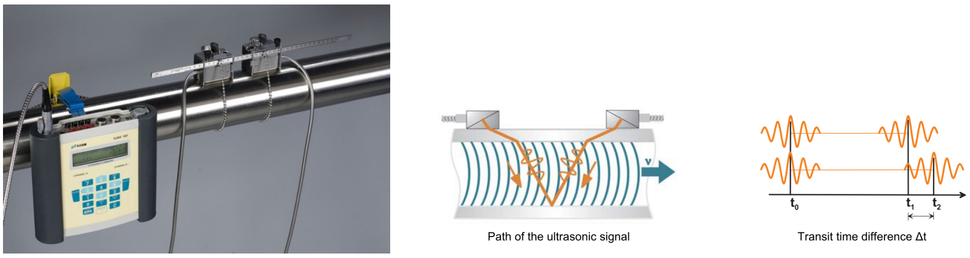

(a) Installed ultrasonic flowmeter.

(b) Illustration of the working principle.

Figure E.1.1: Photo of the installed clamp-on Flexim FLUXUS F601 ultrasonic flowmeter (Flexim, 2017a) and the working schematically illustrated (Flexim, 2017b).

By mounting four sensors such that one set of two sensors measures along another axis than the other two, both in longitudinal direction, fluctuations in velocity might be measured in time between those two sets. This could be an indication of turbulence. However, these meters are usually not used in turbulent flow regimes, so it is unsure how well they perform in turbulent flow and how reliable the measurements are.

Another option could be the Isco Hot Tap which is able to measure a velocity profile across the diameter (Isco, 2017a). It consists of a sensor with four ceramic crystals which can send and receive acoustic signals. When those waves encounter particles in the flow, they are echoed back. By comparing the frequency between the send and received signals the velocities of the particles in the flow can be calculated. See figure E.1.2 for a picture of the sensor and an illustration of its working. However, this tap was invasive and therefore subjected to the temperature and pressure of the flow and also to corrosion by the sludge. The temperature and pressure were too high for the tap, the risk of sludge sticking to the sensor was considered too high, and the costs were not within budget.

E.2 Temperature

The three sludge streams differed in temperature. Therefore another option to validate the model would be to measure the temperature across the diameter and to see whether this was uniform. A uniform temperature accros the diameter would indicate a sufficiently mixed sludge mixture, whereas the presence of a temperature gradient would indicate that the mixture was not sufficiently mixed.

However, validation on temperature is not done for two reasons. The first is that heat transfer in the form of conduction takes place between the different sludge streams and in this way the temperature distribution becomes more uniform. In which amount heat transfer contributes to the temperature distribution is not clear beforehand. The second reason is that temperature measurements are usually done by inserting a probe

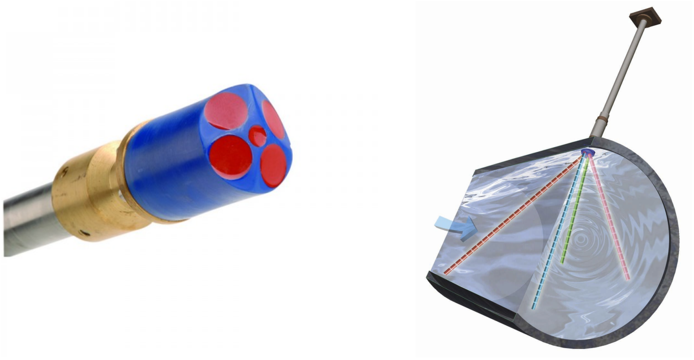

(a) Sensor.

(b) 3D view.

Figure E.1.2: Picture of the sensor of the Isco Hot Tap, (Isco, 2017c), and the working of the tap illustrated by a 3D view, (Isco, 2017b).

in the flow. The risk of sludge sticking to this probe and causing clogging of the pipes was considered too high.

E.3 Density

Because the three sludge streams differed in density when measured at WVS, validation on this variable would also be an option. The Dens-Itometer is able to measure a density profile over the pipe cross-section (ITS, 2017). The measurement is based on electrical resistance tomography and makes use of an electric field to detect conductive and non-conductive particles in the flow. Based on this the density is determined. However, the costs were too high.

E.4 Dry Solids Content

Another option was to validate on dry solids content as these were different for all sludge streams. This could be done by making a sampling point with an expendable sampling tube to sample over the entire diameter. Care should be taken that no short-cut of flow arises and hence flow of a different region is sampled. This could be done by sampling downstream very slowly.

E.5 Conclusion

The dry solids content sampling point was eventually chosen as it provided a direct measurement of the quality of mixing. The other methods had more uncertainty whether the extracted data would be useful and whether the model could be validated when the data was useful. Besides, the costs were lower.

As a venturi was already installed with two pressure meters on each side to measure the pressure drop over the venturi, this instrument was also chosen as a validation instrument.